

# CHIRAL METAMATERIALS FABRICATED BY DYNAMIC SHADOWING GROWTH

by

YIZHUO HE

(Under the Direction of Yiping Zhao)

## ABSTRACT

Metamaterials have demonstrated unusual electromagnetic properties, which enable various novel applications, such as sub-wavelength imaging and optical filters. Now it has come to the time to realize these applications with metamaterial based devices. One of the greatest challenges of the metamaterial applications is the fabrication of large-area metamaterials. In this dissertation, we describe a simple and scalable fabrication technique for chiral metamaterial, which is an important branch of metamaterials with a great capability of manipulating polarizations of light. Our fabrication technique is based on dynamic shadowing growth on self-assembled colloidal monolayers, which mainly employs the shadowing effect of regular colloidal nanospheres during physical vapor depositions to produce ordered arrays of chiral nanostructures.

Using this fabrication technique, two strategies for preparing chiral nanostructures have been demonstrated. The first strategy is to create a single layer of quasi-three-dimensional nanostructure films with chiral shape on nanospheres in one plasmonic material, such as silver. A systematic study reveals that various nanostructures can be created using this method by simply tuning the monolayer orientations with respect to the incident vapor. Fan-shaped chiral nanostructures obtained at a particular monolayer orientation exhibit giant chiral optical response with fabrication conditions optimized. The second strategy is to create three-dimensional multiple

layers of chiral nanostructures with one plasmonic material, such as silver, and one dielectric material, such as silicon dioxide. The plasmonic or dielectric layers are helically stacked forming two helices twisted together. Two different chiral structures have been realized by this method, helically stacked plasmonic layers, and Swiss roll nanostructures.

Finally, we demonstrate that this dynamic shadowing growth fabrication method can be used for developing chiral optical devices. The fan-shaped chiral nanostructures are fabricated on a monocrystalline monolayer on  $1\text{ cm}^2$  substrate, which can be potentially developed as a narrow-band circular polarizer after annealing. Active chiral optical device can be obtained by transferring such large-area chiral metamaterial into a flexible polymer substrate, whose optical property can be tuned by mechanical deformations. The fabricated chiral metamaterial can also be used as a localized surface plasmon resonance based sensor for refractive index sensing, with an enhanced sensitivity.

**INDEX WORDS:** Chiral Metamaterials, Dynamic shadowing growth, Self-assembled colloidal monolayer, Plasmonics, Localized surface plasmon resonance, Chiral optical device

CHIRAL METAMATERIALS FABRICATED BY DYNAMIC SHADOWING GROWTH

by

YIZHUO HE

B.S., Nankai University, China, 2010

A Dissertation Submitted to the Graduate Faculty of The University of Georgia in Partial  
Fulfillment of the Requirements for the Degree

DOCTOR OF PHILOSOPHY

ATHENS, GEORGIA

2016

© 2016

Yizhuo He

All Rights Reserved

CHIRAL METAMATERIALS FABRICATED BY DYNAMIC SHADOWING GROWTH

by

YIZHUO HE

Major Professor:	Yiping Zhao
Committee:	Susanne Ullrich
	William M. Dennis
	Tho Nguyen
	Peter Kner

Electronic Version Approved:

Suzanne Barbour  
Dean of the Graduate School  
The University of Georgia  
May 2016

## DEDICATION

Dedicated to my grandparents, who taught me so much in my childhood.

## ACKNOWLEDGEMENTS

I would like to express my sincere gratitude to my advisor Prof. Yiping Zhao for his support, supervision and guidance through my doctoral program. I also would like to express my appreciation to Prof. Susanne Ullrich for her valuable guidance in optical experiments and Prof. William M. Dennis for his help in numerical simulations. My grateful thanks are also extended to Prof. Tho Nguyen and Prof. Peter Kner for serving on my advisory committee. Finally, I want to express my gratitude to my lab mates and colleagues, Dr. Yuping He, Dr. Kun Yao, Dr. John Gibbs, Dr. Justin Abell, Dr. George Larsen, Dr. Manoj Manjare, Dr. Xiaomeng Wu, Dr. Jing Chen, Dr. Pradip Basnet, Dr. Tomas Lanier, Dr. Nicholas Evans, Dr. Hui Yu, Mr. Weijie Huang, Ms. Whitney Ingram, Ms. Lu Zhu, Mr. Steven Larsen, Mr. Layne Bradley, Mr. Rui Cheng, Mr. Keelan Lawrence, Mr. Keenan Stone, Mr. Daniel Carlson, and Mr. Connor Skehan, for their generous help and the pleasant time we spent.

## TABLE OF CONTENTS

	Page
ACKNOWLEDGEMENTS .....	v
LIST OF TABLES .....	viii
LIST OF FIGURES .....	ix
CHAPTER	
1 INTRODUCTION .....	1
1.1 Metamaterials and chiral metamaterials .....	1
1.2 Plasmonics .....	4
1.3 Chiral optical effects .....	7
1.4 Chiral metamaterial based devices.....	17
1.5 Dissertation overview .....	22
2 FABRICATION, CHARACTERIZATION AND SIMULATION.....	24
2.1 Brief review of current fabrication methods.....	24
2.2 Dynamic shadowing growth .....	30
2.3 Self-assembled colloidal monolayer .....	34
2.4 Morphology calculation .....	36
2.5 Morphological characterizations.....	42
2.6 Optical characterizations.....	43
2.7 Finite-difference time-domain simulation .....	46
3 CHIRAL PATCHY PARTICLES .....	52

3.1	Introduction.....	52
3.2	Racemic patchy particles .....	52
3.3	Effect of monolayer orientations .....	56
3.4	Optimization of chiral optical response of Ag fan-shaped nanostructures .....	66
3.5	Fan-shaped chiral nanostructures in different materials .....	78
3.6	Conclusions.....	80
4	HELICALLY STACKED PLASMONIC NANOSTRUCTURES .....	83
4.1	Introduction.....	83
4.2	Helically stacked plasmonics layers .....	84
4.3	Swiss Roll metamaterials.....	97
4.4	Conclusions.....	107
5	CHIRAL METAMATERIAL BASED OPTICAL DEVICES.....	109
5.1	Introduction.....	109
5.2	Large-area chiral optical device.....	109
5.3	Flexible chiral metamaterials .....	113
5.4	Application for bulk refractive index sensing.....	125
6	SUMMARY AND OUTLOOK.....	135
	REFERENCES .....	137

## LIST OF TABLES

	Page
Table 2.1.1: Representative chiral metamaterials with their fabrication methods and chiral optical response.....	25
Table 2.7.1: The fitting parameters for modified Debye-Drude model of metals .....	50
Table 3.4.1: Structural and spectral parameters of Ag fan-shaped nanostructures with different $\theta$ .....	68
Table 4.2.1: Geometric parameters of HSPLs on nanospheres with different diameter, $d$ .....	89
Table 4.3.1: Structural parameters of Swiss roll nanostructures .....	103
Table 5.4.1: Sensitivity, FWHM, and FOM for peaks and valleys .....	129

## LIST OF FIGURES

	Page
<p>Figure 1.1.1: (A) Illustration of negative refraction at an interface between media with positive and negative refractive indices. (B) Photograph of the metamaterial with negative refractive index in microwave region, which contains copper wires and split ring resonators. (C) Scanning electron microscopy image of the fishnet metamaterial with negative refractive index in optical region. The inset shows alternating layers of 30 nm of Ag and 50 nm of MgF<sub>2</sub>.....</p>	2
<p>Figure 1.2.1: Schematic illustration of (a) surface plasmons, and (b) localized surface plasmons ...</p>	5
<p>Figure 1.3.1: (a) The incident linearly polarized light, which can be decomposed into two coherent components in RCP and LCP. (b) The exiting light after travelling in a medium with CB, which has a linear polarization rotated by an angle of <math>\alpha</math>. (c) The exiting light after travelling in a medium with CD, which an elliptical polarization with an ellipticity <math>\psi</math>. (d) The exiting light after travelling in a medium with both CB and CD, which has an elliptical polarization with an ellipticity <math>\psi</math> and a rotated angle <math>\alpha</math> of the major axis .....</p>	8
<p>Figure 1.3.2: The intuitive illustrations of the interactions between achiral and chiral particles and polarized light. (a) Achiral particles interact with linearly polarized light, causing electron cloud oscillating linearly along the electric field. (b) Achiral particles interact with circularly polarized light, causing electron cloud rotating around the</p>	

particles. Chiral structures interact with (c) RCP, and (d) LCP light. The rotation of the electron cloud can be favored or hindered depending on the combination of chiral geometry and direction of circularly polarized light. ....11

Figure 1.3.3: Chiral molecules and micro/nano-structures with different origins of chiral optical effects. (a)-(f) helical chirality, (g)-(i) chiral coupling, (j)-(l) supramolecular chirality, (m)-(o) pseudo/extrinsic chirality, and (p)-(r) chiral scaffolds .....12

Figure 1.3.4: 3D distribution of the optical chirality enhancement factor  $\hat{C}$  near the multiple Au helices .....17

Figure 1.4.1: (a) Au helical microstructures as a broadband circular polarizer in IR region. (b) Stacked plasmonic rods as a broadband circular polarizer in visible to near-IR region. (c) S-shaped nanohole arrays as a 90°-polarization rotator at a wavelength of 1089 nm. (d) Chiral gyroid networks as a chiral beam splitter around 1.615  $\mu\text{m}$ . (e) Chiral metamaterial based circularly polarized light detector.....18

Figure 1.4.2: (a) Chiral structures consisting of Au bars and Si pads with chiral optical response switched by optical excitation. (b) Chiral plasmonic nanostructures combined with a phase change material  $\text{Ge}_3\text{Sb}_2\text{Te}_6$ . The large change in dielectric constant of  $\text{Ge}_3\text{Sb}_2\text{Te}_6$  induced by phase transition shifts the CD spectra. (c) A planer spiral that can be deformed into a 3D spiral in different handedness by a pneumatic force, with tunable chiral optical response .....20

Figure 1.4.3: (a) Nonlinear optical activity generated by an extrinsic chiral metamaterial. (b) Giant difference in second-harmonic response between LCP and RCP excitation from a twisted arc chiral metamaterial. (c) Superchiral field based sensing for enantiomers using gammadion chiral plasmonic structures .....22

Figure 2.1.1: Schematic illustrations for top-down methods (a) EBL and (b) DLW, bottom-up methods (c) self-assembly on DNA template and (d) self-assembly of block copolymers, and hybrid methods between top-down and bottom-up (e) FIBID and (f) mask-assisted PVD.....27

Figure 2.2.1: (a) Schematic diagram of DSG in a vacuum deposition system. (b) Schematic diagram of the initial nuclei formation, the nanorod growth under shadowing effect, and the obtained nanorod array (from top to bottom) .....31

Figure 2.2.2: (A)–(F) Schematics and (A')–(F') SEM images of typical nanorod arrays fabricated by DSG. (A) Titled nanorods and (A') titled Si nanorods deposited at  $\theta = 80^\circ$ ; (B) vertical nanorods and (B') vertical Si nanorods deposited at  $\theta = 86^\circ$ ; (C) helical nanorods and (C') regular array of helical Si nanorods; (D) and (D') zigzag nanorods; (E) C-shaped nanorods and (E') C-shaped MgF<sub>2</sub> nanorods. (F) bead-like nanorods and (F') bead-like Si nanorods .....33

Figure 2.2.3: (A) Top- and (B) side-view images comparing aperiodic (left) and periodic (right) Si nanorods by DSG. The periodic Si nanorods are grown on a seed layer .....33

Figure 2.3.1: (a) The experimental setup for preparing self-assembled colloidal monolayers. (b) The formation of monolayers in Petri dish. (c) The obtained monolayer on a glass substrate. (d) Top-view SEM image of the nanosphere monolayer with  $d = 750$  nm.....35

Figure 2.4.1: Cross-sectional and (b) top view of DSG on a hexagonal nanosphere array. (c) The surface of the nanosphere is split into many surface elements for calculating the thickness distribution. (d) Each surface element  $(\theta, \varphi)$  with its surface normal  $\hat{n}$  .37

Figure 2.4.2: Graphic user interface of the morphology calculation program.....40

Figure 2.4.3: The calculated morphology of the nanostructures fabricated by an OAD at $\theta_0 = 86^\circ$ and $\varphi_0 = 0^\circ, 5^\circ, 10^\circ \dots 60^\circ$ .....	41
Figure 2.5.1: Top-view SEM image of Ag films on the monolayer with two clusters of extra beads on the top of the monolayer with three-armed star shaped shadowed area. Red arrows indicate the direction of incident vapor flux, and the yellow line passes through the centers of nanospheres.....	43
Figure 2.6.1: Schematic of the custom spectroscopic microscope setup. L: lens, I: iris, LP: linear polarizer, QWP: quarter wave plate, M: mirror. M1 is on a flip mount, which either reflects light to the camera or allows light to transmit to the monochromator .....	45
Figure 2.7.1: Yee's cell.....	47
Figure 2.7.2: The flowchart for FDTD algorithm.....	49
Figure 2.7.3: (a) The geometric model created in XFDTD for an array of nanospheres (b) One unit cell of the nanosphere array as meshed in an FDTD grid .....	51
Figure 3.2.1: Scheme of fabrication process of Ag chiral patchy particles. (a) Ag vapor flux is incident upon the monolayer at an oblique angle $\theta = 86^\circ$ with respect to the substrate normal. (b)–(d) Ag vapor flux is incident upon the monolayer in three azimuthal directions with an interval of $\Delta\varphi = 120^\circ$ . The azimuthal direction of Ag vapor flux and a dashed line going through the centers of the nanospheres form an angle, $\varphi_0$ .....	53
Figure 3.2.2: Simulated morphologies of chiral patchy particles in differently orientated domains with $\varphi_0 = 0^\circ, 5^\circ, 10^\circ, 15^\circ, 20^\circ, 25^\circ, 30^\circ, 35^\circ, 40^\circ, 45^\circ, 50^\circ, 55^\circ$ , and $60^\circ$ .....	54
Figure 3.2.3: (a) Transmission spectra, and (b) CD spectra of Ag patchy particles prepared by CW, CCW, and CW/CCW substrate rotations .....	55

Figure 3.2.4: SEM images of Ag patchy particles prepared by (a) CW and (b) CCW rotations of the substrate during DSG .....56

Figure 3.3.1: (a) SEM images, (b) optical micrographs under LCP and RCP light illuminations, (c) measured circularly polarized transmittance, (d) both measured and simulated differential circularly polarized transmittance  $\Delta T$ , and (e) simulated circularly polarized transmittance, for Domains #1–6. The scale bars in (a) and (b) represent 500 nm and 100  $\mu\text{m}$ , respectively.....58

Figure 3.3.2: Geometric models of Ag nanostructures in Domains #1–6 that are used in FDTD simulations. The green rectangles indicate the simulation space, which is a unit cell of the nanosphere array. The nanosphere diameter is 500 nm .....62

Figure 3.3.3: Simulated near-field current directions of (a) Domain #2 with LCP incident light at  $\lambda = 707$  nm, (b) Domain #2 with RCP incident light at  $\lambda = 943$  nm, (c) Domain #4 with RCP incident light at  $\lambda = 682$  nm, (d) Domain #4 with LCP light at  $\lambda = 833$  nm, (e) Domain #5 with RCP incident light at  $\lambda = 710$  nm, (f) Domain #5 with LCP light at  $\lambda = 1000$  nm, and (g) Domain #6 with RCP incident light at  $\lambda = 913$  nm. The insets are simulated current distributions when the currents are in direction of green arrows .....63

Figure 3.3.4: (a) Optical micrographs at a boundary of Domains #7 and #8 under LCP and RCP illuminations. (b) Measured (dotted lines) and fitted (solid lines)  $\Delta T$  spectra of a mixture of Domains #7 and #8 with different area percentage  $X$  of Domain #7. (c) The relationship between measured  $X$  and fitted  $X$  .....65

Figure 3.4.1: (a) Simulated chiral fan-shaped nanostructures fabricated with  $\varphi_0 = 53^\circ$ , and  $\theta = 82^\circ$ ,  $84^\circ$ ,  $86^\circ$  and  $88^\circ$ . Top-view SEM images of Ag fan-shaped nanostructures with (b)

$\theta = 82^\circ$ ,  $\varphi_0 = 53^\circ$ , (c)  $\theta = 84^\circ$ ,  $\varphi_0 = 54^\circ$ , (d)  $\theta = 86^\circ$ ,  $\varphi_0 = 52^\circ$ , and (e)  $\theta = 88^\circ$   $\varphi_0 = 53^\circ$ . The scale bar in (b)-(e) represents  $1 \mu\text{m}$ .....67

Figure 3.4.2: (a)  $T(\text{RCP})$ , (b)  $T(\text{LCP})$ , (c)  $\Delta T$ , and (d)  $g$ -factor spectra for Ag fan-shaped nanostructures fabricated at  $\theta = 82^\circ$ ,  $84^\circ$ ,  $86^\circ$  and  $88^\circ$  .....69

Figure 3.4.3: Top-view SEM images of Ag fan-shaped nanostructures with (a)  $t_{\text{QCM}} = 4 \times 10 \text{ nm}$ ,  $\varphi_0 = 52^\circ$ , (b)  $t_{\text{QCM}} = 4 \times 20 \text{ nm}$ ,  $\varphi_0 = 54^\circ$ , (c)  $t_{\text{QCM}} = 4 \times 25 \text{ nm}$ ,  $\varphi_0 = 53^\circ$ , (d)  $t_{\text{QCM}} = 4 \times 30 \text{ nm}$ ,  $\varphi_0 = 54^\circ$ , (e)  $t_{\text{QCM}} = 4 \times 35 \text{ nm}$ ,  $\varphi_0 = 53^\circ$ , and (f)  $t_{\text{QCM}} = 4 \times 40 \text{ nm}$ ,  $\varphi_0 = 54^\circ$ . The scale bar in each figure represents  $1 \mu\text{m}$  .....72

Figure 3.4.4: (a)  $T(\text{RCP})$ , (b)  $T(\text{LCP})$ , (c)  $\Delta T$ , and (d)  $g$ -factor spectra for Ag fan-shaped nanostructures fabricated with  $t_{\text{QCM}} = 4 \times 10 \text{ nm}$ ,  $4 \times 20 \text{ nm}$ ,  $4 \times 25 \text{ nm}$ ,  $4 \times 30 \text{ nm}$ ,  $4 \times 35 \text{ nm}$  and  $4 \times 40 \text{ nm}$ .....73

Figure 3.4.5: The SEM images of Ag fan-shaped nanostructures fabricated by DSG with  $\theta = 84^\circ$  and  $t_{\text{QCM}} = 4 \times 30 \text{ nm}$  (a) before and (b) after annealing.  $T(\text{RCP})$  and  $T(\text{LCP})$  spectra of Ag fan-shaped nanostructures (c) before and (d) after annealing. (e)  $T(\text{RCP})$ - $T(\text{LCP})$  and (f)  $T(\text{RCP})/T(\text{LCP})$  spectra of Ag fan-shaped nanostructures before and after annealing .....76

Figure 3.5.1: Measured (a)  $T(\text{RCP})$ , and (b)  $T(\text{LCP})$  spectra of the chiral fan-shaped nanostructures made by Ag, Au, Cu, and Ni. ....79

Figure 3.5.2: (a) Measured, and (b) simulated  $\Delta T$  spectra of the chiral fan-shaped nanostructures made by Ag, Au, Cu, and Ni .....79

Figure 4.2.1: Schematics of deposition processes and expected structures for LH- and RH-HSPLs. The process includes 7 deposition steps: ① Ag, ② SiO<sub>2</sub>, ③ Ag, ④ SiO<sub>2</sub>, ⑤ Ag, ⑥ SiO<sub>2</sub>, and ⑦ Ag. The direction of each deposition is indicated by the white (Ag) or

blue (SiO<sub>2</sub>) arrow. Top-view figures of LH- and RH-HSPLs at each step are shown at the left and right edges. 3D schematics of the expected structures are shown at the bottom.....85

Figure 4.2.2: (a) Top-view SEM images of LH-HSPLs on  $d = 500$  nm nanosphere monolayers. (b)-(d) Higher magnification images for Domains #1–4, respectively. (f)-(h) SEM images of Domain #4 at different fabrication steps. Insets are the morphologies obtained by simulations. The order and directions of depositions are shown at the top. The scale bar represents 10  $\mu\text{m}$  in (a), and represents 1  $\mu\text{m}$  in (b)-(h).....87

Figure 4.2.3: First four columns: the simulated morphology of single layers on nanospheres in four deposition directions on domains with  $\varphi_0 = 0^\circ, 10^\circ, 20^\circ, 30^\circ, 40^\circ,$  and  $50^\circ$ , respectively. The last column: the simulated morphology of the stacked layers. The arrows at the top indicate the deposition directions .....88

Figure 4.2.4: (a) Domain area distributions of  $d = 200, 350,$  and  $500$  nm monolayers. (b) Distribution of domain area versus  $\varphi_0$ .....89

Figure 4.2.5: TEM images of RH-HSPLs on (a) 200nm, and (b) 500nm nanospheres. White and blue dashed lines are artificially added to outline Ag and SiO<sub>2</sub> layers, respectively. Insets are 3D schematics of RH-HSPLs expected from the deposition sequence...90

Figure 4.2.6: (a) Unpolarized transmittance spectra, (b) transmittance difference between RCP and LCP light, and (c)  $g$ -factor spectra, of LH- and RH-HSPLs on  $d = 200$  nm, 350 nm, and 500 nm monolayers. The inset in (a) is an extended wavelength range transmittance spectrum for  $d = 500$  nm. Note that “PS” and the arrows in (a) mark the wavelength locations of the photonic band gap and the Ag LSPR, respectively.....91

Figure 4.2.7: (a) Schematics of geometric models used in FDTD simulations. The yellow rectangle in first three figures illustrates a unit cell of the HSPL arrays. (b) The simulated  $\Delta T$  spectra of HSPL domains with  $\varphi_0 = 0^\circ, 15^\circ, 30^\circ$  and  $45^\circ$ . (c) The averaged simulated  $\Delta T$  spectrum versus the measured  $\Delta T$  spectrum.....93

Figure 4.2.8: (a) The simulated circular polarized transmittance spectra, and (b) the simulated  $\Delta T$  spectra of LH-HSPLs on  $d = 200, 350,$  and  $500$  nm beads, with  $\varphi_0 = 0^\circ$ . (c) The near-field current distribution at the wavelength corresponding with “R”. An illustration of current flow is shown in the middle, and the current density distributions on Ag layers exported from XFDTD software are shown on left and right sides.....95

Figure 4.2.9: (a) The top-view SEM image of a single Ag layer made by DSG with a swing rotation of the substrate. (b) The top-view SEM image of the obtained HSPLs prepared by DSG with a swing rotation of the substrate. (c) The  $\Delta T$  spectra of LH-HSPLs on  $d = 200, 350,$  and  $500$  nm nanospheres, prepared by DSG with a swing rotation of the substrate.....96

Figure 4.3.1: Schematics of the fabrication procedure of RH- and LH-conical Swiss roll nanostructures. The fabrication includes 10 steps: ① preparation of substrates, ② preparation of colloidal monolayers, and depositions of ③ SiO<sub>2</sub> frustum, ④, ⑥<sub>R</sub>, ⑥<sub>L</sub>, ⑧<sub>R</sub>, ⑧<sub>L</sub>, ⑩<sub>R</sub>, ⑩<sub>L</sub> Ag side-coatings, and ⑤, ⑦<sub>R</sub>, ⑦<sub>L</sub>, ⑨<sub>R</sub>, ⑨<sub>L</sub> SiO<sub>2</sub> side-coatings. The black and blue arcs with arrows indicate how the vapor direction rotates with respect to the substrate.....99

Figure 4.3.2: (a) A swing deposition of Ag on an array of SiO<sub>2</sub> frustums on monolayers. (b) Top-view and (c) tilted-view image of the simulated thickness distribution on the SiO<sub>2</sub> frustum and the bead .....100

Figure 4.3.3: (a) Top-view and (b) cross-sectional SEM images of SiO<sub>2</sub> frustums on colloidal monolayers, corresponding to the structure at step ③. (c) Top-view and (d) cross-sectional SEM images of one Ag layer on each SiO<sub>2</sub> frustum, corresponding to the structure at step ④. (e) Top-view and (f) cross-sectional SEM images of LH-Swiss roll nanostructures, corresponding to the structure at step ⑩<sub>L</sub>. (g) TEM images of LH-Swiss roll nanostructures, corresponding to the structure at steps ④ and ⑩<sub>L</sub>. (h) Schematic of a Swiss roll structure. The scale bar in each SEM image represents 500 nm. The insets in (b), (d), and (f) show the schematics of the corresponding structures .....102

Figure 4.3.4: Circularly polarized differential transmittance spectra  $\Delta T$  (solid lines) and unpolarized transmittance spectra  $T$  (dashed lines) of Swiss roll nanostructures on (a)  $d = 350$  nm beads, and (b)  $d = 500$  nm beads .....104

Figure 4.3.5: (a) Geometric model of RH-Swiss roll on  $d = 350$  nm beads. The yellow box illustrates one unit cell of Swiss roll arrays, with absorbing boundary condition for top and bottom sides, and periodic boundary condition for other sides. The simulated  $T(\text{LCP})$  and  $T(\text{RCP})$  spectra for Swiss roll nanostructures on (b)  $d = 350$  nm, and (c)  $d = 500$  nm beads. (d)  $\Delta T$  spectra for Swiss roll nanostructures on  $d = 350$  and  $d = 500$  nm beads.....106

Figure 5.2.1: (a) Schematic of the laser diffraction of the self-assembled colloidal monolayer. (b) The photograph of a 1 cm<sup>2</sup> polycrystalline monolayer on a glass substrate. (c) Laser diffraction pattern of the polycrystalline monolayer .....110

Figure 5.2.2: (a) The photograph of a 1 cm<sup>2</sup> monocrystalline monolayer on a glass substrate. (b) Laser diffraction pattern of the monocrystalline monolayer, and determination of  $\varphi_d$ .

(c)-(j) Laser diffraction patterns of the monocrystalline monolayer, recorded every 1 mm across the substrate, with the measuring spot shown in (a) .....111

Figure 5.2.3:  $\Delta T$  spectra of Ag fan-shaped nanostructures on a 1 cm<sup>2</sup> monocrystalline monolayer and patchy films on a 1 cm<sup>2</sup> polycrystalline monolayer, measured by the spectroscopic microscope with a beam diameter ~ 5 mm .....112

Figure 5.3.1: (a) The process of transferring Ag chiral particles into a PDMS substrate. (b) The photograph of the flexible chiral metamaterial substrate. (c) Top-view, and (d) side-view SEM images of the flexible substrate surface where a thin layer of Au nanoparticles is coated for SEM imaging. The scale bar in (c) and (d) represents 1  $\mu\text{m}$ .....114

Figure 5.3.2: (a) Schematic illustration of how nanospheres move when stretching in  $x$  direction: a nanosphere originally at  $(x_0, y_0)$  moves to  $(x, y_0)$  due to the  $x$  direction stretching of the PDMS substrate, and finally move to  $(x, y)$  due to the shrinking in  $y$  direction of PDMS substrate. (b) Schematic illustration of how nanospheres move when stretching in  $y$  direction: a nanosphere originally at  $(x_0, y_0)$  moves to  $(x_0, y)$  due to the  $x$  direction stretching of the PDMS substrate, and the shrinking of the PDMS substrate does not move the nanosphere due to the rigid body of nanospheres ....116

Figure 5.3.3: The calculated based on the shrinking of the PDMS substrate,  $y = y_0(1 - e_y)$ , and the minimum value for  $y$ , required by the rigid body of nanospheres,  $y_{\min} = \sqrt{D^2 - x^2}$ , as functions of  $e_x$  .....117

Figure 5.3.4: Schematic illustration, and (b) photograph of the stretching and optical measurement setup.....119

Figure 5.3.5: Circularly polarized transmittance and differential transmittance spectra of the

flexible substrates with stretching in $x$ and $y$ directions. $T(\text{RCP})$ spectra with stretching in (a) $x$ and (b) $y$ directions. $T(\text{LCP})$ spectra with stretching in (c) $x$ and (d) $y$ directions. $T(\text{RCP})-T(\text{LCP})$ spectra with stretching in (e) $x$ and (f) $y$ directions .....	120
Figure 5.3.6: (a) $\lambda_{\text{RCP}}$ , (b) $\lambda_{\text{LCP}}$ , (c) $\lambda_{\text{A}}$ , and (d) $\lambda_{\text{B}}$ as a function of strain $e$ with stretching in $x$ and $y$ directions .....	121
Figure 5.3.7: The geometric models of Ag fan-shaped nanostructures embedded in PDMS used in FDTD simulation. (a) Top-view of the flexible substrate with $e_x = 0$ and $e_y = 0$ . (b) Side-view of the flexible substrate. Top-view of the flexible substrate with (c) $e_x = 0.125$ and $e_y = 0$ , and (d) $e_x = 0$ and $e_y = 0.125$ .....	123
Figure 5.3.8: A comparison between simulated and measured $T(\text{RCP})$ , $T(\text{LCP})$ , and $T(\text{RCP})-T(\text{LCP})$ . (a) Simulated spectra and (b) measured spectra with $e_x = 0.125$ , $e_y = 0$ . (c) Simulated spectra and (d) measured spectra with $e_x = 0$ , $e_y = 0.125$ .....	123
Figure 5.3.9: The simulated (a) $T(\text{RCP})$ , (b) $T(\text{LCP})$ , and (c) $T(\text{RCP})-T(\text{LCP})$ at three different stretching states: $e_x = 0$ , $e_y = 0$ ; $e_x = 0.125$ , $e_y = 0$ ; $e_x = 0$ , $e_y = 0.125$ .....	124
Figure 5.4.1: (a), (b) Representative top-view SEM images, (c),(d) Measured $T(\text{RCP})$ and $T(\text{LCP})$ , and (e), (f) Simulated $T(\text{RCP})$ and $T(\text{LCP})$ of Structure R and L, respectively. The insets in (e) and (f) are the geometric models in FDTD simulations.....	126
Figure 5.4.2: (a) $T_{\text{R}}(\text{RCP})$ , (b) $T_{\text{R}}(\text{LCP})$ , and (c) $\Delta T_{\text{R}}$ spectra of Structure R in sucrose solutions at different concentrations .....	128
Figure 5.4.3: Peak wavelength $\lambda_{\text{p}}$ versus refractive index $n$ of sucrose solutions for Structure R. The straight lines are linear fittings of $\lambda_{\text{p}}$ .....	130

Figure 5.4.4:  $T_R(\text{RCP})$  and  $T_R(\text{LCP})$  spectra (a) at  $n = 1.333$ , and (b) at  $n = 1.4307$ . The green line is used to separate the contributions from  $T_R(\text{RCP})$  and  $T_R(\text{LCP})$  peaks to  $\Delta T_R$  peak .....130

Figure 5.4.5: (a) Simulated  $T_R(\text{RCP})$ ,  $T_R(\text{LCP})$  and  $\Delta T_R$  spectra for Structure R at  $n = 1.333$ . (b) Peak wavelength  $\lambda_p$  of the simulated peaks  $B_R$ ,  $D_R$ , and  $F_R$  versus refractive index  $n$ . The straight lines are linear fittings of  $\lambda_p$ . Near-field current distribution of Structure R with  $n = 1.333$  excited at (c) resonance  $A_R$  (RCP,  $\lambda = 650$  nm), and (d) resonance  $D_R$  (LCP,  $\lambda = 720$  nm). The arrows indicate the current oscillation directions. The current flows represented by the three arrows appear in sequences at different phases .....132

## CHAPTER 1

### INTRODUCTION

#### 1.1 Metamaterials and chiral metamaterials

In history of science, the manipulation of material properties has never stopped. The desire of controlling material properties went to extreme in Feynman's talk in 1959, in which he asked "What would the properties of materials be if we could really arrange the atoms the way we want them?".[1] Although arranging atoms has not been realized so far, we have achieved a great progress in creating artificial materials with extraordinary properties, one of which is referred to as metamaterial. In the past two decades, electromagnetic (EM) metamaterials emerged as a new research field and developed rapidly benefitted from the advance of nanofabrication technology. Metamaterials are composite materials consisting of numerous artificially designed unit structures.[2] The size and spacing of the unit structures are required to be much smaller than the target operating wavelength, so that the assembly of unit structures respond to EM radiations as continuous materials with an effective material property in macroscopic scale.[3] The effective material property is primarily determined by the size, shape, material, and arrangement of the unit structures, and can be distinct from those found in natural materials, whose property is mainly determined by their chemical elements and bonding arrangement.

The metamaterial research started with exploring the negative refraction, which cannot be observed in any natural material.[4] In 1968, the concept of metamaterials was first proposed by

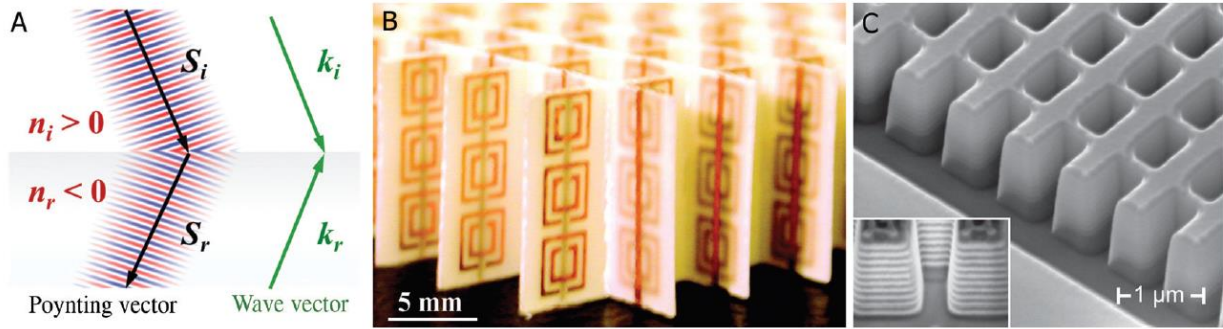


**Figure 1.1.1.** (A) Illustration of negative refraction at an interface between media with positive and negative refractive indices. (B) Photograph of the metamaterial with negative refractive index in microwave region, which contains copper wires and split ring resonators. (C) Scanning electron microscopy image of the fishnet metamaterial with negative refractive index in optical region. The inset shows alternating layers of 30 nm of Ag and 50 nm of MgF<sub>2</sub>. Ref.[5]

Veselago, who found in his theoretical investigation that the refractive index can be expressed as  $n = -\sqrt{\epsilon\mu}$ , with both relative electric permittivity  $\epsilon$  and relative magnetic permeability  $\mu$  negative.[6] A negative refraction occurs at an interface between media with positive and negative refractive indices. According to Snell's law, the refraction angle is negative at such an interface, leading to the fact that the incident and refracted light are on the same side with respect to the surface normal, as illustrated in **Figure 1.1.1A**. When light travels in the media with negative refractive index, the wave vector  $\vec{k}$  and Poynting vector  $\vec{S}$  are in the opposite directions, which is distinctly different from those in the media with positive refractive index. In 2000, the negative refraction was demonstrated experimentally for the first time in microwave region.[7] **Figure 1.1.1B** shows a typical structure design for the metamaterials with negative refractive index in microwave region, which consists of copper wires and split ring resonators. The negative refraction of metamaterials were investigated mostly in microwave region in the early stage,[8-10] and were later moved to terahertz and optical regions with the advance of nanofabrication techniques.[11-13] **Figure 1.1.1C** shows the scanning electron microscopy (SEM) image of the well-known fishnet metamaterial with negative refractive index in optical region.[14] The negative refraction

may enable some promising applications, including cloaking,[15] subwavelength imaging,[16] and hyperbolic dispersion.[17] Recently, more efforts have been made to extend the functionalities of metamaterials, including low or high permittivity,[18, 19] manipulating polarization of light,[20, 21] tunable property,[22, 23] nonlinear optical response,[24, 25] etc.

The exploration of negative refraction leads to the invention of a new type of metamaterial—chiral metamaterial. The unit structure of chiral metamaterials has geometric chirality, which means it cannot be superposed with their mirror images. Chiral metamaterial was proposed as another route to achieve negative refraction by Pendry in 2004.[26] Before chiral metamaterial was proposed, the negative refractive index was primarily achieved by making the relative electric permittivity and relative magnetic permeability negative simultaneously, which required two separate resonances and complicated structure design, such as the one in **Figure 1.1.1B**. Pendry showed that chiral metamaterial with a single chiral resonance could realize the negative refraction of one circular polarization, which simplified the structure design and extended the understanding of negative refraction. In his seminal publication on chiral metamaterial, Pendry also presented the first chiral metamaterial design—Swiss roll structure, which was then studied in microwave region for negative refraction.[27, 28] Recently, Swiss roll nanostructures have been realized in our laboratory with chiral optical response in optical region, as it will be demonstrated in Chapter 4.[29] Besides Swiss roll structure, various two-dimensional (2D) and three-dimensional (3D) chiral metamaterials have been realized in the size scale of tens of nanometers to a few millimeters.[21, 30-49] In 2009, a 3D chiral metamaterials with negative refractive index was experimentally demonstrated in terahertz region.[50] In 2010, the spatial shift of the refracted beam in the negative refraction was first observed experimentally in chiral metamaterial in microwave region.[51] Recently, the research of chiral metamaterials is no longer limited to

exploring negative refraction. Many efforts have been made in developing chiral metamaterials for manipulating the polarization states of light.[21, 52, 53] Additionally, chiral metamaterials have also been investigated for repulsive Casimir forces,[54, 55] unusual spin Hall effects,[56] superchiral field based bio-sensing,[57, 58] nonlinear chiral media,[59-61] and switchable chiral media.[62, 63] With multiple functionalities, chiral metamaterial has grown to be an important class of metamaterials.

## 1.2 Plasmonics

Metamaterials commonly comprise metallic structures, the size of which is required to be smaller than the operating wavelength. More interest has been drawn in the application of metamaterials in optical to near-infrared (near-IR) region, which requires the dimension of the unit structure in metamaterials to be reduced down to nanometer scale. The metallic nanostructures cannot be simply treated as perfect metals with infinite carrier density and zero carrier velocity, and exhibit many new physical properties, which have been investigated in a research field called plasmonics.[64]

Plasmon represents the collective oscillation of conduction electrons in metals. The plasmons existing at the interface between metals and dielectric materials is called surface plasmons, as shown in **Figure 1.2.1a**. Excited by light, the surface plasmons propagate along the interface and are confined evanescently in the perpendicular direction. When the surface plasmons are confined to a metallic structure at a smaller size than the excitation wavelength, a local collection oscillation of conduction electrons can be observed, which is referred to as localized surface plasmon, as shown in **Figure 1.2.1b**. The boundary of the metallic nanostructures implies an effective restoring force on the conduction electrons, which leads to a resonance of localized

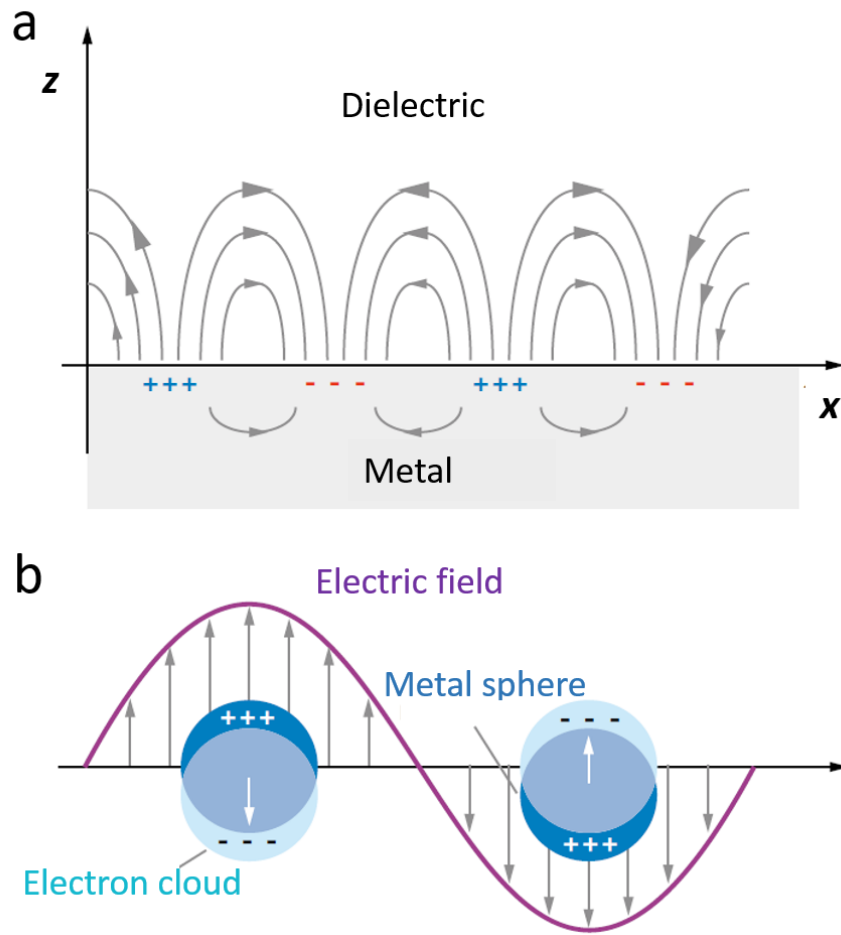


**Figure 1.2.1.** Schematic illustration of (a) surface plasmons, and (b) localized surface plasmons. Ref.[65]

surface plasmon at a specific frequency. This resonance is known as localized surface plasmon resonance (LSPR). LSPR has two major effects, enhanced localized electric field (ELEF) around the nanostructures and maximized optical extinction at the resonance wavelength. LSPR is sensitive to the material, size, shape, and surrounding dielectric constant of the metallic nanostructures. Although these interesting plasmonic effects are associated with nanometer sized structures, they can still be understood based on Maxwell's equations. The extinction cross-section  $\sigma_{\text{ext}}$  for a spherical nanoparticle with a volume  $V$  and a dielectric function  $\epsilon = \epsilon_1 + i\epsilon_2$ , is calculated based on Mie theory to be,[66]

$$\sigma_{ext} = \frac{18\pi\varepsilon_m^{3/2}V}{\lambda} \frac{\varepsilon_2(\lambda)}{[\varepsilon_1(\lambda) + 2\varepsilon_m]^2 + \varepsilon_2(\lambda)^2}, \quad (1.2.1)$$

where  $\varepsilon_m$  is the dielectric function of the surrounding medium, and  $\lambda$  is the wavelength of incident light. According to Equation (1.2.1), the extinction reaches the maximum when  $\varepsilon_1 = -2\varepsilon_m$ , which explains the dependence of LSPR wavelength on the dielectric constant of the surrounding medium.

The mathematical foundation for plasmonics was established around 1900.[67, 68] However, the application of plasmonics was started in 1970s.[69, 70] With the development of nanofabrication techniques, a variety of applications have been enabled based on the unique properties of surface plasmons and localized surface plasmons. For example, the resonance angle of surface plasmon resonance is very sensitive to the refractive index of the surrounding medium, which has been used for chemical and biological sensing.[71] The ELEF of surface plasmons has been utilized for manipulating and trapping micro/nano-sized particles.[72] In addition, the ELEF induced by LSPR of nanostructures is found to be the main origin for the surface-enhanced spectroscopies, such as surface enhanced Raman spectroscopy.[73, 74] Due to the intense extinction of LSPR, the plasmonic nanostructures have been applied for assisting photocatalytic process and local heating.[75-77] The dependence of LSPR wavelength on the refractive index of surrounding medium is used for bio-sensing application.[65, 66] Recently, the broad applications of plasmonics start to include metamaterials when the wavelength of interest for metamaterials moves to optical region. The collective electron oscillation in plasmonic metamaterials enables strong light-matter interaction, which is crucial for the novel optical properties of plasmonic metamaterials. The ELEF can enhance some weak processes, such as nonlinear optical process, which can be further utilized in plasmonic metamaterials. The LSPR wavelength depends on different factors, leading to highly tunable spectra of the plasmonic metamaterials. Benefited from

the spectacular properties of plasmonic effects, a variety of plasmonic metamaterials have been realized with different functionalities.[5, 22]

### 1.3 Chiral optical effects

Chirality is an asymmetry property that is caused by the lack of plane symmetry. Objects are called chiral when they cannot be superimposed with their mirror images. A chiral structure and its mirror image are called enantiomers of each other. The geometric chirality of chiral molecules, crystals, and nanostructures often leads to different interactions with two circular polarizations of light, i.e. right-handed circular polarization (RCP) and left-handed circular polarization (LCP), which gives rise to chiral optical effects.

#### 1.3.1 Optical rotation and circular dichroism

There are two basic linear chiral optical effects, known as circular birefringence (CB) and circular dichroism (CD). The circular birefringence describes the different refractive indices  $n$  (or real part of the complex refractive index  $\tilde{n} = n + ik$ ) for RCP and LCP, while circular dichroism describes the different extinction coefficients  $k$  (or imaginary part of  $\tilde{n}$ ) for RCP and LCP.

Circular birefringence is also called optical rotation (OR) and optical rotatory dispersion (ORD) if it is a function of wavelength. This is because a medium with CB can rotate the polarization of linearly polarized light by an angle  $\alpha$ . In a medium with refractive indices  $n_R$  and  $n_L$  for RCP and LCP, a linearly polarized light can be regarded as a superposition of coherent RCP and LCP light beams of equal magnitude  $E_{RCP}$  and  $E_{LCP}$ , as shown in **Figure 1.3.1a**. Then the polarization direction of the linearly polarized light in the medium depends on the relative phase between RCP and LCP components. The different  $n_R$  and  $n_L$  lead to different light speeds  $v_R$  and

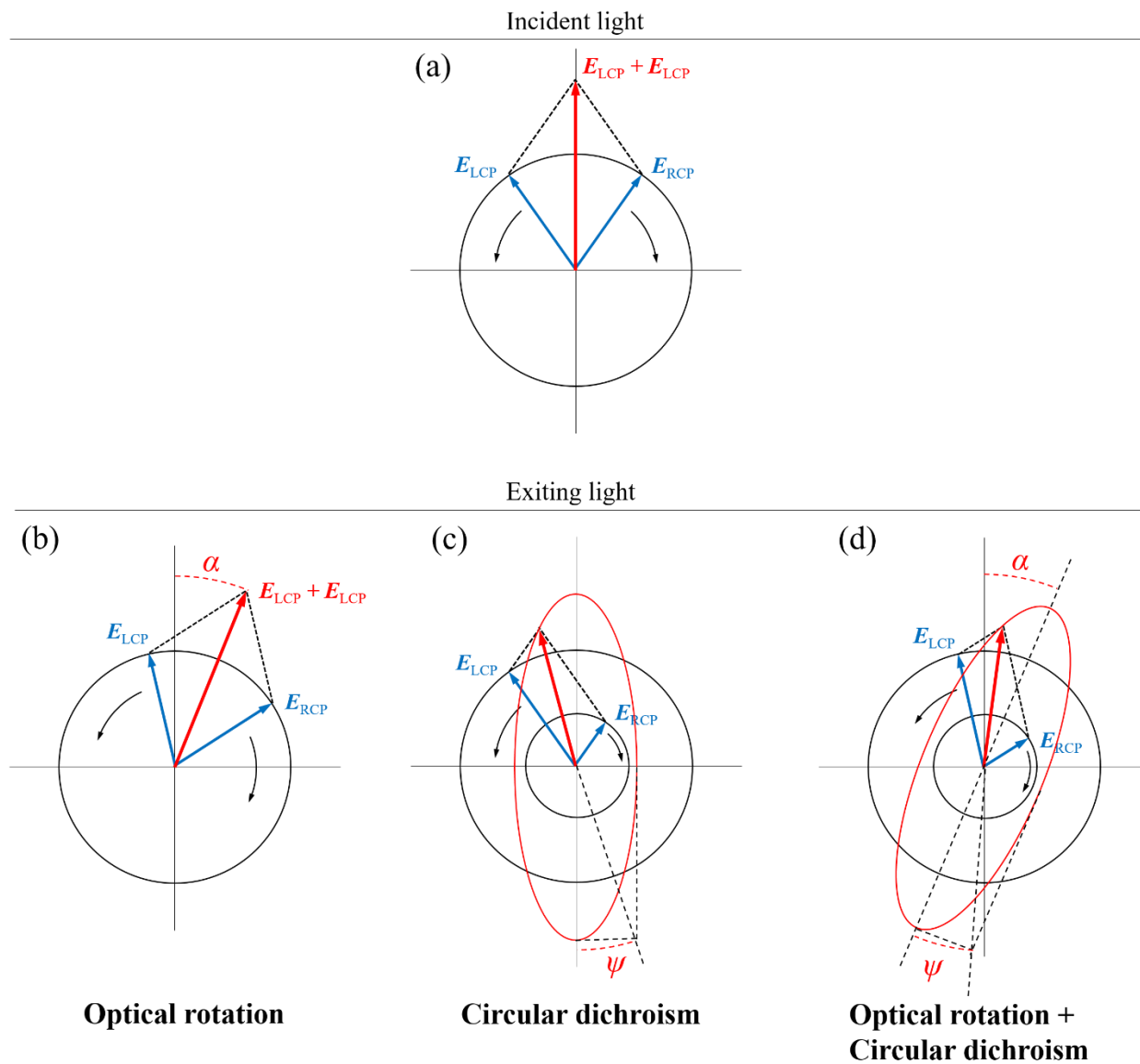


**Figure 1.3.1** (a) The incident linearly polarized light, which can be decomposed into two coherent components in RCP and LCP. (b) The exiting light after travelling in a medium with CB, which has a linear polarization rotated by an angle of  $\alpha$ . (c) The exiting light after travelling in a medium with CD, which an elliptical polarization with an ellipticity  $\psi$ . (d) The exiting light after travelling in a medium with both CB and CD, which has an elliptical polarization with an ellipticity  $\psi$  and a rotated angle  $\alpha$  of the major axis.

$v_L$  in the medium, which subsequently induces a continuously changing relative phase between RCP and LCP components in the light propagation direction. As shown in **Figure 1.3.1b**, the

change in relative phase between RCP and LCP rotates the linear polarization by an angle of  $\alpha$  after a travel distance  $l$  in the medium. The angle of rotation can be calculated by,

$$\alpha = \frac{c\pi}{\lambda} \left( \frac{l}{v_L} - \frac{l}{v_R} \right) = \frac{l\pi}{\lambda} (n_L - n_R), \quad (1.3.1)$$

where  $c$  is the light speed in vacuum. Therefore, the optical rotation is a function of  $n_L - n_R$ .

In the above discussion, only difference between  $n_R$  and  $n_L$  is considered with assuming an equal value of  $k_R$  and  $k_L$ , where  $k_R$  and  $k_L$  are extinction coefficients for RCP and LCP, respectively. Now if  $k_R \neq k_L$  while  $n_R = n_L$ , no difference between  $n_R$  and  $n_L$  indicates no optical rotation of the linear polarization. However, the two circular polarization components would have different magnitudes  $E_{RCP}$  and  $E_{LCP}$  in the medium, which leads to an elliptically polarized light beam with a semi-major axis ( $E_{LCP} + E_{RCP}$ ) and a semi-minor axis ( $E_{LCP} - E_{RCP}$ ), as shown in **Figure 1.3.1c**. The ellipticity  $\psi$  is defined as the ratio between the semi-minor axis and the semi-major axis

$$\tan \psi = \frac{E_{RCP} - E_{LCP}}{E_{RCP} + E_{LCP}}. \quad (1.3.2)$$

When  $E_{RCP} > E_{LCP}$ ,  $\psi$  is positive, corresponding to a clockwise rotation of the electric field vector, and when  $E_{RCP} < E_{LCP}$ ,  $\psi$  is negative, corresponding to a counter-clockwise rotation of the electric field vector. According to the definition of extinction coefficients, the attenuated electric field after a propagation distance  $l$  is  $E_{RCP}(l) = E(0)\exp(-2\pi k_R l / \lambda)$  and  $E_{LCP}(l) = E(0)\exp(-2\pi k_L l / \lambda)$ .

Thus, the ellipticity is then calculated as

$$\tan \psi = \frac{\exp(-2\pi k_R l / \lambda) - \exp(-2\pi k_L l / \lambda)}{\exp(-2\pi k_R l / \lambda) + \exp(-2\pi k_L l / \lambda)} = \tanh \left[ \frac{\pi l}{\lambda} (k_L - k_R) \right]. \quad (1.3.3)$$

When  $\psi$  is small, the ellipticity can be approximately expressed as

$$\psi = \frac{\pi d}{\lambda} (k_L - k_R), \quad (1.3.4)$$

which indicates the ellipticity is a function of  $k_L - k_R$ . Different materials can exhibit different chiral optical response, which can be dominated by CB, CD, or both (**Figure 1.3.1d**).

### 1.3.2 Chiral optical effects of natural molecules

Chiral optical effects have been used to determine the enantiomeric excess of molecules and the conformation states of biological molecules. However, natural molecules generally have very low chiral optical effects. According to the quantum theory of optical activity given by Rosenfeld,[78] the optical rotation  $\alpha$ , in radians per cm, at the frequency  $\nu$ , can be expressed as

$$\alpha = \frac{16\pi^2 N}{2hc} \sum_m \frac{\nu^2 R_{0m}}{\nu_{0m}^2 - \nu^2}, \quad (1.3.5)$$

where  $N$  is the number of molecules per  $\text{cm}^3$ ,  $R_{0m}$  is the rotational strength of the transition from the electron ground state  $\Psi_0$  to an excited state  $\Psi_m$ ,  $h\nu_{0m}$  is the energy difference between the two states. The rotational strength can be written as

$$R_{0m} = \text{Im}[\langle \Psi_0 | \hat{p} | \Psi_m \rangle \cdot \langle \Psi_m | \hat{m} | \Psi_0 \rangle], \quad (1.3.6)$$

where  $\text{Im}$  represents the imaginary part,  $\hat{p}$  is the electric dipole operator and  $\hat{m}$  is the magnetic dipole operator. The electric dipole operator leads to a charge separation, and the magnetic dipole operator leads to a charge circulation. For a planar molecule, the electric dipole operator is in the molecule plane, and the magnetic dipole operator is perpendicular to the plane, which leads to the scalar product of them is zero. This explains no chiral optical effects for planar molecules, which have a plane of symmetry and are thus not chiral. For a helical molecule, the helical structure acts as a guide for the charge circulation, leading to non-zero chiral optical response. The Rosenfeld theory can also be used for the analysis of optical property for helices in macroscale with chiral

optical effects in microwave region.[79, 80]

### 1.3.3 Chiral optical effects of nanostructures

Chiral nanostructures, especially those working in visible region, mostly utilize plasmon resonances, which are usually called chiral plasmonic nanostructures. As discussed in Section 1.2, LSPR can be excited optically in the chiral plasmonic nanostructures. With great light extinction around resonance wavelength and enhanced local electric field, LSPR assists chiral nanostructures to achieve many orders of magnitude larger chiral optical effects than the natural materials. **Figure 1.3.2** shows a simple illustration on how LSPR helps to generate strong chiral optical effects, which are intuitive and not describing a real case. Achiral spherical particles interact with linearly

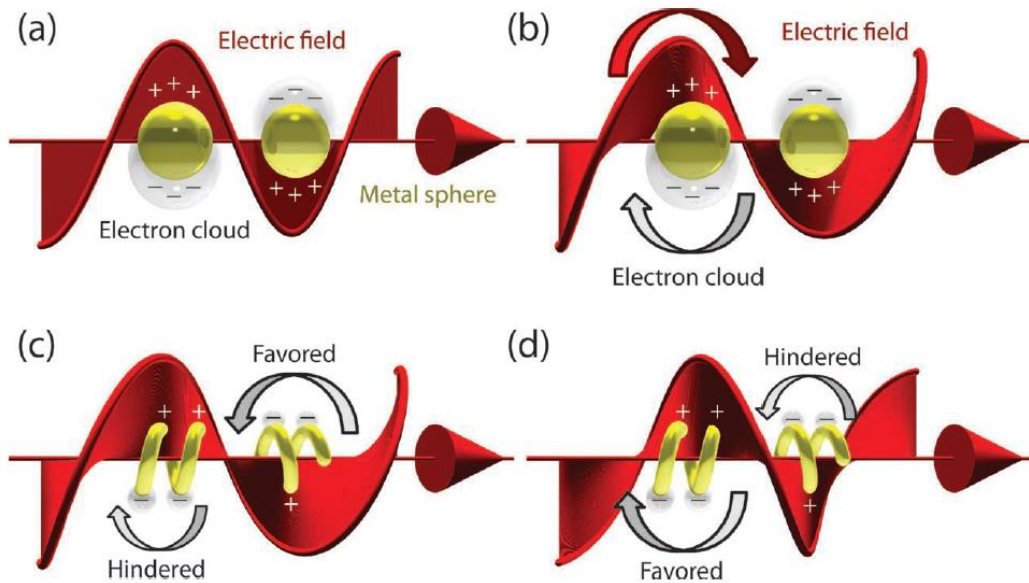


**Figure 1.3.2.** The intuitive illustrations of the interactions between achiral and chiral particles and polarized light. (a) Achiral particles interact with linearly polarized light, causing electron cloud oscillating linearly along the electric field. (b) Achiral particles interact with circularly polarized light, causing electron cloud rotating around the particles. Chiral structures interact with (c) RCP, and (d) LCP light. The rotation of the electron cloud can be favored or hindered depending on the combination of chiral geometry and direction of circularly polarized light.

Ref.[30]

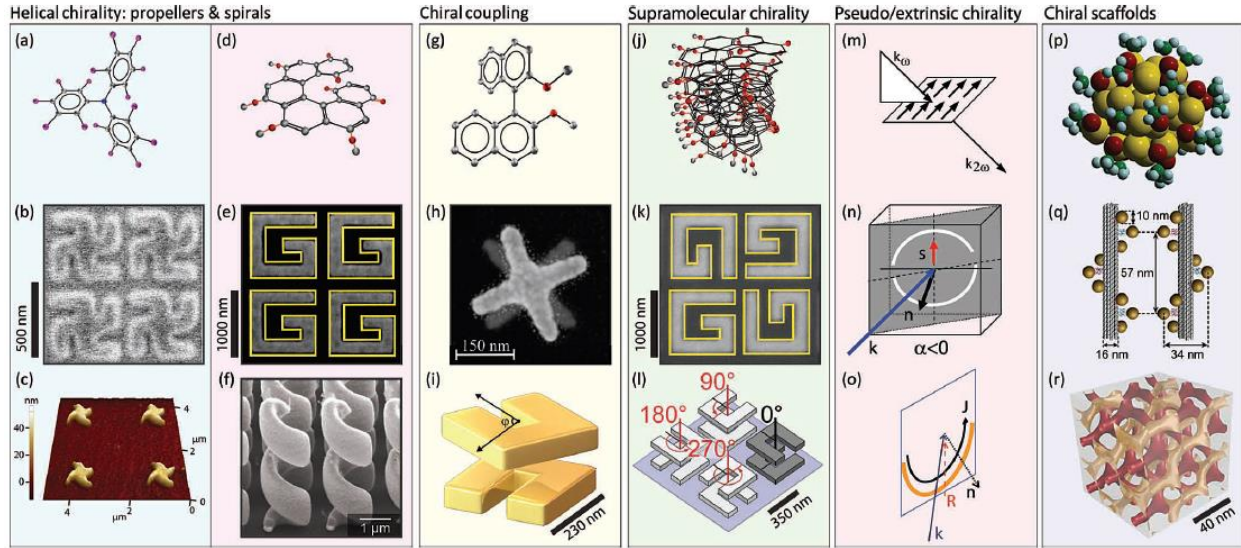


**Figure 1.3.3.** Chiral molecules and micro/nano-structures with different origins of chiral optical effects. (a)-(f) helical chirality, (g)-(i) chiral coupling, (j)-(l) supramolecular chirality, (m)-(o) pseudo/extrinsic chirality, and (p)-(r) chiral scaffolds. Ref.[30]

polarized light in **Figure 1.3.2a** and with circularly polarized light in **Figure 1.3.2b**. The achiral shape generates the symmetric collective electron oscillations for RCP and LCP light, which leads to no chiral optical response. The interactions between two chiral structures in opposite handedness and circularly polarized light are shown in **Figures 1.3.2c** (RCP illumination) and **1.3.2d** (LCP illumination), respectively. The chiral geometry sets the boundary for the collective electron oscillation, leading to asymmetric LSPRs excited under illuminations of RCP and LCP light, with one hindered and the other favored by the chiral geometry of structures, which leads to chiral optical effects.

Theoretical calculation based on Maxwell's equations, such as a modified Mie's theory,[81] can only work with very simple geometries, and is very limited in the investigation of various chiral nanostructures. Additionally, retardation effects are important for structures in sizes of tens of nanometers to several micrometers. The advance of fabrication techniques provides the possibility of more and more complicated chiral structures (see **Figure 1.3.3**). Numerical

simulations of the same structures as the fabricated ones are usually required in order to understand their optical responses. Numerical simulations are mostly run based on solving Maxwell's equations. Solvers with different algorithms have been developed, such as finite element method, finite-difference time domain method, and transmission line matrix method.

So far, a variety of chiral nanostructures have been fabricated with different origins of chiral optical effects, including helical chirality, chiral coupling, supramolecular chirality, pseudo/extrinsic chirality, and chiral scaffolds, as shown in **Figure 1.3.3**, which show orders of magnitude larger chiral optical effects than the natural molecules. Besides the giant CB and CD response, other intriguing optical properties have been discovered for chiral metamaterials, including negative refractive index and superchiral field.

#### ***1.3.4 Negative refraction of chiral metamaterial***

The light propagation in chiral media can still be described by the Maxwell equations, however, the constitutive relations,  $\vec{D} = \epsilon\vec{E}$  and  $\vec{B} = \mu\vec{H}$ , do not apply for the chiral media, where  $\vec{E}$  is the electric field,  $\vec{D}$  is the electric displacement,  $\vec{H}$  is the magnetic field,  $\vec{B}$  is the magnetic induction,  $\epsilon$  is the permittivity, and  $\mu$  is the permeability. According to Condon's study,[82] the constitutive relations in chiral media can be expressed as,

$$\vec{D} = \epsilon\vec{E} - \zeta \frac{\partial \vec{H}}{\partial t}, \quad (1.3.7)$$

$$\vec{B} = \mu\vec{H} + \zeta \frac{\partial \vec{E}}{\partial t}, \quad (1.3.8)$$

where  $\zeta$  is a parameter describing the chirality of the media. For a monochromatic wave at an angular frequency  $\omega$  with a time dependence factor of  $\exp(-i\omega t)$ , the constitutive relations can be expressed as,

$$\vec{D} = \epsilon\vec{E} + i\gamma\vec{H}, \quad (1.3.9)$$

$$\vec{B} = \mu\vec{H} - i\gamma\vec{E}, \quad (1.3.10)$$

where  $\gamma = \omega\zeta$  is the chirality index, and the Maxwell's curl equations in frequency domain are,

$$\nabla \times \vec{E} = i\omega\vec{B}, \quad (1.3.11)$$

$$\nabla \times \vec{H} = -i\omega\vec{D}. \quad (1.3.12)$$

If the chiral medium is homogeneous, i.e.  $\epsilon$ ,  $\mu$ , and  $\gamma$  are constants in the medium at the angular frequency  $\omega$ , combining Equations (1.3.9), (1.3.10), (1.3.11), and (1.3.12), and eliminating  $\vec{D}$ ,  $\vec{H}$ , and  $\vec{B}$  leads to

$$\nabla \times (\nabla \times \vec{E}) - 2\omega\gamma\nabla \times \vec{E} = \omega^2(\epsilon\mu - \gamma^2)\vec{E}. \quad (1.3.13)$$

The electric field of a circularly polarized light propagating in z direction in the chiral medium can be written as,

$$\vec{E}_{RCP,LCP} = E_0(\hat{x} \pm i\hat{y})\exp(iqz), \quad (1.3.14)$$

where  $q$  is the wavevector. Substituting  $\vec{E}$  in Equation (1.3.13) by Equation (1.3.14), then Equation (1.3.13) can be expressed as,

$$q^2(\hat{x} \pm i\hat{y})\exp(iqz) - 2\omega\gamma(\pm q\hat{x} + iq\hat{y})\exp(iqz) - \omega^2(\epsilon\mu - \gamma^2)(\hat{x} \pm i\hat{y})\exp(iqz) = 0. \quad (1.3.15)$$

By equating the x or y component, Equation (1.3.15) can be written as,

$$q^2 \mp 2\omega\gamma q - \omega^2(\epsilon\mu - \gamma^2) = 0. \quad (1.3.16)$$

Since  $q_{RCP,LCP} = (\omega/c)n_{RCP,LCP}$ , where  $c$  is the vacuum speed of light, the refractive indices for RCP and LCP can be obtained by solving  $q$  for RCP and LCP light in Equation 1.3.16, which can be expressed as

$$n_{RCP,LCP} = n \pm \kappa, \quad (1.3.17)$$

where  $n = \sqrt{\frac{\varepsilon\mu}{\varepsilon_0\mu_0}}$  and  $\kappa = \frac{\gamma}{\sqrt{\varepsilon_0\mu_0}}$  ( $\varepsilon_0$  and  $\mu_0$  are the permittivity and permeability in vacuum).

Therefore, the negative refraction can be realized in one circular polarization when  $n < |\kappa|$ . [26]

### 1.3.5 Superchiral field of chiral plasmonic nanostructures

EM fields can be chiral, for example, RCP and LCP lights are a pair of enantiomers with opposite chirality. A quantity defining the chirality of the EM fields, called optical chirality  $C$ , is defined as,

$$C \equiv \frac{\varepsilon_0}{2} \vec{E} \cdot \nabla \times \vec{E} + \frac{1}{2\mu_0} \vec{B} \cdot \nabla \times \vec{B}. \quad (1.3.18)$$

This quantity was first introduced by Lipkin in 1964, who found no physical significance and dismissed it. [83] It was repropoed to measure the chirality of EM fields by Tang et al. in 2010 while exploring the interaction of chiral EM fields with molecules. [58]

A chiral molecule in a monochromatic EM field with  $\vec{E}(t) = \pm \vec{E}_0 \exp(-i\omega t)$  and  $\vec{B}(t) = \vec{B}_0 \exp(-i\omega t)$  has an electric dipole moment  $\vec{p}$  and a magnetic dipole moment  $\vec{m}$ , which can be expressed in the complex format as

$$\vec{p} = \tilde{\alpha} \vec{E} - i \tilde{G} \vec{B}, \quad (1.3.19)$$

$$\vec{m} = \tilde{\chi} \vec{B} + i \tilde{G} \vec{E}, \quad (1.3.20)$$

where  $\tilde{\alpha} = \alpha' + i\alpha''$  is the electric polarizability,  $\tilde{\chi} = \chi' + i\chi''$  is the magnetic susceptibility, and  $\tilde{G} = G' + iG''$  is the isotropic mixed electric-magnetic dipole polarizability, describing the intrinsic chirality of the molecule. The optical chirality  $C$  can be calculated as

$$C = -\frac{\varepsilon_0 \omega}{2} \text{Im}(\vec{E}^* \cdot \vec{B}). \quad (1.3.21)$$

The excitation rate of the molecule is given by

$$A^{\pm} = \langle \bar{\mathbf{E}} \cdot \bar{\mathbf{p}} + \bar{\mathbf{B}} \cdot \bar{\mathbf{m}} \rangle = \frac{\omega}{2} \text{Im}(\tilde{\mathbf{E}}^* \cdot \tilde{\mathbf{p}} + \tilde{\mathbf{B}}^* \cdot \tilde{\mathbf{m}}), \quad (1.3.22)$$

where the brackets represent averaging over time. By substituting  $\tilde{\mathbf{p}}$  and  $\tilde{\mathbf{m}}$  in Equation (1.3.22) by Equations (1.3.19) and (1.3.20), the excitation rate is then written as

$$A^{\pm} = \frac{\omega}{2} (\alpha'' |\tilde{\mathbf{E}}|^2 + \chi'' |\tilde{\mathbf{B}}|^2) \pm G'' \omega \text{Im}(\tilde{\mathbf{E}}^* \cdot \tilde{\mathbf{B}}). \quad (1.3.23)$$

The term  $\chi'' |\tilde{\mathbf{B}}|^2$  is small for most molecules and can be ignored. By applying Equation (1.3.21),

we obtain

$$A^{\pm} = \frac{2}{\varepsilon_0} (\omega U_e \alpha'' \mp CG''), \quad (1.3.24)$$

where  $U_e = \frac{\varepsilon_0}{4} |\tilde{\mathbf{E}}|^2$  is the time-averaged electric energy density.

The differential absorption of the molecule between two chiral fields can be expressed as

$$\Delta A = A^+ - A^- \propto CG''. \quad (1.3.25)$$

For a typical CD measurement, which is the differential absorption of molecules between RCP and LCP light, we obtain

$$\Delta A_{CD} = A^{RCP} - A^{LCP} \propto C_{CPL} G'', \quad (1.3.25)$$

where  $C_{CPL} = \pm \frac{\varepsilon_0 \omega}{2c} |\tilde{\mathbf{E}}|^2$  is the optical chirality for circular polarized light. It is found that the near

fields of chiral plasmonic nanostructures can show larger  $C$  than the circularly polarized light.[84,

85] Then the chiral optical response of the molecule can be greatly enhanced near the chiral

plasmonic nanostructures by an enhancement factor  $\hat{C} = \left| \frac{\Delta A}{\Delta A_{CD}} \right| = \left| \frac{C}{C_{CPL}} \right|$ . **Figure 1.3.4** shows the

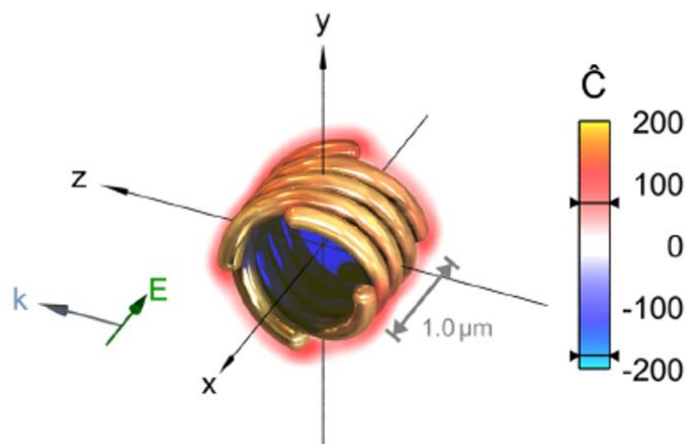


**Figure 1.3.4.** 3D distribution of the optical chirality enhancement factor  $\hat{C}$  near the multiple Au helices. Ref.[84]

near-field distribution of  $\hat{C}$  around the multiple helices obtained by numerical simulations. The superchiral field exhibits two orders of magnitude larger  $C$  than the circularly polarized light, which leads to a great enhancement of the chiral optical response of the molecule. The superchiral field of chiral plasmonic nanostructures provides a promising route for enantiomer sensing.

#### 1.4 Chiral metamaterial based optical devices

Since it was first proposed in 2004, chiral metamaterials have been extensively studied. Extraordinary optical functionalities have been demonstrated, such as negative refraction, giant chiral optical response, and superchiral field based sensing. With the rapid advance of nanofabrication techniques, the research agenda in chiral metamaterial is now moving to realize chiral metamaterial based optical devices. Here, the “devices” represent those chiral metamaterials with unique functionalities and potentials to be developed for practical applications, which are still preliminary products in laboratory.

The most important feature of chiral metamaterial is the giant chiral optical effects that are

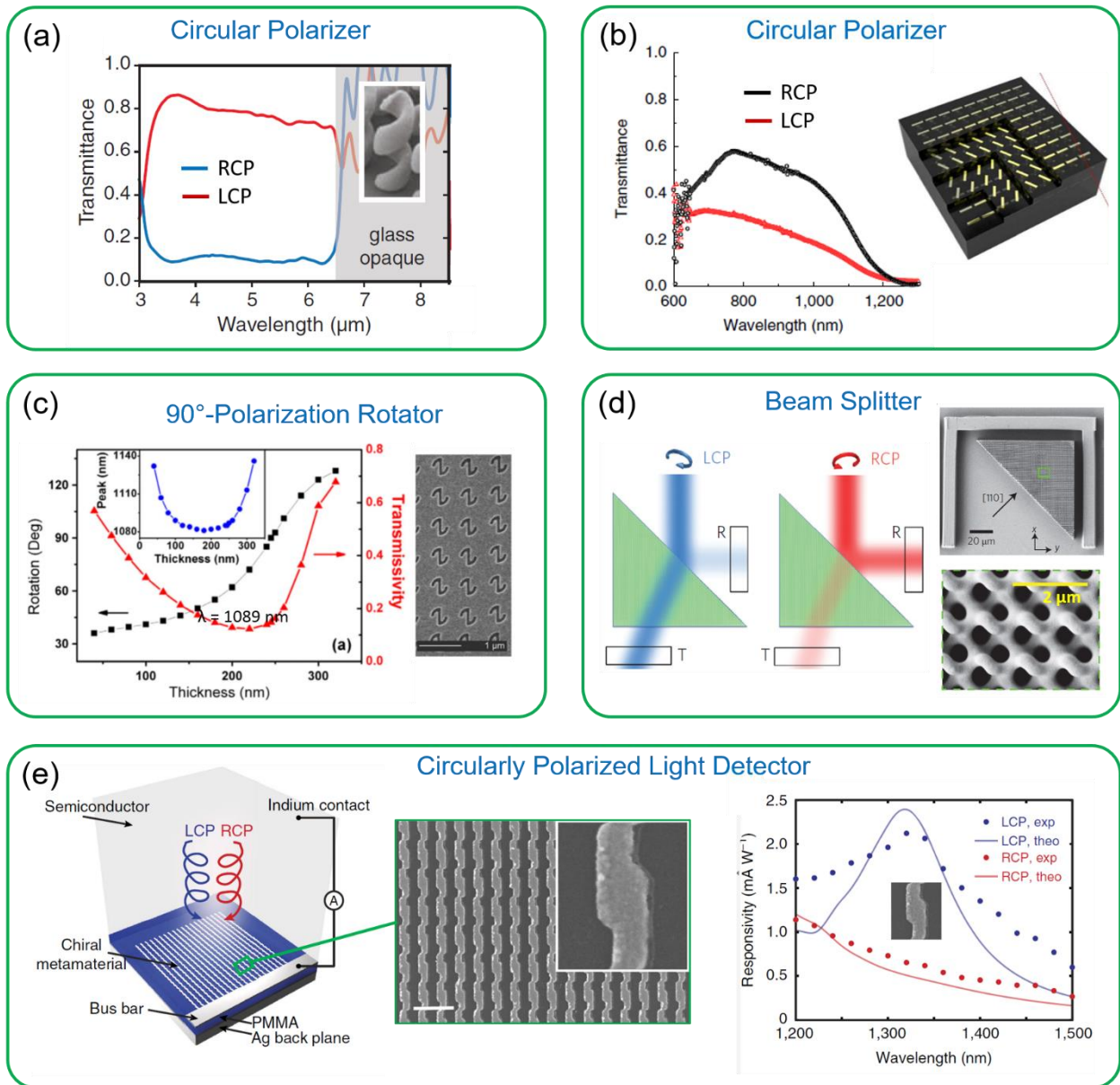


**Figure 1.4.1.** (a) Au helical microstructures as a broadband circular polarizer in IR region. Ref.[21] (b) Stacked plasmonic rods as a broadband circular polarizer in visible to near-IR region. Ref.[35] (c) S-shaped nanohole arrays as a 90°-polarization rotator at a wavelength of 1089 nm. Ref.[52] (d) Chiral gyroid networks as a chiral beam splitter around 1.615  $\mu\text{m}$ . Ref.[53] (e) Chiral metamaterial based circularly polarized light detector. Ref.[86]

many orders of magnitude larger than those of natural materials. This gives chiral metamaterials a great ability to manipulate the polarization states of light within a very thin layer of films. The chiral optical devices for controlling polarizations have been demonstrated. For example, Au

helical microstructure arrays fabricated by Gansel *et al.* in 2009 were applied as a broadband circular polarizer in IR region, as shown in **Figure 1.4.1a**.<sup>[21]</sup> In 2012, Zhao *et al.* fabricated stacked nanorod arrays with a tailored rotational twist to realize a broadband circular polarizer in visible to near-IR region, as displayed in **Figure 1.4.1b**.<sup>[35]</sup> An S-shaped nanohole array prepared by Wu *et al.* in 2013 showed giant optical rotation, which strongly depended on the film thickness, as shown in **Figure 1.4.1c**.<sup>[52]</sup> At a particular film thickness, this nanohole array can cause a 90° optical rotation at a wavelength of 1089 nm, serving as a 90°-polarization rotator. A beam splitter for circular polarization was realized by Turner *et al.* in 2013 using a chiral gyroid network, as shown in **Figure 1.4.1d**.<sup>[53]</sup> The operating wavelength for the chiral beam splitter was around 1.615 μm. Besides the manipulation of polarizations of light, chiral metamaterial can also be applied to detect circular polarizations benefited from the large CD response. Recently, Li *et al.* reported the production of an ultracompact circularly polarized light detector, which employed chiral metamaterial and hot electron injection.<sup>[86]</sup> The detection relied on the photocurrent induced by the hot electrons injection, which were generated by the selective absorption of circularly polarized light in chiral plasmonic structures, as demonstrate in **Figure 1.4.1e**.

Additionally, the smart tunable and switchable functionality of metamaterials has drawn more attentions.<sup>[22]</sup> Active chiral metamaterial devices are also realized with chiral optical response that can be tuned by external stimuli. The first active chiral metamaterial was reported by Zhang *et al.* in 2012, which was carefully designed with plasmonic and semiconductor layers, as shown in **Figure 1.4.2a**.<sup>[63]</sup> The photoexcitation in Si semiconductor (green parts) can switch the handedness of the chiral structure, leading to flipped spectra of circular dichroism and optical rotation. Another active chiral plasmonic structure was prepared by Yin *et al.* in 2015, which combined the Born-Kuhn type chiral plasmonic dimer with the chalcogenide phase change

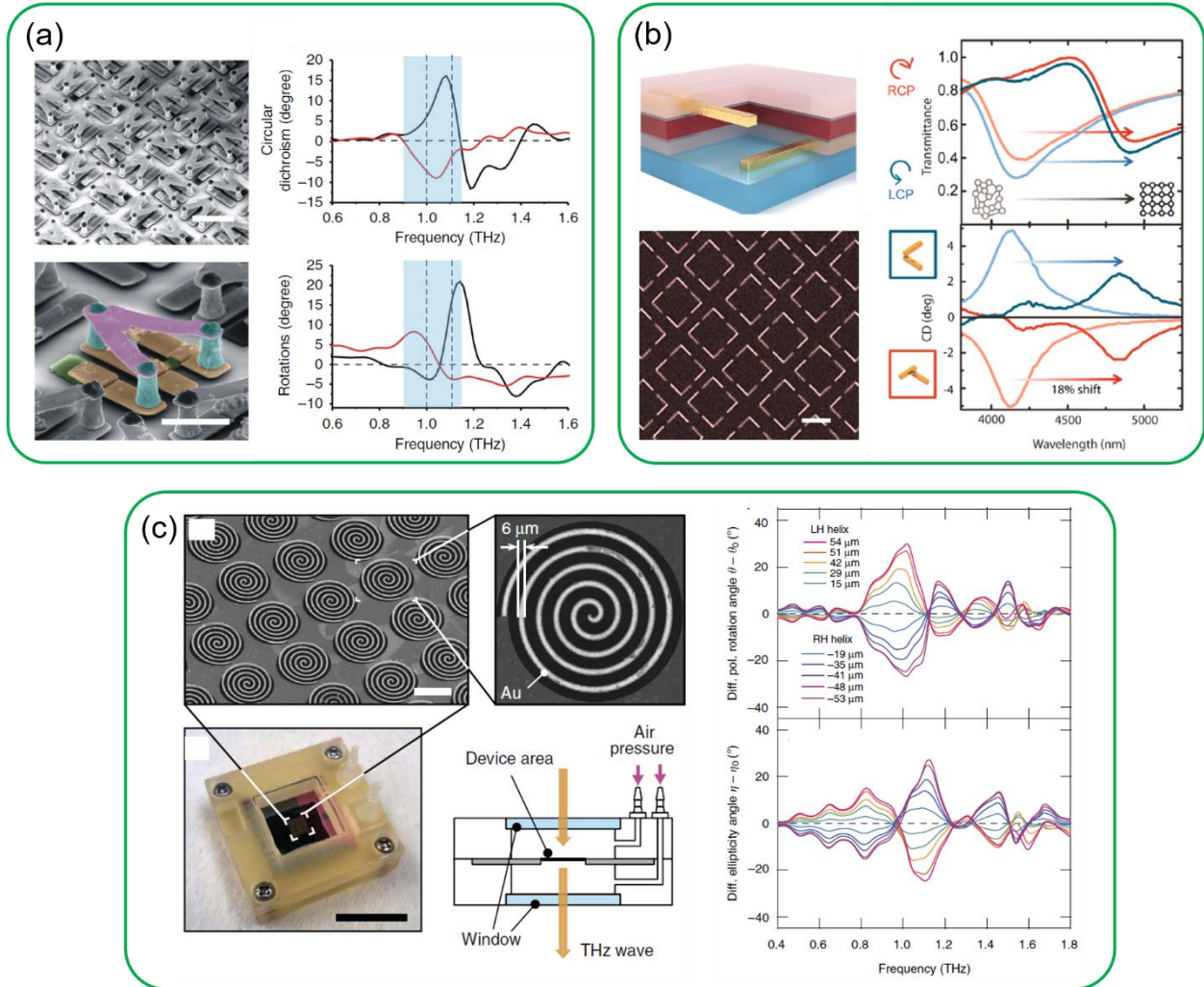


**Figure 1.4.2.** (a) Chiral structures consisting of Au bars and Si pads with chiral optical response switched by optical excitation. Ref.[63] (b) Chiral plasmonic nanostructures combined with a phase change material  $Ge_3Sb_2Te_6$ . The large change in dielectric constant of  $Ge_3Sb_2Te_6$  induced by phase transition shifts the CD spectra. Ref.[87] (c) A planer spiral that can be deformed into a 3D spiral in different handedness by a pneumatic force, with tunable chiral optical response. Ref.[88]

material  $Ge_3Sb_2Te_6$ , as shown in **Figure 1.4.2b**. [87] The transition from amorphous to crystalline phase of  $Ge_3Sb_2Te_6$  could be induced thermally, which caused a large change in the dielectric constant in mid-IR region. The LSPR of chiral plasmonic structure was then shifted significantly. Not only a spectral tunability but also the reverse sign of CD response have been demonstrated. The tunable response of chiral metamaterial can be also activated mechanically. Kan *et al.*

demonstrated a handedness-switchable chiral metamaterial in terahertz region employing vertically deformable micro-electro-mechanical systems, as displayed in **Figure 1.4.2.c**.<sup>[88]</sup> A planer spiral can be vertically deformed into a 3D spiral by a pneumatic force. The chiral optical response can be tuned and reversed with maintaining the spectra shape. In addition, the chiral optical effects of chiral metamaterial can also be modulated by other stimuli, such as magnetic field, <sup>[89, 90]</sup> and biochemical reactions,<sup>[62, 91]</sup> etc.

The exploration of chiral plasmonic metamaterial also extends to nonlinear regime. In 2012, Ren et al. reported the observation of nonlinear optical activity in an extrinsic chiral plasmonic metamaterial, as demonstrated in **Figure 1.4.3a**.<sup>[60]</sup> The observed nonlinear optical activity is millions of times stronger than that in natural crystals. The chiral plasmonic metamaterial provides a good platform for second-harmonic generation due to the plasmonic resonances and the disruption of symmetry for susceptibility tensor. In 2014, Rodrigues *et al.* reported a large chiral second-harmonic generation signal with the imaging ability, as shown in **Figure 1.4.3b**.<sup>[61]</sup> Valev et al. performed a thorough investigation of the properties of nonlinear chiral meta-surfaces, and elaborated the relation between second-harmonic generation and superchiral field.<sup>[92]</sup> The superchiral field is believed as an important tool for enantiomer sensing. Therefore, the second-harmonic generation can help to improve the sensing performance of superchiral field based bio-sensing. The superchiral field is one important functionality of chiral plasmonic structures, which was first theoretically proposed by Tang *et al.* in 2010.<sup>[58]</sup> Later the superchiral field based sensing for enantiomers was realized for the first and only time by Hendry *et al.*<sup>[57]</sup>

This discussion in this section may not cover all the applications of chiral metamaterial as optical devices, but is enough to demonstrate their versatile functionalities and the importance to

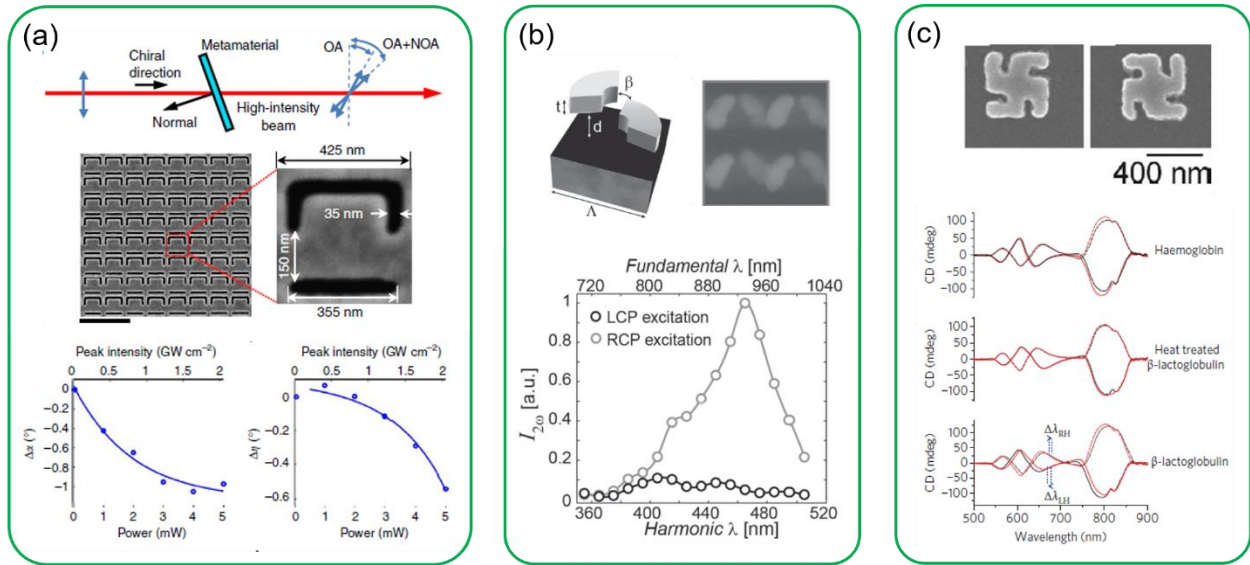


**Figure 1.4.3.** (a) Nonlinear optical activity generated by an extrinsic chiral metamaterial. Ref.[60] (b) Giant difference in second-harmonic response between LCP and RCP excitation from a twisted arc chiral metamaterial. Ref.[61] (c) Superchiral field based sensing for enantiomers using gammadion chiral plasmonic structures. Ref.[57]

realize these chiral optical devices. However, these chiral optical devices, especially those used as polarizers or beam splitters, are not suitable for practical applications. These devices are mostly prepared by top-down methods (discussed in Section 2.1) and in small scale ( $< 1 \text{ mm}^2$ ), which can hardly be used as optical elements. Therefore, scalable fabrication of chiral metamaterial with large chiral optical response is still a challenge that limits the development of chiral material based optical devices. In this dissertation, we aim to develop a simple fabrication technique to realize chiral metamaterials with giant chiral optical effects in large scale, which can be applied for producing chiral metamaterial based devices.

## 1.5 Dissertation overview

This dissertation describes the fabrication of chiral metamaterials using dynamic shadowing growth. Chapter 1 serves as an introduction for this dissertation, by starting with introducing

metamaterials and chiral metamaterials. The concepts of plasmonics and chiral optical effects are then discussed. After a brief review of the chiral metamaterial based optical devices, a challenge in chiral metamaterial fabrication is revealed, which motivates the research work in this dissertation. Chapter 2 introduces the fabrication, characterization, and simulation techniques that are employed in this dissertation. It starts with a brief review of the current fabrication methods for chiral metamaterials, and then describes our fabrication techniques, dynamic shadowing growth (DSG) and self-assembled colloidal monolayer (SACM). The experimental characterization and simulation techniques for both morphological and optical properties are elaborated later. Chapter 3 describes the fabrication method of a quasi-3D chiral patchy particles, followed by systematic investigations on how the chiral optical response depends on the monolayer orientations, incident angle of vapor flux, film thickness, annealing, and materials. These systematic studies help us to find the optimum fabrication parameters for chiral patchy particles with giant circular dichroism response. Chapter 4 presents a 3D chiral metamaterial fabrication strategy using DSG on nanospheres, in which plasmonic thin films are helically stacked on nanospheres. This strategy is demonstrated through preparing two chiral metamaterials, helically stacked plasmonic layers and Swiss roll nanostructures. Chapter 5 describes our effort in developing chiral metamaterials into optical devices. We show that the chiral metamaterials fabricated by DSG can be realized in  $\text{cm}^2$  scale, and also can be developed into flexible chiral metamaterials, whose optical property can be tuned by mechanical deformation. We also demonstrate that the chiral nanostructures can be used as a localized surface plasmon resonance sensor, which exhibits an improved sensitivity by measuring circular dichroism. Chapter 6 summarizes the research work and discusses the future work.

## CHAPTER 2

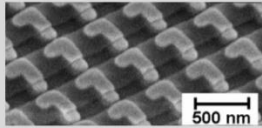
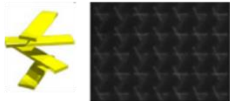
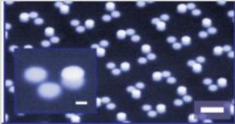
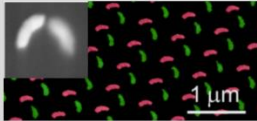
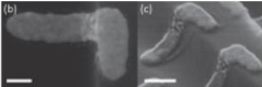
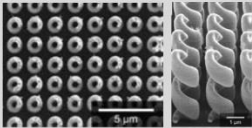
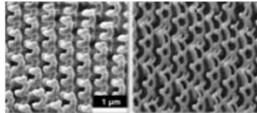
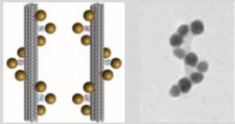
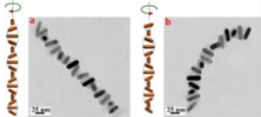
### FABRICATION, CHARACTERIZATION AND SIMULATION

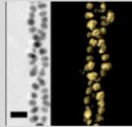
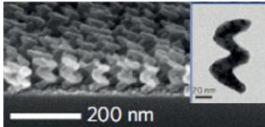
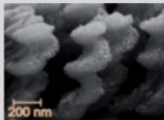
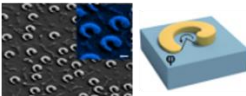
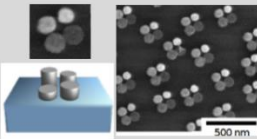
#### 2.1 Brief review of current fabrication methods

In order to produce chiral metamaterials which are optically active in visible to near-IR region, the dimensions of the unit chiral structures should be in nanometer scale. A variety of fabrication techniques have been employed for fabricating chiral nanostructures. **Table 2.1.1** lists some representative chiral metamaterials in literatures, along with their fabrication methods and chiral optical responses. The fabrication techniques for nanostructures can be generally divided into top-down and bottom-up approaches, which have been applied for chiral metamaterial fabrication.

Top-down fabrication is a subtractive process which starts with bulk material and removes unwanted parts to create the desired structures. Among various top-down methods, chiral metamaterial fabrication mostly relies on electron beam lithography (EBL). The principle of EBL is similar to other lithography techniques. **Figure 2.1.1a** shows the schematic of EBL fabrication. In EBL, a focused beam of electrons is used to create custom patterns on a thin layer of resist, which can be chemically changed under exposure to electron beams. The exposed or unexposed area of the resist (depending on positive or negative resist) can be selectively removed by immersing in a specific solvent. With the etched resist layer as a mask, a thin film deposition followed by a lift-off process can produce the desired two-dimensional (2D) nanostructures on substrates. The primary advantages of EBL are the high resolution ( $< 10$  nm) and the ability to

**Table 2.1.1.** Representative chiral metamaterials with their fabrication methods and chiral optical response.

#	Structure	Method	Chiral optical response (max.)	Reference
1		EBL	$\Delta T = 0.45$ (0.6~1.7 $\mu\text{m}$ )	Ref.[32], [93]
2		EBL	$\Delta T \sim 0.25$ (0.6~1.3 $\mu\text{m}$ )	Ref.[35]
3		EBL	$\Delta T = 0.35$ (0.7~3.5 $\mu\text{m}$ )	Ref.[34], [94]
4		EBL	$\Delta T \sim 0.4$ (1.15~1.5 $\mu\text{m}$ )	Ref.[36]
5		EBL	$\Delta T = 0.35$ (1.1~1.6 $\mu\text{m}$ ) $\eta = 9^\circ$	Ref.[37]
6		EBL	$\Delta T = 0.45$ (0.6~2.4 $\mu\text{m}$ )	Ref.[33]
7		DLW	$\Delta T \sim 0.7$ (3~6.5 $\mu\text{m}$ )	Ref.[21]
8		FIBID FEBID	$g \sim 0.4$ (0.5~1.4 $\mu\text{m}$ )	Ref.[38]
9		DNA template	$\eta = 0.04^\circ$ (0.4 ~0.7 $\mu\text{m}$ )	Ref.[40]
10		DNA template	$\eta = 0.08^\circ$ (0.4 ~ 0.9 $\mu\text{m}$ )	Ref.[44]

11		Peptide template	$\eta = 0.04^\circ$ (0.4 ~ 0.7 $\mu\text{m}$ )	Ref.[42]
12		LT GLAD	$\eta = 6^\circ$ (0.4 ~ 1.1 $\mu\text{m}$ )	Ref.[46], [136]
13		GLAD	$g \sim 0.2$ (0.4 ~ 0.9 $\mu\text{m}$ )	Ref.[47]
14		HCL	$\Delta T \sim 0.13$ (100 ~ 400 THz)	Ref.[45]
15		HCL	$\eta = 2^\circ$ (0.5 ~ 0.92 $\mu\text{m}$ )	Ref.[48]

create arbitrary 2D shapes of nanostructures, which provides high flexibility for chiral structure design. For the fabrication of chiral metamaterials, 3D structures are usually required to generate chirality. Therefore, a common strategy to fabricate 3D chiral metamaterials is stacking 2D nanostructures by multiple EBL steps, such as Structures #1–5 in **Table 2.1.1**. [32, 34-37, 93, 94] The main disadvantages of EBL are the long writing time and high cost. For a relatively large area, EBL is a series process with the electron beam scanning across the patterned area pixel by pixel, which takes extremely long time. For example, the write time for an exposure area of 1 cm<sup>2</sup> can take about 12 days. For chiral metamaterial fabrication, the strategy of stacking 2D structures using EBL will further increase the complexity, time, and cost of the fabrication process. Therefore, although EBL is a powerful technique for the chiral metamaterial fabrication intended for fundamental property investigations in laboratories, it can be hardly applied for large-scale

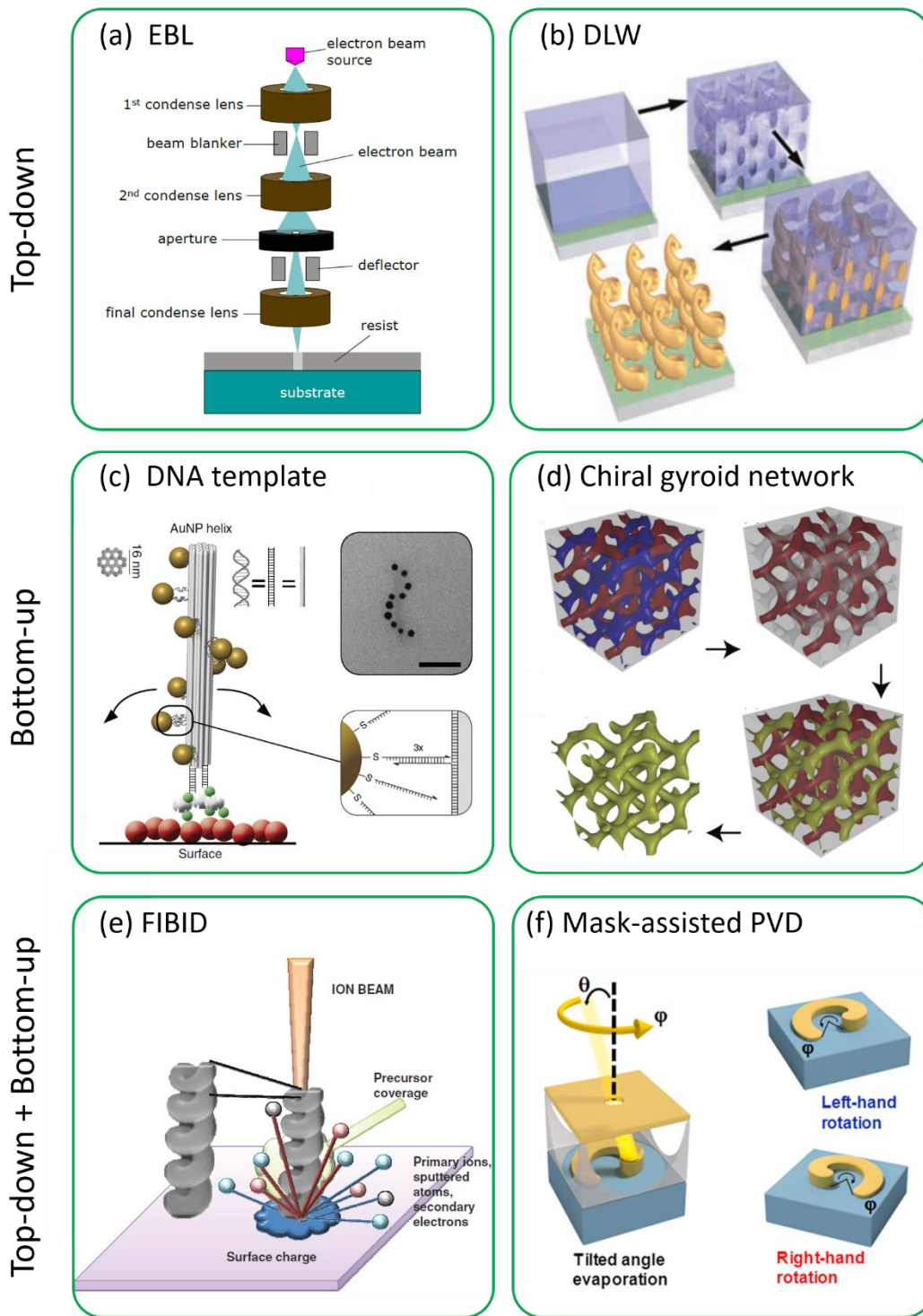


**Figure 2.1.1.** Schematic illustrations for top-down methods (a) EBL and (b) DLW (Ref.[21]), bottom-up methods (c) self-assembly on DNA template (Ref.[41]) and (d) self-assembly of block copolymers (Ref.[95]), and hybrid methods between top-down and bottom-up (e) FIBID. (Ref.[38]) and (f) mask-assisted PVD (Ref.[45]).

fabrication and device development in industries. Direct laser writing (DLW) is another top-down method which has been employed to fabricate helical-shape chiral metamaterials.[21, 96] By using 3D DLW and resist development, helical voids can be created in the positive-tone resist, which are then filled with gold by electrochemical deposition as shown in **Figure 2.1.1b**. The resist is then removed by plasma etching to obtain arrays of gold helices. The DLW technique allows the fabrication of structures with arbitrary 3D shapes. However, DLW is limited by its poor spatial resolution and low writing speed. The obtained structures are in micrometer scale, which are only optically active in IR region. The low writing speed makes DLW not suitable for scalable fabrications

Bottom-up fabrication is an additive process which starts with small and simple building blocks (atoms, molecules or nanoparticles) and produces large and complex structures through self-assembly process. Compared to top-down method, bottom-up method is usually cheaper, faster, and provides a scalable way for the fabrication of chiral metamaterials. The chiral metamaterial fabrication by bottom-up method usually requires chiral templates. Chiral macromolecular scaffolds, such as DNAs,[40, 41, 44] peptides,[42] and proteins,[97] have been used to produce chiral assemblies of plasmonic nanoparticles, as shown in **Figure 2.1.1c**. These chiral nanostructures usually have weak chiral optical response than those fabricated by top-down methods, as shown in **Table 2.1.1**, and are also mostly in liquid without long-range ordering, which can be hardly developed into substrate based devices. Another type of chiral template is the gyroid networks created by self-assembled block copolymers.[95, 98] The chiral structures are prepared by selectively removing the polymers and refilling the porous polymer network with metals, as shown in **Figure 2.1.1d**. The obtained chiral structures show large optical activity in visible to near-IR region, which is a promising bottom-up method for chiral metamaterial fabrication.

Physical vapor deposition (PVD) is a common bottom-up method for preparing thin films, which can also be utilized for chiral metamaterial fabrications. For example, nano-helix arrays have been realized by PVD on a pre-patterned or even not pre-patterned substrate in a slow azimuthal rotation with a large angle between the incident vapor and the substrate normal, which show significant chiral optical response.[46, 47, 99]

Some fabrication techniques take notions from both top-down and bottom-up methods, which are usually thought as hybrid methods between top-down and bottom-up, such as focused ion beam induced deposition (FIBID). FIBID has been employed to fabricate nano-helix arrays as shown in **Figure 2.1.1e**. [38, 39] Precursor molecules are used as the building blocks of nano-helices (bottom-up), which are formed by their interaction with the focused ion beam (top-down). [100] FIBID can be regarded as a localized chemical vapor deposition induced by a direct writing or patterning technique, which is maskless and resistless. FIBID possesses a good resolution in nanometer scale, provides the same freedom in creating arbitrary structures, but suffers from the low processing speed. The mask-assisted PVD is another hybrid method between bottom-up (self-assembly process of mask formation and vapor deposition) and top-down (production of dotted or structured layers in a conventional lithography way) for chiral metamaterial fabrication. It is usually denoted as nanosphere lithography (NSL) with nanospheres as the deposition mask, [101] and hole-mask colloidal lithography (HCL) with nano-holes as the deposition mask. [102] For example, chiral C-shaped nanostructures have been fabricated by HCL, as shown in **Figure 2.1.1f**. [45] Recently, chiral oligomer nanostructures have been realized by both NSL and HCL. [48, 103]

In this dissertation, our research goal is to develop scalable methods to fabricate chiral metamaterials for optical device applications. Therefore, we employ a PVD based fabrication

technique—dynamic shadowing growth (DSG), which will be discussed in details in the next section.

## **2.2 Dynamic shadowing growth**

DSG is a physical vapor deposition based technique for micro/nano-structure fabrication, which is also known as glancing angle deposition (GLAD). DSG is suitable for developing metamaterial devices for three reasons: first, DSG is a simple and scalable fabrication method, which can be applied for wafer-scale fabrication; second, unlike some other bottom-up methods resulting in particles in solutions, DSG leads to arrays of micro/nano-structures on substrates, which is ideal for device developments; finally, the shape of the structures fabricated on regular templates can be designed through computational simulations. A recent study has demonstrated that DSG can be incorporated into a roll-to-roll manufacturing system to increase the throughput, which provides a foundation for industrial productions.[104] So far, DSG has been widely used to produce thin film micro/nano-structures for many applications, including broad-range antireflection coatings,[105] photonic crystals,[106] liquid crystal devices,[107] surface enhanced Raman spectroscopy substrate,[108] mechanical devices,[109] catalysts,[110] solar cells,[111] magnetic tape for data storage,[112] and many other sensor applications.[113-115]

A typical DSG experimental setup is shown in **Figure 2.2.1a**. The vacuum chamber is maintained at a pressure of  $10^{-6}$  Torr during the vapor deposition, which ensures that the mean free path of the vapor molecules is much larger than the dimension of the vacuum chamber. The source material located at the bottom of the vacuum chamber is evaporated and vapor travels upwards from the source material to the substrate. A long distance from the source material to the substrate is used to achieve the collimated vapor flux at the substrate surface. The vapor arrives at

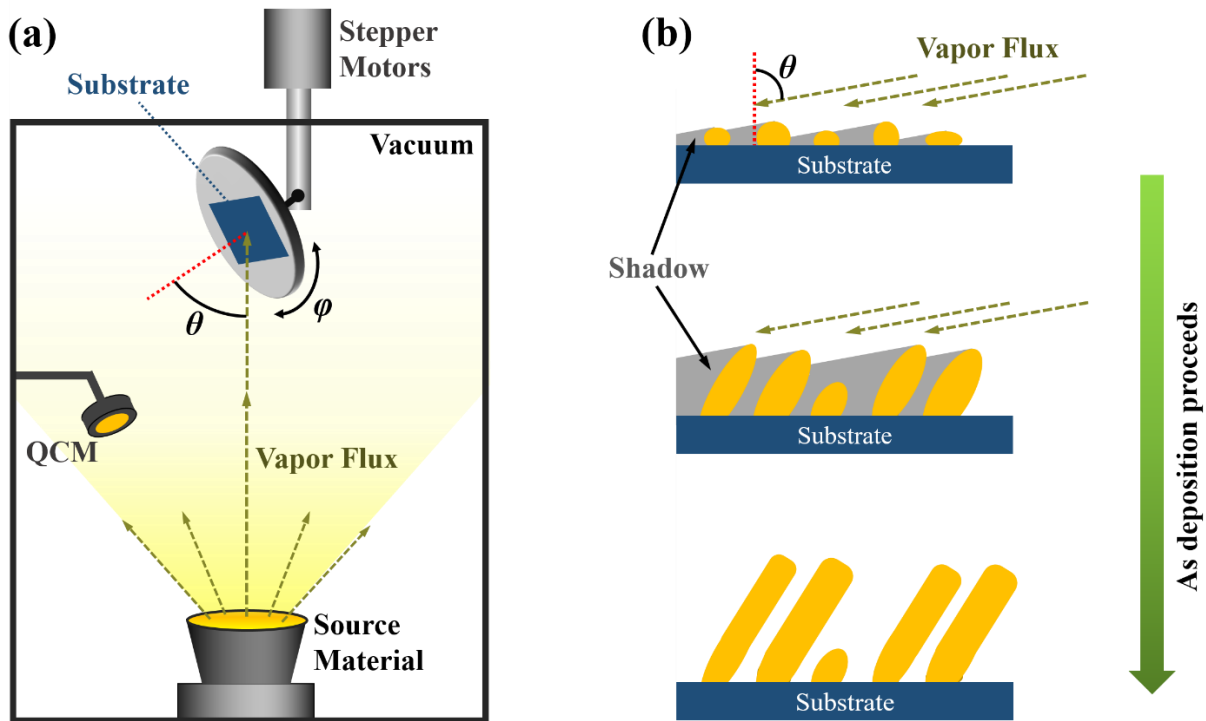


**Figure 2.2.1.** (a) Schematic diagram of DSG in a vacuum deposition system. (b) Schematic diagram of the initial nuclei formation, the nanorod growth under shadowing effect, and the obtained nanorod array (from top to bottom).

the substrate at a polar angle  $\theta$  with respect to the substrate normal and an azimuthal angle  $\phi$ , as defined in **Figure 2.2.1a**. The substrate is mounted on a holder, which can be controlled to rotate in both polar and azimuthal directions by stepper motors. The deposition thickness is monitored by a quartz crystal microbalance (QCM).

The primary growth mechanism of DSG is the geometric shadowing effect. During the vapor deposition, the well collimated vapor flux cannot reach the region behind any existing structures, and material will only accumulate in the region which is not shadowed forming nanostructures. Therefore, the shadowed or not shadowed area plays an important role in determining the growth and resulting shape of nanostructures. The shadowed area is determined

by the geometric shape of the shadowing centers, i.e., the existing structures or templates, and the orientation of the shadowing centers with respect to the vapor flux, which both should be carefully designed for fabricating chiral structures.

DSG at a large  $\theta$  on a static substrate is usually referred to as oblique angle deposition (OAD). OAD on a bare substrate can produce titled nanorods, which can be a simple example to illustrate the DSG process, as shown in **Figure 2.2.1b**. The initially arrived vapor can form randomly distributed nuclei on the substrates. As the deposition proceeds, islands grow into columns, with developing shadows. Some shorter columns may fall into the shadows of the nearby taller ones, receiving no more material, and therefore stop growing (indicated in **Figure 2.2.1b**). The taller columns, on the contrary, can continuously receive vapor and grow longer. The growth of OAD films is a competitive process due to the shadowing effect and adatom surface diffusion, which eventually produce a layer of nanorods tilted towards the vapor source. The obtained titled nanorods by OAD are shown in **Figures 2.2.2A and 2.2.2A'**. More nanostructures with various morphologies can be fabricated by DSG with a controlled substrate rotations, such as vertical nanorods, helical nanorods, zigzag nanorods, C-shaped nanorods, and bead-like nanorods, as shown in **Figures 2.2.2B–F and 2.2.2B'–F'**, respectively. As described above, DSG on a bare flat substrate starts with a random distribution of nuclei, which ends up with randomly distributed nanostructures. However, the metamaterial fabrication requires periodic nanostructure arrays. This requirement can be met by replacing the flat substrate surface by a deposition template with ordered arrays of nucleation centers, such as nanospheres, nanopillars and nanoholes. The templates with regular shadowing centers can help to create ordered arrays of nanostructures. A comparison of helical nanorods grown by DSG with and without a periodic seed layer is shown in

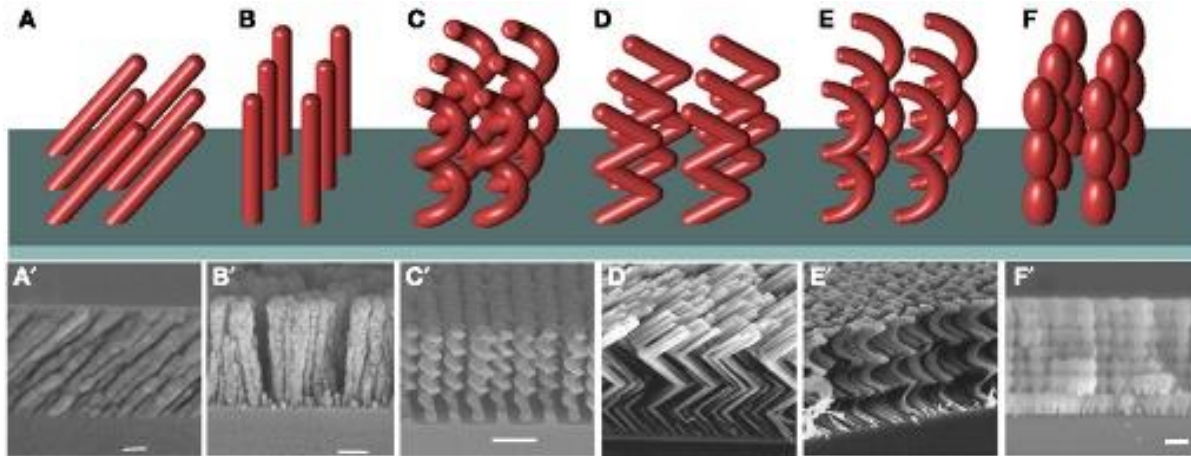


**Figure 2.2.2.** (A)–(F) Schematics and (A')–(F') SEM images of typical nanorod arrays fabricated by DSG. (A) Titled nanorods and (A') titled Si nanorods deposited at  $\theta = 80^\circ$ ; (B) vertical nanorods and (B') vertical Si nanorods deposited at  $\theta = 86^\circ$ ; (C) helical nanorods and (C') regular array of helical Si nanorods; (D) and (D') zigzag nanorods; (E) C-shaped nanorods and (E') C-shaped  $\text{MgF}_2$  nanorods. (F) bead-like nanorods and (F') bead-like Si nanorods. Ref.[116]

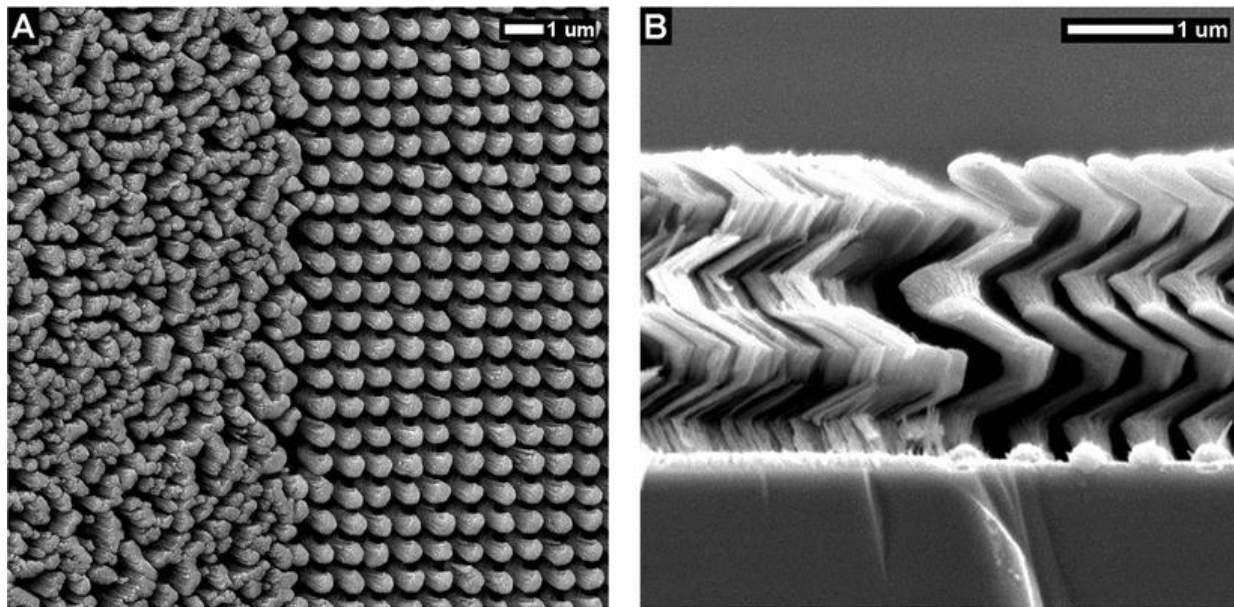


**Figure 2.2.3.** (A) Top- and (B) side-view images comparing aperiodic (left) and periodic (right) Si nanorods by DSG. The periodic Si nanorods are grown on a seed layer. Ref.[117]

**Figure 2.2.3.** The use of the seed layer has a significant impact on the morphology of the nanorod array. The nanorod positions, the rod-to-rod distance, and the nanorod diameter are all determined

by the seed layer, which have very small variations and are almost constants. Additionally, the regular templates can also generate unique shadowing profiles and tailor the shape of nanostructures, which is important for chiral structure fabrications. As it will be demonstrated in the Chapters 3 and 4, the shadowing effect of the regular templates can be utilized to create various chiral nanostructures. Therefore, the template-assisted DSG, with the ability to create regular nanostructure arrays and to engineer the nanostructure shape, can be a powerful fabrication technique for producing chiral metamaterials.

### **2.3 Self-assembled colloidal monolayer**

As it has been demonstrated in Section 2.2, regular templates are needed for chiral metamaterial fabrication by DSG. Among a variety of templates, such as polymer resist patterns by lithography method,[117, 118] ZnO pillars by hydrothermal synthesis,[119] nanohole arrays,[45] and Au nanodot arrays by micellar nanolithography,[46] we select the 2D colloidal crystal or colloidal monolayer as the template for DSG,[120] because its fabrication is simple, cost-effective, and scalable. The self-assembled colloidal monolayers (SACMs) are usually hexagonally close-packed because such a lattice has the lowest free energy. During the fabrication process, the colloidal spheres are influenced by van der Waals forces, electrostatic forces, and steric repulsions, which all govern the self-assembled monolayer formation. There are a few different methods for preparing the SACMs, including solvent evaporation method, spin coating, interface method, and alternating electric field method.[121] Here we use an air-water interface method to fabricate hexagonally close-packed monolayer of polystyrene (PS) nanospheres.[122]

The experimental setup for preparing PS nanosphere monolayers is shown in **Figure 2.3.1a**. First, the PS nanosphere suspension purchased initially at a concentration of 2.6 wt. % in water is diluted to 0.4 wt. % in deionized water, and further diluted with ethanol to a 2:1 volumetric

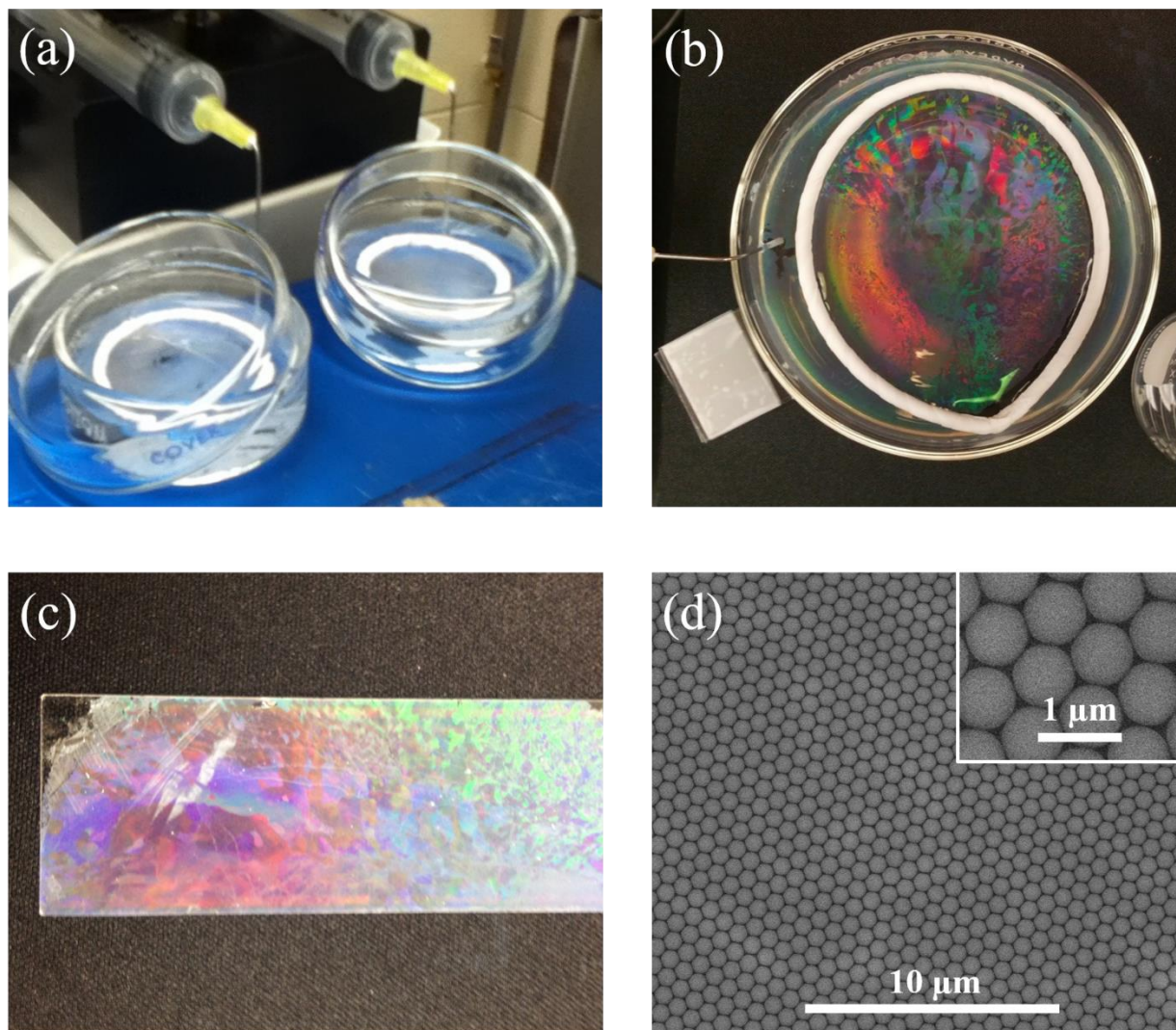


**Figure 2.3.1.** (a) The experimental setup for preparing self-assembled colloidal monolayers. (b) The formation of monolayers in Petri dish. (c) The obtained monolayer on a glass substrate. (d) Top-view SEM image of the nanosphere monolayer with  $d = 750$  nm.

ratio. The suspension is then loaded into a syringe and mounted onto a syringe pump (KD Scientific). A cleaned glass Petri dish (diameter of 10 cm), pre-filled with 24 mL of deionized water, is tilted at an angle of about  $7^\circ$ , and a needle attached to the syringe is bent towards the water within the Petri dish. Droplets of PS solution are dispensed onto the water surface at a rate of 0.015 mL/min. Each drop spreads radially outward from the droplet location, and a monolayer of PS nanospheres is slowly formed on the water surface along the edge of the Petri dish. This

process continues until a monolayer of PS nanospheres covered nearly the entire water surface, as shown in **Figure 2.3.1b**. A Teflon ring, with a diameter smaller than the diameter of the Petri dish, is then placed gently on the water surface to protect the monolayer film against adhering to the side wall of the Petri dish. After the water level is raised, glass and silicon pieces are slid carefully under the water to the area below the monolayer film (inside the Teflon ring). Finally, after slowly pumping water out from the Petri dish, the monolayer film is deposited onto the surface of the submerged substrates, as shown in **Figure 2.3.1c**. The obtained monolayers with a diameter  $d = 750$  nm are hexagonally close-packed nanosphere arrays as shown in the top-view SEM images in **Figure 2.3.1d**. The PS nanospheres are commercially available with different diameters from tens of nanometers to a few micrometers. In this dissertation, we mainly use nanospheres with  $d = 200$ , 350 and 500 nm. The monolayers are usually polycrystalline with large numbers of domains aligned in different orientations. By carefully controlling pH of the solution, a monocrystalline monolayer can be achieved in a large area  $\sim 1$  cm<sup>2</sup>, which is important for optical device fabrication.

## 2.4 Morphology calculation

The morphology of nanostructures fabricated by DSG can be modeled by Monte Carlo or molecular dynamics method.[123, 124] Both methods have their own advantages in the morphology simulations, however, they require a large amount of computer time and also provide many morphological details, such as porosity and surface roughness, which are not necessary for designing chiral structures. To guide the design of chiral structures, a simple and fast calculation is needed, which focuses on modeling the overall shape of nanostructures. I have developed a MATLAB program to estimate the thickness distribution of the thin films coated on the

nanospheres by DSG. As illustrated in **Figures 2.4.1a and 2.4.2b**, a collimated vapor flux approaches a hexagonal array of nanospheres from the direction  $\hat{l}(\theta_0, \varphi_0)$ .  $\theta_0$  is defined as the angle between the vapor flux and the substrate surface normal, while  $\varphi_0$  is defined as the angle between the projection line of the incident vapor flux in substrate surface and an imaginary line going through the centers of nanospheres in a row. Note this definition of  $\varphi_0$  will apply for the rest of this dissertation. The center-to-center distance of nanospheres is defined as  $D$ , and the radius of nanospheres is  $r$ , which satisfy  $D \geq 2r$ . Notice, the close-packed monolayer has  $D = 2r$ , while the

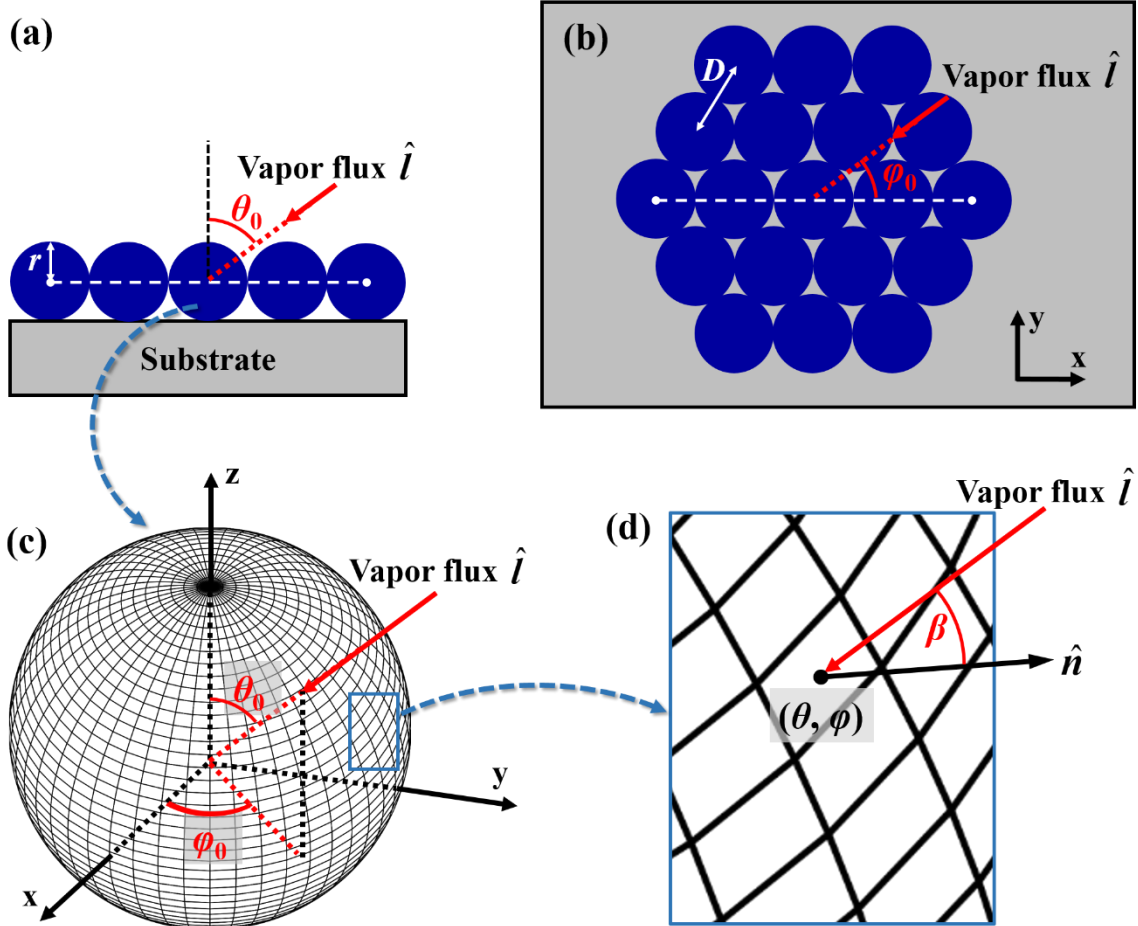


**Figure 2.4.1.** (a) Cross-sectional and (b) top view of DSG on a hexagonal nanosphere array. (c) The surface of the nanosphere is split into many surface elements for calculating the thickness distribution. (d) Each surface element  $(\theta, \varphi)$  with its surface normal  $\hat{n}$ .

non-close-packed monolayer has  $D > 2r$ . In order to calculate the thickness distribution on one nanosphere, the shadowing effect of the nearby nanospheres should be taken into account. As shown in **Figures 2.4.1c** and **2.4.1d**, the surface of a nanosphere is split into small surface elements. Each element is denoted as the coordinate of its center  $(\theta, \varphi)$ , where  $\theta = i \cdot \Delta\theta$ ,  $\varphi = j \cdot \Delta\varphi$ , and we usually set  $\Delta\theta = \Delta\varphi = 0.5^\circ$ ,  $i = 0, 1, \dots, 360$ ,  $j = 0, 1, \dots, 720$ . The surface normal of each element  $\hat{n}$  and the vapor flux form an angle  $\beta$ .

This calculation is based on three assumptions:

- I. Only the shadowing effect of nanospheres are considered. The shadowing effect of the deposited films, and other physical process, such as surface diffusion, are neglected.
- II. The deposition at different surface elements occurs simultaneously and independently, as long as they are directly exposed to vapor flux.
- III. The thickness of the deposited film follows a cosine rule, i.e. the thickness change  $\Delta t \propto \cos \beta$ , [125] and is uniform within each surface element.

The detailed procedure of the morphology calculation is listed below.

1. Initialize the thickness array  $t(r, \theta, \varphi) = 0$ .
2. At the beginning of each deposition step, determine  $\theta_0$ ,  $\varphi_0$ , and  $\Delta t_{QCM}$ , where  $\Delta t_{QCM}$  is the thickness change in QCM or a flat surface with an incident angle of  $0^\circ$ . Calculate the vapor vector  $\hat{l} = (1, \theta_0, \varphi_0) = (\sin \theta_0 \cos \varphi_0, \sin \theta_0 \sin \varphi_0, \cos \theta_0)$ .
3. Find the nearby nanospheres that may potentially affect the deposition. The nanospheres within a distance of  $2r/\cos\theta_0$  should be considered. Put these nanospheres in a library S with center coordinates stored in arrays X, Y, Z, where  $Z_i = 0$  for all spheres. Update the library S by only selecting nanospheres which satisfy  $(X_i, Y_i, 0) \cdot \hat{l} > 0$

4. For one surface element  $(r, \theta, \varphi)$  with surface normal  $\hat{n} = (1, \theta, \varphi)$ , determine whether this surface element is on the hemisphere facing vapor flux.

If  $\hat{n} \cdot \hat{l} > 0$ , then this surface element is facing vapor flux, but can still be shadowed by other spheres. Then go to Step 5.

If  $\hat{n} \cdot \hat{l} \leq 0$ , then this surface element is on the back side of the sphere, which is not facing vapor flux. Then make  $\Delta t = 0$ , skip Steps 5 and 6, and go to Step 7.

5. Determine whether surface element  $(r, \theta, \varphi)$  is shadowed by the nanospheres in library S one by one. Create a vector  $\alpha$ , from the surface element  $(r, \theta, \varphi) = (x, y, z)$  to the center of  $i$ th nanosphere  $(X_i, Y_i, 0)$  in S library,  $\alpha = (X_i, Y_i, 0) - (x, y, z)$ .

If  $\sqrt{|\alpha|^2 - (\alpha \cdot \hat{l})^2} > r$ , then the surface element  $(r, \theta, \varphi)$  does not fall in the shadow of  $i$ th nanosphere. Check  $(i+1)$ th nanosphere by the same method. If this is the last nanosphere in S, then go to Step 6.

If  $\sqrt{|\alpha|^2 - (\alpha \cdot \hat{l})^2} \leq r$ , then the surface element  $(r, \theta, \varphi)$  falls into the shadow of  $i$ th nanosphere. Make  $\Delta t = 0$ , and go to Step 7.

6. If the surface element  $(r, \theta, \varphi)$  does not fall in the shadow of any nanospheres, then  $\Delta t = \Delta t_{QCM} \hat{n} \cdot \hat{l}$ , and go to Step 7.

7. Update the thickness,  $t(r, \theta, \varphi) = t(r, \theta, \varphi) + \Delta t$ .

8. If the element  $(r, \theta, \varphi)$  is not the last one element in the array, go to the next element and repeat Step 4-7.

9. If there is a following deposition step with different  $\theta_0, \varphi_0$ , and  $\Delta t_{QCM}$ , then repeat Steps 2-8 with the new values of  $\theta_0, \varphi_0$ , and  $\Delta t_{QCM}$ .

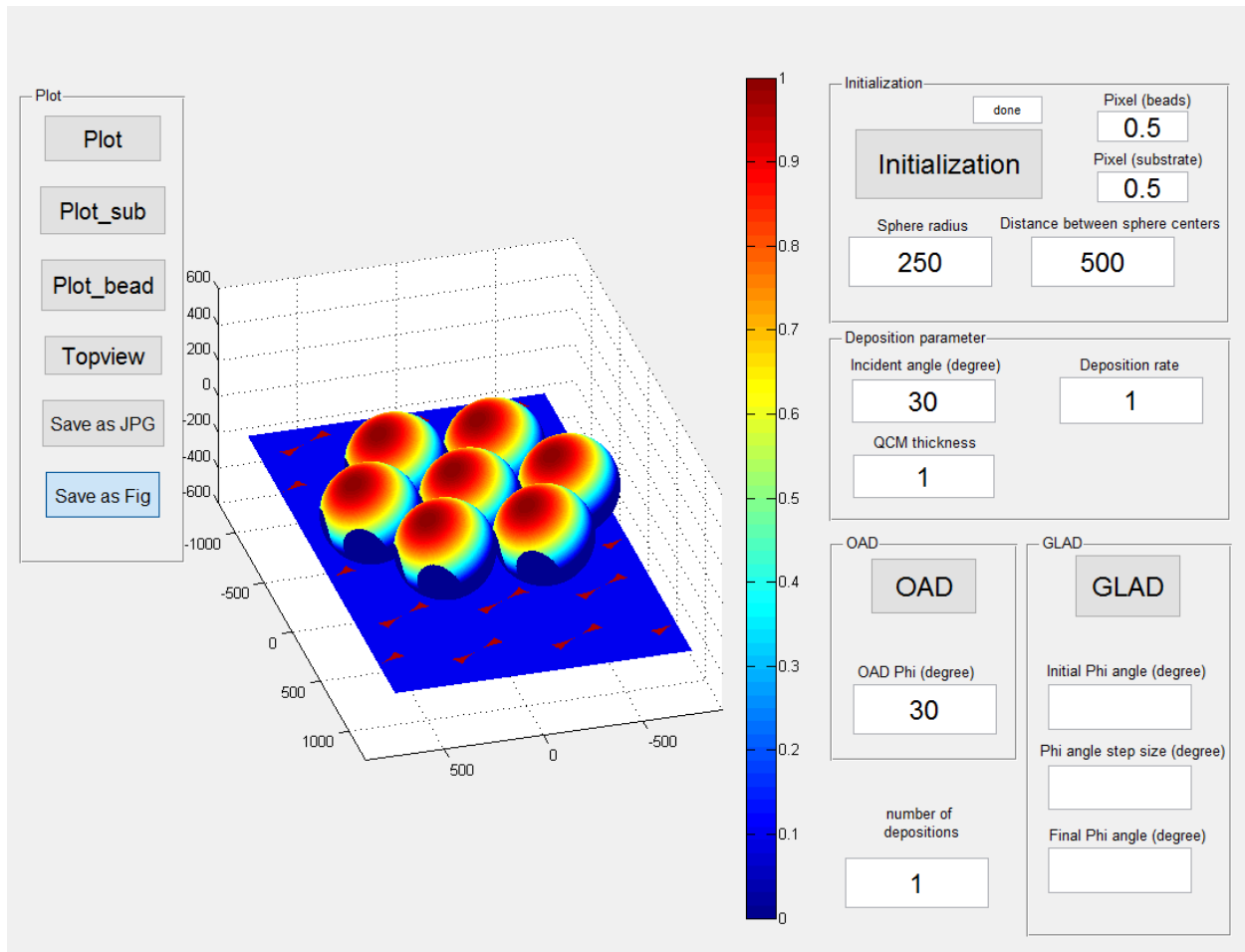


**Figure 2.4.2.** Graphic user interface of the morphology calculation program.

The morphology calculation can generate a thickness distribution of the thin film coated on nanospheres. Similarly, the thickness distribution of the thin films on the substrates can also be estimated. I built a graphic user interface (GUI) that runs the calculation of the thin film thickness distribution on both nanospheres and substrates. **Figure 2.4.2** shows the GUI program that has completed a calculation of an OAD with  $D = 500$  nm,  $r = 250$  nm,  $\theta_0 = 30^\circ$ ,  $\varphi_0 = 30^\circ$ , and  $\Delta t_{QCM} = 1$  nm. The left panel provides functions for plotting and displaying. The middle panel is the output display of the calculated thin film distribution in 3D. The top-right panel includes the input parameters for initialization of the morphology calculation, sphere radius  $r$ , distance between sphere centers  $D$ , pixel (beads), and pixel (substrate), where pixel (beads) is  $\Delta\theta$  or  $\Delta\varphi$ , and pixel

(substrate) defines the size of the surface element on substrates. The middle-right panel provides two input parameters, incident angle (degree)  $\theta_0$  and deposition rate  $\Delta t_{QCM}$ , and one output parameter displaying the total QCM thickness. The two panels at the bottom-right corner allow the calculation with a static  $\varphi_0$  for OAD and a dynamic  $\varphi_0$  for GLAD.

An example of the morphology calculation is shown in **Figure 2.4.3**, which calculates the thickness distribution of the nanostructures obtained by an OAD on hexagonally close-packed nanosphere monolayers at  $\theta_0 = 86^\circ$ , and  $\varphi_0 = 0^\circ, 5^\circ, 10^\circ \dots 60^\circ$ .  $\varphi_0$  between  $0^\circ$  and  $60^\circ$  is chosen, because the depositions at  $\varphi_0$  and  $\varphi_0+60^\circ$  are actually the same due to the six-fold symmetry of the hexagonal monolayer lattice. It should be noted that the calculated thickness distribution can only be qualitatively accurate since many physical processes are ignored. As it has been addressed above, the purpose of this morphology calculation is to provide an estimation of the geometric shapes of the deposited nanostructures, which serves to guide the design of chiral structures. The

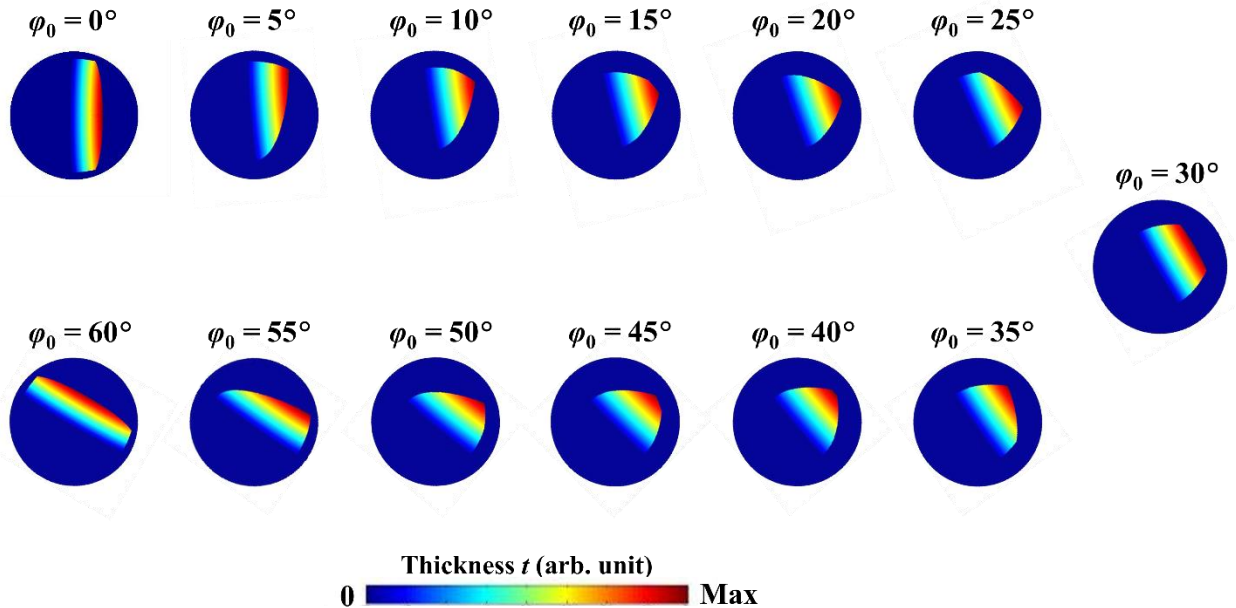


**Figure 2.4.3.** The calculated morphology of the nanostructures fabricated by an OAD at  $\theta_0 = 86^\circ$  and  $\varphi_0 = 0^\circ, 5^\circ, 10^\circ \dots 60^\circ$ .

calculation results in **Figure 2.4.3** clearly show the geometric shapes of the fabricated nanostructures, leading to several conclusions: (i) an OAD at large  $\theta_0$  creates isolated nanostructures coated on nanospheres; (ii) the shape of these isolated nanostructures fabricated at a fixed  $\theta_0$  strongly depends on the domain orientation  $\varphi_0$ ; (iii) the depositions at  $\varphi_0$  and  $60^\circ - \varphi_0$  produce the same shape of nanostructures with reflection symmetry. As it will be demonstrated in the following chapters, this morphology calculation plays an important role in guiding the design of chiral structures.

## 2.5 Morphological characterizations

The morphology of the fabricated chiral nanostructures has been characterized by scanning electron microscopy (SEM) and transmission electron microscopy (TEM). In this dissertation, the SEM images are collected using a field-emission scanning electron microscope (FEI Inspect F), and the TEM images are collected using a transmission electron microscope (Tecnai 20).

One important parameter in morphology characterizations is the orientation of the monolayer domains with respect to the incident vapor flux  $\varphi_0$ , as it will be demonstrated in the next several chapters.  $\varphi_0$  defined in Section 2.4, is determined based on the top-view SEM images of the fabricated nanostructure arrays. **Figure 2.5.1** shows a top-view SEM image of Ag chiral films on the monolayer. The imaginary line that passes through centers of nanospheres can be easily determined as shown by the yellow line. The projection line of the incident vapor can be determined by the shadowing effect. The colloid monolayers have defects, such as extra beads on the top of the monolayer. The extra beads work as a shadowing center during depositions and prevents the incident vapor arriving in the area behind it, resulting in a strip with less or no deposited material. This strip will be parallel with the projection line of the incident vapor. **Figure**

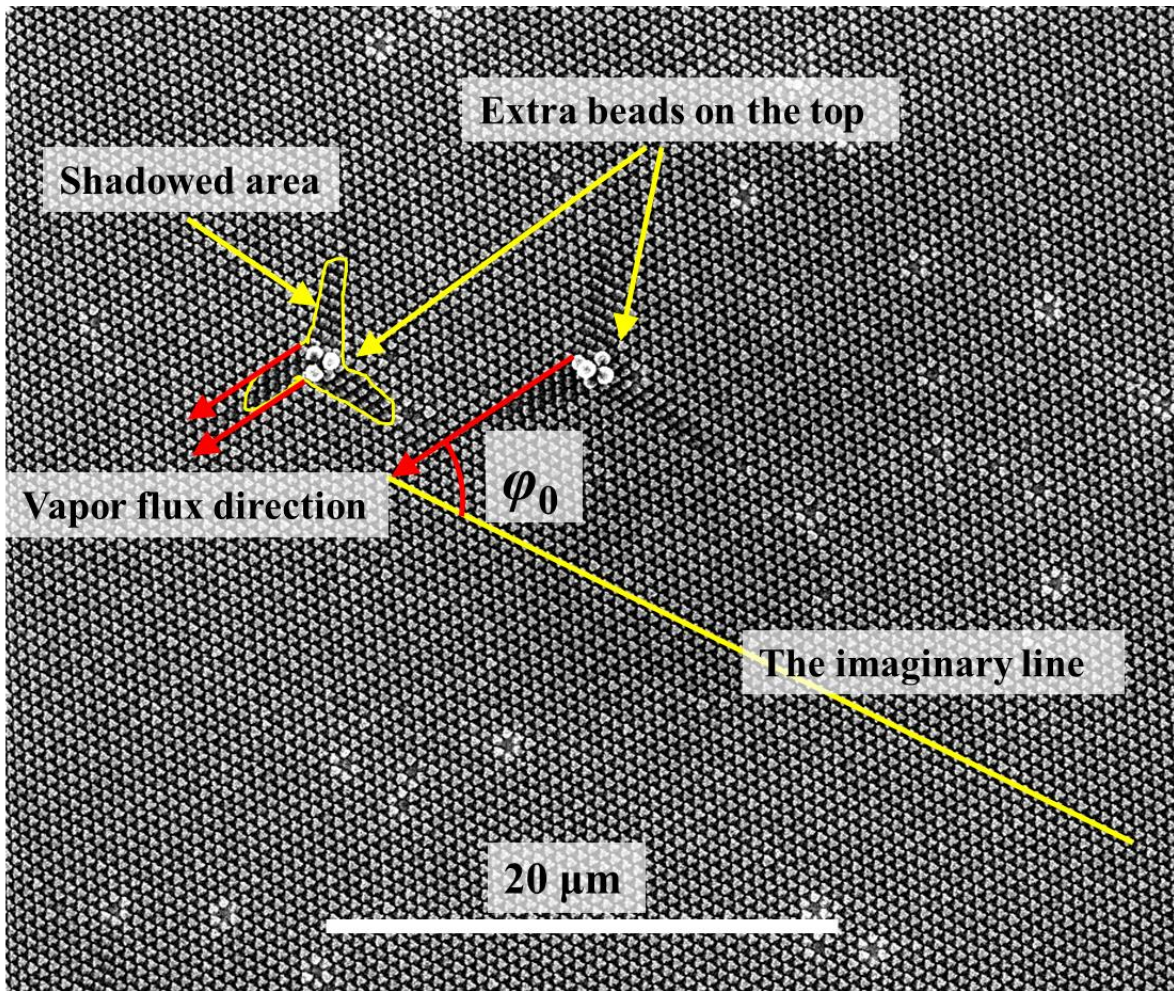


**Figure 2.5.1.** Top-view SEM image of Ag films on the monolayer with two clusters of extra beads on the top of the monolayer with three-armed star shaped shadowed area. Red arrows indicate the direction of incident vapor flux, and the yellow line passes through the centers of nanospheres.

**2.5.1** shows two clusters of extra beads with three-armed star shaped shadowed area, which results from the Ag depositions in three directions. The red arrows in **Figure 2.5.1**, which are parallel with one strip from the shadowed area, are the projection line of the incident vapor. The angle between the red arrow and the yellow straight line is  $\varphi_0$ .

## 2.6 Optical characterizations

Transmittance, especially circularly polarized transmittance,  $T(\text{RCP})$  and  $T(\text{LCP})$ , is usually measured for the optical characterization of chiral metamaterials. The unpolarized transmittance spectra are measured by a UV-vis-NIR double beam spectrophotometer (JASCO V-570). The circularly polarized transmittance spectra are measured by three different experimental setups, the double beam spectrophotometer (JASCO V-570) equipped with a Glan-Thompson polarizer (Thorlabs Inc.) and an achromatic quarter wave plate ( $\lambda = 1100\text{--}2000$  nm, Thorlabs, Inc.), a spectroscopic ellipsometer (M-2000, J. A. Woollam, Inc.,  $\lambda = 370\text{--}1000$  nm), and a custom spectroscopic microscope ( $\lambda = 450\text{--}1000$  nm).

A variable angle spectroscopic ellipsometer (M-2000, J. A. Woollam, Inc.) is used in transmission mode to measure the first three rows of the Mueller matrix with the  $m_{11}(\lambda)$  element normalized to 1. Therefore, each Muller matrix element directly obtained by ellipsometric measurements is  $\frac{m_{ij}(\lambda)}{m_{11}(\lambda)}$ , where  $m_{ij}(\lambda)$  is the un-normalized Muller matrix element of the  $i$ th row and  $j$ th column. The unpolarized transmittance spectra are measured by UV-vis-NIR double beam spectrophotometer (JASCO V-570) and are used to determine the un-normalized  $m_{11}(\lambda)$ . Then the un-normalized  $m_{14}(\lambda)$  can be calculated, which determines the circular polarized differential transmittance,  $\Delta T = T(\text{RCP}) - T(\text{LCP}) = 2m_{14}(\lambda)$ . [126]

The two setups described above have a beam spot size of a few millimeters, which cannot be used to measure the transmittance of the nanostructures on small monolayer domains ( $< 1 \text{ mm}^2$ ). In order to investigate the optical property of nanostructures on individual monolayer domains, a custom spectroscopic microscope was built. **Figure 2.6.1** shows the schematic of the custom spectroscopic microscope setup. The light source is a quartz tungsten-halogen lamp (400–2200 nm Thorlabs, QTH10). The broadband light emitted by the lamp was collimated by two lenses L1 ( $f =$

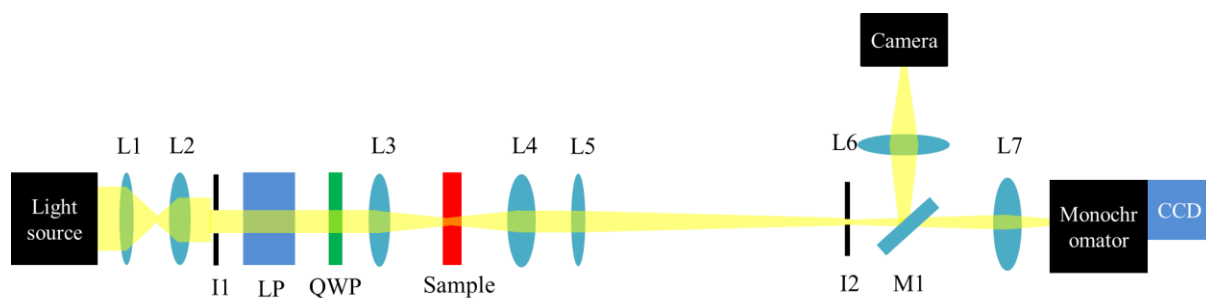


**Figure 2.6.1.** Schematic of the custom spectroscopic microscope setup. *L*: lens, *I*: iris, *LP*: linear polarizer, *QWP*: quarter wave plate, *M*: mirror. *M1* is on a flip mount, which either reflects light to the camera or allows light to transmit to the monochromator.

15 cm) and L2 ( $f = 7$  cm), and sent through an iris I1 (diameter = 1 cm). Then the light traveled through a Glan-Talyor linear polarizer, LP (Thorlabs, DGL10) and then a quarter wave plate, QWP, to generate circularly polarized light. Two QWPs were prepared with different working wavelength ranges (Thorlabs, AQWP05M-600, 400–800 nm, and AQWP05M, 690–1200 nm) in order to obtain a spectrum with wavelength range 450–1000 nm. A lens L3 ( $f = 15$  cm) was used to focus the light on the sample. The sample was mounted on a 3-dimensional translation stage. Two lenses L4 ( $f = 10$  cm) and L5 ( $f = 100$  cm) behind the sample were used to create a magnified image of the sample surface at the position of the iris I2 (diameter = 4 mm). A mirror M1 on a flip mount could be used to reflect the light through a lens L6 ( $f = 10$  cm) to a camera (Thorlabs, DCC1545M, color version) to display the image of the sample surface. M1 could also be flipped down to transmit the light through a lens L7 ( $f = 5$  cm) to a monochromator (Newport, 74126) equipped with a CCD array detector (Newport, 78237) for transmittance measurements. For the characterization of the chiral films on monocryalline monolayers, L5 and I2 were removed and the positions of L4, L7, and the monochromator were changed in order to collect all the transmitted light.

When circularly polarized light travels through chiral metamaterials, the transmitted light

may contain a portion of circularly polarized light in opposite handedness. This circular polarization conversion originates from the anisotropy of chiral metamaterials, and changes its sign when changing the illumination direction. Therefore, the circular polarization transmittance spectra were measured in both front and back illumination modes, and then averaged to obtain the true  $\Delta T$  signal.

## 2.7 Finite-difference time-domain simulation

Finite-difference time-domain (FDTD) method is a numerical modeling technique, which is applied to solve Maxwell's equations in time domain. FDTD method was developed by Kane Yee,[127] and has become an important and effective tool for the analysis of electrodynamic systems, especially those with novel properties, such as metamaterials. In the algorithm of FDTD, the Maxwell's equations are discretized in both space and time. The Maxwell's curl equations in an isotropic medium are:

$$\mu \frac{\partial H}{\partial t} + \nabla \times E = 0, \quad (2.7.1)$$

$$\varepsilon \frac{\partial E}{\partial t} - \nabla \times H = J, \quad (2.7.2)$$

where  $\varepsilon$  is the medium permittivity,  $\mu$  is the medium permeability, and  $J$  is the current density.

These two curl equations generate six coupled scalar equations as follows

$$\mu \frac{\partial H_x}{\partial t} = \frac{\partial E_y}{\partial z} - \frac{\partial E_z}{\partial y}, \quad (2.7.3)$$

$$\mu \frac{\partial H_y}{\partial t} = \frac{\partial E_z}{\partial x} - \frac{\partial E_x}{\partial z}, \quad (2.7.4)$$

$$\mu \frac{\partial H_z}{\partial t} = \frac{\partial E_x}{\partial y} - \frac{\partial E_y}{\partial x}, \quad (2.7.5)$$

$$\varepsilon \frac{\partial E_x}{\partial t} = \frac{\partial H_z}{\partial y} - \frac{\partial H_y}{\partial z} - J_x, \quad (2.7.6)$$

$$\varepsilon \frac{\partial E_y}{\partial t} = \frac{\partial H_x}{\partial z} - \frac{\partial H_z}{\partial x} - J_y, \quad (2.7.7)$$

$$\varepsilon \frac{\partial E_z}{\partial t} = \frac{\partial H_y}{\partial x} - \frac{\partial H_x}{\partial y} - J_z. \quad (2.7.8)$$

In FDTD method, the computational space, including the structures of interest, is segmented into box-shaped cells with dimensions  $\Delta x \times \Delta y \times \Delta z$ , known as Yee's cells, as shown in **Figure 2.7.1**. The electric ( $\vec{E}$ ) and magnetic ( $\vec{H}$ ) fields are placed at the centers of lines or surfaces of the cell with each component at a unique position, so that each  $\vec{E}$  component is surrounded by four

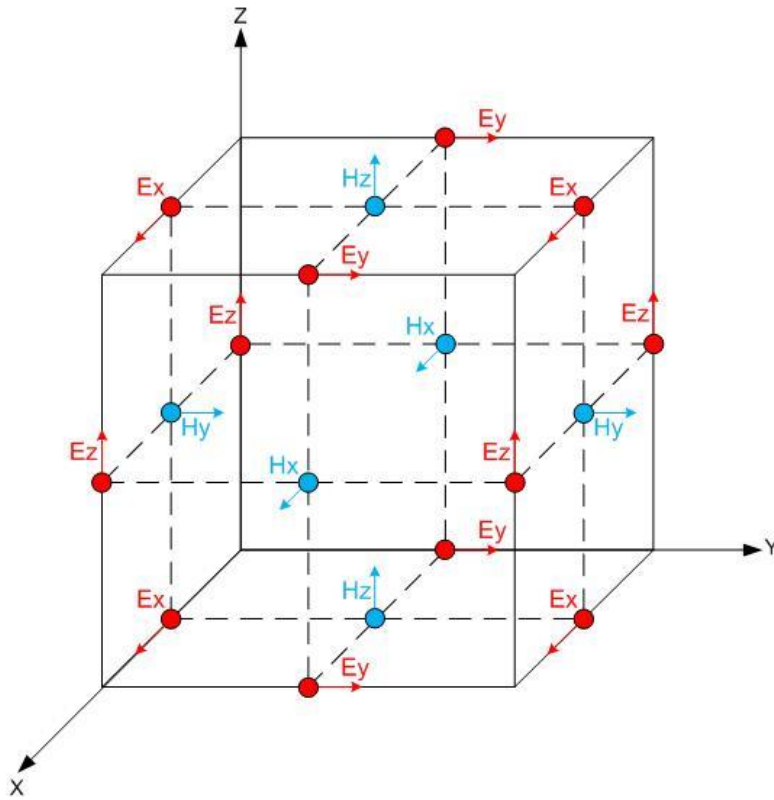


**Figure 2.7.1.** Yee's cell

$\bar{H}$  components and conversely. The electric and magnetic fields are updated at a time step  $\Delta t$ . The value of  $\Delta t$  should be carefully chosen, which needs to satisfy the stability condition[128]

$$\Delta t < \frac{1}{c \sqrt{\frac{1}{\Delta x^2} + \frac{1}{\Delta y^2} + \frac{1}{\Delta z^2}}}, \quad (2.7.9)$$

where  $c$  is the light speed. The electric fields  $E_x$ ,  $E_y$  and  $E_z$  are calculated at time  $n\Delta t$ , while the magnetic fields  $H_x$ ,  $H_y$  and  $H_z$  are calculated at time  $(n+0.5)\Delta t$ , where  $n$  is an integer. The electric field components  $E_{\alpha=x,y,z}^n(i, j, k)$  at position  $(i\Delta x, j\Delta y, k\Delta z)$  and time  $n\Delta t$  is denoted as  $E_{\alpha=x,y,z}^n(i, j, k)$ , which also applies for the magnetic fields. Following the above notations, the finite difference equations for Equations (2.7.3)-(2.7.8) can be obtained. For Equation (2.7.3), the finite difference equation for calculating  $B_x$  can be expressed as

$$\begin{aligned} & \frac{B_x^{n+0.5}(i, j+0.5, k+0.5) - B_x^{n-0.5}(i, j+0.5, k+0.5)}{\Delta t} \\ &= \frac{E_y^n(i, j+0.5, k+1) - E_y^n(i, j+0.5, k)}{\Delta z} - \frac{E_z^n(i, j+1, k+0.5) - E_z^n(i, j, k+0.5)}{\Delta y}, \end{aligned} \quad (2.7.10)$$

and for Equation (2.7.6), the finite difference equation for calculating  $E_x$  is

$$\begin{aligned} & \varepsilon \frac{E_x^n(i+0.5, j, k) - E_x^{n-1}(i+0.5, j, k)}{\Delta t} \\ &= \frac{H_z^{n-0.5}(i+0.5, j+0.5, k) - H_z^{n-0.5}(i+0.5, j-0.5, k)}{\Delta y} \\ & \quad - \frac{H_y^{n-0.5}(i+0.5, j, k+0.5) - H_y^{n-0.5}(i+0.5, j, k-0.5)}{\Delta z} + J_x^{n-0.5}(i+0.5, j, k) \end{aligned} \quad (2.7.11)$$

The finite difference equations for Equations (2.7.4), (2.7.5), (2.7.7) and (2.7.8) can be obtained similarly. According to these equations,  $E$  or  $H$  at a new time step is calculated based on  $E$  and  $H$  at the previous time steps. The simulation process is illustrated in a flowchart in **Figure 2.7.2**.

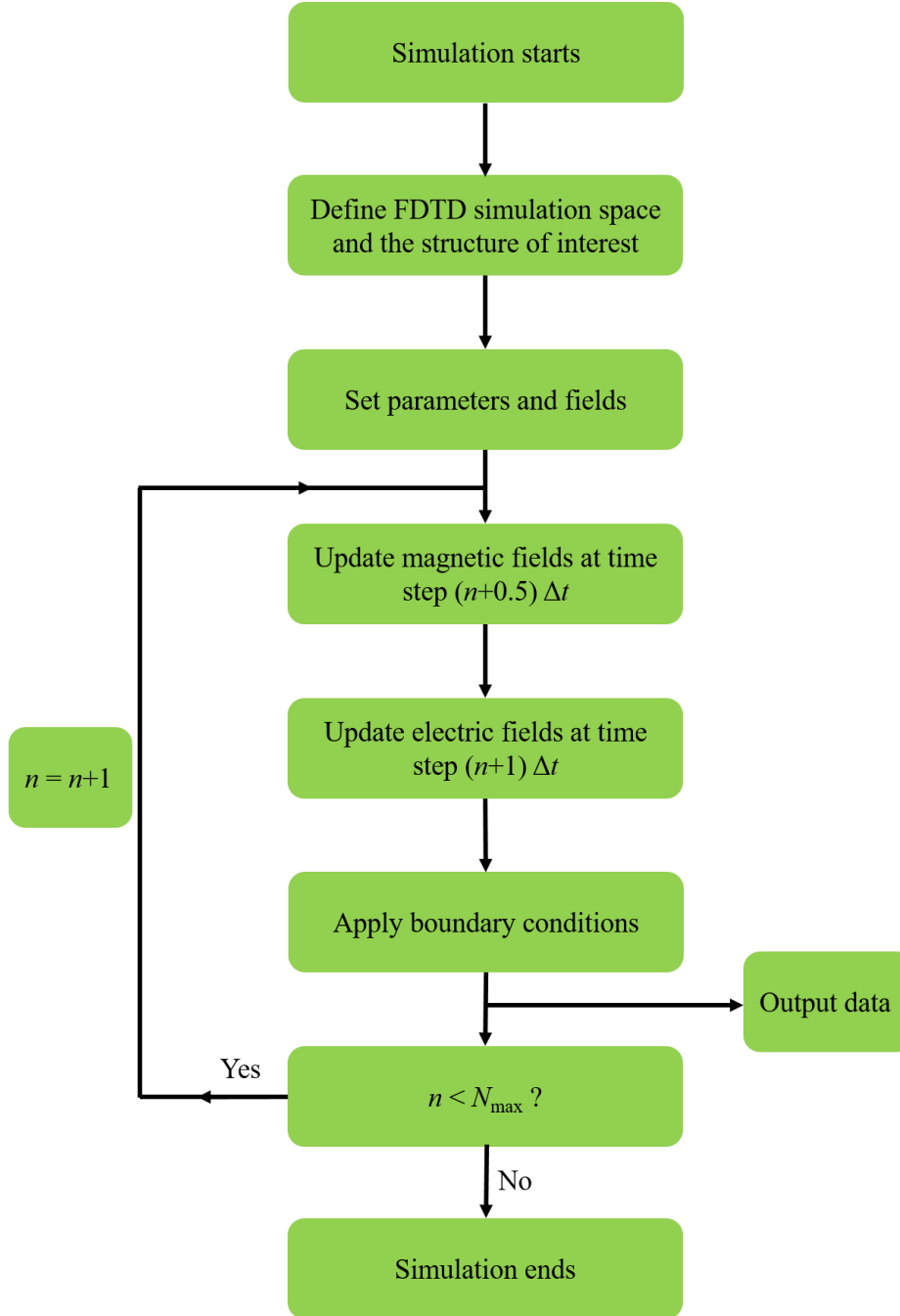


**Figure 2.7.2.** The flowchart for FDTD algorithm

In this dissertation, the FDTD simulations are performed using a commercial software XFDTD 7.3. In these simulations,  $\Delta x = \Delta y = \Delta z = 4$  nm and  $\Delta t$  is automatically determined by the

software, which satisfies Equation (2.7.9). A modified Debye-Drude model

$$\varepsilon(\omega) = \varepsilon_\infty + \frac{\varepsilon_s - \varepsilon_\infty}{1 + i\omega\tau} + \frac{\sigma}{i\omega\varepsilon_0}$$

$\omega$  is the angular frequency,  $\varepsilon_0$  is the vacuum permittivity,  $\varepsilon_\infty$  is the infinite-frequency relative permittivity,  $\varepsilon_s$  is the static relative permittivity,  $\tau$  is the relaxation time, and  $\sigma$  is the conductivity.

These parameters for different metals are listed in **Table 2.7.1**. SiO<sub>2</sub> and polystyrene are assumed to be non-dispersive dielectric materials with a constant  $\varepsilon = 2.3716$  and  $2.5122$ , respectively, for all wavelengths considered. The simulated structures are always a 2D array of nanostructures, and we usually create the nanostructure array in  $x$ - $y$  plane with light propagating from  $z+$  to  $z-$  direction, as shown in **Figure 2.7.3**. The blue rectangular box outline the simulation space. The structure within the simulation space is a unit cell of the periodic nanostructure array. Periodic boundary condition is applied in both  $x$  and  $y$  directions, and perfectly matched layer absorbing condition is applied in  $z$  direction. Since FDTD method is a simulation in time domain, the post data analysis includes a fast Fourier transformation to obtain the spectra in frequency domain.

**Table 2.7.1.** The fitting parameters for modified Debye-Drude model of metals.

Materials	$\varepsilon_s$	$\varepsilon_\infty$	$\sigma$ (S/m)	$\tau$ (s)
Ag	-9530.5	3.8344	$1.1486 \times 10^7$	$7.35 \times 10^{-15}$
Au	-15789	11.575	$1.6062 \times 10^7$	$8.71 \times 10^{-15}$
Ti	-11.99	7.5900	$6.21 \times 10^5$	$2.79 \times 10^{-16}$
Ni	-22.52	2.2986	$6.74 \times 10^5$	$3.26 \times 10^{-16}$
Cu	-6672.7	12.076	$1.0513 \times 10^7$	$5.63 \times 10^{-15}$

Ref.[129]: Ag, Au, and Cu. Ref.[130]: Ti and Ni.

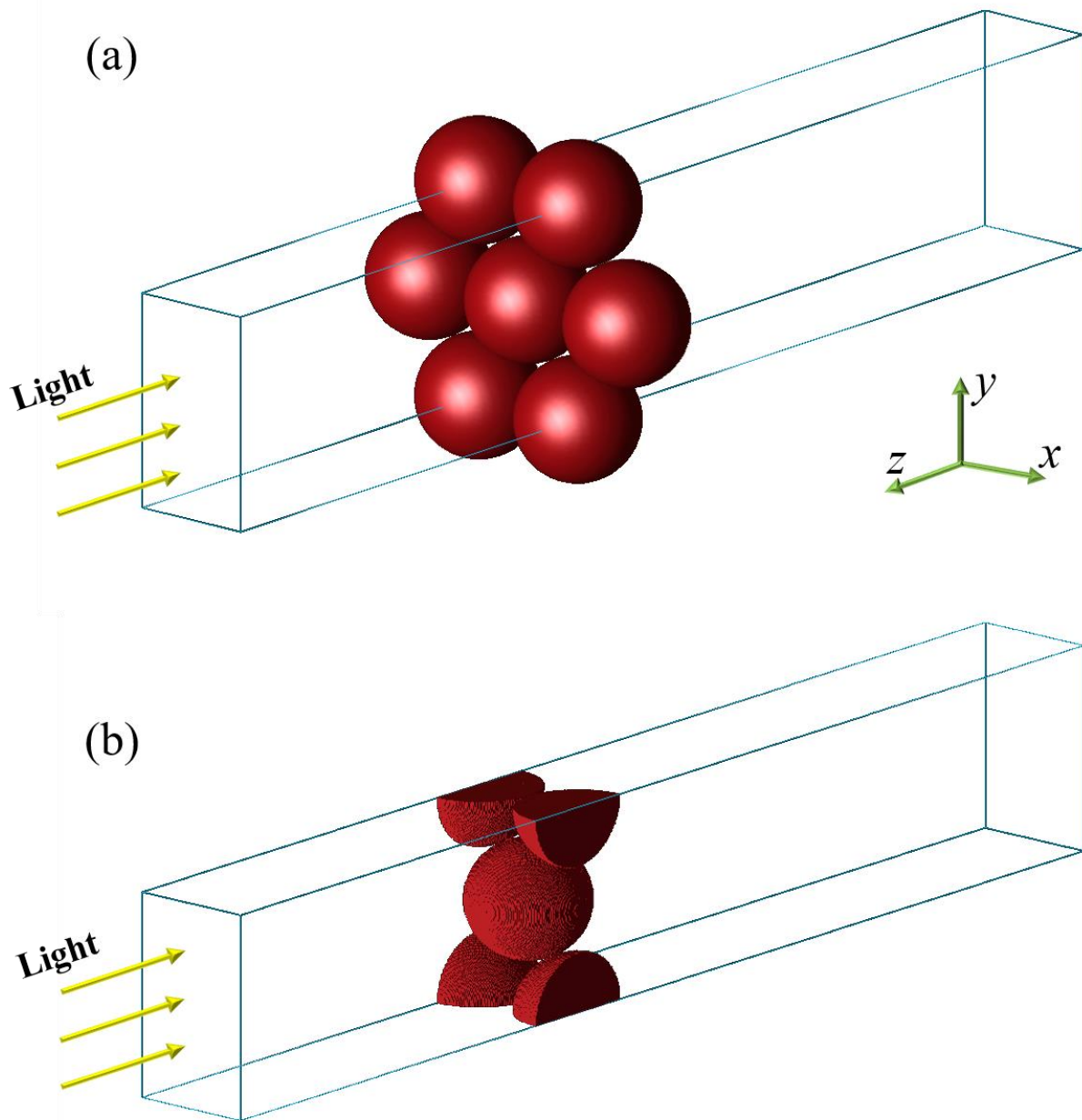


**Figure 2.7.3.** (a) The geometric model created in XFDTD for an array of nanospheres (b) One unit cell of the nanosphere array as meshed in an FDTD grid.

## CHAPTER 3

### CHIRAL PATCHY PARTICLES

#### 3.1 Introduction

By combining DSG with SACMs, well-ordered arrays of chiral plasmonic nanostructures can be created. The morphology simulations in Section 2.4 have demonstrated that shapes of deposited nanostructures on SACMs by an OAD strongly depend on the relative orientations of monolayers with respect to the incident vapor flux. Therefore, DSG on a polycrystalline monolayer consisting of many domains in different relative orientations will lead to “patches” of particles, which are morphologically identical within one patch, but different from the rest. These particles can be called quasi-3D “patchy particles”, with one layer of nanostructured thin film coated on the spherical surface. The patchy particles were first demonstrated to be chiral by Hou *et al.* in 2012.[120] However, these patchy particles exhibit very weak CD response (ellipticity  $\sim 0.04^\circ$ ). Here we proposed a new strategy to fabricate chiral patchy particles, which showed improved bulk CD response (ellipticity  $\sim 2^\circ$ ),[131] and an even larger CD response from the local domains (ellipticity  $\sim 20^\circ$ ).[132] This chapter will describe the fabrication, characterization, and optimization of the chiral patchy particles, especially those in particular domains with extremely strong CD.

#### 3.2 Racemic patchy particles

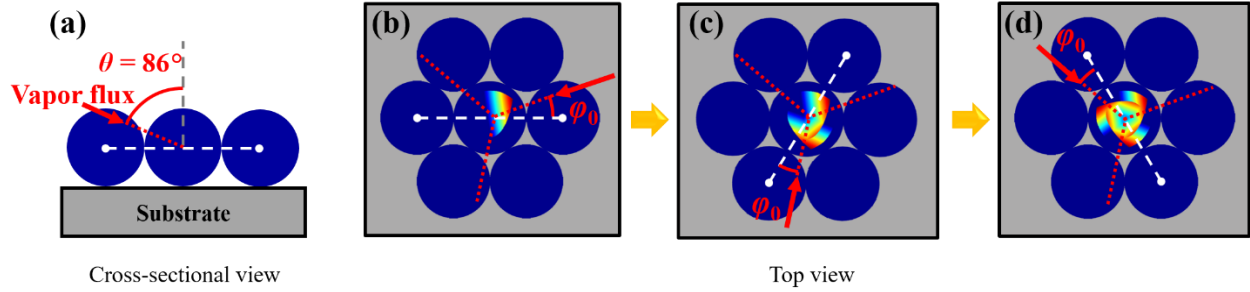


**Figure 3.2.1** Scheme of fabrication process of Ag chiral patchy particles. (a) Ag vapor flux is incident upon the monolayer at an oblique angle  $\theta = 86^\circ$  with respect to the substrate normal. (b)–(d) Ag vapor flux is incident upon the monolayer in three azimuthal directions with an interval of  $\Delta\varphi = 120^\circ$ . The azimuthal direction of Ag vapor flux and a dashed line going through the centers of the nanospheres form an angle,  $\varphi_0$ .

### 3.2.1 Fabrication of chiral patchy particles

The fabrication process is illustrated in **Figure 3.2.1**. First, a hexagonal close-packed monolayer of polystyrene beads with diameter  $d = 500$  nm was prepared as a deposition template on Indium-Tin-Oxide (ITO) coated glass substrates. The monolayers had polycrystalline domains with areas of  $0.0001$ – $1$   $\text{mm}^2$  and were loaded in a custom vacuum deposition system (Pascal Technology). The vacuum chamber was evacuated to a pressure of  $1 \times 10^{-6}$  Torr, and the background pressure was maintained at less than  $5 \times 10^{-6}$  Torr. The source material used in the deposition was Ag (99.999%, Kurt J. Lesker). During the deposition, Ag vapor was deposited onto the monolayer at a polar angle  $\theta = 86^\circ$  with respect to the substrate normal at a QCM deposition rate of  $0.05$  nm/s, as shown in **Figure 3.2.1a**. After one Ag deposition ending with a QCM thickness  $t = 30$  nm, the substrate was azimuthally rotated by  $\Delta\varphi = 120^\circ$  in clockwise (CW) or counter-clockwise (CCW) direction, and then another Ag layer of  $t = 30$  nm was deposited. This process was repeated until a total QCM film thickness  $t = 360$  nm and a total substrate rotation of  $12 \times 120^\circ$  were achieved, i.e. Ag depositions occurred in three azimuthal directions, and a total QCM thickness  $t = 4 \times 30$  nm was reached in each direction with an increment of  $30$  nm at each step. We denote the QCM thickness for such a fabrication process as  $t_{\text{QCM}} = 4 \times 30$  nm. We choose a fabrication strategy to

increase the deposited material in three directions by a small amount (30 nm) at each step and repeatedly in order to minimize the asymmetry caused by the shadowing effect of the deposited films. The azimuthal angle of incident vapor for each monolayer domain  $\varphi_0$  is defined as the relative angle of vapor flux direction with respect to a virtual straight line through the centers of nanospheres in one row, and is chosen properly to ensure  $0^\circ \leq \varphi_0 < 60^\circ$  due to the six-fold rotational symmetry of the hexagonal lattice of the monolayer, as shown in **Figures 3.2.1b–d**. The monolayer domains in the same orientation have the same  $\varphi_0$ , and the differently orientated domains have different  $\varphi_0$ . In other words,  $\varphi_0$  can be used to define the orientation of each domain.

### 3.2.2 Bulk circular dichroism of a racemic mixture of patchy particles

Following the fabrication process described in Section 3.2.1, morphology simulations were performed to obtain the predicted nanostructures in domains with different  $\varphi_0$ , as shown in **Figure 3.2.2**. The morphology simulations reveal that Ag nanostructures with the azimuthal angles of  $\varphi_0$

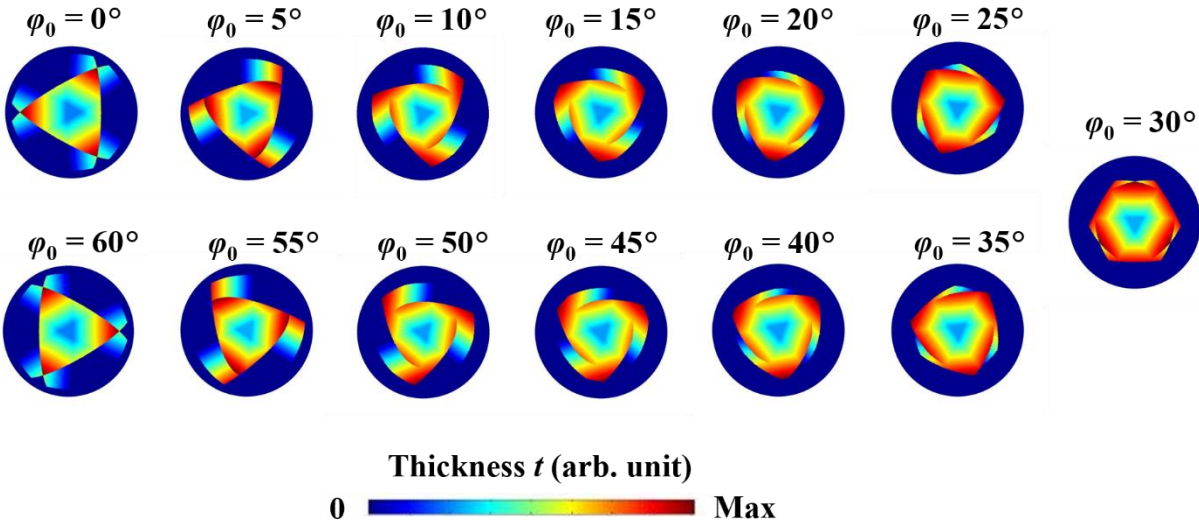


**Figure 3.2.2** Simulated morphologies of chiral patchy particles in differently orientated domains with  $\varphi_0 = 0^\circ, 5^\circ, 10^\circ, 15^\circ, 20^\circ, 25^\circ, 30^\circ, 35^\circ, 40^\circ, 45^\circ, 50^\circ, 55^\circ,$  and  $60^\circ$ .

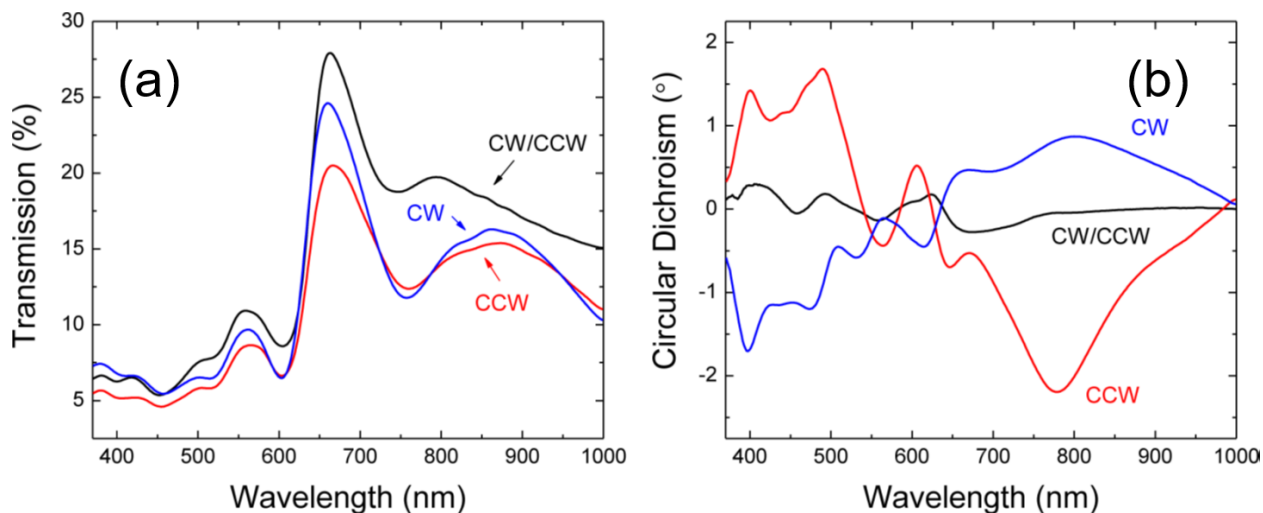


**Figure 3.2.3** (a) Transmission spectra, and (b) CD spectra of Ag patchy particles prepared by CW, CCW, and CW/CCW substrate rotations. Ref.[131]

and  $60^\circ - \varphi_0$ , are morphological enantiomers, if the shadowing effect of deposited films is not taken into account. Since a polycrystalline monolayer ( $\sim 1 \text{ cm}^2$ ) consists of large numbers of PS monolayer domains with random orientations, the DSG process should produce an equal portion of morphological enantiomers. Therefore, no chiral optical response is expected for such a racemic mixture of chiral patchy particles. However, the investigation of bulk CD by the spectroscopic ellipsometer (with a beam size of 4 mm) reveal a dependence of CD response on the azimuthal rotation direction of substrates in the deposition process. **Figure 3.2.3** shows the unpolarized transmission and CD spectra of the racemic patchy Ag films prepared by CW, CCW, and CW/CCW rotations of substrates during DSG, where CW/CCW means an alternating rotation direction. The Ag patchy particles prepared by CW and CCW substrate rotations exhibit opposite CD response, while those prepared by CW/CCW substrate rotation has almost no CD response. The bulk CD measurements demonstrate that the azimuthal rotation of substrates breaks the racemic symmetry of the patchy particles, which should be understood morphologically. The different azimuthal rotations of substrates lead to different deposition orders in three deposition

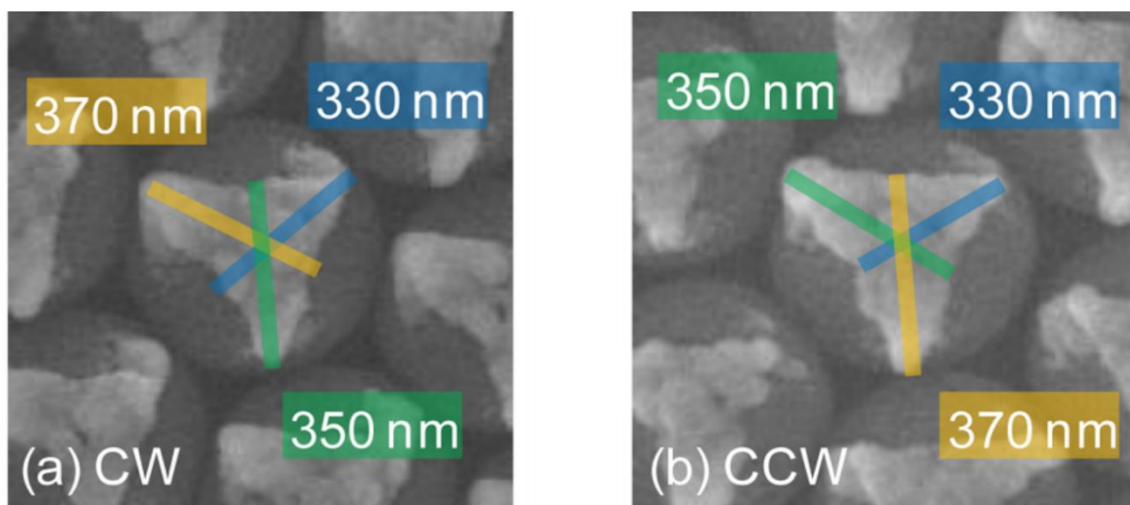


**Figure 3.2.4** SEM images of Ag patchy particles prepared by (a) CW and (b) CCW rotations of the substrate during DSG. Ref.[131]

directions ( $\varphi_0$ ,  $\varphi_0+120^\circ$ ,  $\varphi_0+240^\circ$ ), which causes different material accumulations due to the shadowing effect of the deposited thin films. **Figure 3.2.4** shows the top-view SEM images of two Ag nanostructures fabricated at similar  $\varphi_0$  by CW and CCW substrate rotations. Three characteristic lengths labeled by solid lines measure the structure dimensions in three deposition directions. The characteristic length increases in CW order in CW sample, and in CCW order in CCW sample, which clearly illustrates the asymmetry or chirality of the nanostructures. Such an asymmetry remains the same for nanostructures in different monolayer domains, as long as they are prepared by the same substrate rotation, which leads to an incomplete cancellation in CD responses from many domains, resulting in non-zero bulk CD. The detailed study regarding the bulk CD response of the racemic Ag patchy particles can be found in Ref.[131].

### 3.3 Effect of monolayer orientations

The morphology simulation results in **Figure 3.2.2** have demonstrated that the geometric chirality of patchy particles is directly determined by  $\varphi_0$ , and the nanostructures with  $\varphi_0$  and  $60^\circ-\varphi_0$  are

morphological enantiomers. With  $\varphi_0 = 0^\circ$ , the nanostructure has an achiral shape. As  $\varphi_0$  increases, a chiral fan-shaped structure with three rotating arms appears. The arms of fan-shaped structures gradually become shorter and wider with increasing  $\varphi_0$ . The structure finally becomes achiral as  $\varphi_0$  approaches  $30^\circ$ . This section will describe a systematic investigation of the chiral optical properties of the patchy particles with different  $\varphi_0$  by both experiments and simulations. Note, the Ag patchy particles in this study were fabricated by CCW rotation of substrates during DSG. In order to measure the CD of the patchy particles in small domains (typically  $< 1 \text{ mm}^2$ ), the custom spectroscopic microscope was used for taking both micrographs and transmittance spectra (see Section 2.6).

### ***3.3.1 Effect of monolayer orientations: morphology***

Ag nanostructures on six representative domains (Domains #1–6) are selected for both morphological and optical studies. **Figure 3.3.1a** shows the top-view SEM images of Ag nanostructures in Domains #1–6. Domains #1–6 have  $\varphi_0 = 58^\circ, 3^\circ, 52^\circ, 9^\circ, 23^\circ,$  and  $30^\circ$ , respectively (see Section 2.5 for determining  $\varphi_0$ ). As predicted by the morphology simulations, chiral fan-shaped structures are produced on Domains #1–4 with  $\varphi_0$  close to  $0^\circ$  or  $60^\circ$ , and achiral triangular and hexagonal structures are created on Domains #5 and #6 with  $\varphi_0$  close to  $30^\circ$ , respectively. Particularly, Domains #1, 2 and #3, 4 form two pairs of morphological enantiomers, since the sum of their  $\varphi_0$  is roughly equal to  $60^\circ$ . To characterize the dimensions of Ag nanostructures on different domains, a characteristic length  $l$  is defined as the distance from one vertex to the opposite edge or vertex of the triangular-shaped fans, triangles or hexagons, as illustrated by the solid red lines in **Figure 3.3.1a**.  $l$  is measured to be  $330 \pm 30, 330 \pm 30, 300 \pm 40, 310 \pm 30, 280 \pm 20,$  and  $380 \pm 20$  nm for Domains #1–6, respectively. For Domains #1–4,  $l$  is

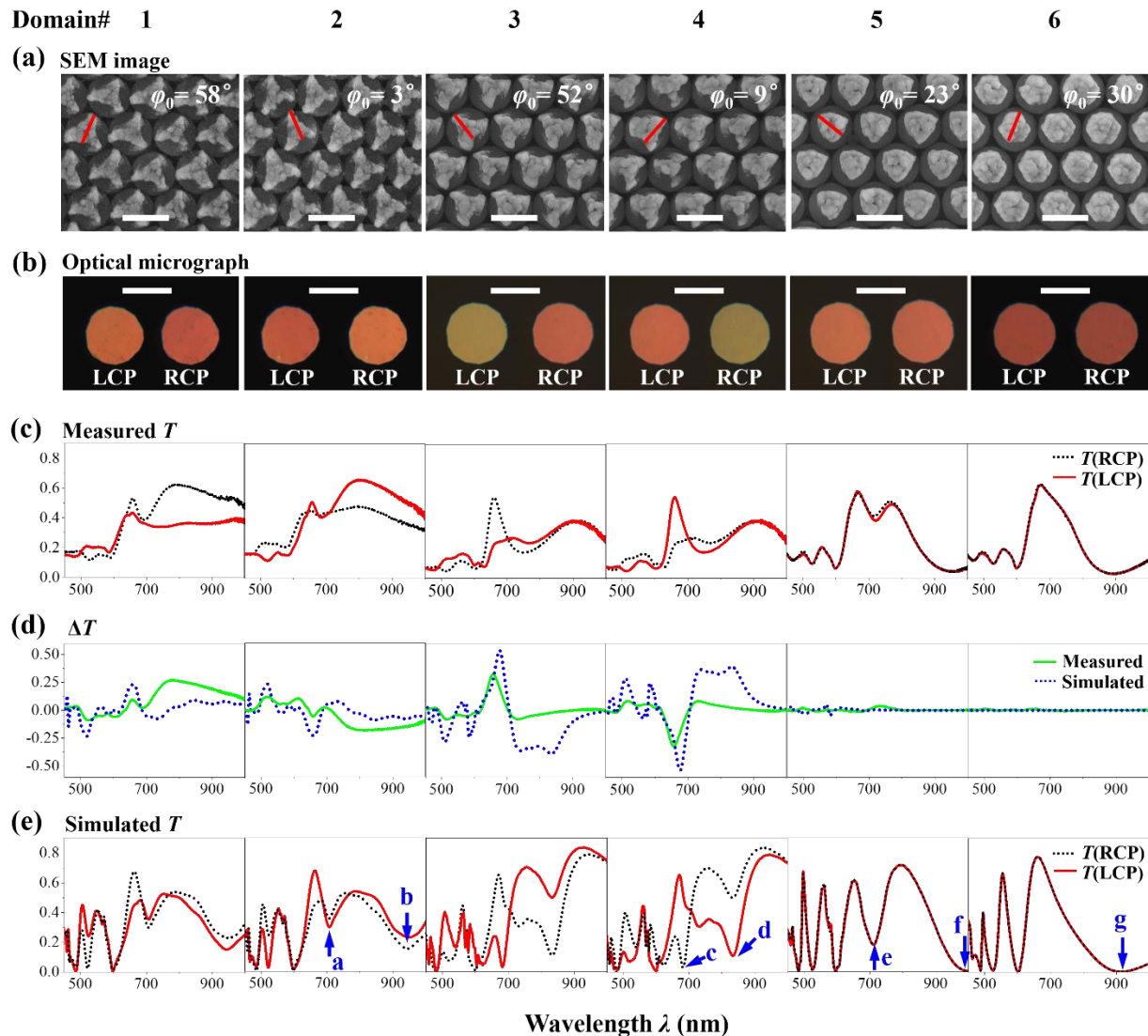


**Figure 3.3.1** (a) SEM images, (b) optical micrographs under LCP and RCP light illuminations, (c) measured circularly polarized transmittance, (d) both measured and simulated differential circularly polarized transmittance  $\Delta T$ , and (e) simulated circularly polarized transmittance, for Domains #1–6. The scale bars in (a) and (b) represent 500 nm and 100  $\mu\text{m}$ , respectively.

approximately equal to the arm length, and it is found that the arm length of Domains #1 and #2 is larger than that of Domains #3 and #4, which agrees with the morphology simulations.

### 3.3.2 Effect of monolayer orientations: optical property

The chiral optical response of individual domains can be visualized and measured by the custom spectroscopic microscope system. **Figure 3.3.1b** shows the optical micrographs of Domains #1–6, under LCP light illumination (left-sided figure) and RCP light illumination (right-sided figure). For each domain, the micrographs under LCP and RCP light illuminations were taken in the same region, and their color differences are resulted from the different transmittance spectra between LCP and RCP light. Domain #1 (Domain #2) appears orange under LCP (RCP) light and red under RCP (LCP) light. Domain #3 (Domain #4) appears green under LCP (RCP) light, and red under RCP (LCP) light. For the morphological enantiomers, Domains #1 and #2 or Domains #3 and #4, their colors are interchanged when switching the circular polarizations, indicating opposite chiral optical responses. Domain #5 shows orange color and Domain #6 shows red color under both LCP and RCP light. No distinct color change between the LCP and RCP micrographs of Domains #5 and #6 indicates weak or no chiral optical response, which originates from their achiral structures.

Differential circularly polarized transmittance,  $\Delta T = T(\text{RCP}) - T(\text{LCP})$ , is used to characterize the CD response of the Ag patchy particles. **Figure 3.3.1c** shows the measured  $T(\text{RCP})$  and  $T(\text{LCP})$  for Domains #1–6. The measured  $\Delta T$  spectra after averaging the front and back illumination measurements are shown with green solid lines in Figure 2d. All the domains have low transmittance ( $\sim 0.05$ – $0.2$ ) in short wavelength range  $\lambda = 450$ – $600$  nm. This is mainly caused by the high-order LSPR of Ag nanostructures and the increased scattered light not being collected in zero-order transmittance measurement.[133] It should be noted that a transmittance dip around  $\lambda = 600$  nm in both  $T(\text{RCP})$  and  $T(\text{LCP})$  spectra for all the domains, corresponds to the photonic band gap of the two-dimensional periodic monolayers, which is determined by the refractive index contrast and the lattice constant of the monolayers.[134] For Domain #1,  $T(\text{RCP})$  is lower than  $T(\text{LCP})$  in wavelength range  $\lambda = 500$ – $600$  nm, leading to negative  $\Delta T$ .  $T(\text{RCP})$

becomes greater than  $T(\text{LCP})$  in long wavelength range  $\lambda = 600\text{--}1000$  nm, leading to positive  $\Delta T$ , which makes the sample surface appear more red under RCP light than LCP light in the microscope. Both  $T(\text{RCP})$  and  $T(\text{LCP})$  have small peaks around  $\lambda = 650$  nm, which results in a small positive peak in  $\Delta T$  spectrum.  $T(\text{RCP})$  has two dips at  $\lambda = 525$  and  $690$  nm due to the LSPR of Ag films, and a broad peak at  $\lambda = 780$  nm, resulting in a positive broad peak in  $\Delta T$  spectrum. For Domain #2,  $T(\text{RCP})$  and  $T(\text{LCP})$  spectra are similar to  $T(\text{LCP})$  and  $T(\text{RCP})$  spectra of Domain #1, respectively, indicating that Domains #1 and #2 have opposite  $\Delta T$ . For Domain #3,  $T(\text{RCP})$  is lower than  $T(\text{LCP})$  in wavelength range  $\lambda = 500\text{--}600$  nm with negative  $\Delta T$ , which makes Domain #3 appear green under LCP light in the microscope. In wavelength range  $\lambda = 600\text{--}703$  nm,  $T(\text{RCP})$  becomes greater than  $T(\text{LCP})$  with positive  $\Delta T$ , which makes Domain #3 appear red under RCP light in the microscope.  $T(\text{RCP})$  shows two dips at  $\lambda = 520$  and  $750$  nm, and  $T(\text{LCP})$  also shows two dips at  $\lambda = 620$  and  $770$  nm, corresponding to the LSPR of Ag films. A sharp transmittance peak appears in  $T(\text{RCP})$  at  $\lambda = 660$  nm, resulting in a sharp  $\Delta T$  peak. As expected, Domain #4 has the similar transmittance spectra as Domain #3, but with  $T(\text{RCP})$  and  $T(\text{LCP})$  spectra interchanged. For Domains #5 and #6, their  $T(\text{RCP})$  and  $T(\text{LCP})$  spectra almost overlap with each other, indicating  $\Delta T$  to be almost 0. Domains #5 and #6 have the same transmittance dip at  $\lambda = 470$  and  $530$  nm, but show different LSPR wavelengths in long wavelength range, due to their different structures. Domain #5 has two resonances at  $\lambda = 720$  and  $950$  nm, while Domain #6 has a resonance at  $\lambda = 890$  nm. The transmittance dip at  $\lambda = 720$  nm makes Domain #5 transmit less red light than Domain #6, which explains their color difference in the microscope. The circularly polarized transmittance measurements confirm the opposite chiral optical response of Domains #1 and #2 (#3 and #4), and weak or no chiral optical response of Domains #5 and #6, which is consistent with their morphological chirality and the observation under the microscope. In addition, two pairs

of enantiomers, Domains #1–2 and #3–4, exhibit different spectral features, which originates from the differences in the shape and size of their structures. Note, since the morphology of Ag patchy films strongly depends on  $\varphi_0$ , other domains with different  $\varphi_0$ , can have different structures and thus show different CD spectra from those of Domains #1–6, which are not shown here. Furthermore, the local CD response of individual domains can be extremely large. The magnitude of  $\Delta T$  can reach 0.27 for Domains #1 and #2, and even 0.32 for Domains #3 and #4. The CD response of certain local domains are one order of magnitude larger than the statistically averaged CD response of the racemic mixture of different domains, which has  $\Delta T = 0.02$  and  $\eta = 2^\circ$  at maximum.

### ***3.3.3 Effect of monolayer orientations: FDTD simulation***

The chiral optical properties were also simulated by FDTD method (see Section 2.7 for the details of FDTD simulations). The simulated  $T(\text{RCP})$  and  $T(\text{LCP})$  spectra for Domains #1–6 are shown in **Figure 3.3.1e**, and the calculated  $\Delta T$  spectra are shown with dotted blue lines in **Figure 3.3.1d**. The geometric models of Ag films in FDTD simulations were created based on the top-view SEM images and are shown in **Figure 3.3.2**. In the simulations, it is assumed that all the Ag films are uniformly coated on nanospheres with a thickness of 100 nm and a smooth surface. The SEM images in **Figure 3.3.1a** show that the three arms of chiral fan-shaped Ag films have different lengths, which results from the substrate rotation during depositions. But in the FDTD simulations, the lengths of three arms of a fan-shaped Ag nanostructure are assumed to be the same. These simple models are meant to capture the essential features of the CD response of each structure, and we have ignored the spatial distribution of Ag thickness and the morphological variation shown in **Figure 3.3.1a**. As shown in **Figures 3.3.1d** and **3.3.1e**, regardless of multiple assumptions are

made on the simulated structures, the FDTD simulations still successfully reproduce the main features of experimental results. For Domains #1–6, all the resonances in the measured transmittance and differential transmittance spectra are well reproduced in the simulated spectra at almost the same wavelength positions. But there are still some small differences between the measured and simulated spectra, such as an extra resonance at  $\lambda = 943$  nm in the simulated transmittance spectra of Domains #1 and #2, and an extraordinary high transmittance in near-infrared region in the simulated spectra of Domains #3 and #4. These deviations could result from small difference in size, shape, or thickness between simulated and actual structures. The near-field FDTD simulations were also performed to reveal the nature of the plasmonic resonances under circularly polarized incident light. **Figure 3.3.3** shows the simulated near-field current directions on Ag films from Domains #2, #4, #5 and #6, at the plasmonic resonance wavelengths,

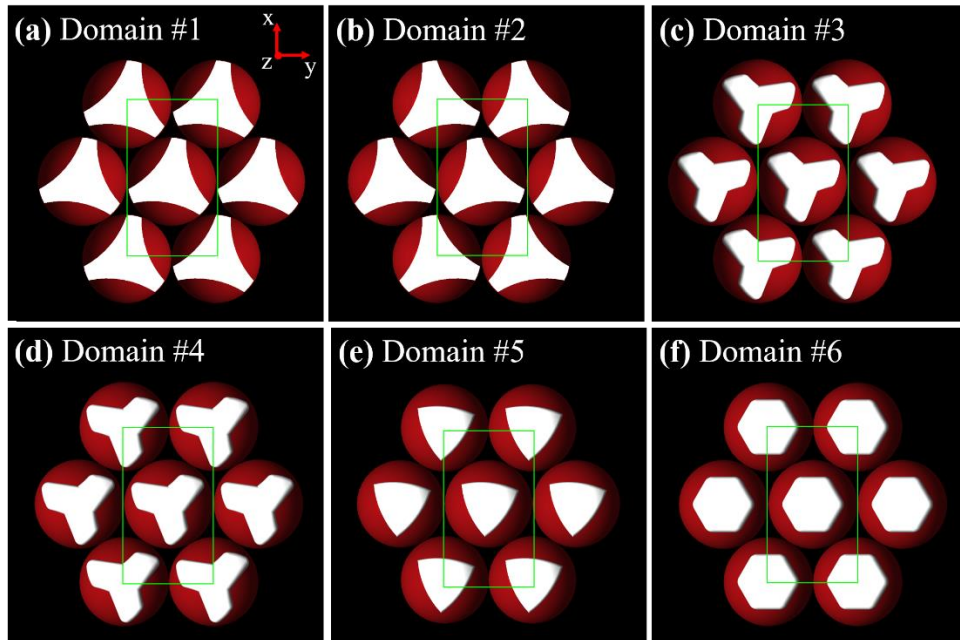


**Figure 3.3.2.** Geometric models of Ag nanostructures in Domains #1–6 that are used in FDTD simulations. The green rectangles indicate the simulation space, which is a unit cell of the nanosphere array. The nanosphere diameter is 500 nm.

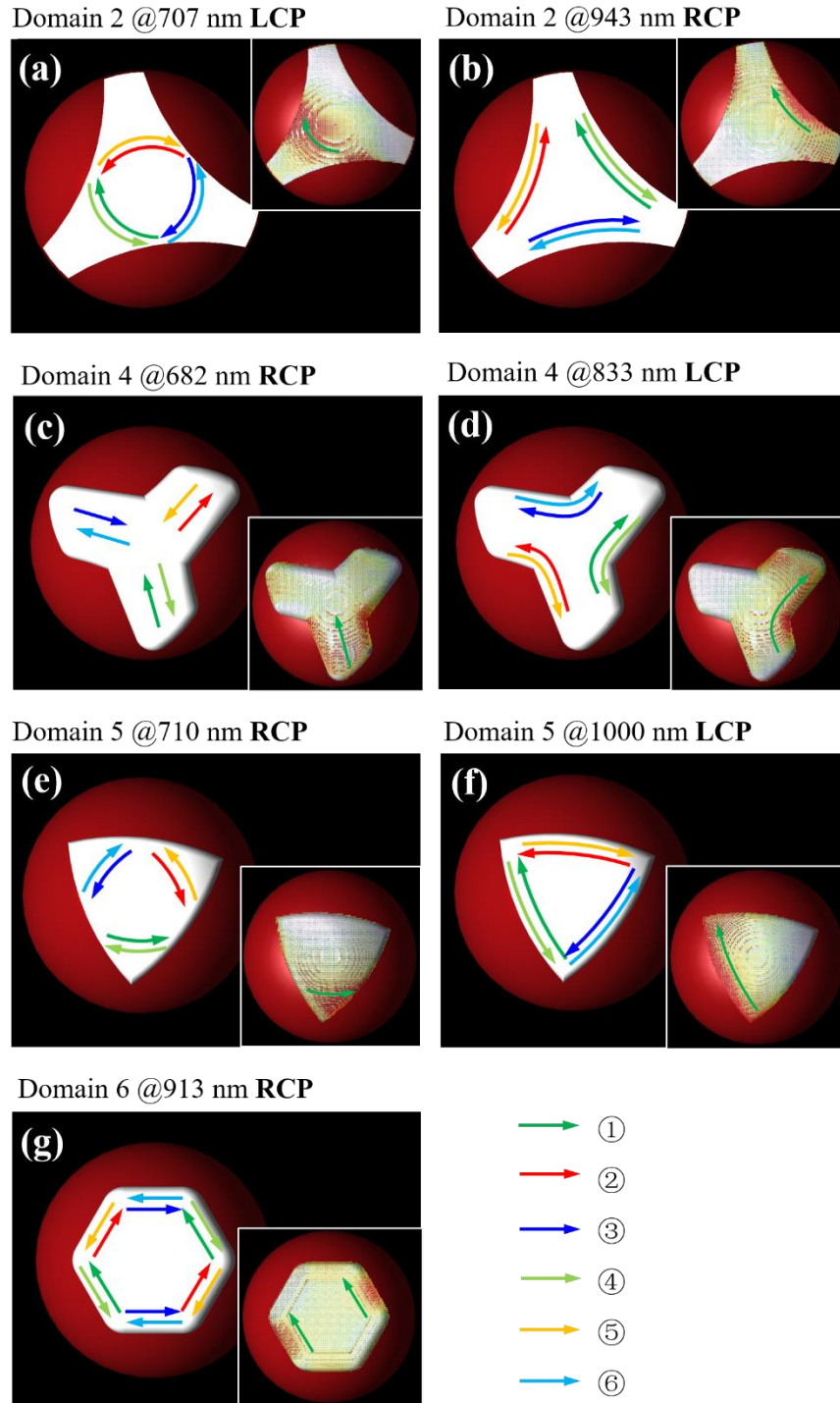


**Figure 3.3.3** Simulated near-field current directions of (a) Domain #2 with LCP incident light at  $\lambda = 707$  nm, (b) Domain #2 with RCP incident light at  $\lambda = 943$  nm, (c) Domain #4 with RCP incident light at  $\lambda = 682$  nm, (d) Domain #4 with LCP light at  $\lambda = 833$  nm, (e) Domain #5 with RCP incident light at  $\lambda = 710$  nm, (f) Domain #5 with LCP light at  $\lambda = 1000$  nm, and (g) Domain #6 with RCP incident light at  $\lambda = 913$  nm. The insets are simulated current distributions when the currents are in direction of green arrows.

which are labeled in blue arrows in **Figure 3.3.1e**. For simplicity, the near-field simulations of Domains #1 and #3 are not shown here, because their current distributions will be the mirror images of those of Domains #2 and #4, respectively. The arrows in different colors represent different plasmon oscillations, which have different phases and appear in the sequence as shown in **Figure 3.3.3**. The current distributions also exhibit three-fold symmetry as the nanostructures. The insets in **Figure 3.3.3** show the current distributions on the Ag film surfaces when the currents are in the directions of the green arrows.

### ***3.3.4 Effect of monolayer orientations: from local CD to bulk CD***

The chiral optical measurements and simulations of individual domains reveal that the Ag patches with different  $\varphi_0$  can exhibit different or even opposite CD responses. The polycrystalline nature of the monolayers allows the coexistence of Ag patches with even opposite CD responses. These Ag patches on the same substrate can be individually examined by the spectroscopic microscope, which provides an excellent platform for the enantiomer sensing, benefiting from both their sharp CD peaks and coexistence of patches with opposite CD responses.[57] When a mixture of these Ag patches is examined in a single CD measurement, their CD responses are supposed to be cancelled out. In order to study how the Ag patches with opposite CD response contribute to the averaged CD signal,  $\Delta T$  spectra of a mixture of two domains with opposite CD response were measured at their boundary by the spectroscopic microscope. The two domains are labeled as Domain #7 and #8, as shown in the micrographs in **Figure 3.3.4a**. Domain #7 (#8) appears red (green) under LCP illumination and green (red) under RCP illumination.  $\Delta T$  spectra were measured with different area percentage of Domain #7,  $X$ , and area percentage of Domain #8,  $1-X$ , which are shown by the dotted lines in **Figure 3.3.4b**. The spectra  $\Delta T_{0\%}$  and  $\Delta T_{100\%}$  are for

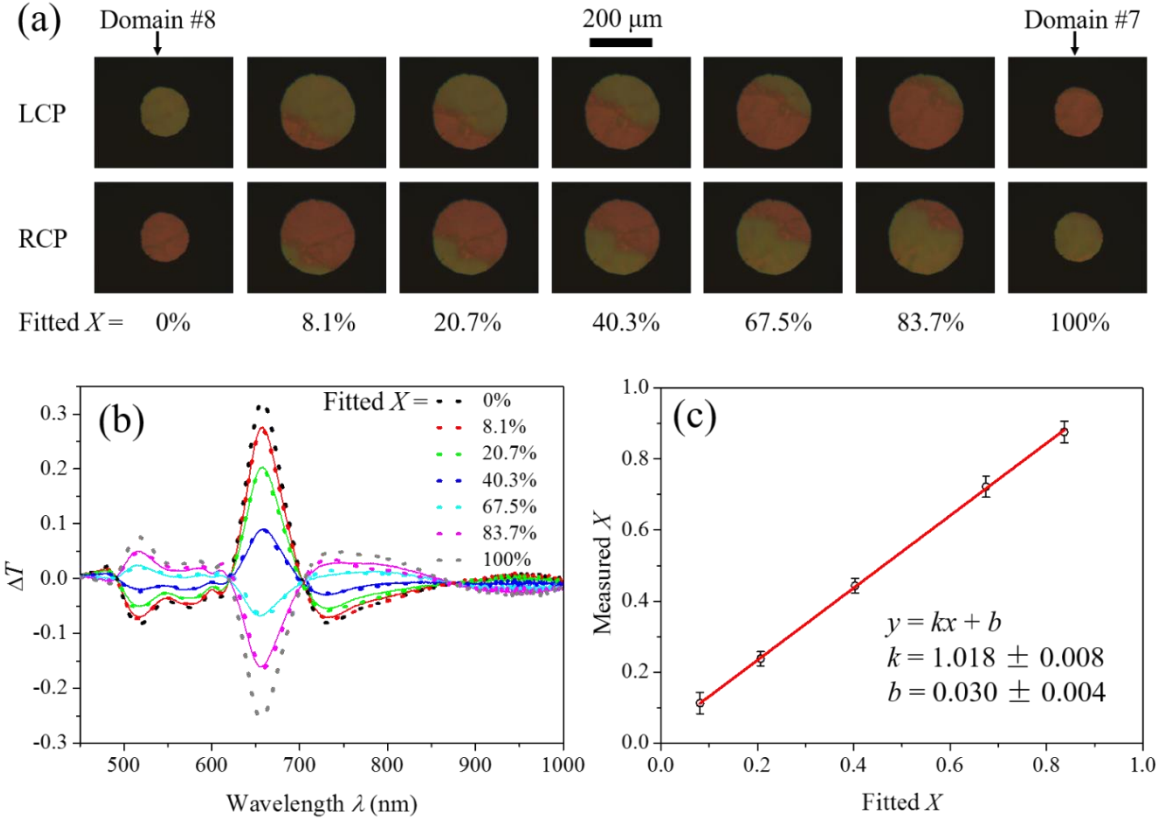


**Figure 3.3.4.** (a) Optical micrographs at a boundary of Domains #7 and #8 under LCP and RCP illuminations. (b) Measured (dotted lines) and fitted (solid lines)  $\Delta T$  spectra of a mixture of Domains #7 and #8 with different area percentage  $X$  of Domain #7. (c) The relationship between measured  $X$  and fitted  $X$ .

sampling area with only Domains #8 and #7, showing similar spectra features as those of Domains #3 and #4, respectively. The differential transmittance spectra  $\Delta T(X)$  of the mixed domains are assumed to be a linear superposition of  $\Delta T_{0\%}$  and  $\Delta T_{100\%}$ , i.e.  $\Delta T(X) = (1-X)\Delta T_{0\%} + X\Delta T_{100\%}$ , which is used to fit the experimental spectra by least square method to obtain the fitted  $X$ . The fitted spectra are shown by the solid lines in **Figure 3.3.4b**.  $X$  can also be measured directly in the micrographs, and is plotted against the fitted  $X$ , as shown in **Figure 3.3.4c**. The relationship between measured  $X$  and fitted  $X$  is fitted by a linear function  $y = kx + b$  with the slope  $k = 1.018 \pm 0.008$  and the intercept  $b = 0.030 \pm 0.004$ , which indicates that the measured and fitted  $X$  are

almost equal. This validates the linear superposition assumption, and demonstrates that the contribution of a domain to the averaged CD signal is proportional to its area.

### **3.4 Optimization of chiral optical response of Ag fan-shaped nanostructures**

In Section 3.3, a systematic study is performed on how the monolayer orientation  $\varphi_0$  affects the chiral optical response of the Ag patchy particles, with incident angle  $\theta = 86^\circ$ , and thickness  $t_{\text{QCM}} = 4 \times 30$  nm. It is found that Ag fan-shaped nanostructures created with  $\varphi_0$  around  $10^\circ$  or  $50^\circ$  exhibit large circular dichroism response. Besides the monolayer orientations, other deposition conditions and post-deposition treatments can affect the chiral optical effects. Here, we systematically investigate how the chiral optical response of the fan-shaped chiral nanostructures with  $\varphi_0 \approx 53^\circ$  depends on other fabrication parameters, such as incident angle of vapor flux  $\theta$ , thickness  $t_{\text{QCM}}$ , and annealing. This study can help to further understand and optimize the chiral optical response of fan-shaped chiral nanostructures.

#### ***3.4.1 Optimization of chiral optical response of Ag fan-shaped nanostructures: tuning $\theta$***

The chiral patchy particles are prepared with  $d = 500$  nm PS nanospheres at four different incident angles  $\theta = 82^\circ, 84^\circ, 86^\circ$  and  $88^\circ$ , with the thickness  $t_{\text{QCM}} = 4 \times 30$  nm. The fan-shaped nanostructures with  $\varphi_0 \approx 53^\circ$  are selected for morphological and optical characterizations. The impact of  $\theta$  on the morphology of Ag fan-shaped nanostructures can be visualized by the morphology simulations, as shown in **Figure 3.4.1a**. According to the simulation results, increasing  $\theta$  reduces the size of the fan-shaped nanostructures, which is caused by a larger shadowing area of nanospheres. Increasing  $\theta$  also decreases the thickness of the fan-shaped nanostructures, which is due to a smaller normal area facing vapor flux.[125] The morphology

(a) Simulated structures at  $\varphi_0 = 53^\circ$

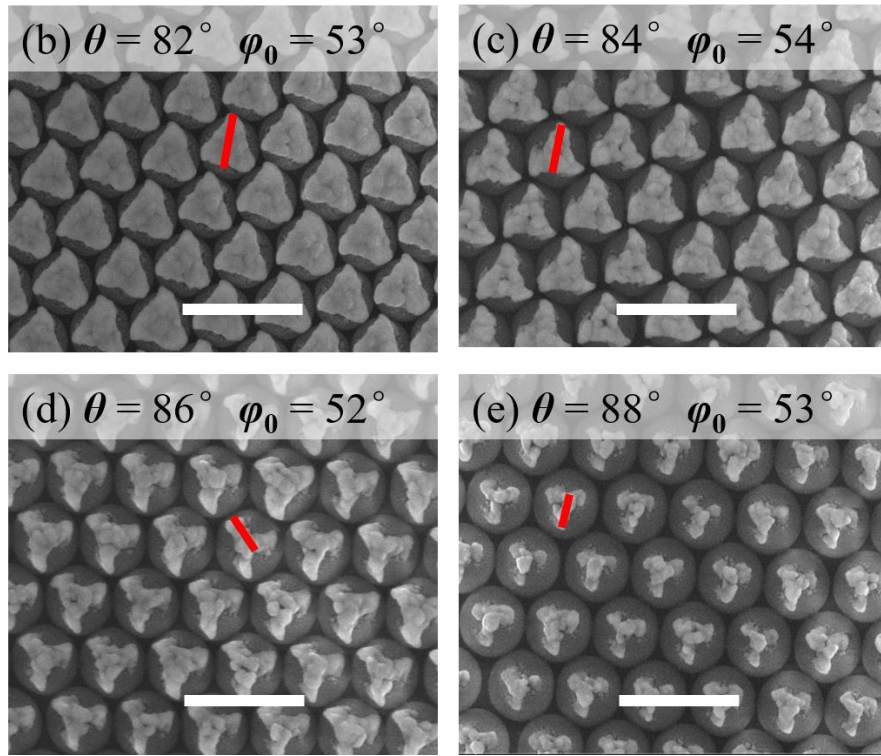
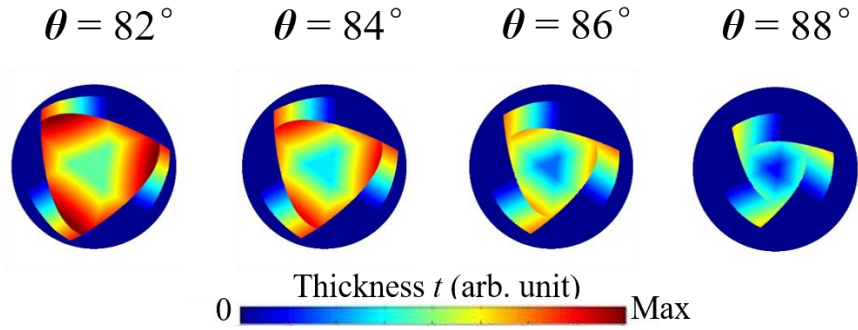


**Figure 3.4.1.** (a) Simulated chiral fan-shaped nanostructures fabricated with  $\varphi_0 = 53^\circ$ , and  $\theta = 82^\circ$ ,  $84^\circ$ ,  $86^\circ$  and  $88^\circ$ . Top-view SEM images of Ag fan-shaped nanostructures with (b)  $\theta = 82^\circ$ ,  $\varphi_0 = 53^\circ$ , (c)  $\theta = 84^\circ$ ,  $\varphi_0 = 54^\circ$ , (d)  $\theta = 86^\circ$ ,  $\varphi_0 = 52^\circ$ , and (e)  $\theta = 88^\circ$ ,  $\varphi_0 = 53^\circ$ . The scale bar in (b)-(e) represents  $1 \mu\text{m}$ .

change is confirmed by the top-view SEM images, as shown in **Figures 3.4.1b–e**. The characteristic length  $l$ , as labelled by a red line in SEM images, and the coverage area  $C$  of the Ag fan-shaped nanostructures, decrease with increasing  $\theta$  as listed in **Table 3.4.1**, which is consistent

**Table 3.4.1.** Structural and spectral parameters of Ag fan-shaped nanostructures with different  $\theta$ 

	$\theta = 82^\circ$	$\theta = 84^\circ$	$\theta = 86^\circ$	$\theta = 88^\circ$
$l$ (nm)	$380 \pm 20$	$330 \pm 20$	$310 \pm 30$	$220 \pm 20$
$C$ ( $\mu\text{m}^2$ )	$0.11 \pm 0.01$	$0.097 \pm 0.009$	$0.089 \pm 0.007$	$0.042 \pm 0.009$
$\lambda_{\text{RCP}}$ (nm)	808	731	749	684
$\lambda_{\text{LCP}}$ (nm)	743	636 684 742	630 685 767	682
$\lambda_{\text{T}}$ (nm)	683	659	660	644
$\lambda_{\text{g}}$ (nm)	688	658	657	659

with the simulated results.  $l$  and  $C$  has a very small difference between the structures with  $\theta = 84^\circ$  and  $86^\circ$ , indicating a slight structural change, while a significant difference in  $l$  and  $C$  between structures with  $\theta = 86^\circ$  and  $88^\circ$ , indicating a large structural change. In addition, both the simulation and SEM reveal that the fan-shaped structure changes its chiral shape with tuning  $\theta$ . Among these four structures, the one fabricated at  $\theta = 82^\circ$  almost has a triangular shape with poor geometric chirality. Furthermore, according to the SEM images, a larger  $\theta$  leads to higher surface roughness and a larger structural variation, which mainly ascribes to the shadowing effect at large  $\theta$ . Therefore, tuning  $\theta$  can change the size, shape, thickness, surface roughness, and structural variation of the fan-shaped nanostructures.

The circularly polarized transmittance spectra of the Ag fan-shaped nanostructures fabricated at different  $\theta$  are measured by the spectroscopic microscope, and are shown in **Figures 3.4.2a and 3.4.2b**. The structures with  $\theta = 82^\circ$ ,  $84^\circ$  and  $88^\circ$  share similar spectral features as the one with  $\theta = 86^\circ$  described in Section 3.3. Their differences in transmittance spectra are in transmittance magnitude and resonance locations. Among these structures, the one with  $\theta = 82^\circ$  has the lowest transmittance due to its largest Ag coverage and film thickness, while the one with

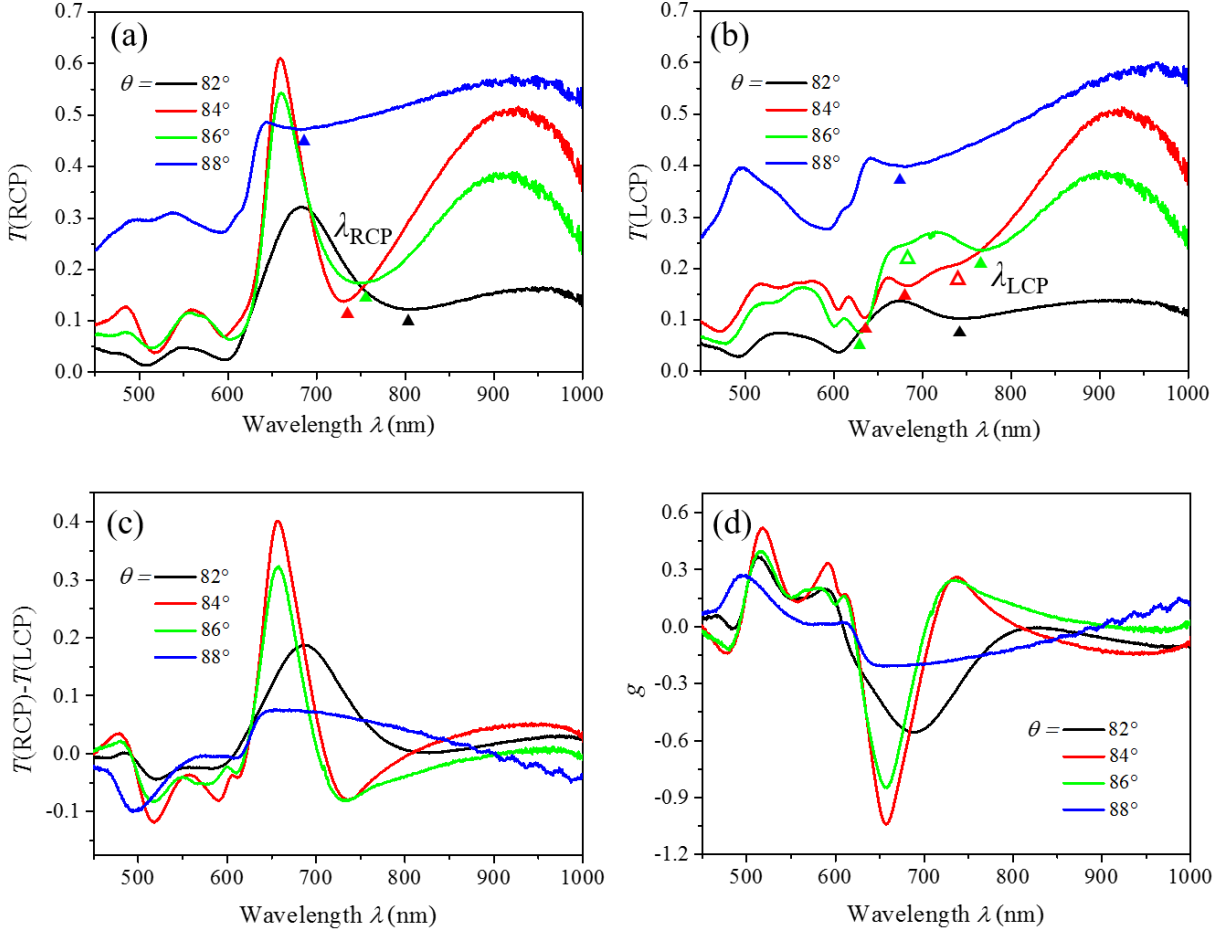


**Figure 3.4.2.** (a)  $T(\text{RCP})$ , (b)  $T(\text{LCP})$ , (c)  $\Delta T$ , and (d)  $g$ -factor spectra for Ag fan-shaped nanostructures fabricated at  $\theta = 82^\circ$ ,  $84^\circ$ ,  $86^\circ$  and  $88^\circ$ .

$\theta = 88^\circ$  has the highest transmittance resulted from its smallest Ag coverage and film thickness. The spectral features of the structures with  $\theta = 84^\circ$  and  $\theta = 86^\circ$  are very close, which originates from their slight structural difference. For  $T(\text{RCP})$ , these four fan-shaped structures exhibit three distinct transmittance valleys, located around  $\lambda = 510$  nm,  $\lambda = 600$  nm and in the range of  $\lambda = 690$ – $800$  nm, and also a sharp transmittance peak  $\lambda_T$  in the range of  $\lambda = 640$ – $690$  nm (see **Table 3.4.1** for  $\lambda_T$ ). The transmittance valley at  $\lambda = 600$  nm is the photonic bandgap of the 2D array of nanospheres, which appears in both  $T(\text{RCP})$  and  $T(\text{LCP})$  spectra. Since the fan-shaped structures have strong chiral optical response in the wavelength range  $\lambda = 600$ – $800$  nm, we will focus our

discussion in that wavelength range. The LSPRs at wavelengths  $\lambda_{\text{RCP}}$  in the range of 690–800 nm, labeled by triangles in **Figure 3.4.2a** and listed in **Table 3.4.1**, should correspond to the plasmon mode as shown in **Figure 3.3.3d**, and show significant wavelength shift with increasing  $\theta$ . Since larger  $\theta$  leads to smaller fan-shaped nanostructures,  $\lambda_{\text{RCP}}$  is expected to shift to shorter wavelength with increasing  $\theta$ . This is true except a comparison between  $\lambda_{\text{RCP}}(\theta = 84^\circ)$  and  $\lambda_{\text{RCP}}(\theta = 86^\circ)$ , according to the experimental results  $\lambda_{\text{RCP}}(\theta = 82^\circ) > \lambda_{\text{RCP}}(\theta = 86^\circ) > \lambda_{\text{RCP}}(\theta = 84^\circ) > \lambda_{\text{RCP}}(\theta = 88^\circ)$ . However,  $\lambda_{\text{RCP}}(\theta = 86^\circ)$  and  $\lambda_{\text{RCP}}(\theta = 84^\circ)$  are very close, which is resulted from their similar structural sizes. The relation  $\lambda_{\text{RCP}}(\theta = 86^\circ) > \lambda_{\text{RCP}}(\theta = 84^\circ)$  should be mainly due to their difference in thickness. This will be confirmed in the next section where fan-shaped nanostructures with  $\theta = 84^\circ$  redshift LSPR in  $T(\text{RCP})$  as the thickness decreases from  $t_{\text{QCM}} = 4 \times 30$  nm. Additionally, the most intense LSPR at  $\lambda_{\text{RCP}}$  is obtained at  $\theta = 84^\circ$ , with the sharpest transmittance peak at  $\lambda = 660$  nm. The LSPR becomes weaker with a broader transmittance peak at shorter wavelengths as  $\theta$  deviates from  $84^\circ$ . For  $T(\text{LCP})$ , the transmittance magnitude has the similar trend as that of  $T(\text{RCP})$ . The structures with  $\theta = 84^\circ$  and  $\theta = 86^\circ$  have similar  $T(\text{LCP})$  spectra with three resonances  $\lambda_{\text{LCP}}$  above the photonic band gap labeled by triangles in **Figure 3.4.2b**, some of which (open triangles) are weak and hard to identify the wavelength. In the contrast, the structures with  $\theta = 82^\circ$  and  $\theta = 88^\circ$  only exhibit one resonance at  $\lambda_{\text{LCP}}$  above  $\lambda = 600$  nm (see **Table 3.4.1** for  $\lambda_{\text{LCP}}$ ). The resonances at  $\lambda_{\text{LCP}} = 636$  nm for  $\theta = 84^\circ$  and  $\lambda_{\text{LCP}} = 630$  nm for  $\theta = 86^\circ$  should correspond to the plasmon mode shown in **Figure 3.3.3c**. The plasmon modes for other resonances need to be revealed by further FDTD simulations, which are hard to accomplish due to the difficulty in extracting the exact 3D models of fan-shape nanostructures fabricated at different  $\theta$ . The circularly polarized differential transmittance  $\Delta T$  spectra and the dissymmetry factor  $g = \Delta A/A$ , where  $\Delta A$  is the differential extinction between RCP and LCP light, and  $A$  is the unpolarized extinction, are

shown in **Figures 3.4.2c** and **3.4.2d**, respectively. Both  $\Delta T$  and  $g$  factor show a significant peak in the wavelength range of  $\lambda = 600\text{--}800$  nm (see Table 3.4.1 for the peak wavelength of  $g$  factor spectra  $\lambda_g$ ).  $\lambda_g$  and  $\lambda_T$  are very close, which indicates the dominant contribution from the transmittance peak in  $T(\text{RCP})$  to the CD signal. The comparison in both  $\Delta T$  and  $g$  factor spectra indicates that  $\theta = 84^\circ$  leads to the fan-shaped structure with the strongest CD response, which benefits from its intense LSPR and sharp transmittance peak. This optimal incident angle  $\theta = 84^\circ$  can be easily understood. When  $\theta$  is smaller, such as  $\theta = 82^\circ$ , the fabricated fan-shaped structure has larger structural size and thickness in a triangular-like shape with less chirality, which results in a lower transmittance and weak CD response. When  $\theta$  is larger, such as  $\theta = 88^\circ$ , the obtained fan-shaped structure has smaller structural size and thickness with higher surface roughness and structural variation. This leads to a higher transmittance but weaker plasmonic resonances, which accounts for the weak CD response.

### ***3.4.2 Optimization of chiral optical response of Ag fan-shaped nanostructures: tuning $t_{\text{QCM}}$***

According to Section 3.4.1, with  $t_{\text{QCM}}$  fixed at  $4 \times 30$  nm,  $\theta = 84^\circ$  leads to the strongest CD response of Ag fan-shaped nanostructures. Therefore, in order to investigate the effect of  $t_{\text{QCM}}$ , we fix  $\theta$  at  $84^\circ$ . Six patchy particle samples were prepared with  $t_{\text{QCM}} = 4 \times 10$  nm,  $4 \times 20$  nm,  $4 \times 25$  nm,  $4 \times 30$  nm,  $4 \times 35$  nm, and  $4 \times 40$  nm, respectively. Domains with  $\varphi_0 \approx 53^\circ$  were selected for morphological and optical characterizations. **Figure 3.4.3** shows the top-view SEM images of these samples. The Ag fan-shaped nanostructures with different  $t_{\text{QCM}}$  have almost the same structural size and shape according to the top-view SEM images. There are small variations in their structural shapes, which may be caused by the small variation of  $\varphi_0$  and the different shadowing effect of the deposited films with different thicknesses. In the following discussion, these small variations in shapes will

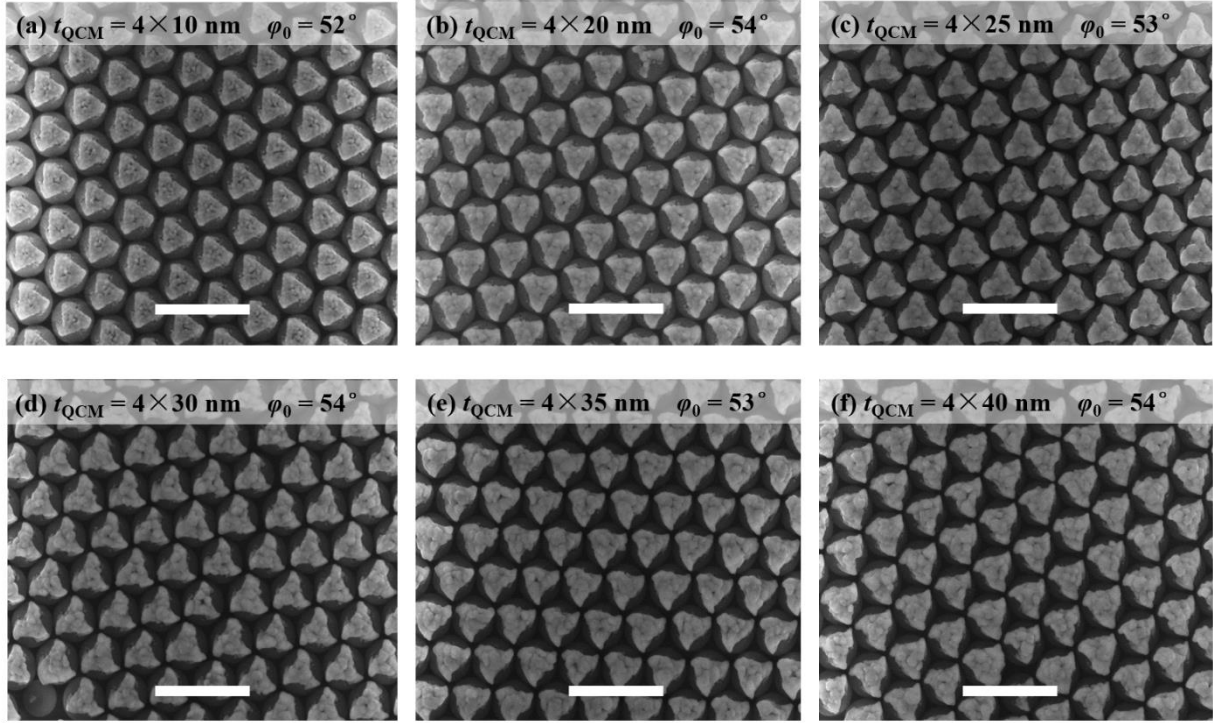


**Figure 3.4.3.** Top-view SEM images of Ag fan-shaped nanostructures with (a)  $t_{\text{QCM}} = 4 \times 10 \text{ nm}$ ,  $\varphi_0 = 52^\circ$ , (b)  $t_{\text{QCM}} = 4 \times 20 \text{ nm}$ ,  $\varphi_0 = 54^\circ$ , (c)  $t_{\text{QCM}} = 4 \times 25 \text{ nm}$ ,  $\varphi_0 = 53^\circ$ , (d)  $t_{\text{QCM}} = 4 \times 30 \text{ nm}$ ,  $\varphi_0 = 54^\circ$ , (e)  $t_{\text{QCM}} = 4 \times 35 \text{ nm}$ ,  $\varphi_0 = 53^\circ$ , and (f)  $t_{\text{QCM}} = 4 \times 40 \text{ nm}$ ,  $\varphi_0 = 54^\circ$ . The scale bar in each figure represents  $1 \mu\text{m}$ .

be ignored, and we assume that the only difference among these fan-shaped nanostructures is thickness.

The  $T(\text{RCP})$  and  $T(\text{LCP})$  spectra for Ag fan-shaped nanostructures fabricated with different  $t_{\text{QCM}}$  are measured by the spectroscopic microscope, and are shown in **Figures 3.4.4a** and **3.4.4b**, respectively. The  $\Delta T$  and  $g$  factor spectra are calculated and shown in **Figures 3.4.4c** and **3.4.4d**, respectively, to compare the CD response of different structures. Similar to Section 3.4.1, we will focus our discussion in the wavelength range above the photonic band gap of the nanosphere monolayer i.e.  $\lambda > 600 \text{ nm}$ . For  $T(\text{RCP})$ , all the structures have the same spectral features, with a LSPR in the range of  $\lambda = 730\text{--}790 \text{ nm}$  and a sharp transmittance peak around  $\lambda = 660 \text{ nm}$ . The resonance wavelength  $\lambda_{\text{RCP}}$  is plotted against  $t_{\text{QCM}}$ , as shown in **Figure 3.4.4e**. The  $\lambda_{\text{RCP}}$  has almost

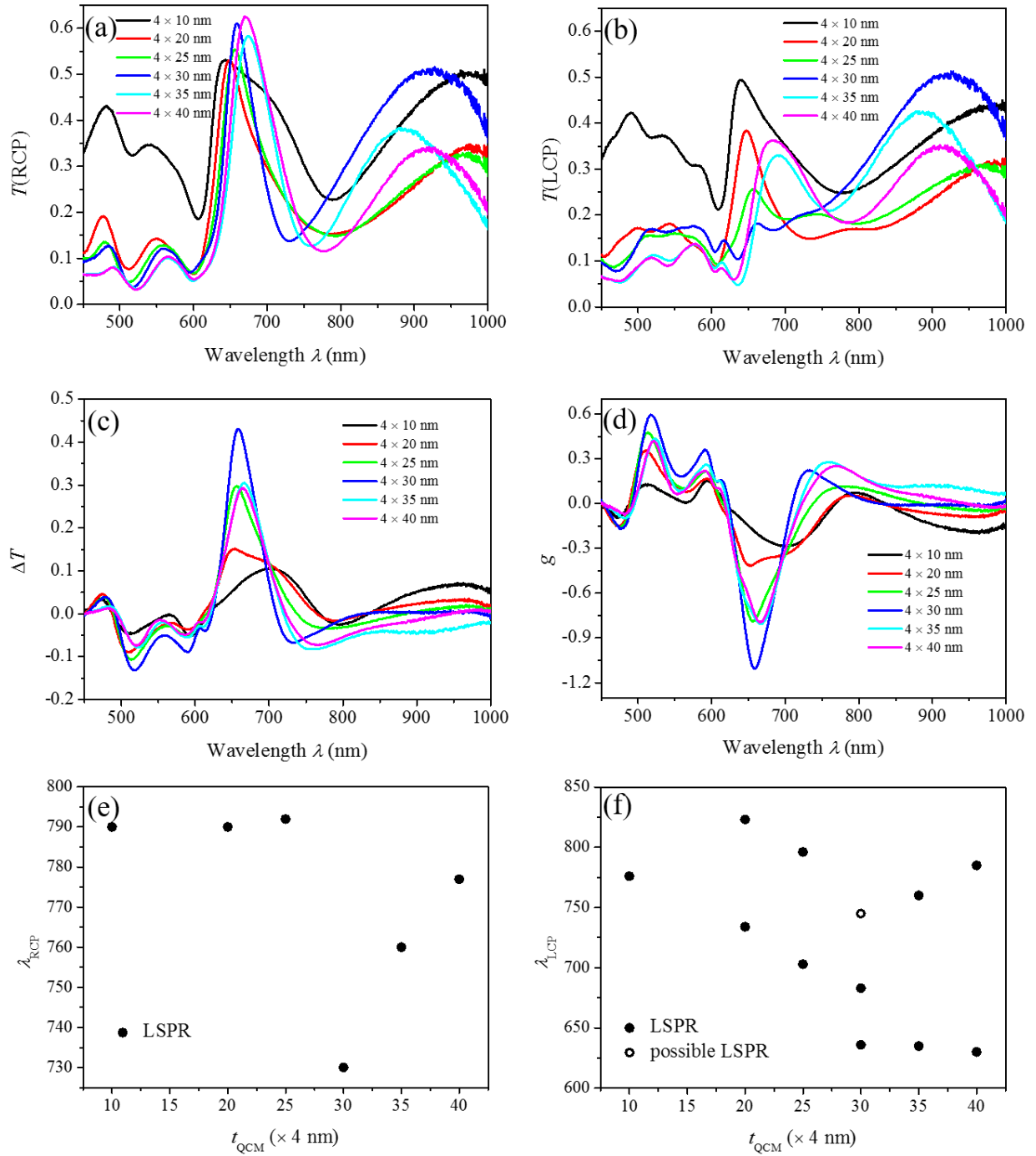


**Figure 3.4.4.** (a)  $T(\text{RCP})$ , (b)  $T(\text{LCP})$ , (c)  $\Delta T$ , and (d)  $g$ -factor spectra for Ag fan-shaped nanostructures fabricated with  $t_{\text{QCM}} = 4 \times 10 \text{ nm}$ ,  $4 \times 20 \text{ nm}$ ,  $4 \times 25 \text{ nm}$ ,  $4 \times 30 \text{ nm}$ ,  $4 \times 35 \text{ nm}$  and  $4 \times 40 \text{ nm}$ . LSPR wavelengths (e)  $\lambda_{\text{RCP}}$  and (f)  $\lambda_{\text{LCP}}$  as functions of  $t_{\text{QCM}}$ .

no change as  $t_{\text{QCM}}$  increases from  $4 \times 10$  nm to  $4 \times 25$  nm, shifts to a shorter wavelength by 60 nm as  $t_{\text{QCM}}$  reaches  $4 \times 30$  nm, and then shifts to longer wavelengths as  $t_{\text{QCM}}$  increases further. According to the near-field FDTD simulations in Section 3.3.3, these LSPRs should correspond to one LSPR mode with the current oscillation shown in **Figure 3.3.3d**. For  $T(\text{LCP})$ , Ag fan-shaped nanostructures with different thicknesses show a transmittance peak located in the range of  $\lambda = 650\text{--}700$  nm and multiple resonances. The resonance wavelength  $\lambda_{\text{LCP}}$  is plotted against  $t_{\text{QCM}}$ , as shown in **Figure 3.4.4f**. With  $t_{\text{QCM}} = 4 \times 10$  nm, only one LSPR appears at  $\lambda = 775$  nm. As  $t_{\text{QCM}} = 4 \times 20$  nm, two resonances appear at  $\lambda = 730$  nm and 830 nm, and shift to shorter wavelengths with increasing  $t_{\text{QCM}}$ . With  $t_{\text{QCM}} = 4 \times 30$  nm, one resonance becomes very weak and can be hardly identified, labeled as possible LSPR in **Figure 3.4.4f**, which then shifts to longer wavelengths with increasing  $t_{\text{QCM}}$ . The other resonance disappears as  $t_{\text{QCM}}$  becomes  $4 \times 35$  nm and even larger. A new resonance at  $\lambda = 630$  nm only exists with  $t_{\text{QCM}} = 4 \times 30$  nm,  $4 \times 35$  nm, and  $4 \times 40$  nm, and almost does not shift with thickness change. The multiple resonances observed in  $T(\text{LCP})$  are complicated and hard to analyze. However, according to **Figures 3.4.4.e** and **3.4.4f**, we can find a general trend for resonance shift. The LSPR wavelength first blueshifts with increasing  $t_{\text{QCM}}$ , reaches the minimum at  $t_{\text{QCM}} = 4 \times 30$  nm, and then redshifts. The only exception is the resonance in  $T(\text{LCP})$  at  $\lambda = 630$  nm. Under the assumption that the only difference among these fan-shaped structures is their thickness, we attribute the complicated change in LSPR to the thickness or thickness distribution change at different  $t_{\text{QCM}}$ . It should be noted that the charge or current oscillation modes obtained by near-field FDTD simulations shown in **Figure 3.3.3** are actually in 3D, which definitely involve electron oscillation in  $z$  direction. Therefore, the thickness or thickness distribution change of the nanostructures, which cannot be verified and quantified in top-view SEM images, may cause the LSPR wavelength shift and even the appearance of a new surface

plasmon mode. Due to the lack of 3D information of the fan-shaped nanostructures with different  $t_{\text{QCM}}$ , FDTD simulations are not performed to further study the effect of thickness. With the goal of optimizing the chiral optical response of Ag fan-shaped nanostructures, we focus on the comparison in  $\Delta T$  and  $g$  factor of these structures with different thicknesses. According to **Figures 3.4.4c** and **3.4.4d**, the fan-shaped structure fabricated with  $t_{\text{QCM}} = 4 \times 30$  nm shows the highest CD response, which coincides with the shortest LSPR wavelengths. The highest CD signal is generated by the sharp transmittance peak around  $\lambda = 660$  nm in  $T(\text{RCP})$ , which varies slightly for different thicknesses. With  $t_{\text{QCM}} = 4 \times 30$  nm, multiple LSPR at their shortest wavelengths fall in the wavelength range of this sharp  $T(\text{RCP})$  peak, which leads to the largest transmittance difference between RCP and LCP polarizations.

### ***3.4.3 Optimization of chiral optical response of Ag fan-shaped nanostructures: annealing***

Another factor that can affect the chiral optical effects of the fan-shaped nanostructures is the post-deposition annealing. The as-deposited Ag nanostructures may be porous with small Ag crystals and their property may be different from continuous large Ag crystals. Here we investigate how annealing can change the morphology and chiral optical response of Ag fan-shaped nanostructures. According to the discussion above, Ag fan-shaped nanostructures fabricated with  $\theta = 84^\circ$  and  $t_{\text{QCM}} = 4 \times 30$  nm exhibit the largest CD response, which is used in this study. The substrate is annealed in vacuum at a pressure of 60 mTorr and at a temperature of 200°C for 60 min. The annealing temperature is much higher than the glass transition temperature of polystyrene ( $\sim 100^\circ\text{C}$ ). Therefore, the polystyrene nanospheres become pliable and the nanosphere monolayer is transformed into a flat layer of polystyrene. The disappearance of nanospheres is confirmed by the SEM images taken before and after annealing, as shown in **Figures 3.4.5a** and **3.4.5b**, respectively.

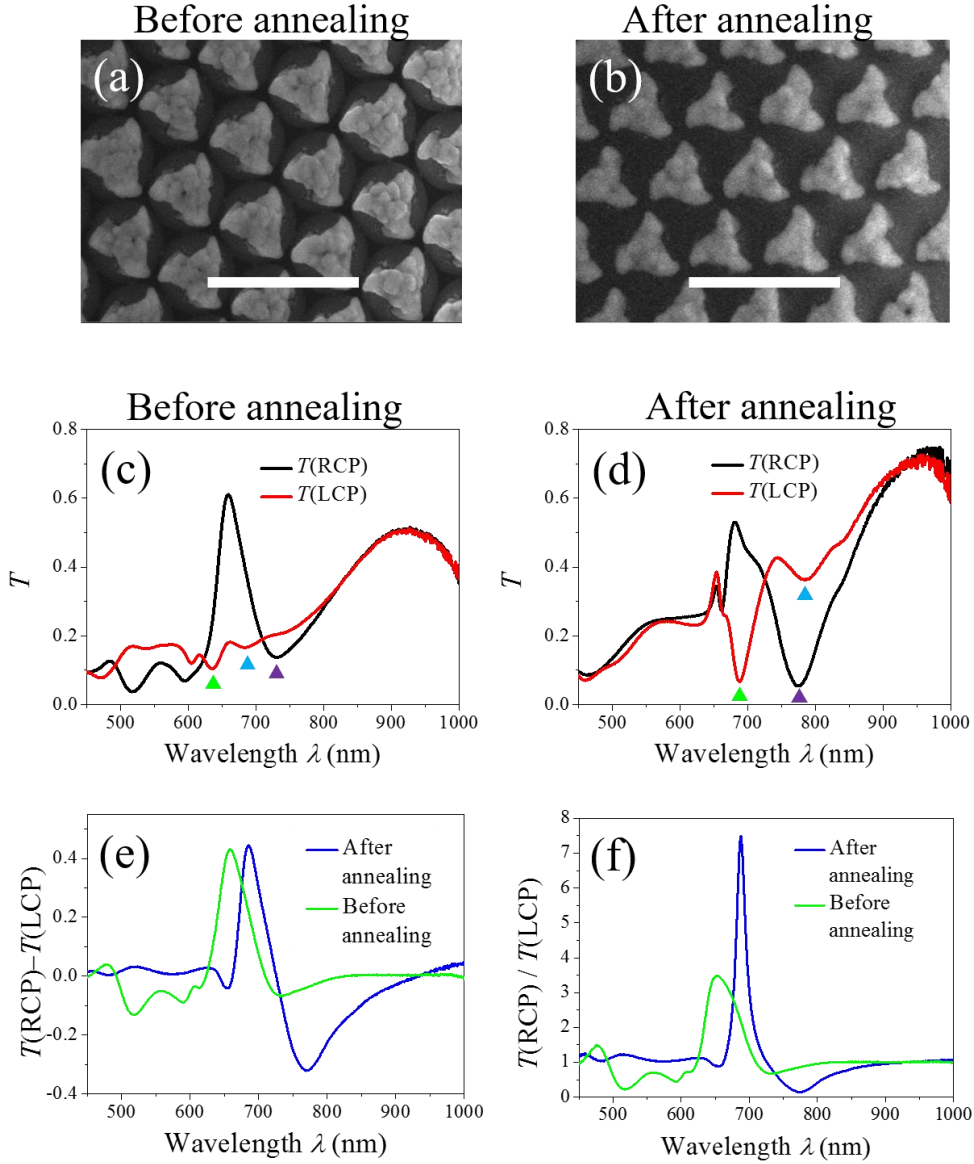


**Figure 3.4.5.** The SEM images of Ag fan-shaped nanostructures fabricated by DSG with  $\theta = 84^\circ$  and  $t_{\text{QCM}} = 4 \times 30$  nm (a) before and (b) after annealing.  $T(\text{RCP})$  and  $T(\text{LCP})$  spectra of Ag fan-shaped nanostructures (c) before and (d) after annealing. (e)  $T(\text{RCP}) - T(\text{LCP})$  and (f)  $T(\text{RCP}) / T(\text{LCP})$  spectra of Ag fan-shaped nanostructures before and after annealing.

According to the SEM images, the Ag nanostructures have no obvious change in the geometric shape, but a significant change in surface roughness. As shown in **Figure 3.4.5a**, the surface of the nanostructures is rough with many Ag nanoparticles before annealing. After annealing, the nanostructure surface becomes smooth without obvious Ag nanoparticles. The reduced surface

roughness is caused by the diffusion and coalescence of Ag nanoparticles with high surface energy in the annealing process.[135] Another possible morphology change is that the fan-shaped structures have less 3D features, because the nanosphere array becomes a flat layer, which cannot be confirmed by top-view SEM images.

The annealing has a significant impact on the chiral optical property. **Figures 3.4.5c** and **3.4.5d** show the circularly polarized transmittance spectra before and after annealing, respectively. After annealing, the transmittance magnitude increases in the wavelength range without resonances. The disappearance of polystyrene nanospheres and Ag nanoparticle reduces the light scattering and thus enhances the transmittance. In addition, the photonic band gap at  $\lambda = 600$  nm is removed after annealing due to no periodic nanosphere array. The most significant change in chiral optical property is that the LSPRs redshift and becomes more intense with sharper transmittance valleys. The resonances are labeled by the colored triangles in **Figures 3.4.5c** and **3.4.5d**. After annealing, the reduced surface roughness helps to decrease the variation in structural size and shape, which along with the reduced light scattering leads to a narrower and stronger plasmonic resonance. There are two possible reasons for the redshift of LSPR wavelengths, the structural change and the surrounding refractive index change. As discussed above, the fan-shaped nanostructures may become more like 2D structure after annealing, and thus have structural changes in the substrate normal direction. Additionally, the polystyrene becomes flexible in the annealing process, and Ag nanostructures may be partially embedded in the polystyrene, which changes the surrounding refractive index of the Ag nanostructures. Both the structural change and surrounding refractive index change can lead to the LSPR wavelength shift. However, these two possible reasons cannot be verified in SEM images. The redshift of the LSPR wavelengths in  $T(\text{RCP})$  and  $T(\text{LCP})$  spectra leads to the redshift of  $T(\text{RCP})-T(\text{LCP})$  spectrum after annealing. The

intense resonance in  $T(\text{RCP})$  at  $\lambda = 770$  nm results in a strong negative peak in  $T(\text{RCP})-T(\text{LCP})$  spectrum.

One interesting effect caused by the annealing is that the narrow transmittance valley in  $T(\text{LCP})$  and the sharp transmittance peak in  $T(\text{RCP})$  are at the same wavelength  $\lambda = 690$  nm, which leads to a huge transmittance contrast between RCP and LCP. **Figure 3.4.5f** shows the polarization extinction ratio  $T(\text{RCP})/T(\text{LCP})$  of the Ag fan-shaped nanostructures before and after annealing. The maximum of  $T(\text{RCP})/T(\text{LCP})$  is 3.5 before annealing and reaches 7.5 after annealing. We propose that such a large-area substrate can work as a narrow-band circular polarizer with a band width of 18 nm.

### 3.5 Fan-shaped chiral nanostructures in different materials

One important question needs to be asked: “Does the chiral optical property of the fan-shaped nanostructures originate from the intrinsic property of the chiral geometry or have to require surface plasmon?” To answer this question, we explore the chiral optical property of the fan-shaped chiral nanostructures in other metal materials, including Au, Cu, and Ni. The fan-shaped nanostructures are fabricated by DSG with  $\theta = 86^\circ$  and  $t_{\text{QCM}} = 4 \times 30$  nm, on hexagonal close-packed nanosphere arrays with diameter  $d = 500$  nm. The monolayer domains with  $\varphi_0 \approx 10^\circ$  are selected for optical characterizations, which have chiral fan-shaped nanostructures similar to those in Domain #4 in Section 3.3. The measured  $T(\text{RCP})$  and  $T(\text{LCP})$  of fan-shaped nanostructures in different materials are shown in **Figure 3.5.1**, along with those of Ag fan-shaped nanostructures for comparison. All the structures have transmittance valley at  $\lambda = 600$  nm due to the photonic band gap of the nanosphere monolayer, and also similar transmittance magnitude. Au and Cu are plasmonic materials as well as Ag. Therefore, Au and Cu fan-shaped nanostructures exhibit LSPR

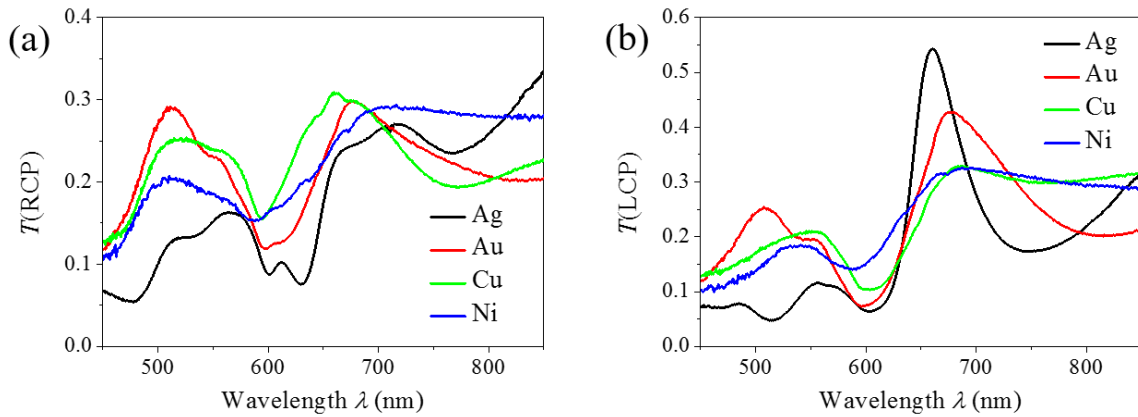


**Figure 3.5.1.** Measured (a)  $T(\text{RCP})$ , and (b)  $T(\text{LCP})$  spectra of the chiral fan-shaped nanostructures made by Ag, Au, Cu, and Ni.

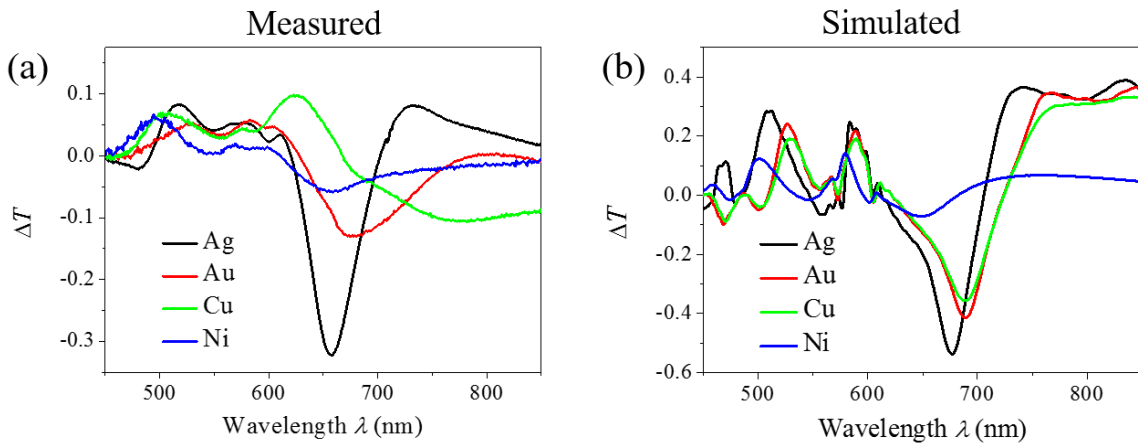


**Figure 3.5.2** (a) Measured, and (b) simulated  $\Delta T$  spectra of the chiral fan-shaped nanostructures made by Ag, Au, Cu, and Ni.

in visible to near-IR wavelength range. Au nanostructure has LSPR around  $\lambda = 820$  nm, and Cu nanostructure shows LSPR around  $\lambda = 770$  nm, in both RCP and LCP polarizations. Since Ni is not a plasmonic material, no LSPR is observed for Ni fan-shaped nanostructure. All the fan-shaped nanostructures show a transmittance peak around  $\lambda = 670$  nm, which is possibly caused by the photonic band gap at  $\lambda = 600$  nm and LSPRs or absorbance in longer wavelength range. **Figure 3.5.2a** shows the measured  $\Delta T$  spectra for fan-shaped nanostructures in different materials. Surprisingly, all the fan-shaped nanostructures show similar spectral features for  $\Delta T$  spectra:  $\Delta T$

is positive in short wavelength range ( $< 600$  nm), and becomes negative in longer wavelength range with a negative peak. The wavelengths of the negative peak in  $\Delta T$  spectra are close for Ag, Au and Ni structures, which are mainly determined by the transmittance peaks around  $\lambda = 670$  nm. The  $\Delta T$  negative peak for Cu structure is located at an even longer wavelength, which is mainly caused by the resonance in  $T(\text{RCP})$  at  $\lambda = 770$  nm. Ag structure shows the strongest CD response due to its intense LSPR, while Ni structure without any plasmonic resonance shows the weakest response. The similar spectral feature in CD response of different structures may originate from the intrinsic chiral geometry of the fan-shaped structures. The different magnitude and peak wavelength of CD spectra are determined by the material properties. The CD response is confirmed by FDTD simulations. The simulations were performed by assuming the structures in different materials are all the same as Ag fan-shaped nanostructures. The simulated  $\Delta T$  spectra agree well with the measured ones, as shown in **Figure 3.5.2b**.

This study demonstrates that the fan-shaped chiral nanostructures show similar CD spectra. The CD magnitude may vary with material property, but the spectral features are determined by the intrinsic chirality of fan-shaped structures. In addition, the demonstration of chiral optical response for fan-shaped nanostructures in different materials opens up the possibility for different functionalities. For example, Ni chiral nanostructures can exhibit magnetic circular dichroism, which is from the coupling between structural chirality and magnetism.[89, 90] Au has an inert surface, which cannot be easily oxidized and is excellent for chemical and biological sensing, unlike Ag. Therefore, Au chiral nanostructures have been utilized for sensing,[57] as it will be demonstrated in Section 5.4.

### 3.6 Conclusions

In summary, we have presented a fabrication strategy for chiral metamaterial by DSG on SACMs. The obtained plasmonic patchy particles contain various nanostructures with different chirality and shapes, which are determined by the relative orientation of monolayers with respect to the incident vapor during the fabrication. The racemic mixtures of patchy particles show a bulk CD response, which is caused by the dissymmetry in shadowing growth. A systematic investigation exploring the monolayer orientation effect reveals that the local nanostructures can exhibit different or even opposite CD response. At a particular monolayer orientation, fan-shaped chiral structures can be obtained, which show giant CD response, one order of magnitude larger than the bulk CD, and comparable to highest CD of those prepared by EBL. Another systematic study explores how the CD response of the Ag fan-shaped structures is influenced by different fabrication parameters, including incident angle of vapor flux  $\theta$ , thickness  $t_{\text{QCM}}$ , and annealing.  $\theta$  is found to influence the CD response through changing the size, shape, thickness, surface roughness and structural variation of the fan-shaped nanostructure. The optimal value for  $\theta$  is  $84^\circ$  in order to achieve largest CD response with  $t_{\text{QCM}}$  fixed at  $4 \times 30$  nm. A smaller  $\theta$  leads to a less chiral shape and higher Ag coverage, and a larger  $\theta$  leads to a highly rough surface and large structural variation, which both results in a poor CD signal. The thickness  $t_{\text{QCM}}$  can affect the CD response by tuning the LSPR. The optimal thickness  $t_{\text{QCM}}$  is  $4 \times 30$  nm with  $\theta$  fixed at  $84^\circ$ . The post-deposition annealing can change the structural morphology primarily in the substrate normal direction, and reduce the surface roughness, leading to an improved CD signal. It is found that the Ag fan-shaped structures after annealing can be developed as a narrow-band circular polarizer if they are fabricated on a large-area substrate without structural variations. The CD response of fan-shaped nanostructures in different metal materials is also investigated, which opens up the possibility for different functionalities, such as magnetic circular dichroism and sensing. The giant

CD signal, tunable structures and optical response, and great advantage in scalable fabrication, make this DSG based fabrication method very suitable for developing chiral metamaterial based optical devices, which will be further discussed in Chapter 5.

## CHAPTER 4

### HELICALLY STACKED PLASMONIC NANOSTRUCTURES

#### 4.1 Introduction

In Chapter 3, a fabrication strategy for quasi-3D chiral metamaterial based on DSG on SACMs has been described. In this strategy, one layer of metal thin film is coated on nanospheres, whose shape or geometric chirality is directly related to the monolayer orientation. The dependence of chirality on the monolayer orientation originates from the different nanostructure shapes resulted from the shadowing effect during DSG process. Therefore, with polycrystalline monolayers, one can only achieve the racemic mixture of Ag patches, which has poor uniformity and weak bulk CD response. In this chapter, we introduce another DSG based fabrication strategy for 3D chiral metamaterials, which produces chiral nanostructures with almost no monolayer orientation effect and good uniformity on polycrystalline monolayers. In this fabrication strategy, plasmonic thin films are helically stacked on nanospheres by vapor depositions alternated between metals and dielectric materials. The dielectric thin films are created to support the plasmonic layers to form 3D helical structures. Although the shapes of plasmonic thin films still depend on the monolayer orientations, the chirality does not exhibit such a dependence. Instead, the chirality is primarily determined by in which handedness the plasmonic thin films are helically stacked. By applying this strategy, two types of chiral metamaterials have been realized, helically stacked plasmonic layers and Swiss Roll nanostructures.

## 4.2 Helically stacked plasmonic layers

Helix or helical-shaped structure is one common structure design for chiral metamaterials. Plasmonic helices and some other helically arranged nanostructures have been prepared by a variety of techniques,[21, 39, 40, 42] including DSG.[46, 47, 99, 136] Here, by applying helically-stacking strategy, we fabricate a helical-shaped nanostructure—helically stacked plasmonic layers (HSPLs). The morphology simulations in Section 2.4 have demonstrated that an oblique angle deposition on nanosphere monolayers produces patchy films with various shapes depending on the monolayer orientations with respect to the vapor flux. The deposited thin film nanostructures are mainly distributed on one side of the nanospheres facing the incident vapor. These asymmetric thin films can be stacked in left-handed (LH) or right-handed (RH) helical fashions. HSPLs are different from other reported structures having helically arranged plasmonic layers,[34, 35] because HSPLs form true, continuous, nanoscale helices. They are also distinct from the traditional helices made by DSG.[46, 47, 99] The helix pitch and helix diameter are decoupled from each other and from material constraints, which can be significant in the case of noble metals.

### 4.2.1 Helically stacked plasmonic layers: fabrication

The fabrication process of HSPLs starts with preparation of SACMs on both Si and glass substrates. Three different substrate types were prepared that contain different sphere diameters  $d = 200, 350, \text{ and } 500 \text{ nm}$ , and were loaded on a substrate holder in a custom-designed vacuum deposition system (Pascal Technology). Before deposition, the chamber was evacuated to a base pressure of  $1 \times 10^{-6}$  Torr, and the background pressure during depositions was maintained at less than  $5 \times 10^{-6}$  Torr. Ag (99.999%, Kurt J. Lesker) and SiO<sub>2</sub> (99.99%, International Advanced Materials) source materials were used for depositions. During the deposition process, Ag and SiO<sub>2</sub>

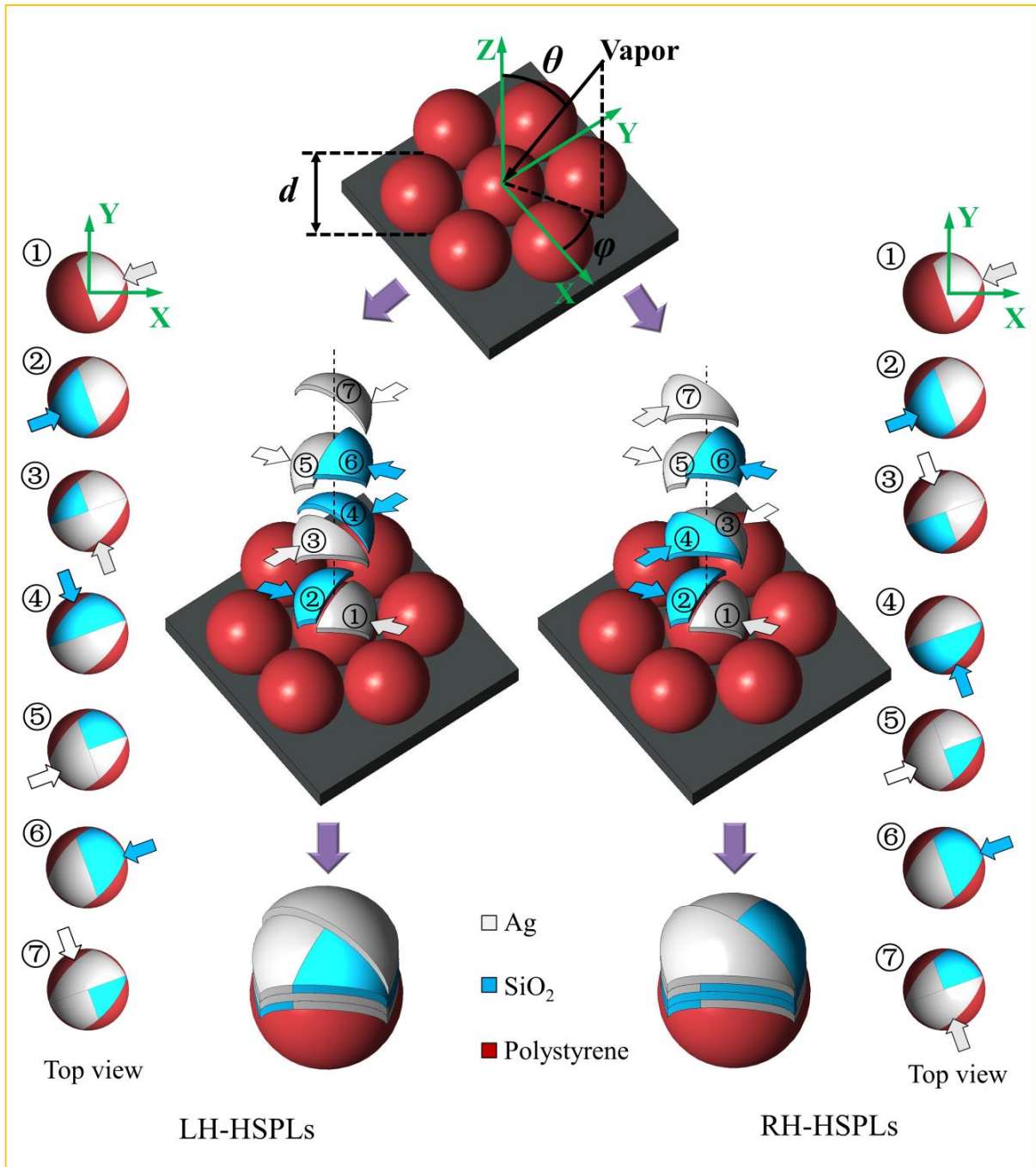


**Figure 4.2.1.** Schematics of deposition processes and expected structures for LH- and RH-HSPLs. The process includes 7 deposition steps: ①Ag, ②SiO<sub>2</sub>, ③Ag, ④SiO<sub>2</sub>, ⑤Ag, ⑥SiO<sub>2</sub>, and ⑦Ag. The direction of each deposition is indicated by the white (Ag) or blue (SiO<sub>2</sub>) arrow. Top-view figures of LH- and RH-HSPLs at each step are shown at the left and right edges. 3D schematics of the expected structures are shown at the bottom.

vapors were deposited onto the monolayers alternately at a polar angle,  $\theta = 80^\circ$ , with respect to the substrate normal, following the procedure shown in **Figure 4.2.1**. Specifically, if we define  $\Delta\varphi$  as the relative change in azimuthal orientation of the substrates with respect to the previous step, and denote “+” and “-” for CCW and CW rotations, respectively, then the sequence of depositions for the RH-HSPLs (LH-HSPLs) can be described by: ①Ag:  $\Delta\varphi = 0^\circ$ , ②SiO<sub>2</sub>:  $\Delta\varphi = 180^\circ$ , ③Ag:  $\Delta\varphi = -90^\circ$  (+90°), ④SiO<sub>2</sub>:  $\Delta\varphi = 180^\circ$ , ⑤Ag:  $\Delta\varphi = -90^\circ$  (+90°), ⑥SiO<sub>2</sub>:  $\Delta\varphi = 180^\circ$ , and ⑦Ag:  $\Delta\varphi = -90^\circ$  (+90°), where each Ag or SiO<sub>2</sub> layer has a QCM thickness of 30 nm. The deposition rate for both Ag and SiO<sub>2</sub> is maintained at 0.05 nm/s throughout the depositions. This deposition formula produces four Ag layers that are all connected to form a one-turn 3D helix, and the three SiO<sub>2</sub> layers act to support the Ag layers and fill the space surrounding the helix.

#### **4.2.2 Helically stacked plasmonic layers: morphology**

HSPLs obtained through the process are observed to have polycrystalline domains of nanospheres. **Figure 4.2.2a** shows a representative top-view SEM image of LH-HSPLs on  $d = 500$  nm monolayer. Four distinct domains, Domains #1–4, can be clearly identified, and their higher magnification SEM images are shown in **Figures 4.2.2b-4.4.2e**, respectively. **Figures 4.2.2f-4.4.2g** show the SEM images of Domain #4 in different fabrication steps, which demonstrates that the obtained HSPLs consist of four connected Ag layers as expected. In order to clearly distinguish different domains, we can designate each domain using the azimuthal angle,  $\varphi$ , of the first Ag deposition, as shown at the top of **Figure 4.2.1**. There is some degeneracy in this initial  $\varphi$  angle due to the symmetry of the HCP lattice, where  $\varphi$  can be expressed as  $\varphi = \varphi_0 + n \cdot 60^\circ$ , for  $0^\circ \leq \varphi_0 < 60^\circ$  and an integer,  $n$ . Similar to the definition of monolayer orientations in Chapter 3,  $\varphi_0$  is used to define each domain. Given the direction of first Ag deposition as indicated by the arrow at the

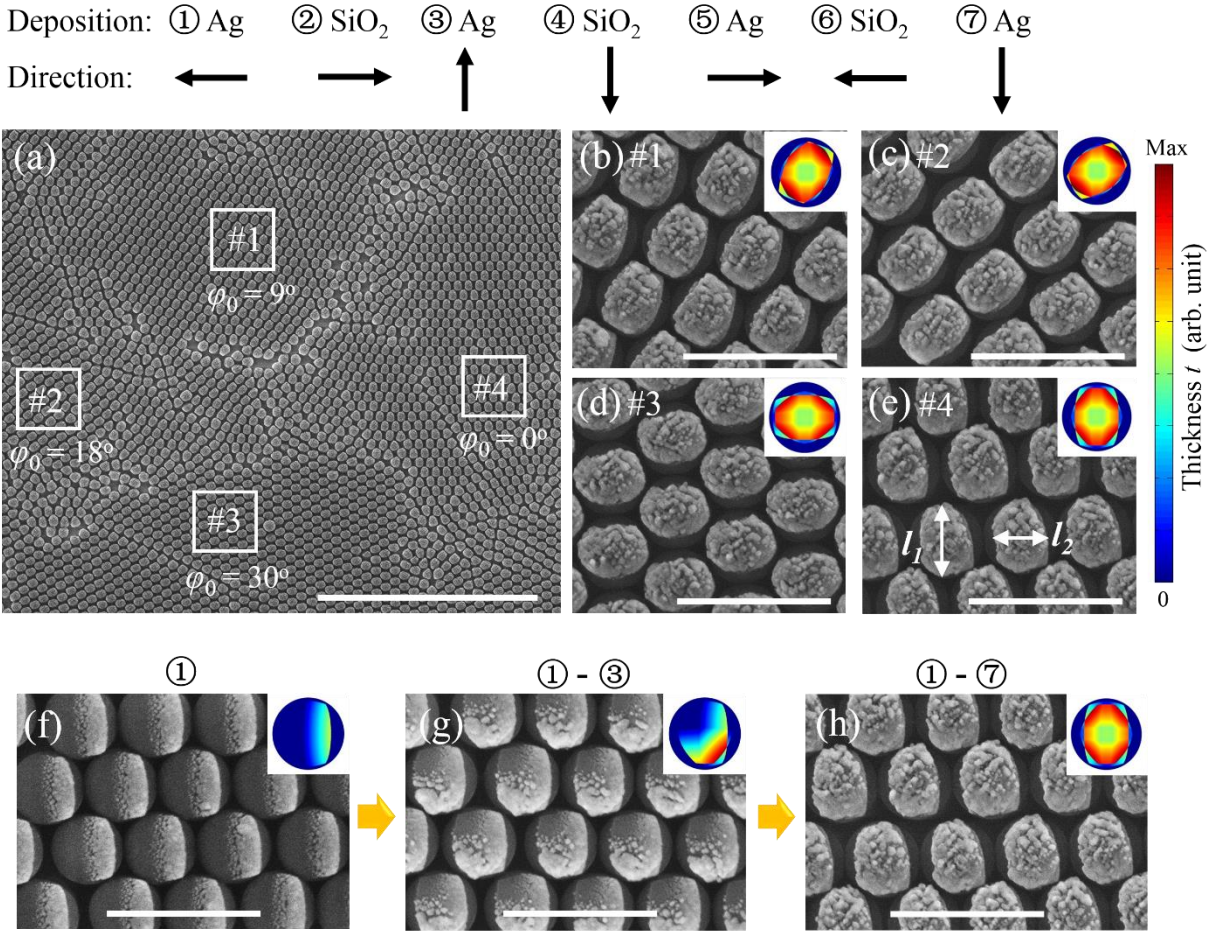


**Figure 4.2.2.** (a) Top-view SEM images of LH-HSPLs on  $d = 500$  nm nanosphere monolayers. (b)-(d) Higher magnification images for Domains #1–4, respectively. (f)-(h) SEM images of Domain #4 at different fabrication steps. Insets are the morphologies obtained by simulations. The order and directions of depositions are shown at the top. The scale bar represents  $10 \mu\text{m}$  in (a), and represents  $1 \mu\text{m}$  in (b)-(h).

top of **Figure 4.2.2**, Domains #1–4 have  $\varphi_0 = 9^\circ$ ,  $18^\circ$ ,  $0^\circ$ , and  $30^\circ$ , respectively. The morphology simulations in Section 2.4 have demonstrated that the morphology of a single Ag or SiO<sub>2</sub> layer strongly depends on  $\varphi_0$ . However, these SEM images reveal a consistent rectangular-like shape for the material patches on different monolayer domains, which is also confirmed by the morphology simulations shown in the corresponding insets in **Figure 4.2.2** and a systematic morphology simulation shown in **Figure 4.2.3**. These rectangular-like shapes have different

orientations but almost the same dimensions across the different domains. The dimensions of the individual patches are characterized by the lengths,  $l_1$ , and widths,  $l_2$ , which are defined in **Figure 4.2.2e**. The measured  $l_1$  and  $l_2$  values for HSPLs on nanospheres of different diameters are listed in **Table 4.2.1**. The aspect ratio,  $l_2/l_1$ , for different bead sizes is almost a constant, as expected

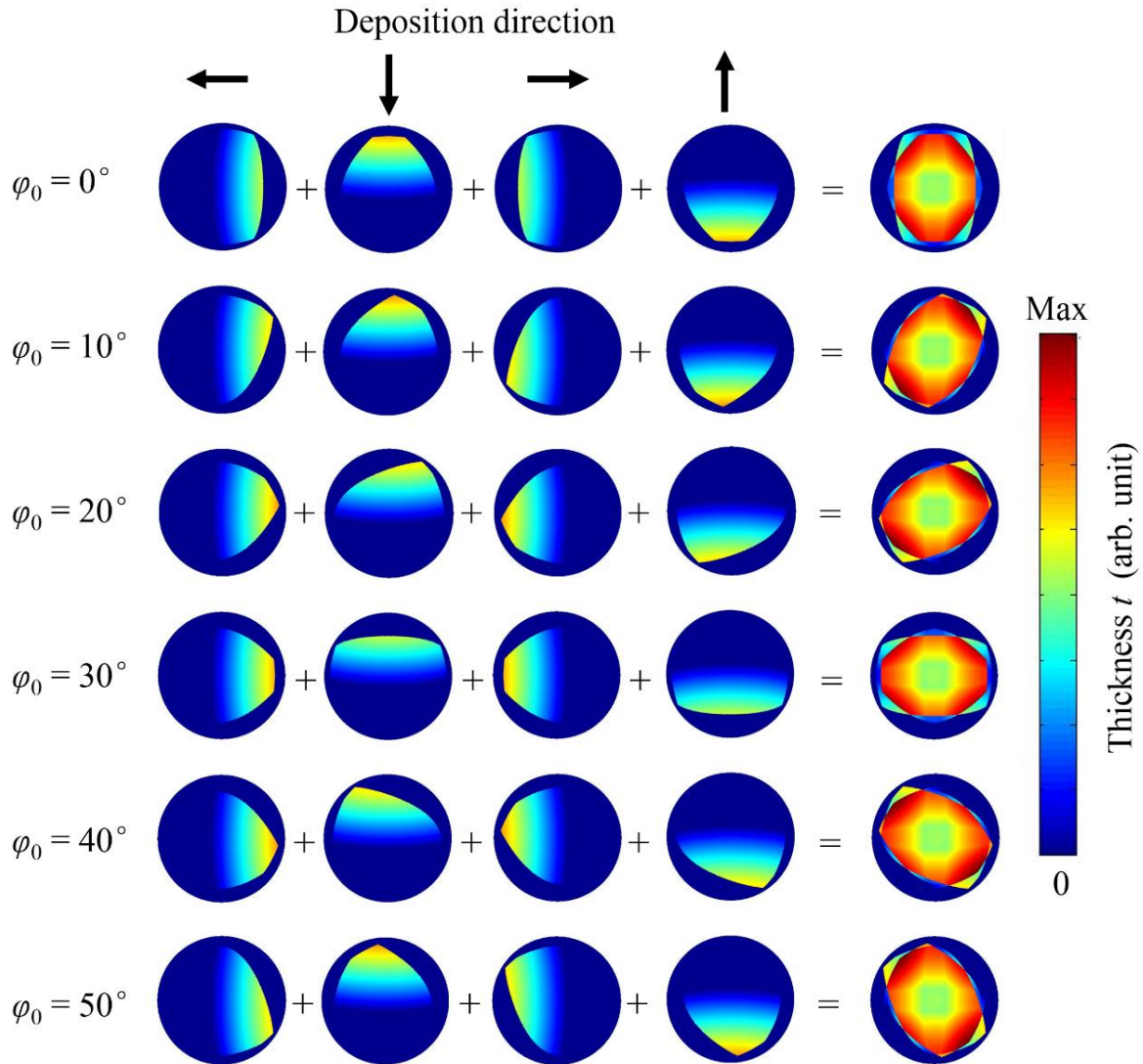


**Figure 4.2.3.** First four columns: the simulated morphology of single layers on nanospheres in four deposition directions on domains with  $\varphi_0 = 0^\circ, 10^\circ, 20^\circ, 30^\circ, 40^\circ,$  and  $50^\circ$ , respectively. The last column: the simulated morphology of the stacked layers. The arrows at the top indicate the deposition directions.

**Table 4.2.1.** Geometric parameters of HSPLs on nanospheres with different diameter,  $d$ 

	$d = 200 \text{ nm}$	$d = 350 \text{ nm}$	$d = 500 \text{ nm}$
$l_1$ (nm)	$200 \pm 10$	$330 \pm 10$	$460 \pm 10$
$l_2$ (nm)	$160 \pm 10$	$240 \pm 10$	$340 \pm 20$
<b>Aspect Ratio, <math>l_2/l_1</math></b>	$0.80 \pm 0.06$	$0.73 \pm 0.04$	$0.74 \pm 0.05$

from the morphology simulations. A statistical study was performed on the domain area distribution, as shown in **Figure 4.2.4**. Domains areas were found to be mostly distributed between 0 and  $120 \mu\text{m}^2$ . The distribution of domain area versus  $\varphi_0$  was also found to be uniform, indicating that there is no preferred orientation for the polycrystalline domains. Therefore, although individual HSPLs have consistent anisotropic structures within each domain, the mixture of HSPL domains is isotropic on the macroscale.

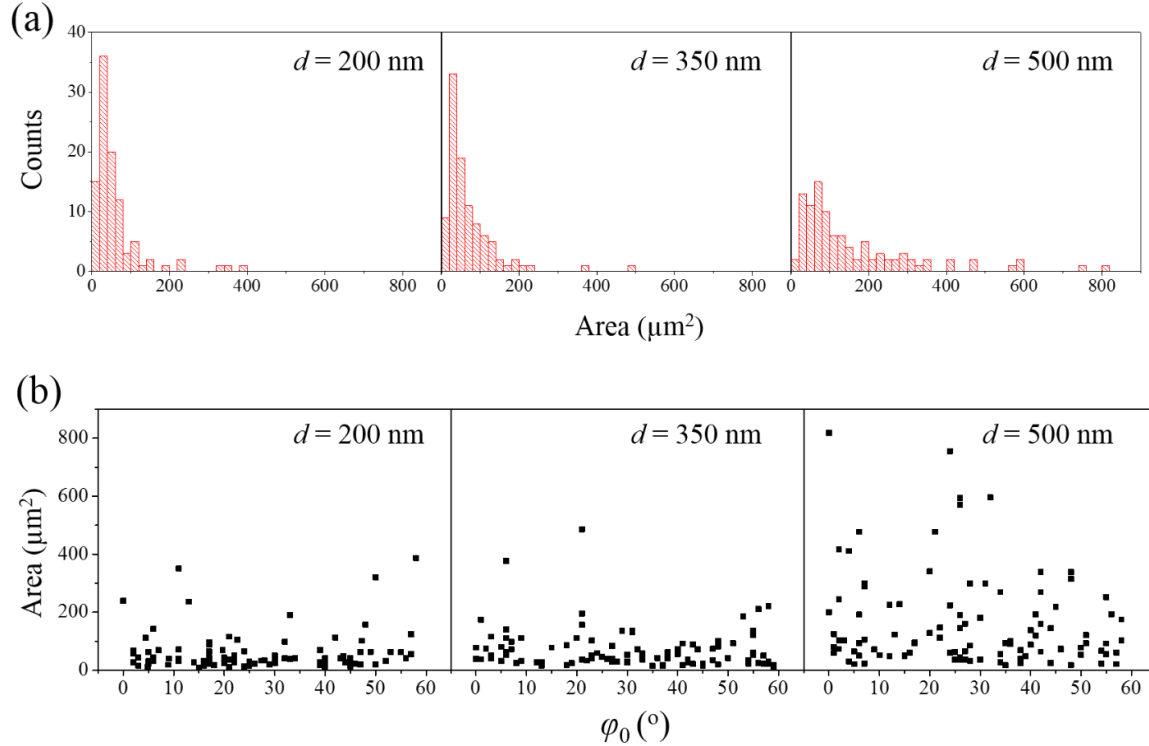


**Figure 4.2.4.** (a) Domain area distributions of  $d = 200, 350,$  and  $500 \text{ nm}$  monolayers. (b) Distribution of domain area versus  $\varphi_0$ .

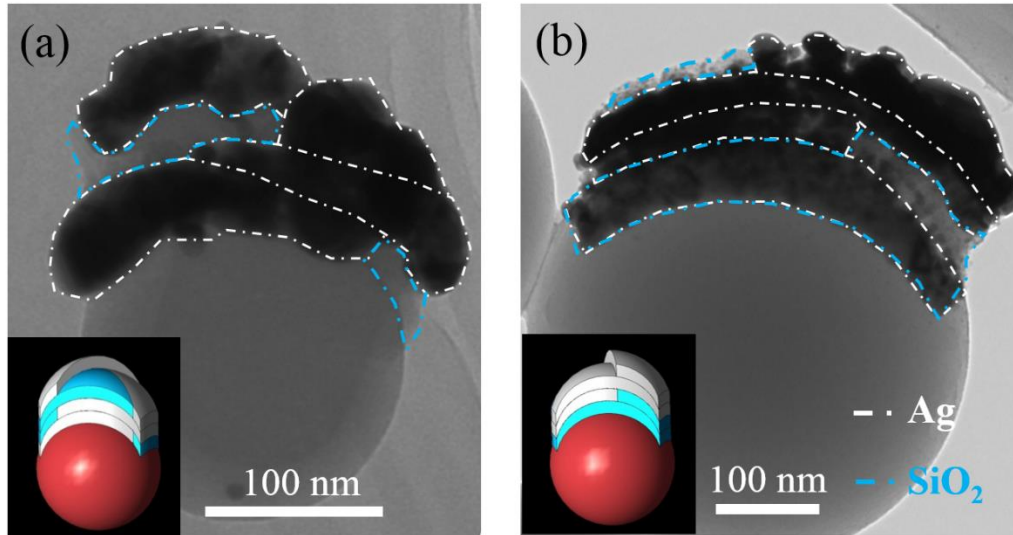


**Figure 4.2.5.** TEM images of RH-HSPLs on (a) 200nm, and (b) 500nm nanospheres. White and blue dashed lines are artificially added to outline Ag and SiO<sub>2</sub> layers, respectively. Insets are 3D schematics of RH-HSPLs expected from the deposition sequence.

The cross-section of HSPLs is revealed by TEM. **Figure 4.2.5** shows the TEM images of RH-HSPLs on  $d = 200$  and 500 nm nanospheres. Note that Ag appears much darker than SiO<sub>2</sub> in TEM images due to a larger scattering cross-section, and that the white and blue dashed lines are artificially added to better illustrate the stacked layers, where white lines represent Ag and blue lines represent SiO<sub>2</sub>. The thickness of each Ag or SiO<sub>2</sub> layer is estimated to be about 30 nm for both samples. The insets show the corresponding 3D schematics of RH-HSPLs. The similarity between TEM images and 3D schematics demonstrate that the desired HSPLs have been achieved.

#### 4.2.3 Helically stacked plasmonic layers: optical property

The optical properties of HSPLs are studied using both unpolarized transmittance spectroscopy and Mueller matrix transmittance spectroscopy. As shown in **Figure 4.2.6**, the unpolarized transmittance spectra of HSPLs strongly depend on  $d$ , but not on handedness. For  $d = 200$  nm, a broad transmittance dip appears around wavelength  $\lambda = 520$  nm, corresponding to the LSPR of Ag

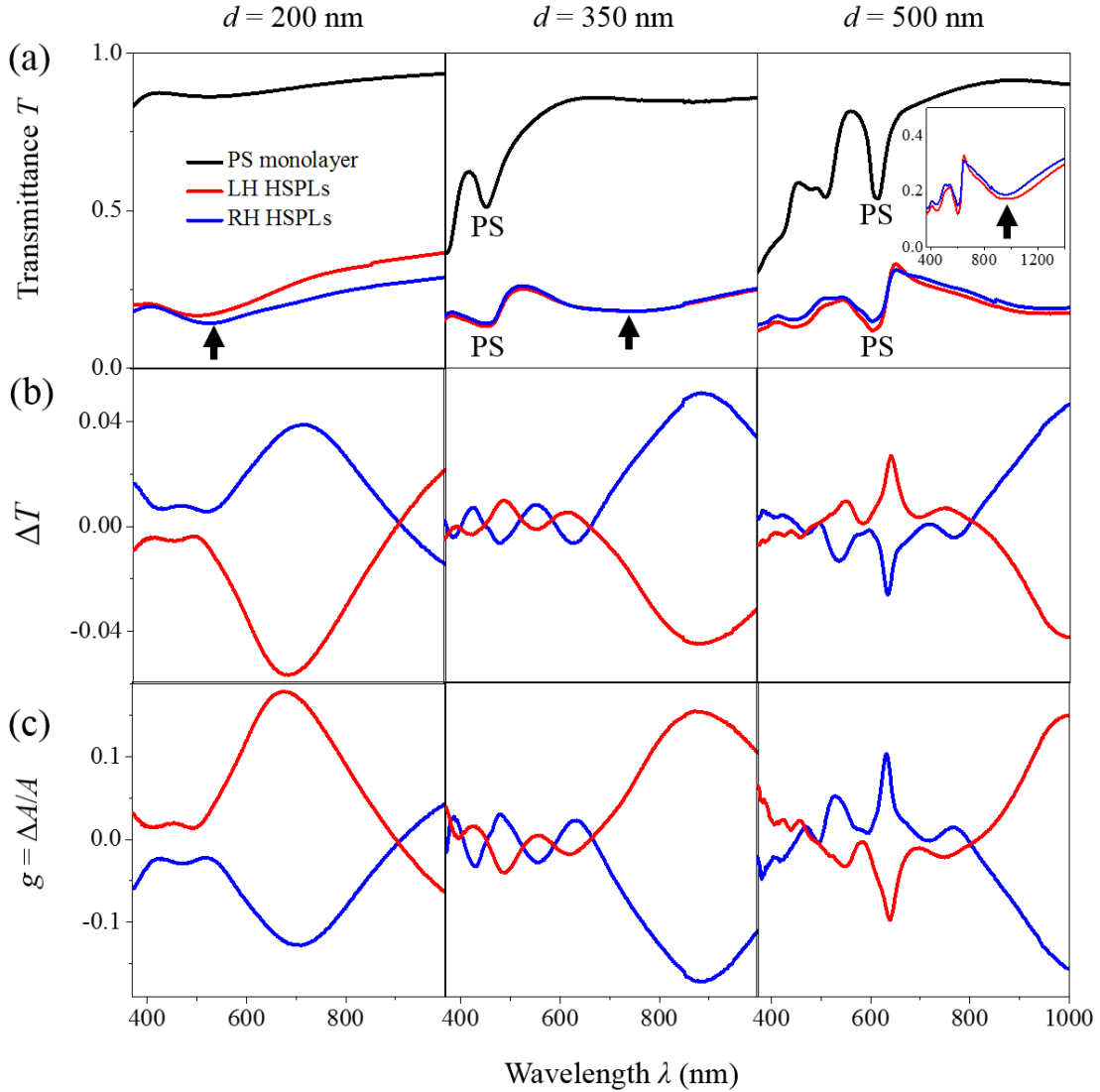


**Figure 4.2.6.** (a) Unpolarized transmittance spectra, (b) transmittance difference between RCP and LCP light, and (c)  $g$ -factor spectra, of LH- and RH-HSPLs on  $d = 200$  nm, 350 nm, and 500 nm monolayers. The inset in (a) is an extended wavelength range transmittance spectrum for  $d = 500$  nm. Note that “PS” and the arrows in (a) mark the wavelength locations of the photonic band gap and the Ag LSPR, respectively.

layers. This transmittance dip becomes broader and redshifts to  $\lambda = 750$  and 1000 nm as  $d$  increases to 350 and 500 nm, respectively. These transmittance dips are marked with an arrow in **Figure 4.2.6a**. This observation is consistent with plasmonics theory: the LSPR wavelength should redshift with an increase in  $d$  since  $d$  is proportional to the size of HSPLs.[137] For HSPLs on  $d = 350$  nm and 500 nm monolayers, transmittance dips at  $\lambda = 470$  nm and 600 nm correspond to the

photonic band gap of the periodic monolayer structures,[138, 139] which also appear in the transmittance spectra of bare monolayers. These are labeled with “PS” in **Figure 4.2.6a**. In order to characterize the chiral optical properties of HSPLs, the transmittance difference between RCP and LCP light,  $\Delta T = T(\text{RCP}) - T(\text{LCP})$ , are obtained by measuring the Mueller matrix element  $m_{14}$  and are shown in **Figure 4.2.6b**. It should be noted that the linear birefringence and linear dichroism may not be negligible for each domain due to the anisotropic morphology. However, thousands of domains with randomly distributed  $\varphi_0$  are illuminated by a 4 mm diameter beam during the optical measurement, which will eliminate linear effects from the measurement. As expected, the LH- and RH-HSPLs exhibit opposite CD response in the wavelength range  $\lambda = 370\text{--}1000$  nm. For LH-HSPLs on  $d = 200$  nm monolayers,  $\Delta T$  has a broad negative peak in wavelength range  $\lambda = 550\text{--}900$  nm, indicating larger transmittance of LCP light than RCP light. It reaches the maximum magnitude  $|\Delta T| = 0.056$  around  $\lambda = 700$  nm, and becomes positive above 900 nm, indicating larger transmittance of RCP light than LCP light. The CD response is reversed for RH-HSPLs on  $d = 200$  nm monolayers. As  $d$  increases to 350 nm and 500 nm, the magnitude of the  $\Delta T$  peak remains almost the same, but the wavelength of  $\Delta T$  peak redshifts to  $\lambda = 900$  nm and above  $\lambda = 1000$  nm, respectively, due to the redshift of the LSPR. The dissymmetry factor  $g$  of the HSPLs is also estimated as shown in **Figure 4.2.6c**, which is defined as  $g = \Delta A/A$ , where  $\Delta A$  is the differential extinction between RCP and LCP light, and  $A$  is the unpolarized extinction of only the HSPLs. Here we assume that  $A = A_{total} - A_{PS}$  for simplicity, where  $A_{total}$  and  $A_{PS}$  are the unpolarized extinction of the total structures and the bare PS monolayers, respectively. The  $g$  factor has the same feature as  $\Delta T$ , but with the opposite sign for each samples. The magnitude of  $g$  can reach higher than 0.15 around the peak, which is comparable with those of recent studies.[47, 119]

#### 4.2.4 Helically stacked plasmonic layers: FDTD simulation

FDTD simulations were performed to verify the chiral optical response of the HSPLs (see Section 2.7 for the details of FDTD simulations). Since the morphology of HSPLs depends on the orientation of domains, we first investigate the chiral optical properties of HSPLs in different domains. The LH-HSPLs on  $d = 200$  nm monolayers in 12 domains with  $\varphi_0 = 0^\circ - 55^\circ$ , in increments of  $5^\circ$ , are selected for FDTD simulation. The geometric models in FDTD simulations are created by based on the morphology simulations. For simplicity, we assumed that each Ag or  $\text{SiO}_2$  layer is uniform with thickness  $t = 30$  nm. Each domain is assumed to be infinitely large and contribute to the bulk optical response equally. **Figure 4.2.7a** shows the geometric models of LH-HSPLs on  $d = 200$  nm monolayers with  $\varphi_0 = 0^\circ$ ,  $15^\circ$ , and  $30^\circ$ , respectively. The circular transmittances of different domains are calculated under normal incidence of light. **Figure 4.2.7b** shows the  $\Delta T$

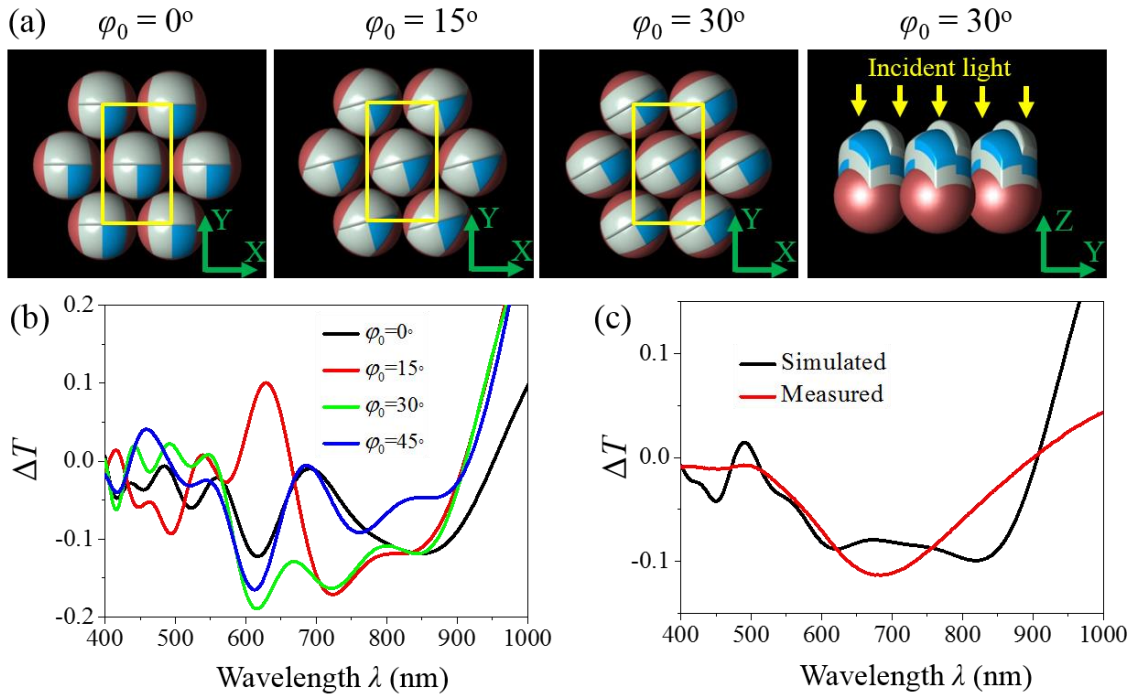


**Figure 4.2.7.** (a) Schematics of geometric models used in FDTD simulations. The yellow rectangle in first three figures illustrates a unit cell of the HSPL arrays. (b) The simulated  $\Delta T$  spectra of HSPL domains with  $\varphi_0 = 0^\circ$ ,  $15^\circ$ ,  $30^\circ$  and  $45^\circ$ . (c) The averaged simulated  $\Delta T$  spectrum versus the measured  $\Delta T$  spectrum.

spectra of LH-HSPLs with  $\varphi_0 = 0^\circ, 15^\circ, 30^\circ,$  and  $45^\circ$ . The spectra vary with  $\varphi_0$ , but are very similar in trend. Most of them exhibit negative features over wavelengths  $\lambda = 550 - 900$  nm and become positive above  $\lambda = 900$  nm. The variation in the simulated  $\Delta T$  among different domains is caused by their structural differences, which lead to slightly different LSPR wavelengths. The similar trend in the simulated  $\Delta T$  originates from their similarity in helical-shape and handedness. An average  $\Delta T$  spectrum over 12 different domains is plotted in comparison with the experimentally measured  $\Delta T$  spectrum in **Figure 4.2.7c**. The simulated spectrum agrees with the measured spectrum qualitatively. In addition, we also investigate the chiral optical properties of HSPLs on monolayers with different  $d$ . FDTD simulations are performed with LH-HSPLs on  $d = 200, 350,$  and  $500$  nm monolayers, with  $\varphi_0$  fixed at  $0^\circ$ . The calculated  $T(\text{LCP}), T(\text{RCP})$  and  $\Delta T$  for  $\varphi_0 = 0^\circ$  are shown in **Figures 4.2.8a** and **4.2.8b**, respectively. An intense plasmon resonance is observed in the transmittance spectrum,  $T(\text{RCP})$ , of each HSPLs structure, and occurs at  $\lambda = 815, 1035,$  and  $1355$  nm for  $d = 200, 350,$  and  $500$  nm, respectively. The near-field FDTD simulations at these wavelengths on the corresponding HSPLs reveal that these resonances have identical current distributions, as illustrated in **Figure 4.2.8c**. This resonance, labeled as “R” in **Figures 4.2.8a**, is found to result in a negative peak “A” in the  $\Delta T$  spectrum (**Figures 4.2.8b**) for each structure. The resonance “R” redshifts with increasing  $d$ , which leads to a redshift of the peak “A”. Another pronounced spectral feature is an intense transmittance peak in the  $T(\text{LCP})$  spectrum, labeled as “L” in **Figure 6a**, which results in another negative peak, “B”, in the  $\Delta T$  spectrum (**Figures 4.2.8b**). The peak “L” also redshifts with increasing  $d$ , occurring at  $\lambda = 610, 685,$  and  $850$  nm for  $d = 200, 350,$  and  $500$  nm, respectively. As a result, the peak “B” redshifts in  $\Delta T$  spectra. The FDTD simulation results confirm that the redshift of the spectral features in the simulated and experimental  $\Delta T$  spectra with  $d$  results from the redshift of LSPR.

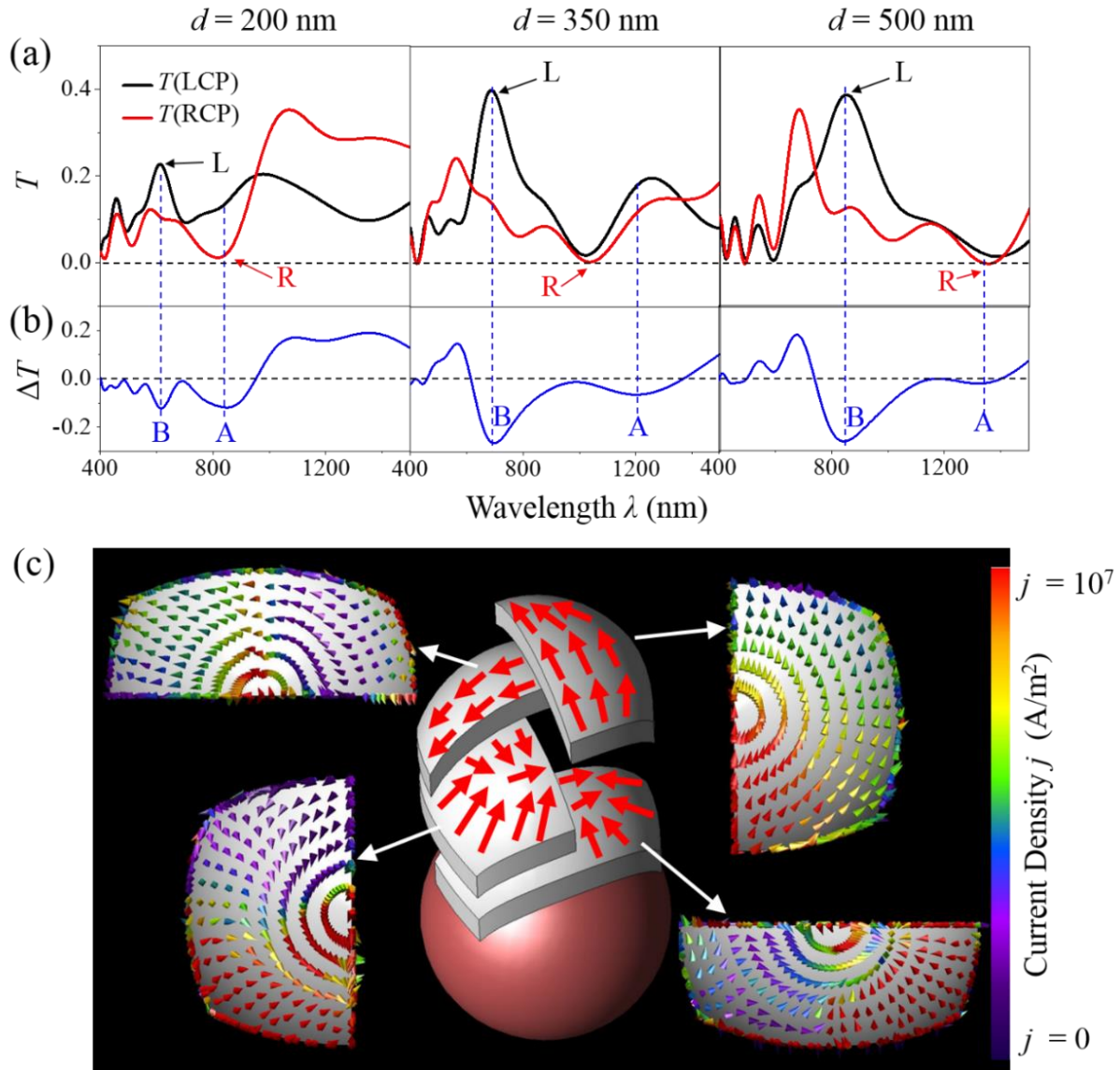


**Figure 4.2.8.** (a) The simulated circular polarized transmittance spectra, and (b) the simulated  $\Delta T$  spectra of LH-HSPLs on  $d = 200, 350,$  and  $500$  nm beads, with  $\varphi_0 = 0^\circ$ . (c) The near-field current distribution at the wavelength corresponding with “R”. An illustration of current flow is shown in the middle, and the current density distributions on Ag layers exported from XFDTD software are shown on left and right sides.

#### 4.2.5 Helically stacked plasmonic layers: conclusion and future work

In conclusion, large-area 3D chiral plasmonic nanostructures, HSPLs, have been fabricated by a series of Ag and SiO<sub>2</sub> depositions on the nanosphere monolayers. Ag and SiO<sub>2</sub> layers are helically stacked to form LH- and RH-HSPLs, which is realized by the azimuthal rotation of substrates

between depositions. In visible to near-IR region, HSPLs exhibit localized surface plasmon resonances and strong chiral optical responses. The most important feature of HSPLs is the great tunability of chiral optical spectra. By increasing the nanosphere diameter, the HSPL structure can be scaled up and the spectral features of the chiral optical response redshifts from visible to near-IR region without a significant change in magnitude. Another important feature of HSPLs is the capability for large-scale fabrication, even on polycrystalline monolayers. HSPLs may have different morphologies in different domains, but share very similar chiral optical response due to the same chirality. This minor limitation can be overcome by a swing rotation of the substrate during depositions. In each deposition, the substrate will not be static, and instead will be rotated back and forth with an angular magnitude of  $90^\circ$ , which leads to a crescent-shaped nanostructure on each nanosphere, as shown in **Figure 4.2.9a**. With the other fabrication conditions unchanged, the resulted HSPLs will have a circular shape, which does not vary with the monolayer orientations as shown in **Figure 4.2.9b**. However, the circular HSPLs show weaker CD response than the rectangular HSPLs, as shown in **Figure 4.2.9c**. With the same QCM thickness, the swing rotation may decrease the actual thickness of each layer by increasing the deposition area. The reduced

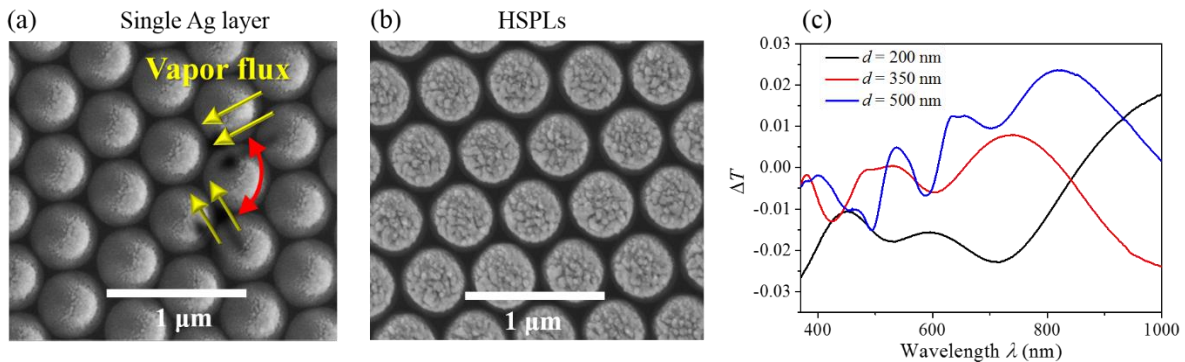


**Figure 4.2.9.** (a) The top-view SEM image of a single Ag layer made by DSG with a swing rotation of the substrate. (b) The top-view SEM image of the obtained HSPLs prepared by DSG with a swing rotation of the substrate. (c) The  $\Delta T$  spectra of LH-HSPLs on  $d = 200, 350,$  and  $500$  nm nanospheres, prepared by DSG with a swing rotation of the substrate.

thickness probably leads to weaker CD response. The future work will be focused on the optimization of the circular HSPLs.

### **4.3 Swiss roll metamaterial**

Chiral metamaterial was first proposed as a different and easier way to achieve negative refraction by Pendry in 2004.[26] In this seminal publication, Swiss roll structure, which is constructed by a thin insulated conducting sheet helically wound around a dielectric mandrel was introduced and served as the model structure for theoretical analysis due to its ideal chirality.[140, 141] Since then, the Swiss roll structure has been investigated as a chiral metamaterial in radio frequency (RF) region.[27, 28] For example, the Swiss roll structure in millimeter scale exhibits strong magnetic response, which has been utilized to realize RF flux guiding.[142, 143] Furthermore, the effective permeability of the Swiss roll structure has been demonstrated to be strongly negative at resonant frequency.[144] The negative permeability enables the Swiss roll structure to work as a super lens to realize the sub-wavelength imaging in RF region.[145] Finally, in experimental support of Pendry's theoretical insight, the negative refraction of Swiss roll structures has been realized in RF region.[146] In order to achieve the Swiss roll metamaterials in the highly important optical frequency region, the dimension of the Swiss roll structure has to be reduced to be in nanometer scale, which is a great challenge for fabrication. The most common method to fabricate rolled-up nanostructures relies on strain-induced self-rolling technique.[147, 148] In this technique, thin films are deposited on a sacrificial layer first, which is then removed, causing the thin films to minimize the strain energy. The thin films will bend into a curved structure if the strain gradient is large.[147, 148] So far, only one group reported the fabrication of Swiss roll microstructure with optical and near-IR response using this technique.[149-151] This Swiss roll microstructure was

demonstrated to have a tunable plasma frequency and could be potentially applied for sub-wavelength imaging.[149, 150] By drilling holes on this Swiss roll structure, three-dimensional fishnet structure was created to realize negative refraction in near-IR region.[151] While these results are impressive, additional fabrication techniques are needed to further investigate the potential of this remarkable structure. Here we apply the DSG based helically-stacking strategy for the fabrication of Swiss roll nanostructures.

#### **4.3.1 Swiss roll metamaterial: fabrication**

The fabrication procedure of Swiss roll metamaterial is illustrated in **Figure 4.3.1**. Two types of monolayers are prepared with different bead diameter  $d = 350$  and  $500$  nm on pre-cleaned glass and Si substrates, and are loaded in a custom vacuum deposition system (Pascal Technology). Before deposition, the chamber is evacuated to a base pressure of  $1 \times 10^{-6}$  Torr, and the background pressure during depositions is maintained at less than  $5 \times 10^{-6}$  Torr. Ag (99.999%, Kurt J. Lesker) and SiO<sub>2</sub> (99.99%, International Advanced Materials) are used in depositions. The vapor flux is incident upon the substrates at a polar angle  $\theta$  and an azimuthal angle  $\varphi$  during depositions, as defined in **Figure 4.3.1**①. Then, SiO<sub>2</sub> is deposited on monolayers at a deposition rate of  $0.2$  nm/s with  $\theta = 87^\circ$  and  $\varphi = \omega_s T$ , where  $\omega_s$  is the substrate azimuthal rotation speed,  $\omega_s = 5$  rpm and  $T$  is time. The SiO<sub>2</sub> deposition ends with a QCM thickness of  $350$  nm and  $500$  nm for  $d = 350$  nm and  $d = 500$  nm beads, respectively. As a result, a SiO<sub>2</sub> frustum is formed on each bead, which acts as the mandrel to support Swiss roll as shown in **Figure 4.3.1**③. Next, Ag and SiO<sub>2</sub> are deposited alternately at a deposition rate of  $0.02$  nm/s with  $\theta = 70^\circ$ . During each deposition, the substrate is rotated azimuthally back and forth so that  $\varphi$  sweeps between  $\varphi_c - 45^\circ$  and  $\varphi_c + 45^\circ$ , where  $\varphi_c$  is the central azimuthal angle of a swing rotation.[152] Each deposition ends with a QCM thickness

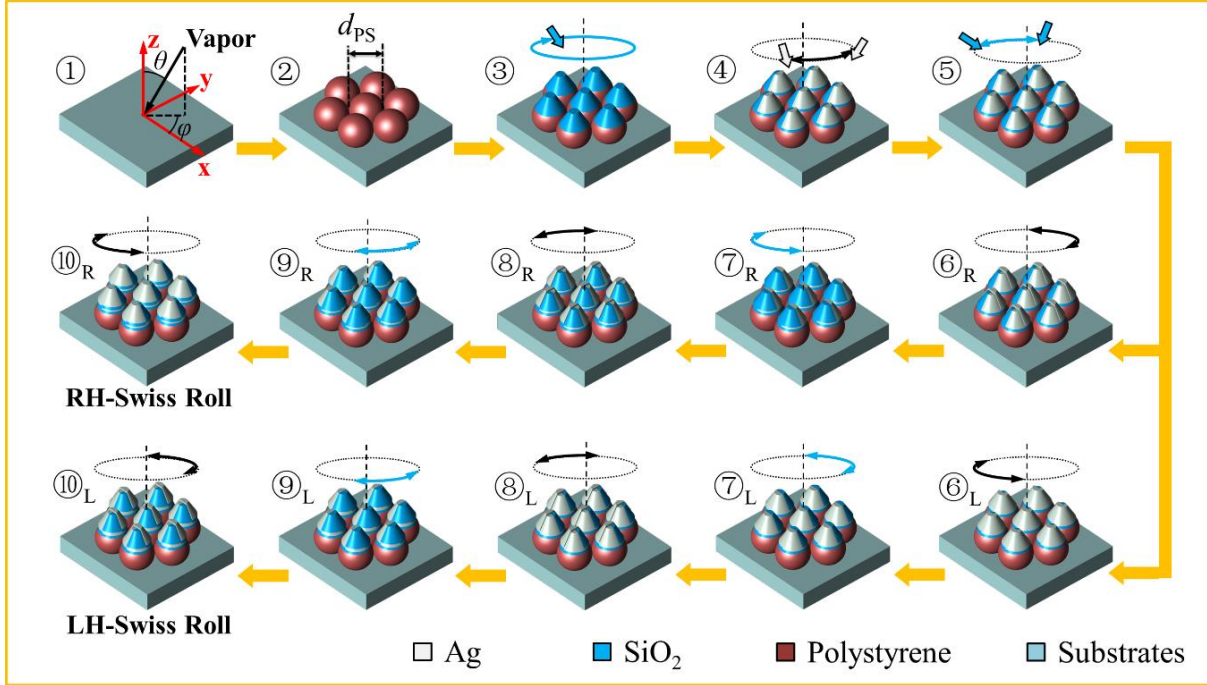


**Figure 4.3.1.** Schematics of the fabrication procedure of RH- and LH-conical Swiss roll nanostructures. The fabrication includes 10 steps: (1) preparation of substrates, (2) preparation of colloidal monolayers, and depositions of (3) SiO<sub>2</sub> frustum, (4), (6<sub>R</sub>), (6<sub>L</sub>), (8<sub>R</sub>), (8<sub>L</sub>), (10<sub>R</sub>), (10<sub>L</sub>) Ag side-coatings, and (5), (7<sub>R</sub>), (7<sub>L</sub>), (9<sub>R</sub>), (9<sub>L</sub>) SiO<sub>2</sub> side-coatings. The black and blue arcs with arrows indicate how the vapor direction rotates with respect to the substrate.

of 40 nm and results in a thin film mainly side-coated on half of the frustum. By controlling  $\varphi_c$  for each deposition, Ag films can be helically stacked and wrapped around the SiO<sub>2</sub> mandrel with SiO<sub>2</sub> film as the insulated layer, in both right handed (RH) or left handed (LH) fashions, as shown in (4)-(10<sub>R</sub>) and (4)-(10<sub>L</sub>) of **Figure 4.3.1**, respectively. Each deposition can be described by its material and  $\varphi_c$  as (4) Ag,  $\varphi_c = 0^\circ$ ; (5) SiO<sub>2</sub>,  $\varphi_c = 180^\circ$ ; (6<sub>R</sub>) Ag,  $\varphi_c = 90^\circ$ ; (6<sub>L</sub>) Ag,  $\varphi_c = -90^\circ$ ; (7<sub>R</sub>) SiO<sub>2</sub>,  $\varphi_c = -90^\circ$ ; (7<sub>L</sub>) SiO<sub>2</sub>,  $\varphi_c = 90^\circ$ ; (8<sub>R</sub>) and (8<sub>L</sub>) Ag,  $\varphi_c = 180^\circ$ ; (9<sub>R</sub>) and (9<sub>L</sub>) SiO<sub>2</sub>,  $\varphi_c = 0^\circ$ ; (10<sub>R</sub>) Ag,  $\varphi_c = -90^\circ$ ; (10<sub>L</sub>) Ag,  $\varphi_c = 90^\circ$ . Finally, Ag films are all connected forming a one-turn conical Swiss roll structure. The Ag and SiO<sub>2</sub> depositions can be continued to fabricate Swiss roll nanostructures with more turns. The fabrication of Swiss roll structures employs the helically-stacking strategy, which is similar to that of HSPLs. The main difference in fabrication between

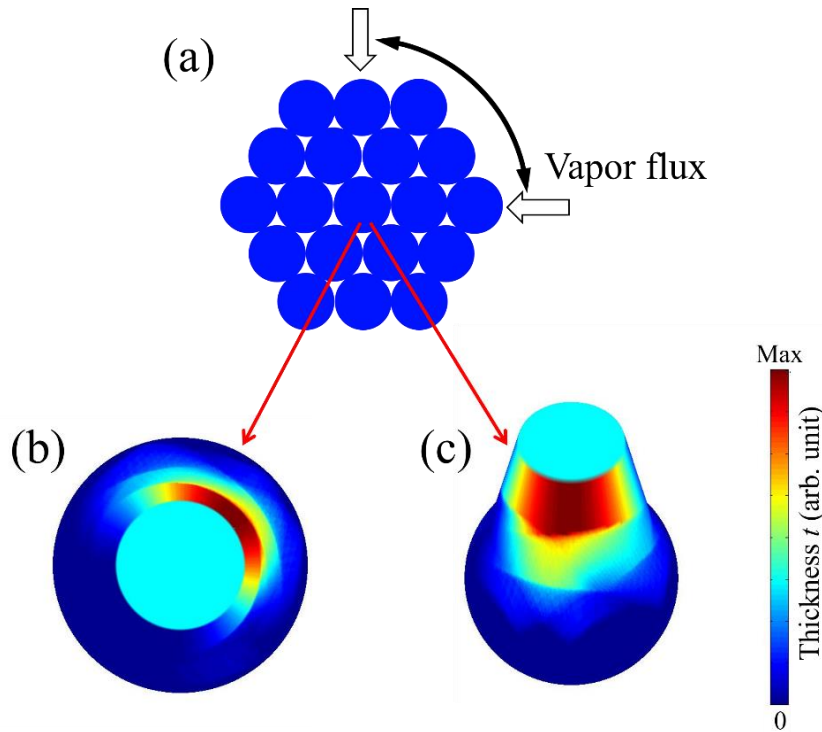


**Figure 4.3.2.** (a) A swing deposition of Ag on an array of SiO<sub>2</sub> frustums on monolayers. (b) Top-view and (c) tilted-view image of the simulated thickness distribution on the SiO<sub>2</sub> frustum and the bead.

Swiss roll and HSPL is the deposition template. The Swiss roll requires a SiO<sub>2</sub> frustum on nanosphere, while HSPL does not. Section 4.2.5 describes a way to overcome the effect of monolayer orientations for HSPLs by a swing rotation of substrates during depositions, which is also applied in the fabrication of Swiss roll structures. A morphology simulation has been performed to simulate the thin film distribution on the SiO<sub>2</sub> frustum in one swing deposition, as shown in **Figure 4.3.2**. The simulation results confirm that the thin film is mainly coated on half of the SiO<sub>2</sub> frustum and has a rounded edge, which will minimize the effect of the monolayer orientations.

#### 4.3.2 Swiss roll metamaterial: morphology

The morphology of Swiss roll nanostructures has been investigated. The SEM and TEM images of Swiss roll nanostructures on  $d = 500$  nm monolayers at different fabrication steps are shown in **Figure 4.3.3**. **Figures 4.3.3a** and **4.3.3b** show the top and cross-section SEM images of Swiss roll nanostructures at fabrication step ③, respectively, which confirms the formation of SiO<sub>2</sub> frustums. The SiO<sub>2</sub> frustums have the top diameter  $d_T$ , the bottom diameter  $d_B$ , and the height  $h_F$ . The side and top surfaces of SiO<sub>2</sub> frustum are rough due to the nature of DSG. The surface roughness can be minimized by create the frustum using other techniques, such as reactive-ion etching.[153] The top and cross-section SEM images of Swiss roll structures with only one Ag layer at fabrication step ④ are shown in **Figures 4.3.3c** and **4.3.3d**, respectively. As expected, half of the SiO<sub>2</sub> frustum and part of beads is coated by Ag films, which have rounded edges. The height of Ag layer is  $h_{\text{layer}}$ . The surface of Ag films is also not smooth, which originates from the rough surface of SiO<sub>2</sub> frustum. **Figures 4.3.3e** and **4.3.3f** show the top and cross-section SEM images of Swiss roll nanostructures at fabrication step ⑩<sub>L</sub>. The obtained Swiss roll nanostructures have a cylinder shape with diameter  $d_{\text{SR}}$  and height  $h_{\text{SR}}$ . In the top-view image, the Swiss roll nanostructure has a circular shape, which indicates no significant change in morphology across different monolayer domains, which benefits from the azimuthal swing of substrates during depositions. All the structural parameters  $d$ ,  $d_T$ ,  $d_B$ ,  $h_F$ ,  $h_{\text{layer}}$ ,  $d_{\text{SR}}$ , and  $h_{\text{SR}}$  are listed in **Table 4.3.1**. Obviously, a larger bead diameter  $d$  leads to larger Swiss roll diameter  $d_{\text{SR}}$ , which indicates the diameter of Swiss roll can be easily tuned by adjusting the size of beads. The insets in **Figures 4.3.3b**, **4.3.3d**, and **4.3.3f** show the schematics of the corresponding structures. After each layer is deposited, the structure grows taller, which leads to a small vertical upward displacement of the next layer due to shadowing effect. Therefore, Ag and SiO<sub>2</sub> layers are stacked helically on the side of the SiO<sub>2</sub> frustum to form the chiral conical Swiss roll nanostructures as illustrated in **Figure 4.3.3g**. **Figure**

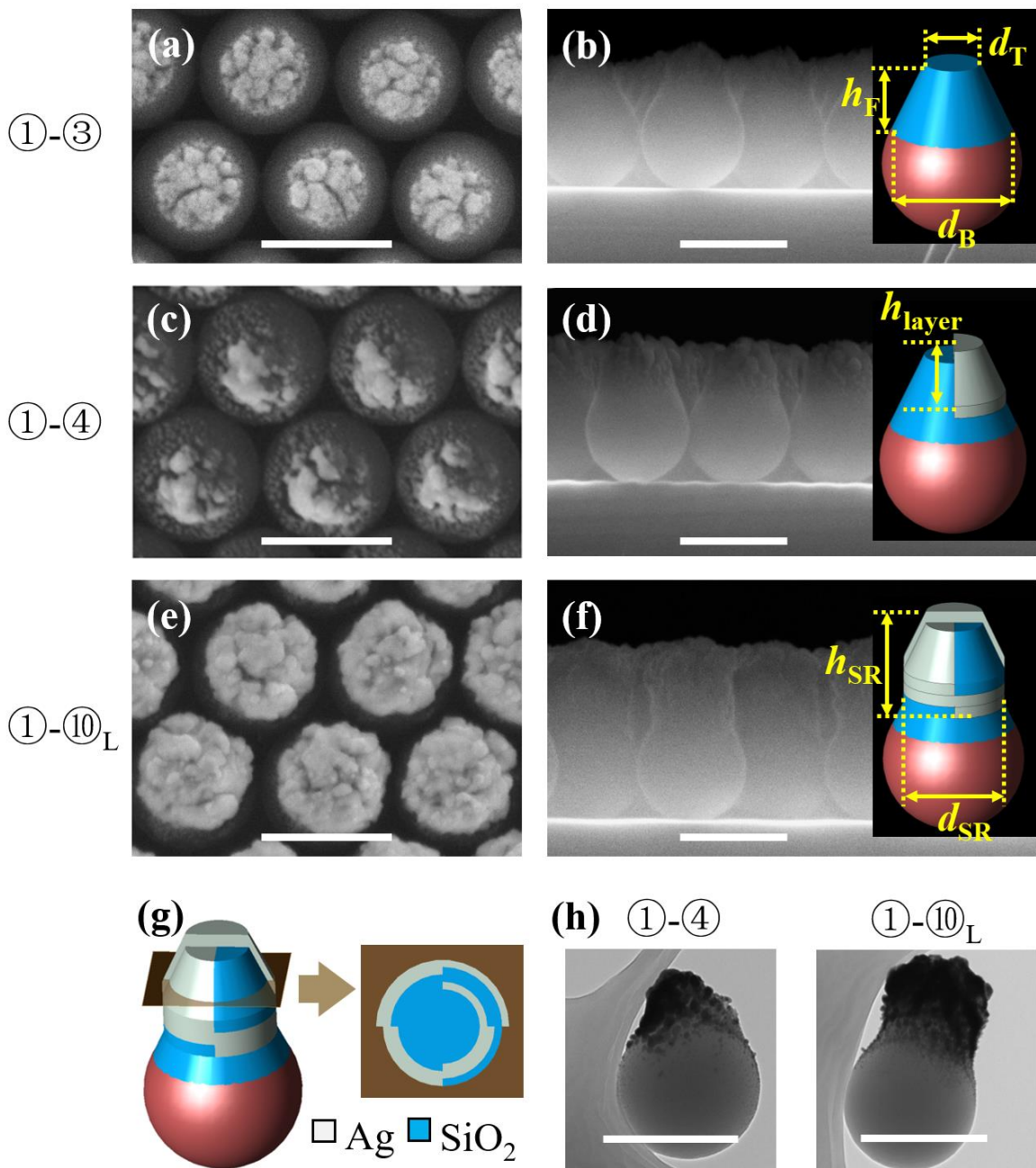


**Figure 4.3.3.** (a) Top-view and (b) cross-sectional SEM images of SiO<sub>2</sub> frustums on colloidal monolayers, corresponding to the structure at step ③. (c) Top-view and (d) cross-sectional SEM images of one Ag layer on each SiO<sub>2</sub> frustum, corresponding to the structure at step ④. (e) Top-view and (f) cross-sectional SEM images of LH-Swiss roll nanostructures, corresponding to the structure at step ⑩<sub>L</sub>. (g) TEM images of LH-Swiss roll nanostructures, corresponding to the structure at steps ④ and ⑩<sub>L</sub>. (h) Schematic of a Swiss roll structure. The scale bar in each SEM image represents 500 nm. The insets in (b), (d), and (f) show the schematics of the corresponding structures.

**Table 4.3.1.** Structural parameters of Swiss roll nanostructures

Bead diameter $d$ (nm)	Frustum top diameter $D_T$ (nm)	Frustum bottom diameter $D_B$ (nm)	Frustum height $h_F$ (nm)	One layer height $h_{\text{layer}}$ (nm)	Ag Swiss roll diameter $D_{\text{SR}}$ (nm)	Swiss roll height $h_{\text{SR}}$ (nm)
350	$170 \pm 10$	$300 \pm 20$	$180 \pm 20$	$150 \pm 20$	$261 \pm 8$	$280 \pm 20$
500	$290 \pm 20$	$430 \pm 30$	$300 \pm 30$	$250 \pm 20$	$390 \pm 10$	$400 \pm 30$

**4.3.3h** shows the TEM images of Swiss roll nanostructure at fabrication step ④ and ⑩<sub>L</sub>, which clearly confirm that the desired Swiss roll structures are created.

### 4.3.3 Swiss roll metamaterial: optical property

The optical properties of Swiss roll nanostructures are characterized by both unpolarized transmittance spectroscopy at normal incidence of light. The dashed lines in **Figures 4.3.4a** and **4.3.4b** show the unpolarized transmittance spectra  $T$  of both RH- and LH-Swiss roll nanostructures on  $d = 350$  and  $500$  nm beads, respectively. No significant difference in unpolarized transmittance between LH- and RH-Swiss roll nanostructures is observed, which is expected from their structural similarity but not the chirality. A broad transmittance valley appears in each spectrum around  $\lambda = 800$  nm for  $d = 350$  nm and around  $\lambda = 1200$  nm for  $d = 500$  nm, respectively, as labeled by the blue arrows in **Figure 4.3.4**. This transmittance valley corresponds to the effective excitation of localized surface plasmon resonance (LSPR) of Ag films. As  $d_{\text{PS}}$  increases, the lateral size of Ag films increases, leading to a redshift of LSPR wavelength, which agrees with the LSPR theory.

Due to the geometric chirality, the Swiss roll nanostructures are expected to exhibit CD response. In order to characterize the CD response of Swiss roll nanostructures, the transmittance difference between RCP and LCP light,  $\Delta T = T(\text{RCP}) - T(\text{LCP})$ , are measured by a spectroscopic

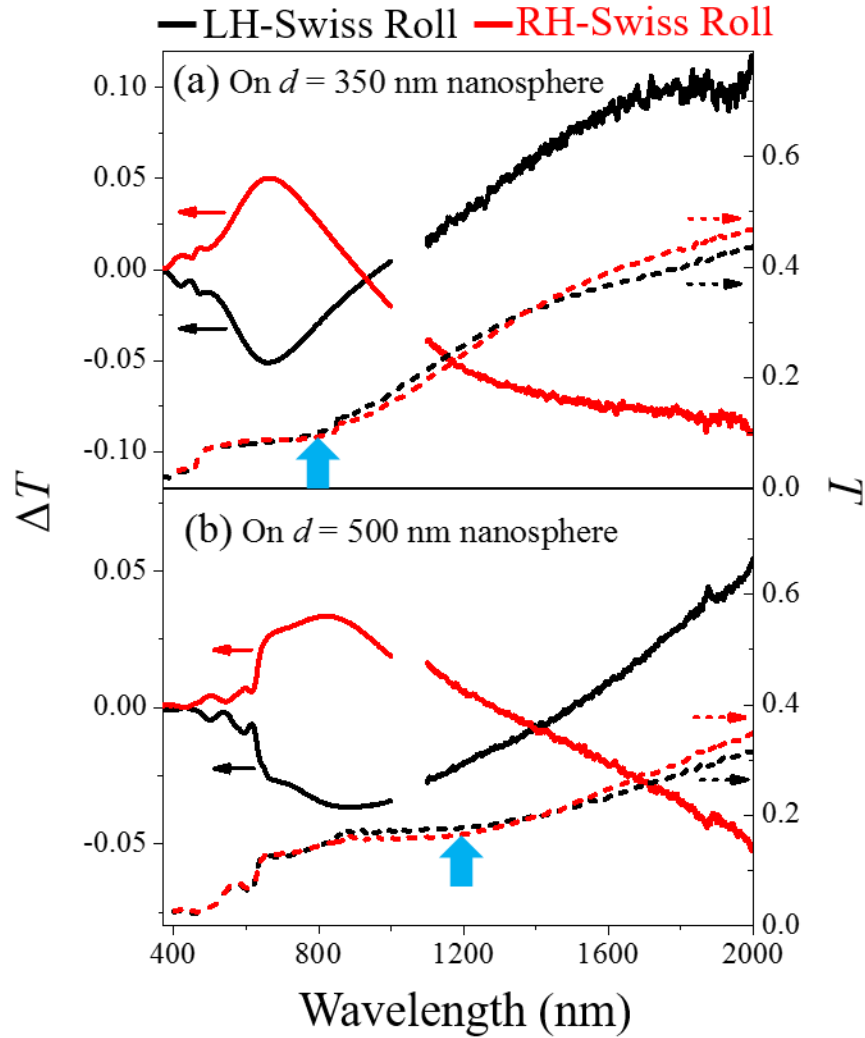


**Figure 4.3.4.** Circularly polarized differential transmittance spectra  $\Delta T$  (solid lines) and unpolarized transmittance spectra  $T$  (dashed lines) of Swiss roll nanostructures on (a)  $d = 350$  nm beads, and (b)  $d = 500$  nm beads.

ellipsometer (M-2000, J. A. Woollam, Inc.,  $\lambda = 370\text{--}1000$  nm) and UV-vis-IR double beam spectrophotometer (JASCO V-570,  $\lambda = 1100\text{--}2000$  nm) equipped with a Glan Thompson polarizer (Thorlabs Inc.) and an achromatic quarter wave plate (Thorlabs, Inc). The solid curves in Figures 4.3.4a and 4.3.4b show the measured  $\Delta T$  spectra. As expected, the CD response of LH- and RH-Swiss roll nanostructures exhibit good symmetry. For LH-Swiss roll on  $d = 350$  nm beads,  $\Delta T$  has a broad negative peak in wavelength range  $\lambda = 370\text{--}940$  nm with a peak magnitude of 5% around

$\lambda = 660$  nm, and becomes positive in wavelength range  $\lambda = 940\text{--}2000$  nm with a maximum magnitude of 10% around  $\lambda = 2000$  nm. The CD response is reversed for RH-Swiss roll on  $d = 350$  nm beads. As  $d$  increases to 500 nm, the  $\Delta T$  spectra redshift with a reduced magnitude. For Swiss rolls on  $d = 500$  nm beads,  $\Delta T$  has a broad peak in wavelength range  $\lambda = 370\text{--}1400$  nm with a peak magnitude of 3.5% around  $\lambda = 860$  nm, changes the sign above  $\lambda = 1400$  nm, and reaches a magnitude of 5% at  $\lambda = 2000$  nm. The redshift of  $\Delta T$  spectra with increasing  $d$  is believed to originate from the redshift of LSPR wavelength. The strong chiral optical response of the Swiss roll nanostructures validates Pendry's prediction.

#### **4.3.4 Swiss roll metamaterial: FDTD simulation**

FDTD simulations are performed to confirm the chiral optical response of the Swiss roll nanostructures. RH-Swiss roll on  $d = 350$  nm and 500 nm beads are selected for simulations (see Section 2.7 for the details of FDTD simulations). **Figure 4.3.5a** shows the geometric model of the RH-Swiss roll on  $d = 350$  nm beads. The geometric models have the same structural parameters as listed in **Table 4.3.1**. Each Ag or SiO<sub>2</sub> side-coated layer is assumed to be uniform with a constant vertical thickness  $t_{\text{layer}}$  of 30 nm. **Figures 4.3.5b** and **4.3.5c** show the simulated circularly polarized transmittance spectra for Swiss rolls on  $d = 350$  and 500 nm beads, respectively. Two resonances appear in each simulated transmittance spectrum. One resonance occurs at  $\lambda = 1600$  nm, which leads to an intense negative peak in the simulated  $\Delta T$  spectrum, as shown in **Figure 4.3.5d**. The other resonance occurs around  $\lambda = 1000$  nm, which leads to a positive peak in the simulated  $\Delta T$  spectrum. The simulated  $\Delta T$  spectrum redshifts as the bead diameter increases from 350 nm to 500 nm. Compared with the measured  $\Delta T$  spectrum, the simulated one has larger peak magnitude, different peak wavelength, and sharper peaks. This is because the coated films in

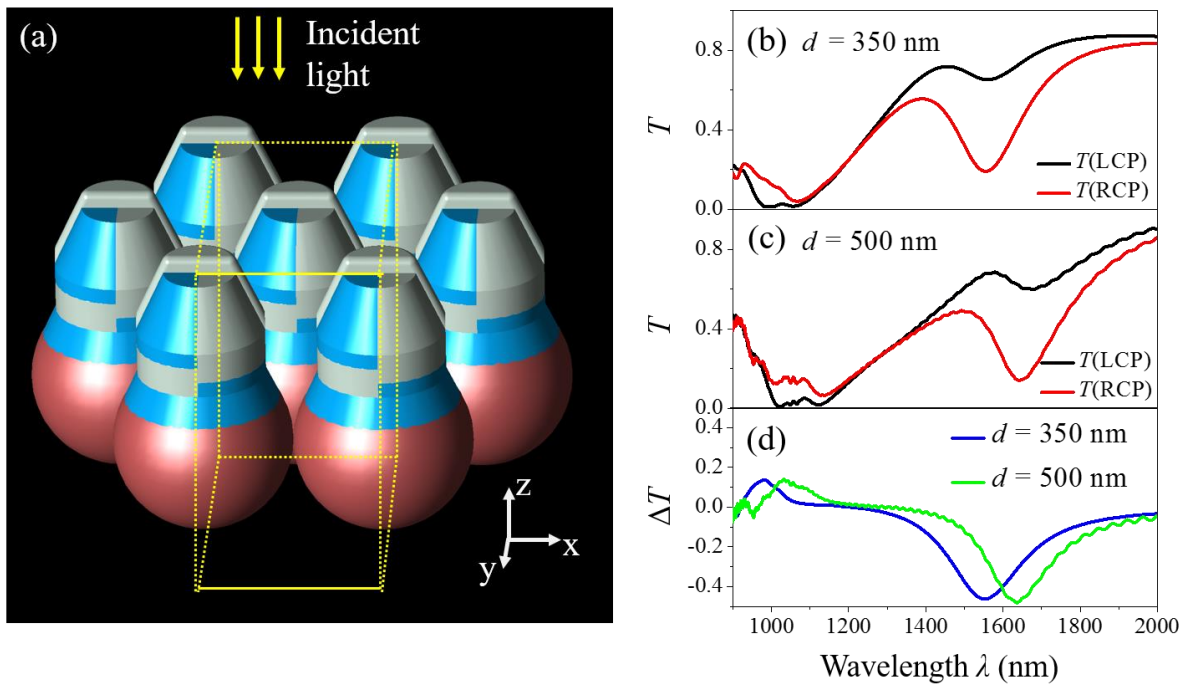


**Figure 4.3.5.** (a) Geometric model of RH-Swiss roll on  $d = 350$  nm beads. The yellow box illustrates one unit cell of Swiss roll arrays, with absorbing boundary condition for top and bottom sides, and periodic boundary condition for other sides. The simulated  $T(\text{LCP})$  and  $T(\text{RCP})$  spectra for Swiss roll nanostructures on (b)  $d = 350$  nm, and (c)  $d = 500$  nm beads. (d)  $\Delta T$  spectra for Swiss roll nanostructures on  $d = 350$  and  $d = 500$  nm beads.

FDTD simulations are simply assumed to be smooth and uniform, while the actual films have rough surface and non-uniform thickness distribution. However, the FDTD simulation still successfully reproduces the main experimental feature of Swiss roll nanostructure's CD response.

#### 4.3.5 Swiss roll metamaterial: conclusion

In conclusion, the helically-stacking strategy based on DSG has been applied to fabricate large-scale chiral Swiss roll nanostructures. Ag films are helically stacked on a  $\text{SiO}_2$  frustum with  $\text{SiO}_2$  films as insulated layers forming a chiral conical Swiss roll nanostructure. The diameter of the Swiss rolls can be easily controlled by adjusting the bead diameter. The morphology of the Swiss rolls does not strongly depend on the orientations of monolayer domains, which leads to a very

uniform array of the Swiss roll structures. The fabricated conical Swiss roll nanostructures exhibit strong chirality as predicted by Pendry,[26] which is characterized by CD spectroscopy. By making the bead diameter a few hundred nanometers, broadband CD response in visible to near-IR region is achieved. The CD spectral feature can be tuned by changing the bead diameter. As the bead diameter increases, the LSPR of Ag films redshifts, resulting in a redshift of CD spectrum. With the great advantage in scalable fabrication and tunability in structural size, this DSG based method can serve as a general technique to fabricate Swiss roll nanostructures for different applications.

#### **4.4 Conclusion**

In summary, a DSG based fabrication strategy for chiral metamaterials has been described and demonstrated by the success in preparing two chiral metamaterials, HSPLs and Swiss roll structures. This strategy relies on a series of vapor depositions alternated between metal and dielectric material at a large incident angle onto SACMs based templates, and the manipulation of the azimuthal rotation of the substrate between depositions. As a result, thin film layers of metal and dielectric material can be helically stacked on the SACMs, forming one metallic and one dielectric helical-shaped structures twisted together. The metallic helical structures interact with light and generate chiral optical response due to its geometric chirality, and the dielectric helical structures serve as support for the metallic helical structures. The fabricated chiral nanostructures can exhibit strong chiral optical response with great tunability, as demonstrated in Sections 4.2 and 4.3. The size of the chiral nanostructures can be tuned by adjusting the diameter of the colloid beads, which leads to the spectrum shift of the chiral nanostructures. This fabrication strategy not only allows scalable fabrication, but also can create uniform arrays of chiral nanostructures with

polycrystalline monolayers. It should be noted that the morphology of structures created by oblique angle depositions on pre-patterned templates usually depend on the relative azimuthal orientation of vapors with respect to the domains, which leads to different structures on different domains.[118, 131, 154] The monolayer orientation effect limits the uniformity in optical response of chiral metamaterials prepared by DSG on polycrystalline monolayers. This effect has been overcome by the helically-stacking fabrication strategy for two mechanisms: first, the structures on different monolayer domains share the same chirality, which is determined by the substrate rotation between depositions; second, a swing rotation during depositions can minimize the difference in structural morphology among different monolayer domains. Therefore, benefited from this strategy, chiral metamaterials with strong, uniform, and tunable chiral optical response can be realized in large scale, even on polycrystalline monolayers.

## CHAPTER 5

### CHIRAL METAMATERIAL BASED OPTICAL DEVICES

#### 5.1 Introduction

Born in the exploration of negative refraction, chiral metamaterials have evolved with some novel functionalities, such as manipulating polarizations of light, detecting circular polarizations, enantiomer sensing, tunable and nonlinear chiral optical response. In Section 1.4, we have briefly reviewed the current status of chiral metamaterial based optical devices. Although promising applications have been demonstrated with chiral optical devices, their fabrication techniques keep them away from the industrial production due to the poor scalability. Currently, most chiral metamaterial based optical devices are prepared by top-down methods, such as EBL and DLW, which have very low throughput leading to a small area of devices ( $< 1 \text{ mm}^2$ ). In this chapter, we demonstrate that our DSG based fabrication method can produce large-area chiral metamaterials ( $\sim 1 \text{ cm}^2$ ). Furthermore, the fabricated chiral metamaterial can be developed as an active chiral optical device with tunable optical response by being transferred into a flexible substrate and as a LSPR sensor with an enhanced sensitivity.

#### 5.2 Large-area chiral optical device

DSG has great advantage in large-scale fabrication, and is thus suitable for optical device fabrication in industry. However, the nanostructures fabricated by DSG on nanosphere monolayers

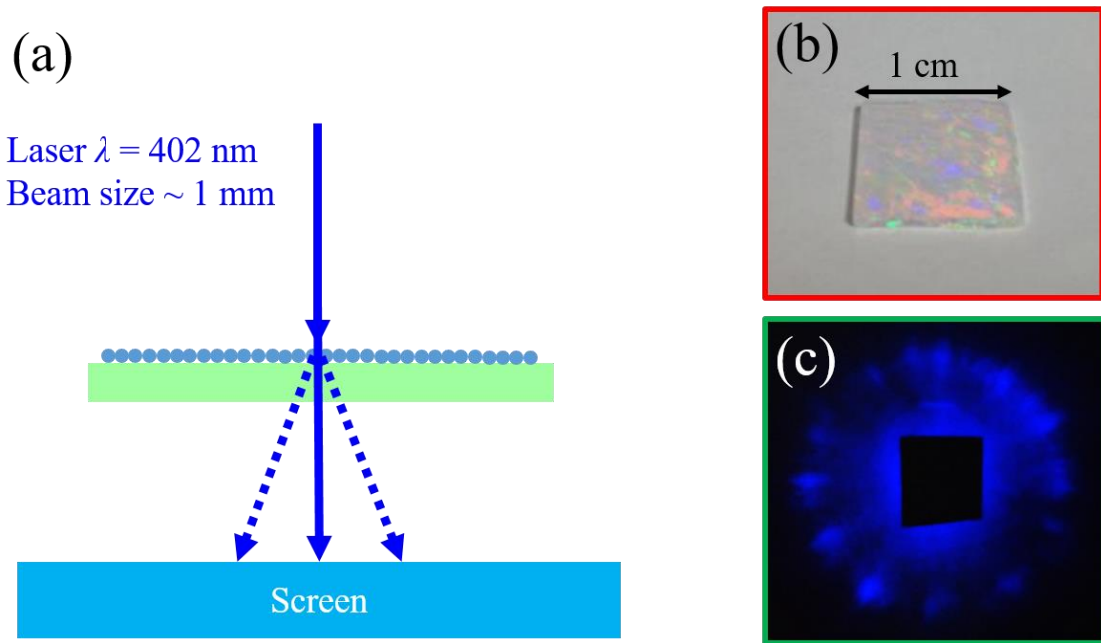


**Figure 5.2.1.** (a) Schematic of the laser diffraction of the self-assembled colloidal monolayer. (b) The photograph of a 1 cm<sup>2</sup> polycrystalline monolayer on a glass substrate. (c) Laser diffraction pattern of the polycrystalline monolayer.

have a unique feature: their morphology strongly depends on the relative orientation of the monolayer with respect to the incident vapor flux, which leads to poor uniformity of chiral metamaterials fabricated on polycrystalline monolayers. A strategy by employing swing rotation of substrates in DSG process has been implemented to overcome such an effect (see Section 4.2.5), but this strategy cannot be applied for the fabrication of all chiral structures, for example, fan-shaped nanostructures. Another way to obtain highly uniform chiral substrates is to use a large-area monocrystalline monolayer as the deposition template for DSG, which has nanospheres aligned in the same orientation across the whole substrate, leading to good uniformity of the fabricated chiral nanostructure arrays. Therefore, preparing monocrystalline monolayers is an important step in developing chiral metamaterials to chiral optical devices.

We fabricate the monocrystalline monolayers with an area of about 1 cm<sup>2</sup>, whose quality is examined by the laser diffraction experiment (see **Figure 5.2.1a**). The diffraction pattern can be

used to determine whether the illuminated area has a monocrystalline or polycrystalline monolayer. For the hexagonally packed monolayers, a diffraction pattern of six hexagonally arranged bright dots indicates a monocrystalline monolayer, while a diffraction pattern of many blur dots forming a ring indicates a polycrystalline monolayer. In addition, the diffraction pattern can be used to determine the monolayer orientation for the monocrystalline monolayers. If the diffraction patterns at two different spots appear to be in the same orientation, then they have the same monolayer orientation. In the laser diffraction experiment, the monolayer is illuminated normally by a laser beam at wavelength of 402 nm with a spot size of 1 mm. **Figures 5.2.1b** and

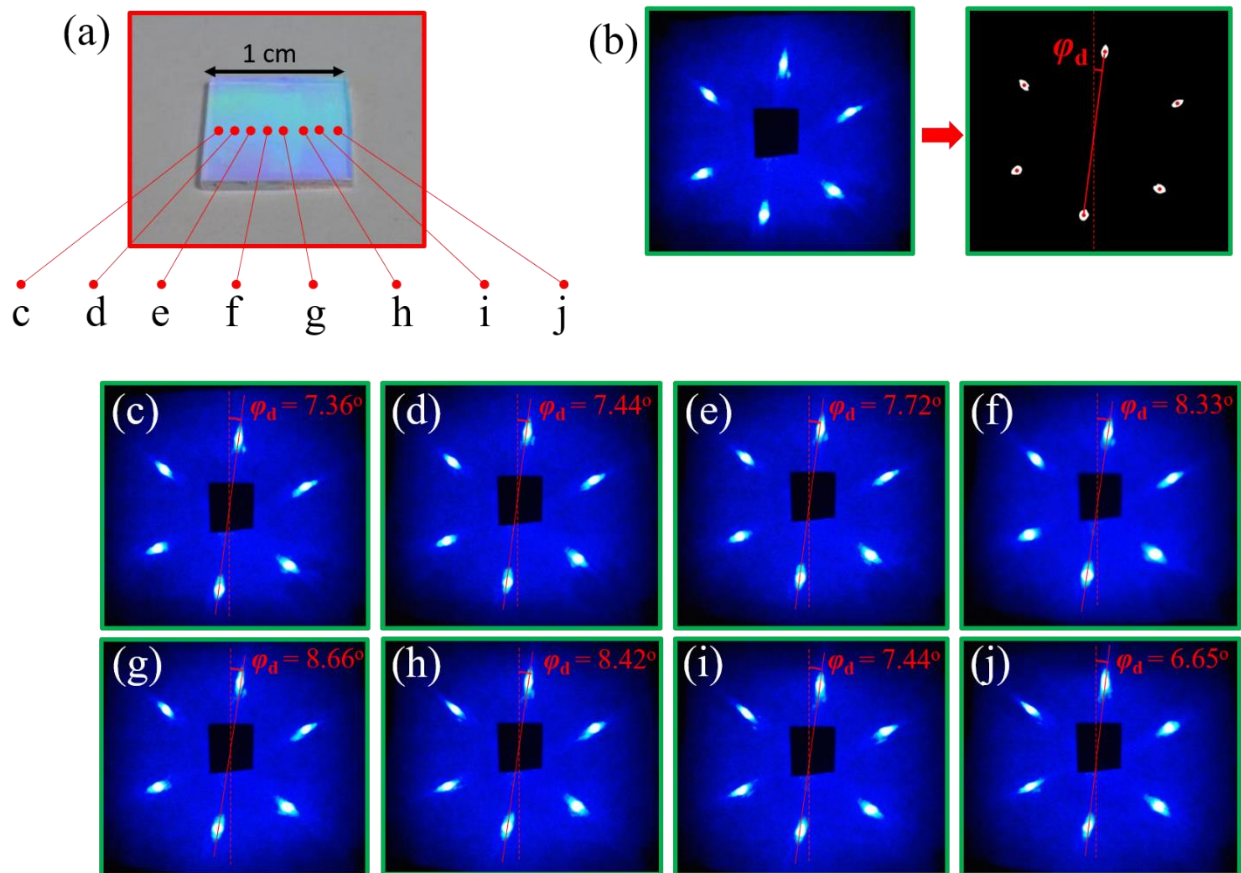


**Figure 5.2.2.** (a) The photograph of a 1 cm<sup>2</sup> monocrystalline monolayer on a glass substrate. (b) Laser diffraction pattern of the monocrystalline monolayer, and determination of  $\varphi_d$ . (c)-(j) Laser diffraction patterns of the monocrystalline monolayer, recorded every 1 mm across the substrate, with the measuring spot shown in (a).

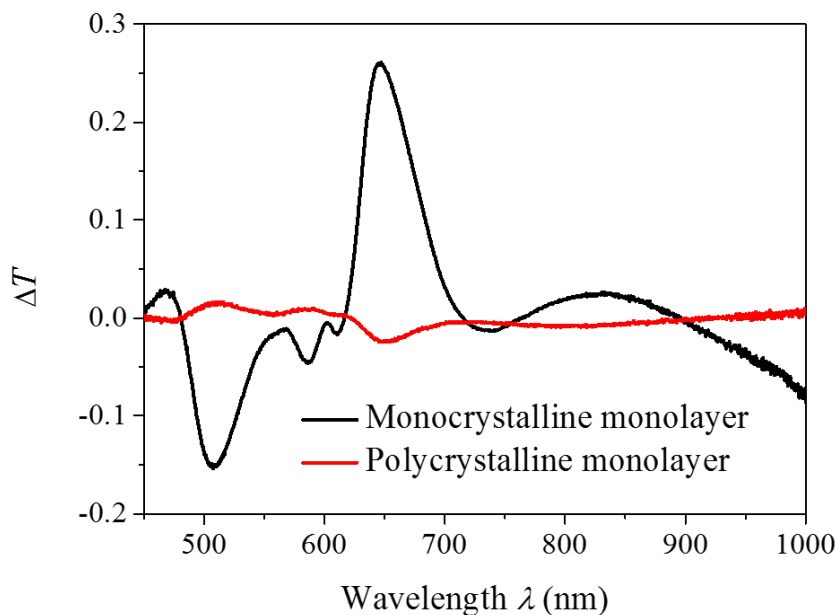


**Figure 5.2.3.**  $\Delta T$  spectra of Ag fan-shaped nanostructures on a  $1 \text{ cm}^2$  monocrystalline monolayer and patchy films on a  $1 \text{ cm}^2$  polycrystalline monolayer, measured by the spectroscopic microscope with a beam diameter  $\sim 5 \text{ mm}$ .

**5.2.1c** show a polycrystalline monolayer on a glass substrate and its diffraction pattern with zero-order transmission blocked, respectively. The diffraction pattern with many blur dots, which almost merge to form a ring, indicates multiple small domains in different orientations within the illuminated area. The monocrystalline monolayer and its diffraction pattern are shown in **Figures 5.2.2a** and **5.2.2b**, respectively. The diffraction pattern with 6 sharp and bright dots, which form a hexagonal shape, indicating a single domain within the illuminated area. In order to characterize the orientation of diffraction patterns, an azimuthal angle  $\varphi_d$  is defined as shown in **Figure 5.2.2b**. In order to determine  $\varphi_d$ , the diffraction pattern was converted into grayscale, and the centroid position of each dot is calculated by only considering the brightest pixels (intensity = 255). To characterize the uniformity of the monocrystalline monolayer, the laser diffraction patterns are recorded every 1 mm across the substrate, as shown in **Figures 5.2.2c–j**.  $\varphi_d$  exhibits a fluctuation of about  $2^\circ$ , which indicates a good long-range ordering.

With such a high-quality monocrystalline monolayer, the optimized Ag fan-shaped chiral nanostructures ( $\theta = 84^\circ$ ,  $\varphi_0 = 53^\circ$ ,  $t_{\text{QCM}} = 4 \times 30 \text{ nm}$ ) can be realized in an area of at least  $1 \text{ cm}^2$ , by carefully aligning the monolayer in the deposition system. **Figure 5.2.3** shows the measured  $\Delta T$  spectrum of the large-area Ag fan-shaped nanostructures on monocrystalline monolayers, as well as that of the patchy films on polycrystalline monolayers for comparison. It should be noted that the optical measurement was performed with a large beam diameter  $\sim 5 \text{ mm}$ . As expected, the obtained  $1 \text{ cm}^2$  monocrystalline sample exhibits similar CD response as that of the individual domain shown in **Figure 3.4.2c**, but with a smaller measured  $\Delta T$  magnitude probably due to the fluctuation of  $\varphi_0$  and monolayer defects. Further optimization of the fabrication is still needed to improve the quality of the chiral substrates, such as minimizing the defects and  $\varphi_0$  fluctuation in monolayers. The successful realization of this  $1 \text{ cm}^2$  chiral substrate with Ag fan-shaped nanostructures makes the application as a narrow-band circular polarizer possible, which has been proposed with optical performance demonstrated in Section 3.4.3.

### 5.3 Flexible chiral metamaterials

The optical properties of metamaterials are determined by the geometry, size, arrangement, and material of the unit structure. If any parameters mentioned above is changed, the optical properties of the metamaterial will be tuned. Active metamaterials are one type of metamaterials with optical properties that can be controlled by applying external stimuli, including photon, mechanical deformation, electric field, magnetic field, heat, etc. The active control of metamaterials' optical properties is very important for practical applications. Here we demonstrate that the chiral metamaterials fabricated by DSG on nanosphere monolayers can be developed to be an active optical device, with chiral optical response tuned by mechanical deformation.

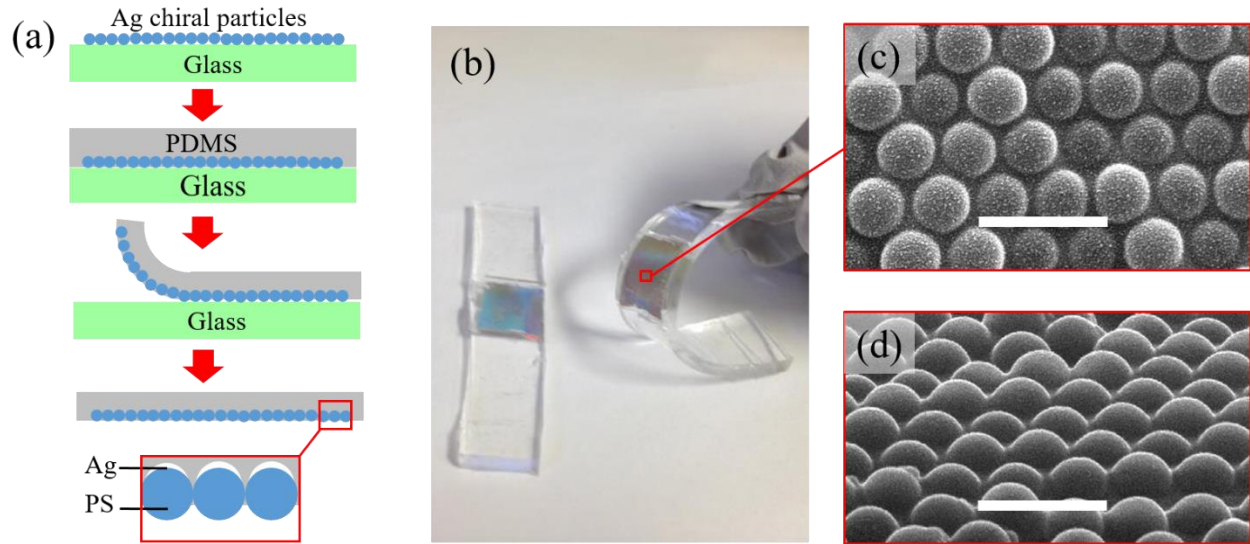


**Figure 5.3.1.** (a) The process of transferring Ag chiral particles into a PDMS substrate. (b) The photograph of the flexible chiral metamaterial substrate. (c) Top-view, and (d) side-view SEM images of the flexible substrate surface where a thin layer of Au nanoparticles is coated for SEM imaging. The scale bar in (c) and (d) represents 1  $\mu\text{m}$ .

### 5.3.1 Flexible chiral metamaterials: fabrication and morphology

The flexible chiral metamaterial is obtained by transferring the optimized Ag fan-shaped chiral nanostructures ( $\theta = 84^\circ$ ,  $\varphi_0 = 53^\circ$ ,  $t_{\text{QCM}} = 4 \times 30 \text{ nm}$ ) on nanospheres into a transparent polydimethylsiloxane (PDMS) substrate, which is an elastomeric polymer with low surface energy, excellent flexibility and elasticity. PDMS adheres to all surfaces in a conformal way, and can be easily integrated with non-planar structures, which serves as an excellent material for flexible substrates. The process of transferring chiral particles into PDMS is shown in **Figure 5.3.1a** and starts with mixing the PDMS base and the curing agent (Sylgard® 184 Silicone Elastomer Kit, Dow Corning) by a weight ratio of 10:1. After degassing, the liquid PDMS is poured onto the surface of the substrate with Ag chiral nanostructure arrays. Then the substrate with PDMS is placed in a benchtop oven (Barnstead Int. LabLine 3510 L-C) at 60 °C for 120 min to allow PDMS to cure. After the substrate cools down to room temperature, the solid PDMS sheet

is peeled off the substrate, with chiral particles embedded on one side of the PDMS sheet. The obtained flexible chiral substrate is shown in **Figure 5.3.1b**.

The top-view and side-view SEM images of the flexible substrate surface are shown in **Figures 5.3.1c** and **5.3.1d**, respectively. The Ag fan-shaped nanostructures are embedded in PDMS, and the SEM images can only reveal the bottom side of the nanosphere arrays without Ag nanostructures. The surface is coated with a thin layer of Au nanoparticles for SEM imaging. According to the SEM images, we can identify that only part of the nanosphere is inside the PDMS. The top-view SEM image shows that the part of nanospheres outside the PDMS has a diameter of about 400 nm, which indicates that 10.4% of a nanosphere is outside the PDMS.

### **5.3.2 Flexible chiral metamaterials: deformation modeling**

The obtained flexible chiral substrate can be stretched with the nanosphere position changed. However, the stretching process cannot be easily observed by a regular SEM. Here we employ a simple model to simulate the position change of the nanospheres when the PDMS substrate is stretched. We assume that PDMS is incompressible with Poisson ratio = 0.5,[155] polystyrene nanospheres are rigid bodies, and there is no relative movement of the nanospheres with respect to the surrounding PDMS. For simplicity, we only simulate two 1D stretching cases: stretching in  $x$  direction and  $y$  direction, respectively, where  $x$  direction is defined as the direction along one row of nanospheres and  $y$  direction is perpendicular to  $x$  direction, as illustrated in **Figures 5.3.2a** and **5.3.2b**.

For the case of stretching in  $x$  direction, the PDMS slab is stretched in  $x$  direction and will shrink in  $y$  and  $z$  directions due to its incompressibility. The incompressibility gives

$$l_{x0}l_{y0}l_{z0} = (l_{x0} + \Delta l_x)(l_{y0} - \Delta l_y)(l_{z0} - \Delta l_z), \quad (5.3.1)$$

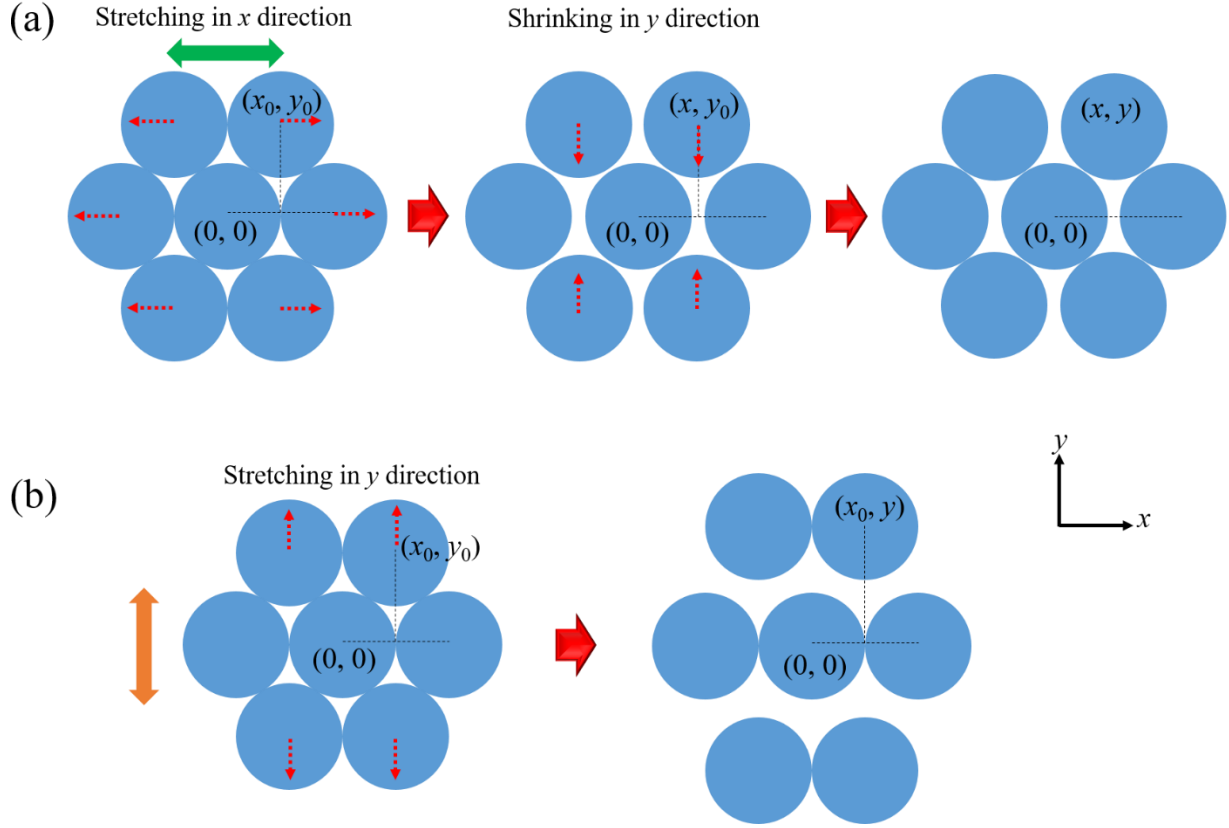


**Figure 5.3.2.** (a) Schematic illustration of how nanospheres move when stretching in x direction: a nanosphere originally at  $(x_0, y_0)$  moves to  $(x, y_0)$  due to the x direction stretching of the PDMS substrate, and finally move to  $(x, y)$  due to the shrinking in y direction of PDMS substrate. (b) Schematic illustration of how nanospheres move when stretching in y direction: a nanosphere originally at  $(x_0, y_0)$  moves to  $(x_0, y)$  due to the x direction stretching of the PDMS substrate, and the shrinking of the PDMS substrate does not move the nanosphere due to the rigid body of nanospheres.

where  $l_{x0}$ ,  $l_{y0}$ , and  $l_{z0}$  are the original lengths of the PDMS slab before stretching, and  $\Delta l_x$ ,  $\Delta l_y$ , and  $\Delta l_z$  are the length changes after stretching. Since  $l_{x0}$  is much greater than  $l_{y0}$  and  $l_{z0}$ , we assume

$$\frac{\Delta l_y}{l_{y0}} = \frac{\Delta l_z}{l_{z0}}. \quad (5.3.2)$$

Combining Equations (5.3.1) and (5.3.2) leads to

$$\frac{\Delta l_y}{l_{y0}} = 1 - \sqrt{\frac{1}{1 + \frac{\Delta l_x}{l_{x0}}}} \quad \text{or} \quad e_y = 1 - \sqrt{\frac{1}{1 + e_x}}, \quad (5.3.3)$$

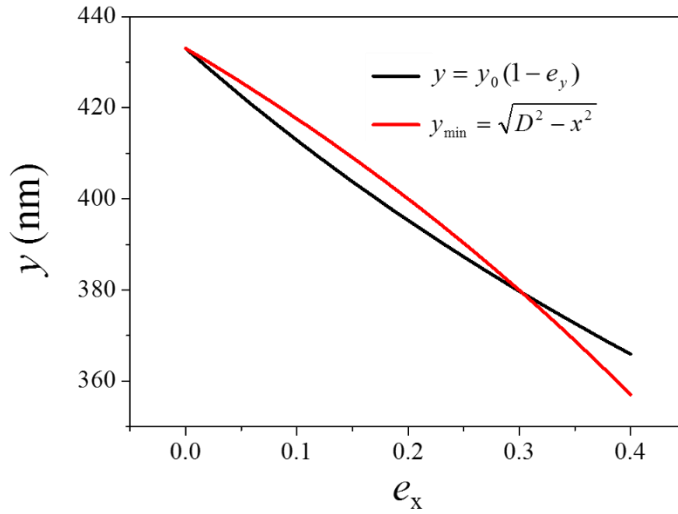


**Figure 5.3.3.** The calculated based on the shrinking of the PDMS substrate,  $y = y_0(1 - e_y)$ , and the minimum value for  $y$ , required by the rigid body of nanospheres,  $y_{\min} = \sqrt{D^2 - x^2}$ , as functions of  $e_x$ .

where  $e$  is the strain defined as  $e = \frac{\Delta l}{l_0}$ . Therefore, a nanosphere with a diameter of  $D$  originally

located at  $(x_0 = D/2, y_0 = \sqrt{3}D/2)$ , as shown in **Figure 5.3.2a**, will move to a new position  $(x, y)$ ,

where

$$x = x_0(1 + e_x) \quad (5.3.4)$$

$$y = y_0(1 - e_y). \quad (5.3.5)$$

However, Equation (5.3.5) is only valid only when the rigid edge of nanospheres are not taken into account. Considering that nanospheres are rigid bodies, there is a minimum value for  $y$ ,

$$y_{\min} = \sqrt{D^2 - x^2}. \quad (5.3.6)$$

Equations (5.3.5) and (5.3.6) are plotted in **Figure 5.3.3**. It is found that  $y_{\min} > y_0(1 - e_y)$  when

$0 < e_x < 0.3$ , and  $y_{\min} < y_0(1 - e_y)$  when  $e_x > 0.3$ . Then the final expression for  $y$  is

$$\begin{aligned}
y &= \frac{D}{2} \sqrt{4 - (1 + e_x)^2} \quad (0 < e_x < 0.3) \\
&= \frac{D}{2} \sqrt{\frac{3}{1 + e_x}} \quad (e_x > 0.3)
\end{aligned} \tag{5.3.7}$$

For the case of stretching in  $y$  direction, the PDMS will shrink in  $x$  direction. However, the nanospheres cannot move in  $x$  direction due to their rigid bodies. Therefore a simple expression is obtained for the new position of a nanosphere originally located at  $(x_0 = D/2, y_0 = \sqrt{3}D/2)$ ,

$$x = x_0 = D/2, \tag{5.3.8}$$

$$y = y_0(1 + e_y) = \sqrt{3}(1 + e_y)D/2. \tag{5.3.9}$$

This simulation is only based on three assumptions as described above, and neglects other physical processes, such as buckling of surface. A more accurate simulation may be done by using finite element analysis. But this simple simulation can qualitatively reflect how nanospheres change their positions when the flexible substrate is stretched in one dimension. The simulated position changes will be applied in the FDTD simulation for creating geometric models.

### ***5.3.3 Flexible chiral metamaterials: optical characterization***

The circularly polarized transmittance spectra are measured by the spectroscopic microscope, with the flexible substrates mounted on a stretching stage and stretched in one dimension. The schematic illustration and photograph of the measurement setup are shown in **Figure 5.3.4**. The laser diffraction patterns are used to align the samples with respect to  $x$  and  $y$  directions. Two separate flexible substrates, Sample #1 and Sample #2, are used in the optical measurements, with Sample #1 stretched in  $x$  direction and Sample #2 stretched in  $y$  direction.  $T(\text{RCP})$  and  $T(\text{LCP})$  spectra are measured at different stretching states with  $e_x$  or  $e_y = 0(+), 0.0625(+), 0.125(+), 0.1875, 0.125(-), 0.0625(-),$  and  $0(-)$ , where (+) and (-) represent stretching and relaxing of the substrate,

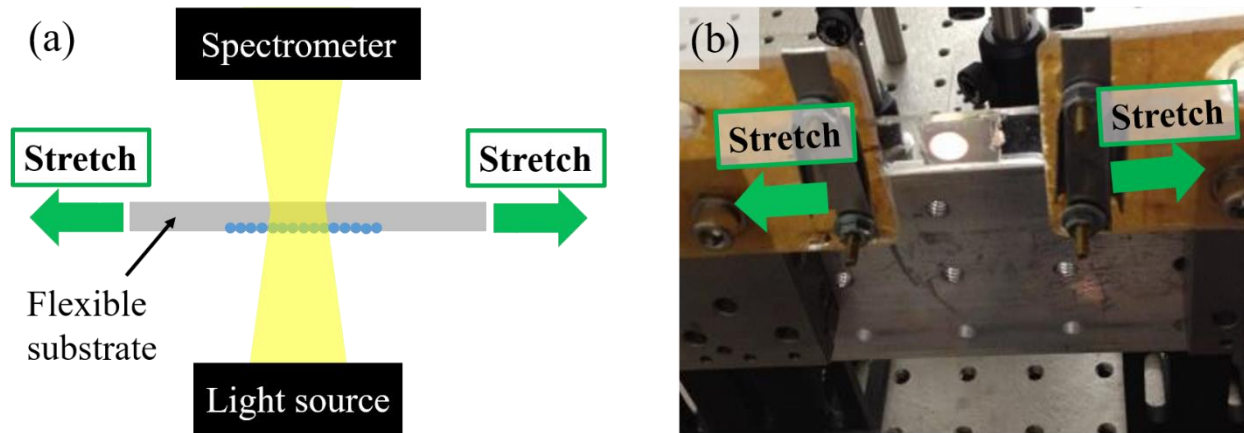


**Figure 5.3.4.** (a) Schematic illustration, and (b) photograph of the stretching and optical measurement setup.

respectively. The measured  $T(\text{RCP})$  and  $T(\text{LCP})$ , along with the calculated  $T(\text{RCP})-T(\text{LCP})$ , are shown in **Figure 5.3.5**. The spectra are vertically stacked to clearly show the change in spectra.

Samples #1 and #2 show similar spectral features at the non-stretching state, as shown by the red curves in **Figure 5.3.5**. The transmittance spectra of the flexible substrate are not exactly the same as those of chiral particles on glass substrates, which is caused by the refractive index change of the surrounding. The refractive index of PDMS is larger than air, leading to a redshift of the LSPR. Both Samples #1 and #2 have a resonance in  $T(\text{RCP})$  at a wavelength  $\lambda_{\text{RCP}} \approx 770$  nm, and another resonance in  $T(\text{LCP})$  at a wavelength  $\lambda_{\text{LCP}} \approx 750$  nm. Note, there are also other LSPRs, which will not be discussed here since these resonances show similar trends. The only significant difference between Sample #1 and #2 is that  $T(\text{LCP})$  of Sample #2 has a stronger resonance at  $\lambda = 875$  nm than that of Sample #1. The difference may originate from their slightly different monolayer orientations during the fabrication process, which cause small variations in optical response. As the strain  $e_x$  or  $e_y$  increases (stretching), Samples #1 and #2 change the spectra slightly and gradually redshift the LSPR wavelength. As the strain  $e_x$  or  $e_y$  decreases (relaxing), Samples #1 and #2 shift the LSPR wavelength to shorter wavelength. The resonance wavelength

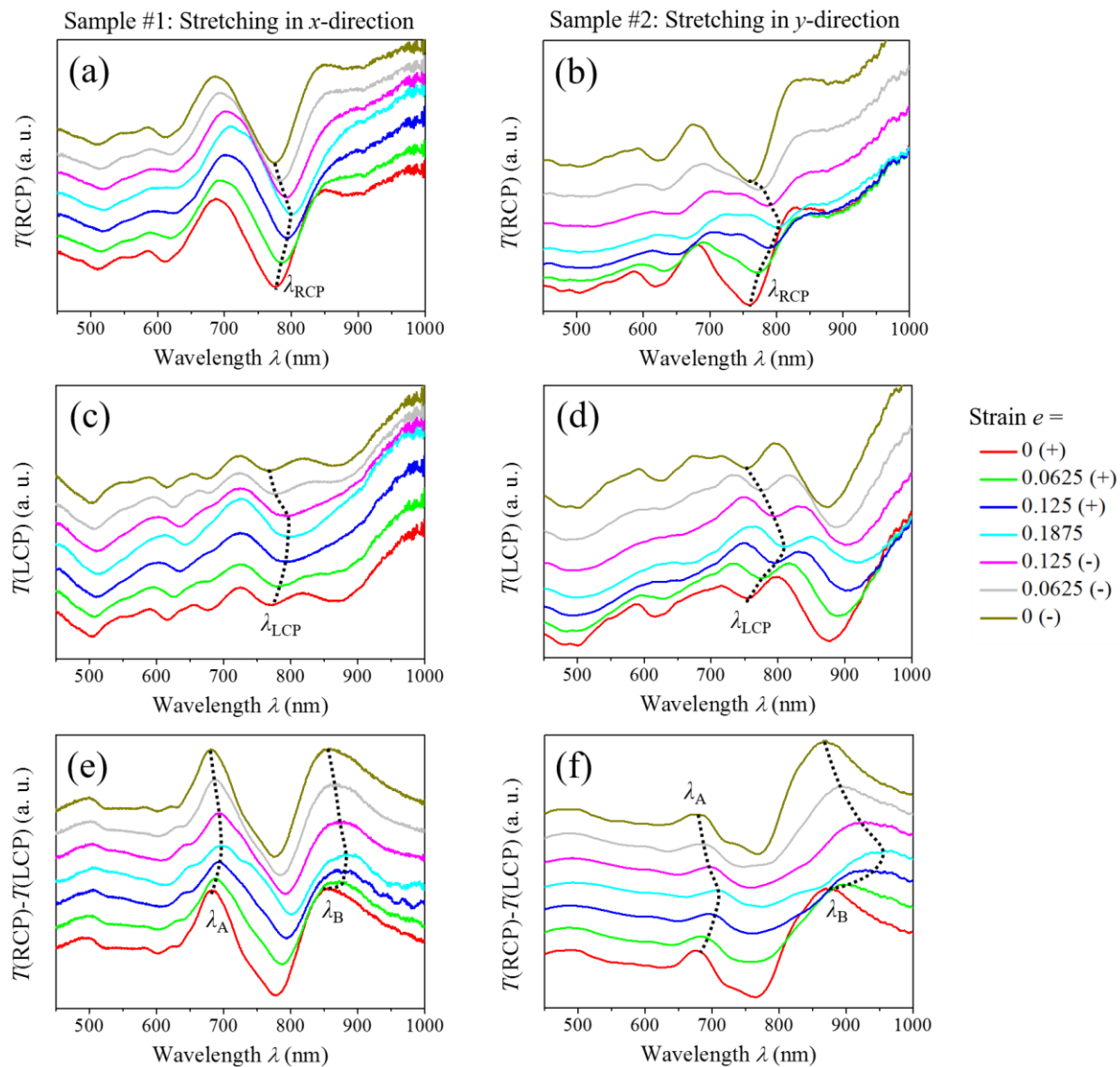


**Figure 5.3.5.** Circularly polarized transmittance and differential transmittance spectra of the flexible substrates with stretching in  $x$  and  $y$  directions.  $T(\text{RCP})$  spectra with stretching in (a) and (b)  $y$  directions.  $T(\text{LCP})$  spectra with stretching in (c)  $x$  and (d)  $y$  directions.  $T(\text{RCP})-T(\text{LCP})$  spectra with stretching in (e)  $x$  and (f)  $y$  directions.

shift is believed to originate from the change in LSPR coupling of adjacent fan-shape nanostructures. The LSPR wavelength  $\lambda_{\text{RCP}}$  and  $\lambda_{\text{LCP}}$  are plotted against the strain in **Figures 5.3.6a** and **5.3.6b**, respectively. It is found that the LSPR wavelengths at the same strain of stretching (+) and relaxing (-) are almost the same, which indicates that the deformation of PDMS is elastic or reversible in this range of strain. Approximately, the LSPR wavelength  $\lambda_{\text{RCP}}$  or  $\lambda_{\text{LCP}}$

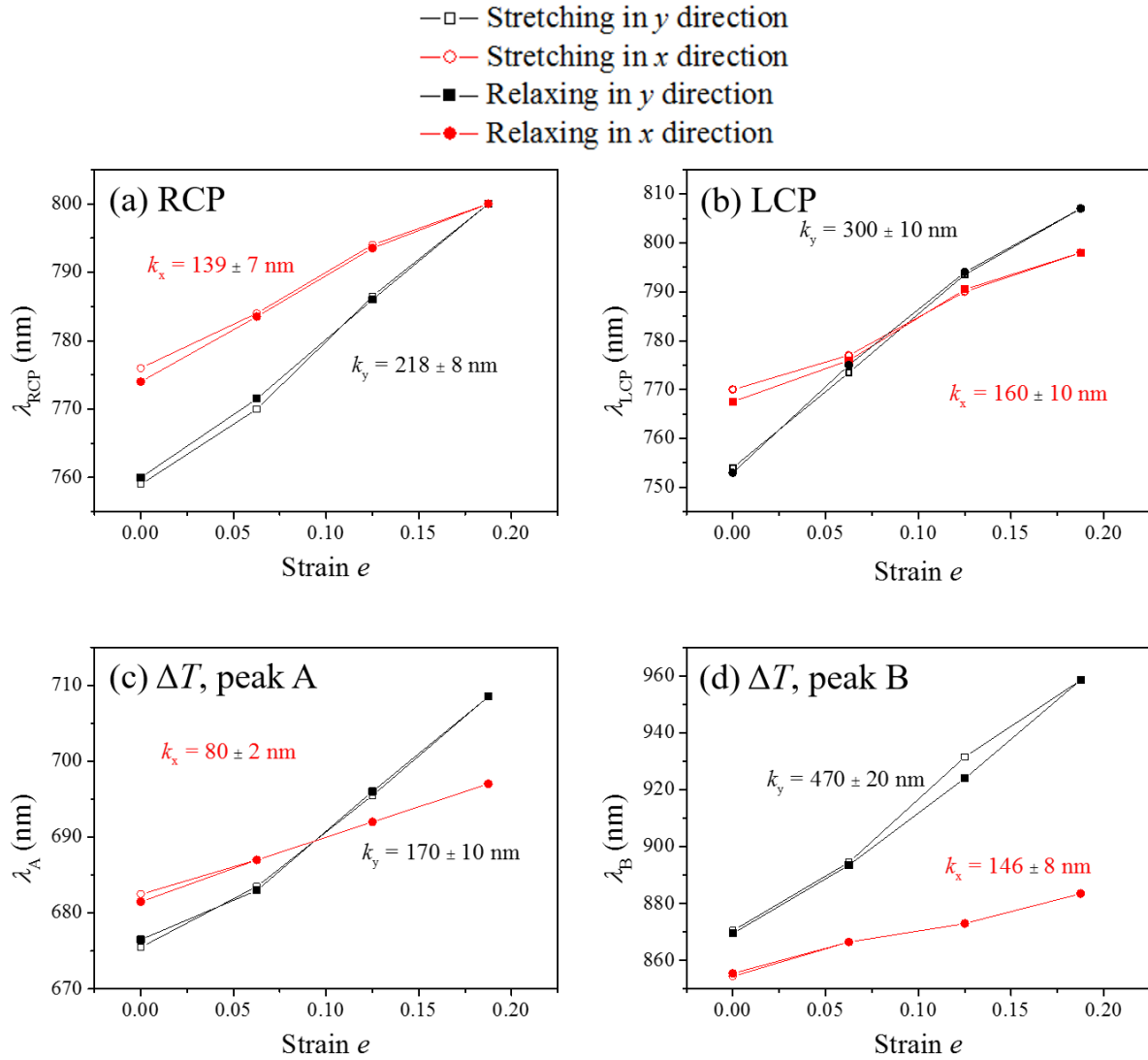


**Figure 5.3.6.** (a)  $\lambda_{RCP}$ , (b)  $\lambda_{LCP}$ , (c)  $\lambda_A$ , and (d)  $\lambda_B$  as a function of strain  $e$  with stretching in  $x$  and  $y$  directions.

has a linear relationship with the strain  $e$ . According to a linear fitting, the slopes of the fitted line are  $139 \pm 7$  nm and  $218 \pm 8$  nm for  $\lambda_{RCP}$  of Samples #1 and #2, respectively, and  $160 \pm 10$  nm and  $300 \pm 10$  nm for  $\lambda_{LCP}$  of Samples #1 and #2, respectively. This slope represents the sensitivity of the LSPR wavelength with respect to the change in strain. Sample #1 has a smaller sensitivity than Sample #2 in both  $T(RCP)$  and  $T(LCP)$ . If we assume Samples #1 and #2 are identical, then we can attribute their different sensitivity to the different stretching directions. As it has been

demonstrated in Section 5.3.2, stretching in  $x$  and  $y$  direction leads to completely different arrangements of Ag fan-shaped nanostructures. The differently arranged nanostructures should have different LSPR coupling, which leads to the different sensitivity of LSPR wavelength to the strain change.

$\Delta T = T(\text{RCP}) - T(\text{LCP})$  is expected to exhibit the same property as  $T(\text{RCP})$  and  $T(\text{LCP})$ . Here we select two  $\Delta T$  peaks A and B at wavelengths  $\lambda_A$  and  $\lambda_B$ , which can be clearly identified in **Figures 5.3.5e** and **5.3.5f**. The negative peak around  $\lambda = 780$  nm is not chosen because it seems to contain two overlapped peaks and its peak wavelength cannot be clearly defined for Sample #2.  $\lambda_A$  and  $\lambda_B$  are plotted against the strain in **Figures 5.3.6c** and **5.3.6d**, respectively. For  $\lambda_A$ , the linear fitting gives a sensitivity of  $80 \pm 2$  nm for Sample #1, and  $170 \pm 10$  nm for Sample #2. For  $\lambda_B$ , the linear fitting shows a sensitivity of  $146 \pm 8$  nm for Sample #1, and  $470 \pm 20$  nm for Sample #2. Therefore, the analysis of  $\Delta T$  spectra also confirms that stretching in  $y$  direction shows a larger sensitivity than stretching in  $x$  direction, which is caused by the different coupling of the adjacent chiral plasmonic nanostructures.

#### **5.3.4 Flexible chiral metamaterials: FDTD simulation**

The FDTD simulations are performed to simulate the chiral optical property of the flexible substrate at different stretching states. Here three cases are simulated:  $e_x = 0, e_y = 0$ ;  $e_x = 0.125, e_y = 0$ ;  $e_x = 0, e_y = 0.125$ . The geometric models in FDTD simulations are based on the deformation modeling results in Section 5.3.2, and are shown in **Figure 5.3.7**. The simulated  $T(\text{RCP})$ ,  $T(\text{LCP})$ , and  $T(\text{RCP})-T(\text{LCP})$  spectra at two states,  $e_x = 0.125, e_y = 0$  and  $e_x = 0, e_y = 0.125$ , are shown in **Figure 5.3.8** along with the corresponding measured spectra for comparison. The FDTD simulations successfully reproduce the main features in the measured spectra. However, the

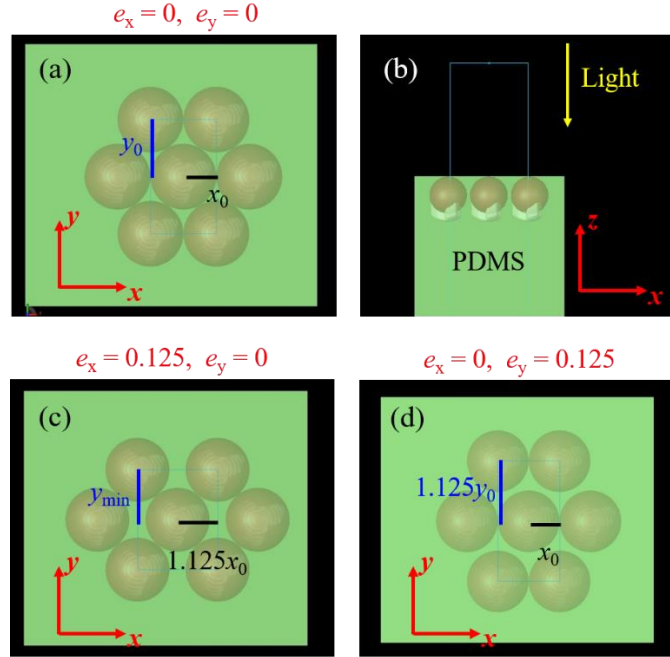


**Figure 5.3.7.** The geometric models of Ag fan-shaped nanostructures embedded in PDMS used in FDTD simulation. (a) Top-view of the flexible substrate with  $e_x = 0$  and  $e_y = 0$ . (b) Side-view of the flexible substrate. Top-view of the flexible substrate with (c)  $e_x = 0.125$  and  $e_y = 0$ , and (d)  $e_x = 0$  and  $e_y = 0.125$ .

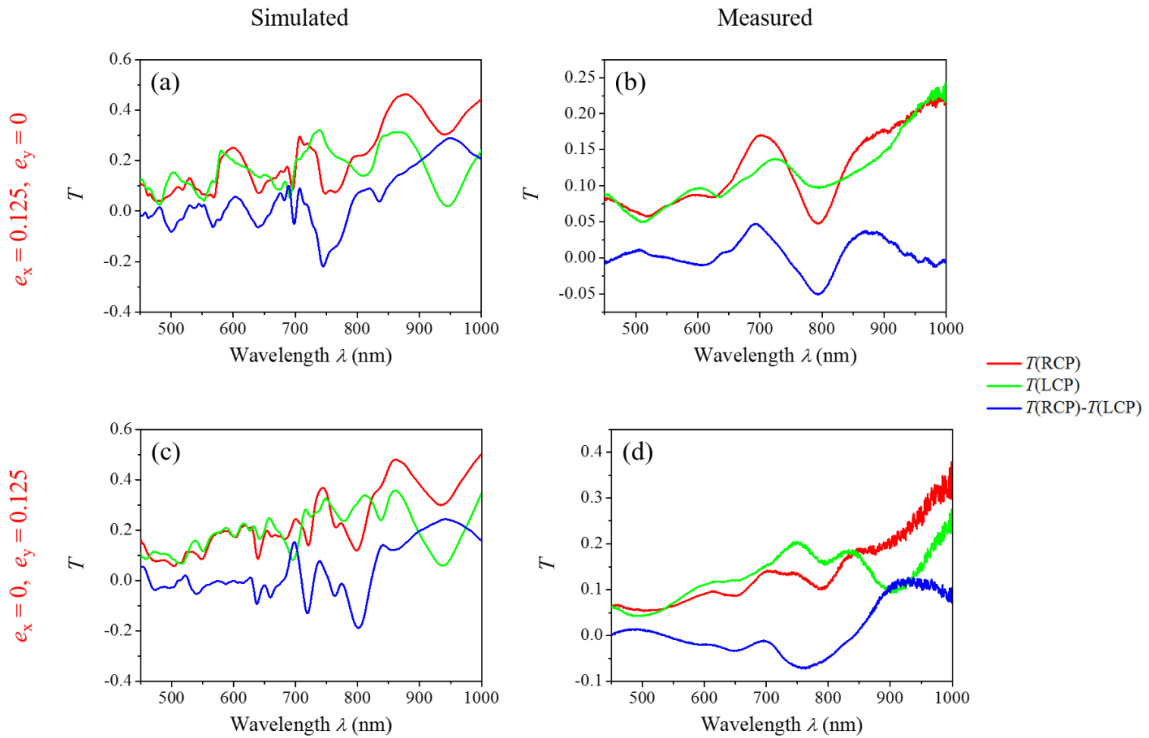


**Figure 5.3.8.** A comparison between simulated and measured  $T(\text{RCP})$ ,  $T(\text{LCP})$ , and  $T(\text{RCP})-T(\text{LCP})$ . (a) Simulated spectra and (b) measured spectra with  $e_x = 0.125$ ,  $e_y = 0$ . (c) Simulated spectra and (d) measured spectra with  $e_x = 0$ ,  $e_y = 0.125$ .

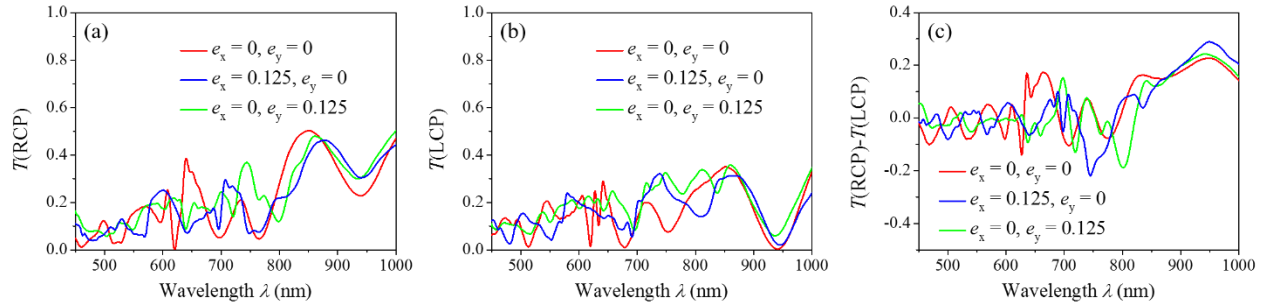


**Figure 5.3.9.** The simulated (a)  $T(\text{RCP})$ , (b)  $T(\text{LCP})$ , and (c)  $T(\text{RCP})-T(\text{LCP})$  at three different stretching states:  $e_x = 0, e_y = 0$ ;  $e_x = 0.125, e_y = 0$ ;  $e_x = 0, e_y = 0.125$ .

simulation results show more resonances, some of which may not be real and come from the data processing. This makes it difficult to keep track of each resonance to reveal the wavelength change, as shown in **Figure 5.3.9**. Therefore, this FDTD simulation cannot confirm that the stretching direction affects the sensitivity of LSPR with respect to the strain change, which is probably due to the too simple assumptions in the simulation. The real location change of the nanospheres is very complicated and should include displacement in  $z$  direction of nanospheres. The dielectric constant of PDMS may also change at different stretching states. Both the location change and dielectric constant change can cause a significant difference between the simulation and experimental results.

### 5.3.5 Flexible chiral metamaterials: conclusion

In summary, we have fabricated the flexible chiral metamaterial by transferring Ag fan-shaped nanostructure arrays into a PDMS substrate. The chiral optical response of the flexible chiral metamaterial exhibits a dependence on the strain magnitude and direction, which is caused by the different plasmonic couplings of the adjacent chiral nanostructures. The measured spectrum redshifts with increasing strain and blueshifts with decreasing strain. The stretching direction also

affects how much the spectrum shifts with a certain change in strain. This study demonstrates that the chiral optical response of our large-area chiral metamaterial can be tuned by mechanical deformations, which can be potentially developed into tunable chiral optical devices.

#### **5.4 Application for bulk refractive index sensing**

The dependence of LSPR wavelength on the refractive index of the surrounding medium has been employed for refractive index based sensing.[65, 66, 156-158] In this section, we employ chiral plasmonic nanostructures for refractive index sensing and demonstrate a new mechanism to improve the sensitivity by detecting the circularly polarized differential transmittance spectra.

##### ***5.4.1 Application for bulk refractive index sensing: Au Fan-shaped nanostructures***

Au fan-shaped chiral nanostructures are used for refractive index sensing in this study. The material is chosen to be Au instead of Ag because Ag will be oxidized in aqueous solution.[114] Here we select two chiral fan-shaped nanostructures for refractive index sensing, Structures R and L, which are essentially geometric enantiomers, and their SEM images are shown in **Figures 5.4.1a** and **5.4.1b**.

The chiral optical properties of the Au fan-shaped nanostructures are characterized by circularly polarized transmittance in wavelength range of  $\lambda = 600 \sim 1000$  nm. **Figures 5.4.1c** and **5.4.1d** show the circularly polarized transmittance spectra  $T_R(\text{RCP})$  and  $T_R(\text{LCP})$  of Structures R, and  $T_L(\text{RCP})$  and  $T_L(\text{LCP})$  of Structure L, respectively, which are all measured in air. For Structure R, both  $T_R(\text{RCP})$  and  $T_R(\text{LCP})$  spectra show a transmittance peak around  $\lambda = 680$  nm and transmittance valley around  $\lambda = 810$  nm.  $T_R(\text{RCP})$  is lower

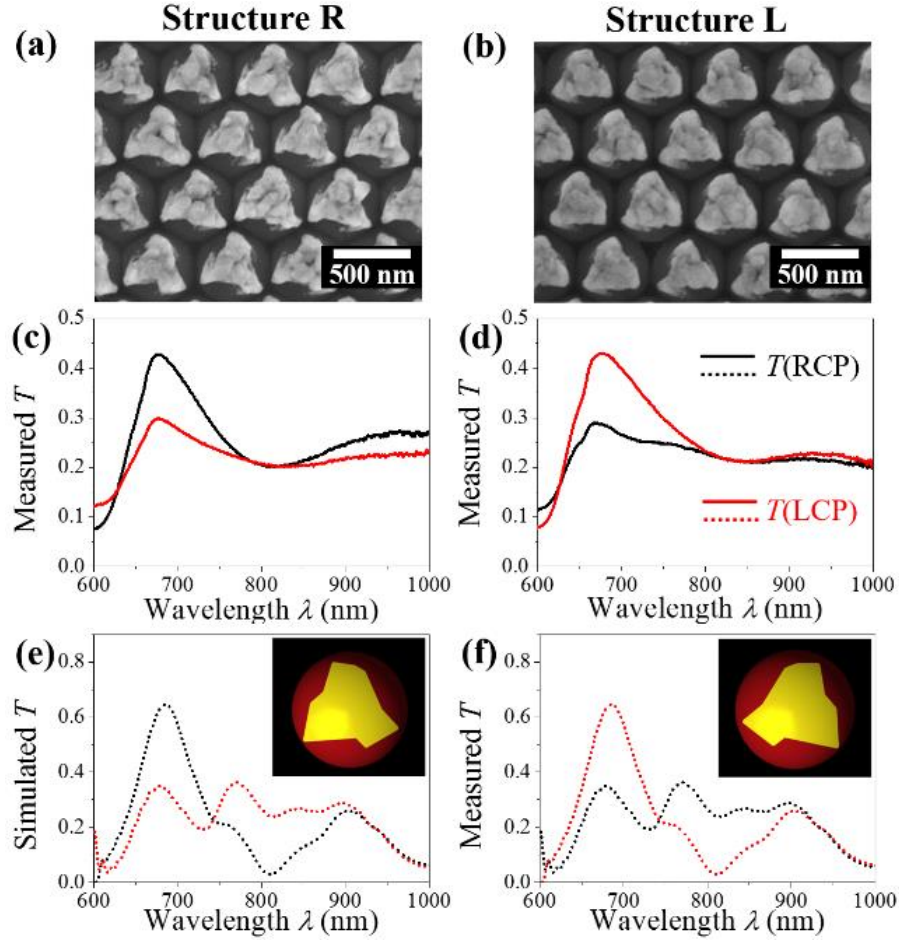


**Figure 5.4.1** (a), (b) Representative top-view SEM images, (c),(d) Measured  $T(\text{RCP})$  and  $T(\text{LCP})$ , and (e), (f) Simulated  $T(\text{RCP})$  and  $T(\text{LCP})$  of Structure R and L, respectively. The insets in (e) and (f) are the geometric models in FDTD simulations.

than  $T_{\text{R}}(\text{LCP})$  when  $\lambda < 640$  nm and becomes greater than  $T_{\text{R}}(\text{LCP})$  when  $\lambda > 640$  nm. For Structure L,  $T_{\text{L}}(\text{RCP})$  and  $T_{\text{L}}(\text{LCP})$  are similar to  $T_{\text{R}}(\text{LCP})$  and  $T_{\text{R}}(\text{RCP})$  of Structure R, respectively. This indicates that Structures R and L show opposite chiral optical response, which is consistent with their opposite geometric chirality. The chiral optical property of Structures R and L are simulated using FDTD method. **Figures 5.4.1e** and **5.4.1f** show the simulated  $T_{\text{R}}(\text{RCP})$ ,  $T_{\text{R}}(\text{LCP})$ ,  $T_{\text{L}}(\text{RCP})$ , and  $T_{\text{L}}(\text{LCP})$  spectra, respectively. The insets in **Figures 5.4.1e** and **5.4.1f** show the geometric models in FDTD simulations, which are created based on the SEM images. The simulated results are consistent with the

experimental results, where the transmittance peak at  $\lambda = 680$  nm and transmittance dips around  $\lambda = 600$  nm and 810 nm are well reproduced in the simulated spectra.

#### ***5.4.2 Application for bulk refractive index sensing: refractive index sensing experiment***

The refractive index sensing experiments are performed by measuring circularly polarized transmittance spectra of Structures R and L in sucrose aqueous solutions of different concentrations,  $c(\text{mass}\%) = 0\%, 18\%, 26\%, 36\%, 44\%, 50\%$ , and  $55\%$ , with corresponding refractive indices  $n = 1.333, 1.3606, 1.3741, 1.3922, 1.4078, 1.4201$ , and  $1.4307$ , respectively.[159] These sucrose solutions are used in the order of low to high concentrations in the experiments. When changing solutions, the substrate is rinsed with the sucrose solution at the next concentration to ensure that the measurement is taken under the desired bulk refractive index.

**Figures 5.4.2a** and **5.4.2b** show  $T_R(\text{RCP})$  and  $T_R(\text{LCP})$  spectra, respectively.  $T_R(\text{RCP})$  exhibits two transmittance peaks around  $\lambda = 650$  nm and  $\lambda = 750$  nm, and two transmittance valleys around  $\lambda = 680$  nm and  $\lambda = 850$  nm.  $T_R(\text{LCP})$  shows a transmittance peak around  $\lambda = 680$  nm and a transmittance valley around  $\lambda = 750$  nm.  $T_L(\text{RCP})$  and  $T_L(\text{LCP})$  spectra are not shown here and similar to  $T_R(\text{LCP})$  and  $T_R(\text{RCP})$ , respectively. The transmittance valley and peak around  $\lambda = 680$  nm are labeled as  $A_R$  and  $C_R$  for Structure R ( $A_L$  and  $C_L$  for Structure L), respectively. The transmittance peak and valley around  $\lambda = 750$  nm are labeled as  $B_R$  and  $D_R$  for Structure R, ( $B_L$  and  $D_L$  for Structure L), respectively. As the refractive index of sucrose solutions  $n$  increases, peaks  $A_R$ – $D_R$  and  $A_L$ – $D_L$  shift toward longer wavelength.

For chiral metamaterials, circular dichroism can be characterized by  $\Delta T = T(\text{RCP}) - T(\text{LCP})$ . **Figure 5.4.2c** shows  $\Delta T_R$  spectra of Structure R in sucrose solutions of different  $c$ . Since Structures R and L have the opposite chiral optical response, the following

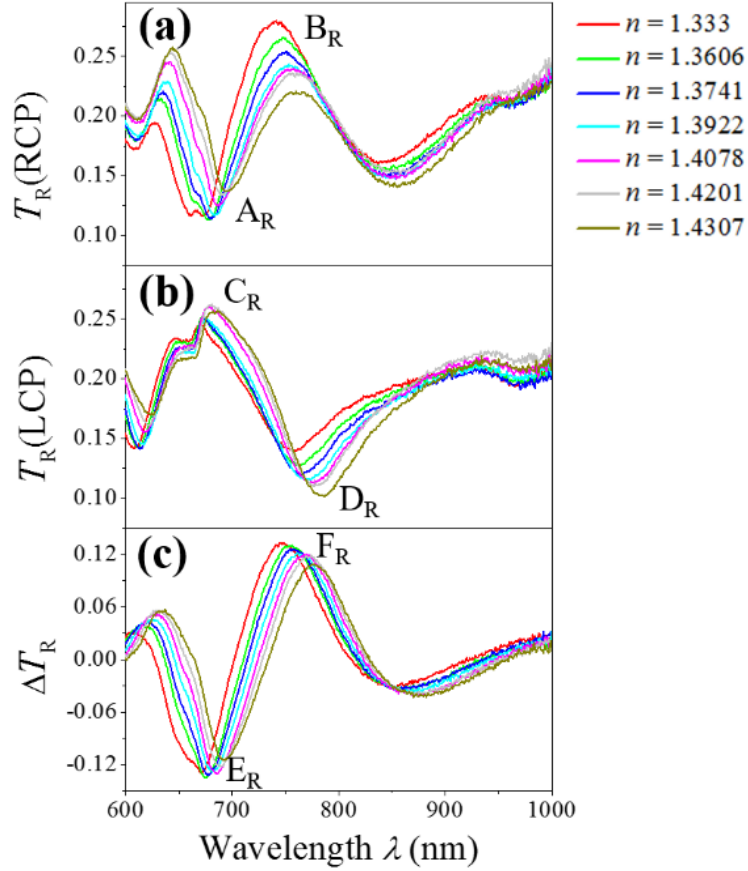


**Figure 5.4.2.** (a)  $T_R(\text{RCP})$ , (b)  $T_R(\text{LCP})$ , and (c)  $\Delta T_R$  spectra of Structure R in sucrose solutions at different concentrations.

discussion will only focus on Structure R, and similar discussion will apply to Structure L. Two significant sharp peaks are observed around  $\lambda = 680$  nm and  $\lambda = 750$  nm in  $\Delta T_R$  spectra, which are labeled as  $E_R$  and  $F_R$  for Structure R ( $E_L$  and  $F_L$  for Structure L), respectively.  $E_R$  ( $E_L$ ) is resulted from the subtraction between  $A_R$  ( $A_L$ ) and  $C_R$  ( $C_L$ ), while  $F_R$  ( $F_L$ ) originates from the subtraction between  $B_R$  ( $B_L$ ) and  $D_R$  ( $D_L$ ). Since peaks  $A_R$ – $D_R$  redshift with  $n$ , their differential spectra  $\Delta T_R$  exhibit the same trend. The peak wavelengths  $\lambda_p$  of peaks  $A_R$ – $F_R$  are plotted against the refractive indices  $n$  of sucrose solutions in **Figure 5.4.3**. The bulk LSPR refractive index sensitivity  $S = \Delta\lambda/\Delta n$  (nm/RIU) can be extracted by a linear fit to these data and the obtained  $S$  for all the peaks are shown in **Table 5.4.1**, where RIU

represents refractive index unit. Around  $\lambda = 680$  nm,  $A_R$  has  $S = 220$  nm/RIU,  $C_R$  has  $S = 110$  nm/RIU, and  $E_R$  has  $S = 210$  nm/RIU. Around  $\lambda = 750$  nm,  $B_R$  has  $S = 210$  nm/RIU,  $D_R$  has  $S = 260$  nm/RIU, and  $F_R$  has  $S = 310$  nm/RIU. It can be seen that the sensitivity of the transmittance valley  $A_R$  ( $D_R$ ) is greater than that of the transmittance peak  $C_R$  ( $B_R$ ) in the same wavelength range. In addition,  $\Delta T_R$  peak  $E_R$  has a sensitivity close to that of  $A_R$ , while  $\Delta T_R$  peak  $F_R$  has a sensitivity greater than that of  $D_R$ . Therefore, a subtraction between  $T(\text{RCP})$  and  $T(\text{LCP})$  may lead to an enhanced bulk refractive index sensitivity.

The enhanced sensitivity can be visualized in **Figure 5.4.3**. For all  $n$  values,  $\lambda_p(D_R) > \lambda_p(F_R) > \lambda_p(B_R)$ .  $\lambda_p(F_R)$  is close to  $\lambda_p(B_R)$  when  $n$  is small, and becomes closer to  $\lambda_p(D_R)$  as  $n$  increases. This leads to that  $\lambda_p(F_R)$  shifts to longer wavelength faster than  $\lambda_p(B_R)$  and  $\lambda_p(D_R)$  and thus exhibits a larger sensitivity. This phenomenon can be explained by the different contributions from transmittance valley  $B_R$  and peak  $D_R$  to the formation of  $\Delta T_R$  peak  $F_R$ . This contribution from different peaks can be quantified by the integrated area of

**Table 5.4.1** Sensitivity, FWHM, and FOM for peaks and valleys

Peak	$S$ (nm/RIU)	FWHM (nm)	FOM
$A_R$	$220 \pm 10$	-	-
$A_L$	$245 \pm 7$	-	-
$B_R$	$210 \pm 9$	$84 \pm 1$	$2.5 \pm 0.1$
$B_L$	$170 \pm 10$	$92 \pm 4$	$1.8 \pm 0.1$
$C_R$	$110 \pm 10$	-	-
$C_L$	$190 \pm 5$	-	-
$D_R$	$260 \pm 20$	$99 \pm 3$	$2.6 \pm 0.2$
$D_L$	$250 \pm 10$	$85 \pm 3$	$2.9 \pm 0.2$
$E_R$	$210 \pm 20$	-	-
$E_L$	$220 \pm 10$	-	-
$F_R$	$310 \pm 10$	$86 \pm 2$	$3.6 \pm 0.1$
$F_L$	$270 \pm 10$	$89 \pm 3$	$3.0 \pm 0.2$

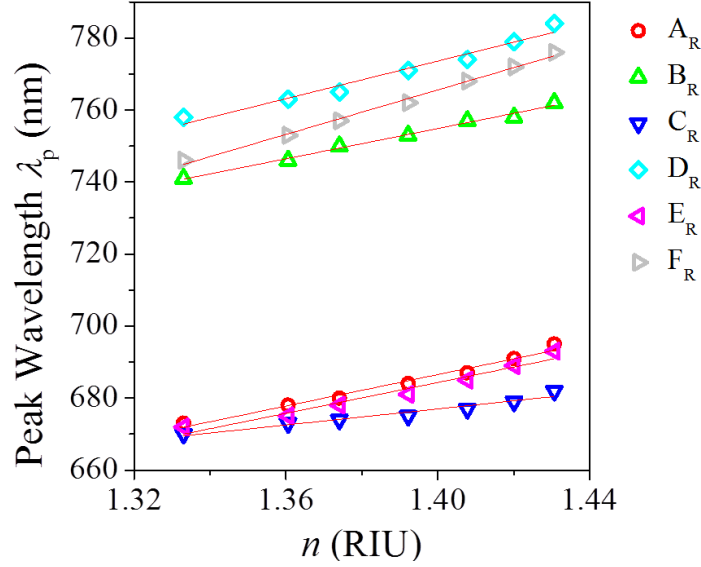


**Figure 5.4.3.** Peak wavelength  $\lambda_p$  versus refractive index  $n$  of sucrose solutions for Structure R. The straight lines are linear fittings of  $\lambda_p$ .

the peak in the wavelength range of  $\Delta T$  peak, as illustrated by the area of  $B_R$ ,  $A_B$ , and the area of  $D_R$ ,  $A_D$ , in **Figure 5.4.4**. **Figures 5.5.4a** and **5.4.4b** show the  $T_R(\text{RCP})$  and  $T_R(\text{LCP})$  at  $n = 1.333$  and  $n = 1.4307$ , respectively. The two intersection points of  $T(\text{RCP})$  and  $T(\text{LCP})$  curves on both sides of  $B_R$  and  $D_R$  are connected by a green line, and the area above

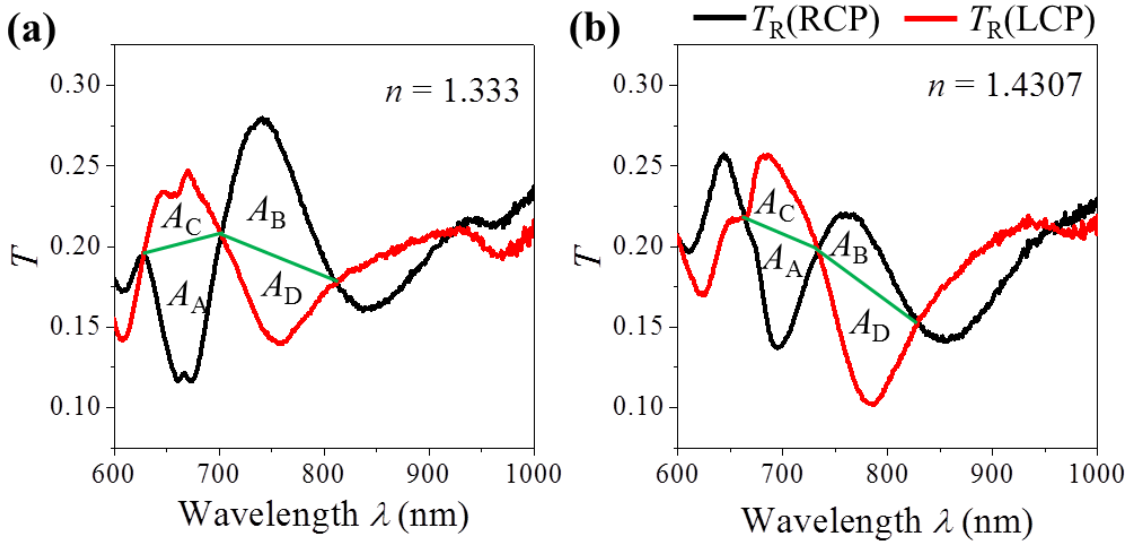


**Figure 5.4.4.**  $T_R(\text{RCP})$  and  $T_R(\text{LCP})$  spectra (a) at  $n = 1.333$ , and (b) at  $n = 1.4307$ . The green line is used to separate the contributions from  $T_R(\text{RCP})$  and  $T_R(\text{LCP})$  peaks to  $\Delta T_R$  peaks.

the line is  $A_B$  and the area below the line is  $A_D$ . At  $n = 1.333$ ,  $A_D / (A_B + A_D) = 38.6\%$ , which indicates that  $B_R$  is dominant in determining  $\lambda_p(F_R)$ , and  $\lambda_p(F_R)$  should be close to  $\lambda_p(B_R)$ . At  $n = 1.4307$ ,  $A_D / (A_B + A_D) = 65.2\%$ , which means that  $D_R$  becomes dominant and  $\lambda_p(F_R)$  should be close to  $\lambda_p(D_R)$ . This mechanism can also explain why  $E_R$  shows no greater sensitivity than  $A_R$ . It can be seen that  $\lambda_p(A_R) > \lambda_p(E_R) > \lambda_p(C_R)$  in **Figure 5.4.3**. The calculated contribution of  $A_R$  to  $E_R$  is  $A_A / (A_A + A_C) = 64.9\%$  for  $n = 1.333$ , and  $A_A / (A_A + A_C) = 58.9\%$  for  $n = 1.4307$ , which decreases slightly with increasing  $n$ . This indicates that  $E_R$  moves to longer wavelength slower than  $A_R$ , resulting in a smaller sensitivity of  $E_R$ . Therefore, based on the discussion on the sensitivities of  $E_R$  and  $F_R$ , one should find that the enhanced sensitivity of a  $\Delta T$  peak can be achieved only if the corresponding transmittance peak or valley in longer wavelength increases its contribution with increasing  $n$ .

#### **5.4.3 Application for bulk refractive index sensing: FDTD simulation**

This mechanism of the enhanced sensitivity is confirmed by FDTD simulations. By using the geometric model as shown in the inset of **Figure 5.4.1e**,  $T_R(\text{RCP})$  and  $T_R(\text{LCP})$  in media at different  $n$  were simulated. **Figure 5.4.5a** shows the simulated  $T_R(\text{RCP})$ ,  $T_R(\text{LCP})$ , and  $\Delta T_R$  spectra with  $n = 1.333$ . The experimental peaks  $A_R$ – $F_R$  are all reproduced in the simulation. A small transmittance valley appears around  $\lambda = 770$  nm in both  $T_R(\text{RCP})$  and  $T_R(\text{LCP})$  simulated spectra, which is not observed in the experimental spectra, probably due to its weak resonance. The peak wavelength  $\lambda_p$  of the simulated peaks  $B_R$ ,  $D_R$ , and  $F_R$  is plotted against  $n$  in **Figure 5.4.5b**. The linear fitting gives the sensitivity to be  $S = 103 \pm 8$ ,  $228 \pm 6$ , and  $260 \pm 10$  nm/RIU for peaks  $B_R$ ,  $D_R$ , and  $F_R$ , respectively. The sensitivity of

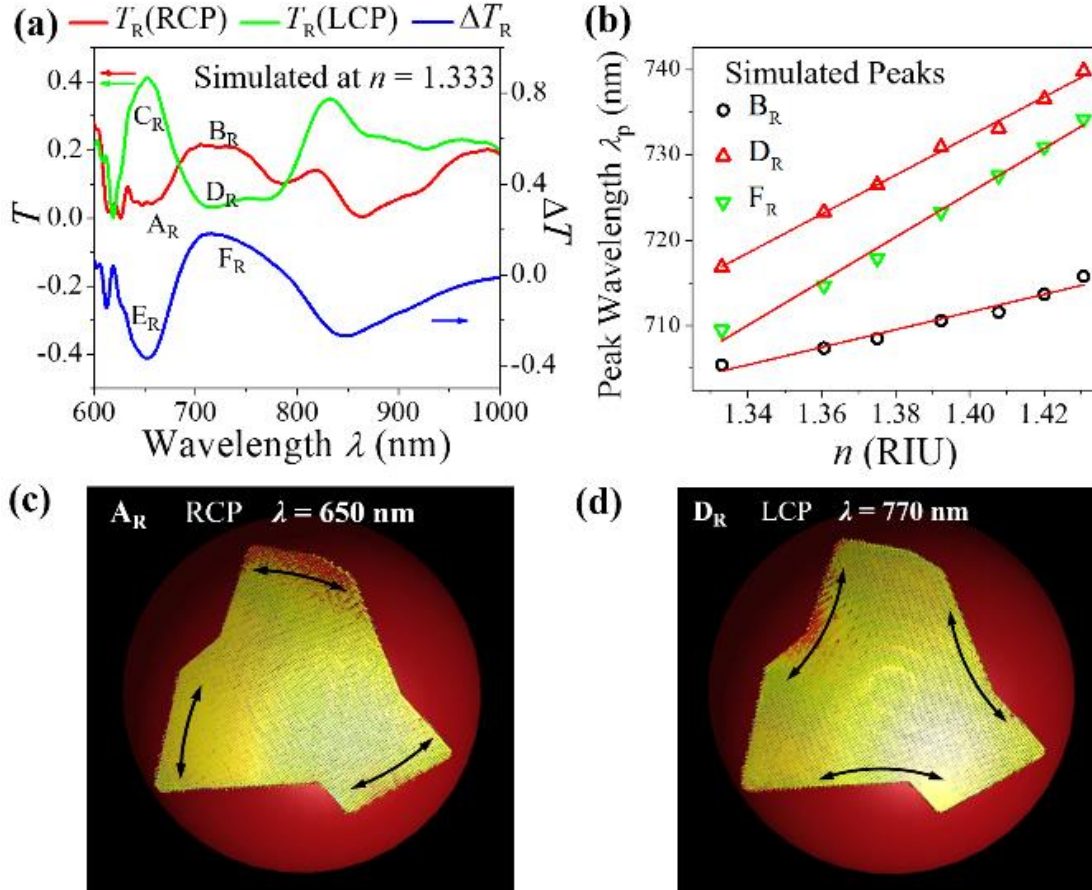


**Figure 5.4.5** (a) Simulated  $T_R(\text{RCP})$ ,  $T_R(\text{LCP})$  and  $\Delta T_R$  spectra for Structure R at  $n = 1.333$ . (b) Peak wavelength  $\lambda_p$  of the simulated peaks  $B_R$ ,  $D_R$ , and  $F_R$  versus refractive index  $n$ . The straight lines are linear fittings of  $\lambda_p$ . Near-field current distribution of Structure R with  $n = 1.333$  excited at (c) resonance  $A_R$  (RCP,  $\lambda = 650$  nm), and (d) resonance  $D_R$  (LCP,  $\lambda = 720$  nm). The arrows indicate the current oscillation directions. The current flows represented by the three arrows appear in sequences at different phases.

$F_R$  is greater than that of  $B_R$  or  $D_R$ , which is consistent with the experimental result. For the simulated peaks  $B_R$ ,  $D_R$ , and  $F_R$ ,  $A_D / (A_B + A_D) = 59.0\%$  at  $n = 1.333$  and  $A_D / (A_B + A_D) = 69.4\%$  at  $n = 1.4307$ . As  $n$  increases, the contribution from  $D_R$  to  $F_R$  increases, which causes  $\lambda_p(F_R)$  to shift closer to  $\lambda_p(D_R)$  and thus greater than that of  $B_R$  or  $D_R$ , which is consistent with the experimental result. For the simulated peaks  $B_R$ ,  $D_R$ , and  $F_R$ ,  $A_D / (A_B + A_D) = 59.0\%$  at  $n = 1.333$  and  $A_D / (A_B + A_D) = 69.4\%$  at  $n = 1.4307$ . As  $n$  increases, the contribution from  $D_R$  to  $F_R$  increases, which causes  $\lambda_p(F_R)$  to shift closer to  $\lambda_p(D_R)$  and thus

results in a larger sensitivity. The near-field current distributions of Structure R at resonances  $A_R$  and  $D_R$  were simulated as shown in **Figures 5.4.5c** and **5.4.5d**, respectively. The arrows in **Figures 5.4.5c** and **5.4.5d** indicate the current oscillation directions. The current flows represented by the three arrows occur in sequence at different phases. The near-field simulations reveal different plasmon modes at resonances  $A_R$  and  $D_R$ , which results in their different LSPR sensitivities.

Besides sensitivity  $S$ , figure of merit (FOM) is another parameter to characterize the sensing ability of LSPR sensor, which determines the detection limit. There are two ways to calculate FOM, (1)  $FOM = S/FWHM$ , where FWHM is the full width at half maximum of the resonance peak, (2)  $FOM^* = [dI/(I \cdot dn)]_{max}$ , where  $dI/I$  is the relative intensity change and  $dn$  is the refractive index change.[160] Here we use the first definition to calculate FOM because the second definition cannot be applied for  $\Delta T$  spectra, which gives  $FOM^* = \infty$  at where  $\Delta T = 0$ . To obtain FOM, the determination of FWHM could be very subjective and difficult for some complicated peaks. Here we only select three peaks,  $B_R$  ( $B_L$ ),  $D_R$  ( $D_L$ ), and  $F_R$  ( $F_L$ ) for FWHM determination. The obtained FWHM and FOM are listed in **Table 5.4.1**. The FWHM of  $\Delta T$  peak  $F_R$  ( $F_L$ ) lies between that of peaks  $B_R$  ( $B_L$ ) and  $D_R$  ( $D_L$ ). Therefore, subtraction between  $T(RCP)$  and  $T(LCP)$  does not reduce the FWHM significantly, but the FOM of  $\Delta T$  peak  $F_R$  ( $F_L$ ) is greater than that of  $B_R$  ( $B_L$ ) and  $D_R$  ( $D_L$ ), which is mainly caused by the increased sensitivity.

#### ***5.4.4 Application for bulk refractive index sensing: conclusion***

In conclusion, Au fan-shaped chiral nanostructures have been fabricated in large area and showed significant CD response. The fan-shaped chiral nanostructures have been applied

for refractive index sensing. The circularly polarized transmittance  $T(\text{RCP})$  and  $T(\text{LCP})$  show multiple resonances with different sensitivities. It is observed that  $\Delta T = T(\text{RCP}) - T(\text{LCP})$  can show an enhanced sensitivity compared with  $T(\text{RCP})$  and  $T(\text{LCP})$ . The mechanism of the enhanced sensitivity has been investigated. It is found that one transmittance peak and one transmittance valley in different circular polarizations in a similar wavelength range contribute to one  $\Delta T$  peak. The enhanced sensitivity can be achieved only if the transmittance peak or valley located at longer wavelength increases its contribution with increasing  $n$ , which is also confirmed by FDTD simulation. Such a chiral structure and optical measurements can serve as a new strategy to improve the performance of LSPR sensors.

## CHAPTER 6

### SUMMARY AND OUTLOOK

In this dissertation we have demonstrated that DSG on SACMs is a promising fabrication technique for chiral metamaterials and chiral metamaterial based optical devices. In this fabrication method, the relative orientation of monolayers with respect to the incident vapor is dynamically controlled to engineer the shadowing profiles of nanospheres so that various chiral nanostructures can be produced on nanospheres. Two distinct fabrication strategies based on this method have been proposed and applied, including a single-layer plasmonic nanostructure with chiral shapes, and a multi-layer nanostructure with plasmonic and dielectric layer helically stacked. The former strategy creates nanostructures with tunable chiral shapes and optical response, which depend on the monolayer orientations. The later one produces helical nanostructures with no dependence on the monolayer orientations. Different 3D chiral nanostructures have been realized with these two strategies, such as fan-shaped nanostructure, and Swiss roll nanostructure. The chiral optical properties of these nanostructures have been well investigated, and also confirmed by FDTD numerical simulations. Particularly, fan-shaped chiral nanostructures show the strongest chiral optical response, which is comparable with the highest response of those fabricated by EBL. Then the chiral optical response of this fan-shaped nanostructure is optimized experimentally by tuning the fabrication conditions.

The optimized fan-shape chiral nanostructures, produced on a  $1 \text{ cm}^2$  monocrystalline monolayer, can be potentially developed to be a chiral optical device. We have demonstrated that it can be used as a narrow-band circular polarizer after annealed. In addition, the fan-shaped nanostructure array has been transferred onto a flexible substrate to become an active chiral optical device, with chiral optical response tuned by mechanical deformations. The sensing ability of the fan-shaped nanostructure is also demonstrated, which shows an enhanced sensitivity for bulk refractive index sensing by measuring CD.

Although this DSG method has been demonstrated as a powerful fabrication technique for developing chiral meta-devices in the future, there is still much room for improvements. First, the quality of the template (monolayers) should be improved for device applications. For SACMs, the numbers of defects should be minimized and the area of a single monocrystalline monolayer needs to be increased further. Besides self-assembly, the deposition template can also be fabricated by other techniques to achieve a better quality, such as nanoimprint lithography. Second, the variation in structural shapes and surface roughness caused by the nature of DSG, need to be minimized. In Section 3.4.3, we have shown that annealing in vacuum is a promising and effective way, but further investigations are still needed. Finally, new fabrication strategies need to be developed to achieve chiral metamaterials with better chiral optical response or different functionalities. For example, metasurfaces have been prepared on substrates by the shadowing growth through nanosphere arrays,[161] which is a promising research direction in the future. Another promising fabrication strategy is to utilize co-deposition on SACMs or nano-hole arrays, in which two or more materials are evaporated and deposited onto templates simultaneously. The co-depositions can lead to double helices through nano-hole arrays, and even more complicated chiral nanostructures on other templates, which remains to be investigated further in the future.

## REFERENCE

1. Feynman, R.P., *There's plenty of room at the bottom*. Caltech Engineering and Science, 1960. **23**(5): p. 22-36.
2. Cui, T.J., D. Smith, and R. Liu, *Metamaterials: Theory, Design, and Applications*. 2009: Springer US.
3. Smith, D.R., S. Schultz, P. Markos, and C.M. Soukoulis, *Determination of effective permittivity and permeability of metamaterials from reflection and transmission coefficients*. Physical Review B, 2002. **65**(19): p. 195104.
4. Eleftheriades, G.V. and K.G. Balmain, *Negative-Refractive Metamaterials: Fundamental Principles and Applications*. 2005: Wiley.
5. Yao, K. and Y. Liu, *Plasmonic metamaterials*. Nanotechnology Reviews, 2014. **3**(2): p. 177-210.
6. Veselago, V.G., *The electrodynamics of substances with simultaneously negative values of  $\epsilon$  and  $\mu$* . Soviet Physics Uspekhi, 1968. **10**(4): p. 509-514.
7. Smith, D.R., W.J. Padilla, D.C. Vier, S.C. Nemat-Nasser, and S. Schultz, *Composite medium with simultaneously negative permeability and permittivity*. Physical Review Letters, 2000. **84**(18): p. 4184-4187.
8. Padilla, W.J., D.N. Basov, and D.R. Smith, *Negative refractive index metamaterials*. Materials Today, 2006. **9**(7-8): p. 28-35.

9. Ozbay, E., K. Guven, and K. Aydin, *Metamaterials with negative permeability and negative refractive index: experiments and simulations*. Journal of Optics a-Pure and Applied Optics, 2007. **9**(9): p. S301-S307.
10. Schurig, D., J.J. Mock, B.J. Justice, S.A. Cummer, J.B. Pendry, A.F. Starr, and D.R. Smith, *Metamaterial electromagnetic cloak at microwave frequencies*. Science, 2006. **314**(5801): p. 977-980.
11. Soukoulis, C.M., S. Linden, and M. Wegener, *Negative refractive index at optical wavelengths*. Science, 2007. **315**(5808): p. 47-49.
12. Liu, N., H. Guo, L. Fu, S. Kaiser, H. Schweizer, and H. Giessen, *Three-dimensional photonic metamaterials at optical frequencies*. Nature Materials, 2008. **7**(1): p. 31-37.
13. Shalaev, V.M., *Optical negative-index metamaterials*. Nature Photonics, 2007. **1**(1): p. 41-48.
14. Valentine, J., S. Zhang, T. Zentgraf, E. Ulin-Avila, D.A. Genov, G. Bartal, and X. Zhang, *Three-dimensional optical metamaterial with a negative refractive index*. Nature, 2008. **455**(7211): p. 376-379.
15. Ulf, L. and R.S. David, *Focus on cloaking and transformation optics*. New Journal of Physics, 2008. **10**(11): p. 115019.
16. Zhang, X. and Z.W. Liu, *Superlenses to overcome the diffraction limit*. Nature Materials, 2008. **7**(6): p. 435-441.
17. Drachev, V.P., V.A. Podolskiy, and A.V. Kildishev, *Hyperbolic metamaterials: new physics behind a classical problem*. Optics Express, 2013. **21**(12): p. 15048-15064.

18. Moitra, P., Y.M. Yang, Z. Anderson, I.I. Kravchenko, D.P. Briggs, and J. Valentine, *Realization of an all-dielectric zero-index optical metamaterial*. Nature Photonics, 2013. **7**(10): p. 791-795.
19. Choi, M., S.H. Lee, Y. Kim, S.B. Kang, J. Shin, M.H. Kwak, K.Y. Kang, Y.H. Lee, N. Park, and B. Min, *A terahertz metamaterial with unnaturally high refractive index*. Nature, 2011. **470**(7334): p. 369-373.
20. Iwanaga, M., *Photonic metamaterials: a new class of materials for manipulating light waves*. Science and Technology of Advanced Materials, 2012. **13**(5): p. 053002.
21. Gansel, J.K., M. Thiel, M.S. Rill, M. Decker, K. Bade, V. Saile, G. von Freymann, S. Linden, and M. Wegener, *Gold helix photonic metamaterial as broadband circular polarizer*. Science, 2009. **325**(5947): p. 1513-1515.
22. Hess, O., J.B. Pendry, S.A. Maier, R.F. Oulton, J.M. Hamm, and K.L. Tsakmakidis, *Active nanoplasmonic metamaterials*. Nature Materials, 2012. **11**(7): p. 573-584.
23. Shadrivov, I.V., M. Lapine, and Y.S. Kivshar, *Nonlinear, Tunable and Active Metamaterials*. 2014: Springer International Publishing.
24. Lapine, M., I.V. Shadrivov, and Y.S. Kivshar, *Colloquium: Nonlinear metamaterials*. Reviews of Modern Physics, 2014. **86**(3): p. 1093-1123.
25. Minovich, A.E., A.E. Miroshnichenko, A.Y. Bykov, T.V. Murzina, D.N. Neshev, and Y.S. Kivshar, *Functional and nonlinear optical metasurfaces*. Laser & Photonics Reviews, 2015. **9**(2): p. 195-213.
26. Pendry, J.B., *A chiral route to negative refraction*. Science, 2004. **306**(5700): p. 1353-5.
27. Smith, D.R., J.B. Pendry, and M.C. Wiltshire, *Metamaterials and negative refractive index*. Science, 2004. **305**(5685): p. 788-92.

28. Wiltshire, M.C.K., *Radio frequency (RF) metamaterials*. *Physica Status Solidi B*, 2007. **244**(4): p. 1227-1236.
29. He, Y., G. Larsen, X. Li, W. Ingram, F. Chen, and Y. Zhao, *Nanoscale conical Swiss Roll with broadband visible and NIR circular dichroism*. *Advanced Optical Materials*, 2015. **3**(3): p. 342-346.
30. Valev, V.K., J.J. Baumberg, C. Sibilia, and T. Verbiest, *Chirality and chiroptical effects in plasmonic nanostructures: fundamentals, recent progress, and outlook*. *Advanced Materials*, 2013. **25**(18): p. 2517-2534.
31. Wang, B., J. Zhou, T. Koschny, M. Kafesaki, and C.M. Soukoulis, *Chiral metamaterials: simulations and experiments*. *Journal of Optics A: Pure and Applied Optics*, 2009. **11**(11): p. 114003.
32. Helgert, C., E. Pshenay-Severin, M. Falkner, C. Menzel, C. Rockstuhl, E.B. Kley, A. Tunnermann, F. Lederer, and T. Pertsch, *Chiral metamaterial composed of three-dimensional plasmonic nanostructures*. *Nano Letters*, 2011. **11**(10): p. 4400-4404.
33. Dietrich, K., D. Lehr, C. Helgert, A. Tunnermann, and E.B. Kley, *Circular dichroism from chiral nanomaterial fabricated by on-edge lithography*. *Advanced Materials*, 2012. **24**(44): p. OP321-325.
34. Hentschel, M., M. Schaferling, T. Weiss, N. Liu, and H. Giessen, *Three-dimensional chiral plasmonic oligomers*. *Nano Letters*, 2012. **12**(5): p. 2542-2547.
35. Zhao, Y., M.A. Belkin, and A. Alu, *Twisted optical metamaterials for planarized ultrathin broadband circular polarizers*. *Nature Communications*, 2012. **3**: p. 870.
36. Yin, X., M. Schaferling, B. Metzger, and H. Giessen, *Interpreting chiral nanophotonic spectra: the plasmonic Born-Kuhn model*. *Nano Letters*, 2013. **13**(12): p. 6238-6243.

37. Cui, Y., L. Kang, S. Lan, S. Rodrigues, and W. Cai, *Giant chiral optical response from a twisted-arc metamaterial*. Nano Letters, 2014. **14**(2): p. 1021-1025.
38. Esposito, M., V. Tasco, F. Todisco, A. Benedetti, D. Sanvitto, and A. Passaseo, *Three dimensional chiral metamaterial nanospirals in the visible range by vertically compensated focused Ion beam induced-deposition*. Advanced Optical Materials, 2014. **2**(2): p. 154-161.
39. Esposito, M., V. Tasco, M. Cuscunà, F. Todisco, A. Benedetti, I. Tarantini, M.D. Giorgi, D. Sanvitto, and A. Passaseo, *Nanoscale 3D chiral plasmonic helices with circular dichroism at Visible frequencies*. ACS Photonics, 2015. **2**(1): p. 105-114.
40. Kuzyk, A., R. Schreiber, Z. Fan, G. Pardatscher, E.M. Roller, A. Hogele, F.C. Simmel, A.O. Govorov, and T. Liedl, *DNA-based self-assembly of chiral plasmonic nanostructures with tailored optical response*. Nature, 2012. **483**(7389): p. 311-314.
41. Schreiber, R., N. Luong, Z. Fan, A. Kuzyk, P.C. Nickels, T. Zhang, D.M. Smith, B. Yurke, W. Kuang, A.O. Govorov, and T. Liedl, *Chiral plasmonic DNA nanostructures with switchable circular dichroism*. Nature Communications, 2013. **4**: p. 2948.
42. Song, C., M.G. Blaber, G. Zhao, P. Zhang, H.C. Fry, G.C. Schatz, and N.L. Rosi, *Tailorable plasmonic circular dichroism properties of helical nanoparticle superstructures*. Nano Letters, 2013. **13**(7): p. 3256-3261.
43. Querejeta-Fernandez, A., G. Chauve, M. Methot, J. Bouchard, and E. Kumacheva, *Chiral plasmonic films formed by gold nanorods and cellulose nanocrystals*. Journal of the American Chemical Society, 2014. **136**(12): p. 4788-4793.

44. Lan, X., X. Lu, C. Shen, Y. Ke, W. Ni, and Q. Wang, *Au nanorod helical superstructures with designed chirality*. Journal of the American Chemical Society, 2015. **137**(1): p. 457-462.
45. Frank, B., X.H. Yin, M. Schaferling, J. Zhao, S.M. Hein, P.V. Braun, and H. Giessen, *Large-Area 3D Chiral Plasmonic Structures*. ACS Nano, 2013. **7**(7): p. 6321-6329.
46. Mark, A.G., J.G. Gibbs, T.C. Lee, and P. Fischer, *Hybrid nanocolloids with programmed three-dimensional shape and material composition*. Nature Materials, 2013. **12**(9): p. 802-807.
47. Singh, J.H., G. Nair, A. Ghosh, and A. Ghosh, *Wafer scale fabrication of porous three-dimensional plasmonic metamaterials for the visible region: chiral and beyond*. Nanoscale, 2013. **5**(16): p. 7224-7228.
48. Ogier, R., Y.R. Fang, M. Svedendahl, P. Johansson, and M. Kall, *Macroscopic layers of chiral plasmonic nanoparticle oligomers from colloidal lithography*. ACS Photonics, 2014. **1**(10): p. 1074-1081.
49. Zhou, J.F., D.R. Chowdhury, R.K. Zhao, A.K. Azad, H.T. Chen, C.M. Soukoulis, A.J. Taylor, and J.F. O'Hara, *Terahertz chiral metamaterials with giant and dynamically tunable optical activity*. Physical Review B, 2012. **86**(3): p. 035448.
50. Zhang, S., Y.S. Park, J.S. Li, X.C. Lu, W.L. Zhang, and X. Zhang, *Negative refractive index in chiral metamaterials*. Physical Review Letters, 2009. **102**(2): p. 023901.
51. Wu, C., H.Q. Li, Z.Y. Wei, X.T. Yu, and C.T. Chan, *Theory and experimental realization of negative refraction in a metallic helix array*. Physical Review Letters, 2010. **105**(24): p. 247401.

52. Wu, S., Z. Zhang, Y. Zhang, K. Zhang, L. Zhou, X. Zhang, and Y. Zhu, *Enhanced rotation of the polarization of a light beam transmitted through a silver film with an array of perforated S-shaped holes*. Physical Review Letters, 2013. **110**(20): p. 207401.
53. Turner, M.D., M. Saba, Q. Zhang, B.P. Cumming, G.E. Schröder-Turk, and M. Gu, *Miniature chiral beamsplitter based on gyroid photonic crystals*. Nature Photonics, 2013. **7**(10): p. 801-805.
54. Zhao, R., J. Zhou, T. Koschny, E.N. Economou, and C.M. Soukoulis, *Repulsive Casimir Force in Chiral Metamaterials*. Physical Review Letters, 2009. **103**(10): p. 103602.
55. Zhao, R., T. Koschny, E.N. Economou, and C.M. Soukoulis, *Comparison of chiral metamaterial designs for repulsive Casimir force*. Physical Review B, 2010. **81**(23): p. 235126.
56. Wang, H.L. and X.D. Zhang, *Unusual spin Hall effect of a light beam in chiral metamaterials*. Physical Review A, 2011. **83**(5): p. 053820.
57. Hendry, E., T. Carpy, J. Johnston, M. Popland, R.V. Mikhaylovskiy, A.J. Laphorn, S.M. Kelly, L.D. Barron, N. Gadegaard, and M. Kadodwala, *Ultrasensitive detection and characterization of biomolecules using superchiral fields*. Nature Nanotechnology, 2010. **5**(11): p. 783-787.
58. Tang, Y. and A.E. Cohen, *Optical chirality and its interaction with matter*. Physical Review Letters, 2010. **104**(16): p. 163901.
59. Valev, V.K., *Characterization of nanostructured plasmonic surfaces with second harmonic generation*. Langmuir, 2012. **28**(44): p. 15454-15471.
60. Ren, M., E. Plum, J. Xu, and N.I. Zheludev, *Giant nonlinear optical activity in a plasmonic metamaterial*. Nature Communications, 2012. **3**: p. 833.

61. Rodrigues, S.P., S. Lan, L. Kang, Y. Cui, and W. Cai, *Nonlinear imaging and spectroscopy of chiral metamaterials*. *Advanced Materials*, 2014. **26**(35): p. 6157-6162.
62. Kuzyk, A., R. Schreiber, H. Zhang, A.O. Govorov, T. Liedl, and N. Liu, *Reconfigurable 3D plasmonic metamolecules*. *Nature Materials*, 2014. **13**(9): p. 862-866.
63. Zhang, S., J. Zhou, Y.S. Park, J. Rho, R. Singh, S. Nam, A.K. Azad, H.T. Chen, X. Yin, A.J. Taylor, and X. Zhang, *Photoinduced handedness switching in terahertz chiral metamolecules*. *Nature Communications*, 2012. **3**: p. 942.
64. Shvets, G. and I. Tsukerman, *Plasmonics and Plasmonic Metamaterials: Analysis and Applications*. 2012: World Scientific Publishing Company.
65. Willets, K.A. and R.P. Van Duyne, *Localized surface plasmon resonance spectroscopy and sensing*. *Annual Review of Physical Chemistry*, 2007. **58**: p. 267-297.
66. Mayer, K.M. and J.H. Hafner, *Localized surface plasmon resonance sensors*. *Chemical Reviews*, 2011. **111**(6): p. 3828-3857.
67. Sommerfeld, A., *Ueber die Fortpflanzung elektrodynamischer Wellen längs eines Drahtes*. *Annalen der Physik*, 1899. **303**(2): p. 233-290.
68. Mie, G., *Beiträge zur Optik trüber Medien, speziell kolloidaler Metallösungen*. *Annalen der Physik*, 1908. **330**(3): p. 377-445.
69. Fleischmann, M., P.J. Hendra, and A.J. McQuillan, *Raman spectra of pyridine adsorbed at a silver electrode*. *Chemical Physics Letters*, 1974. **26**(2): p. 163-166.
70. Jeanmaire, D.L. and R.P. Van Duyne, *Surface Raman spectroelectrochemistry*. *Journal of electroanalytical chemistry and interfacial electrochemistry*, 1977. **84**(1): p. 1-20.

71. Daghestani, H.N. and B.W. Day, *Theory and applications of surface plasmon resonance, resonant mirror, resonant waveguide grating, and dual polarization interferometry biosensors*. Sensors, 2010. **10**(11): p. 9630-9646.
72. Juan, M.L., M. Righini, and R. Quidant, *Plasmon nano-optical tweezers*. Nature Photonics, 2011. **5**(6): p. 349-356.
73. Stiles, P.L., J.A. Dieringer, N.C. Shah, and R.R. Van Duyne, *Surface-enhanced Raman spectroscopy*. Annual Review of Analytical Chemistry, 2008. **1**: p. 601-626.
74. Schlucker, S., *Surface-enhanced Raman spectroscopy: concepts and chemical applications*. Angewandte Chemie International Edition, 2014. **53**(19): p. 4756-4795.
75. Hou, W.B. and S.B. Cronin, *A review of surface plasmon resonance-enhanced photocatalysis*. Advanced Functional Materials, 2013. **23**(13): p. 1612-1619.
76. Zhang, X.M., Y.L. Chen, R.S. Liu, and D.P. Tsai, *Plasmonic photocatalysis*. Reports on Progress in Physics, 2013. **76**(4): p. 046401.
77. Herzog, J.B., M.W. Knight, and D. Natelson, *Thermoplasmonics: quantifying plasmonic heating in single nanowires*. Nano Letters, 2014. **14**(2): p. 499-503.
78. Rosenfeld, L., *Quantum-mechanical theory of the natural optical activity of liquids and gases*. Zeitschrift für Physik, 1928. **52**: p. 161-174.
79. Tinoco, I. and R.W. Woody, *Optical rotation of oriented helices .IV. free electron on helix*. Journal of Chemical Physics, 1964. **40**(1): p. 160.
80. Moore, D. and I. Tinoco, *The circular-dichroism of large helices - a free particle on a helix*. Journal of Chemical Physics, 1980. **72**(5): p. 3396-3400.
81. Bohren, C.F., *Light-scattering by an optically-active sphere*. Chemical Physics Letters, 1974. **29**(3): p. 458-462.

82. Condon, E.U., *Theories of optical rotatory power*. Reviews of Modern Physics, 1937. **9**(4): p. 432-457.
83. Lipkin, D.M., *Existence of a new conservation law in electromagnetic theory*. Journal of Mathematical Physics, 1964. **5**(5): p. 696-700.
84. Schaferling, M., X.H. Yin, N. Engheta, and H. Giessen, *Helical plasmonic nanostructures as prototypical chiral near-field sources*. ACS Photonics, 2014. **1**(6): p. 530-537.
85. Schaferling, M., D. Dregely, M. Hentschel, and H. Giessen, *Tailoring enhanced optical chirality: design principles for chiral plasmonic nanostructures*. Physical Review X, 2012. **2**(3): p. 031010.
86. Li, W., Z.J. Coppens, L.V. Besteiro, W. Wang, A.O. Govorov, and J. Valentine, *Circularly polarized light detection with hot electrons in chiral plasmonic metamaterials*. Nature Communications, 2015. **6**: p. 8379.
87. Yin, X., M. Schaferling, A.K. Michel, A. Tittl, M. Wuttig, T. Taubner, and H. Giessen, *Active chiral plasmonics*. Nano Letters, 2015. **15**(7): p. 4255-4260.
88. Kan, T., A. Isozaki, N. Kanda, N. Nemoto, K. Konishi, H. Takahashi, M. Kuwata-Gonokami, K. Matsumoto, and I. Shimoyama, *Enantiomeric switching of chiral metamaterial for terahertz polarization modulation employing vertically deformable MEMS spirals*. Nature Communications, 2015. **6**: p. 8422.
89. Armelles, G., B. Caballero, P. Prieto, F. Garcia, A. Cebollada, M.U. Gonzalez, and A. Garcia-Martin, *Magnetic field modulation of chiroptical effects in magnetoplasmonic structures*. Nanoscale, 2014. **6**(7): p. 3737-3741.

90. Eslami, S., J.G. Gibbs, Y. Rechkemmer, J. van Slageren, M. Alarcón-Correa, T.-C. Lee, A.G. Mark, G.L.J.A. Rikken, and P. Fischer, *Chiral nanomagnets*. ACS Photonics, 2014. **1**(11): p. 1231-1236.
91. Yan, W., L. Xu, W. Ma, L. Liu, L. Wang, H. Kuang, and C. Xu, *Pyramidal sensor platform with reversible chiroptical signals for DNA detection*. Small, 2014. **10**(21): p. 4293-4297.
92. Valev, V.K., J.J. Baumberg, B. De Clercq, N. Braz, X. Zheng, E.J. Osley, S. Vandendriessche, M. Hojeij, C. Blejean, J. Mertens, C.G. Biris, V. Volskiy, M. Ameloot, Y. Ekinici, G.A. Vandenbosch, P.A. Warburton, V.V. Moshchalkov, N.C. Panoiu, and T. Verbiest, *Nonlinear superchiral meta-surfaces: tuning chirality and disentangling non-reciprocity at the nanoscale*. Advanced Materials, 2014. **26**(24): p. 4074-4081.
93. Helgert, C., K. Dietrich, D. Lehr, T. Käsebier, T. Pertsch, and E.B. Kley, *A dedicated multilayer technique for the fabrication of three-dimensional metallic nanoparticles*. Microelectronic Engineering, 2012. **97**: p. 181-184.
94. Hentschel, M., L. Wu, M. Schaferling, P. Bai, E.P. Li, and H. Giessen, *Optical properties of chiral three-dimensional plasmonic oligomers at the onset of charge-transfer plasmons*. ACS Nano, 2012. **6**(11): p. 10355-10365.
95. Vignolini, S., N.A. Yufa, P.S. Cunha, S. Guldin, I. Rushkin, M. Stefik, K. Hur, U. Wiesner, J.J. Baumberg, and U. Steiner, *A 3D optical metamaterial made by self-assembly*. Advanced Materials, 2012. **24**(10): p. OP23-27.
96. Gansel, J.K., M. Latzel, A. Frölich, J. Kaschke, M. Thiel, and M. Wegener, *Tapered gold-helix metamaterials as improved circular polarizers*. Applied Physics Letters, 2012. **100**(10): p. 101109.

97. Leroux, F., M. Gysemans, S. Bals, K.J. Batenburg, J. Snauwaert, T. Verbiest, C. Van Haesendonck, and G. Van Tendeloo, *Three-dimensional characterization of helical silver nanochains mediated by protein assemblies*. *Advanced Materials*, 2010. **22**(19): p. 2193-2197.
98. Hur, K., Y. Francescato, V. Giannini, S.A. Maier, R.G. Hennig, and U. Wiesner, *Three-dimensionally isotropic negative refractive index materials from block copolymer self-assembled chiral gyroid networks*. *Angewandte Chemie International Edition*, 2011. **50**(50): p. 11985-11989.
99. Larsen, G.K., Y.Z. He, J. Wang, and Y.P. Zhao, *Scalable fabrication of composite Ti/Ag plasmonic helices: controlling Morphology and optical activity by tailoring material properties*. *Advanced Optical Materials*, 2014. **2**(3): p. 245-249.
100. Wang, Z.M., *FIB Nanostructures*. 2014: Springer International Publishing.
101. Colson, P., C. Henrist, and R. Cloots, *Nanosphere lithography: A powerful method for the controlled manufacturing of nanomaterials*. *Journal of Nanomaterials*, 2013. **2013**: p. 1-19.
102. Fredriksson, H., Y. Alaverdyan, A. Dmitriev, C. Langhammer, D.S. Sutherland, M. Zaech, and B. Kasemo, *Hole-mask colloidal lithography*. *Advanced Materials*, 2007. **19**(23): p. 4297-4302.
103. Xie, S.W., J.Z. Yang, X. Xiao, Y.D. Hou, J.L. Du, L. Pang, X. Li, and F.H. Gao, *Scalable fabrication of quasi-three-dimensional chiral plasmonic oligomers based on stepwise colloid sphere lithography technology*. *Nanoscale Research Letters*, 2015. **10**: p. 393.

104. Krause, K.M., M.T. Taschuk, and M.J. Brett, *Glancing angle deposition on a roll: Towards high-throughput nanostructured thin films*. Journal of Vacuum Science & Technology A, 2013. **31**(3): p. 031507.
105. Kennedy, S.R. and M.J. Brett, *Porous broadband antireflection coating by glancing angle deposition*. Applied Optics, 2003. **42**(22): p. 4573-4579.
106. Summers, M.A. and M.J. Brett, *Optimization of periodic column growth in glancing angle deposition for photonic crystal fabrication*. Nanotechnology, 2008. **19**(41): p. 415203.
107. Robbie, K., D.J. Broer, and M.J. Brett, *Chiral nematic order in liquid crystals imposed by an engineered inorganic nanostructure*. Nature, 1999. **399**(6738): p. 764-766.
108. Chaney, S.B., S. Shanmukh, R.A. Dluhy, and Y.P. Zhao, *Aligned silver nanorod arrays produce high sensitivity surface-enhanced Raman spectroscopy substrates*. Applied Physics Letters, 2005. **87**(3): p. 031908.
109. Singh, J.P., D.L. Liu, D.X. Ye, R.C. Picu, T.M. Lu, and G.C. Wang, *Metal-coated Si springs: Nanoelectromechanical actuators*. Applied Physics Letters, 2004. **84**(18): p. 3657-3659.
110. He, Y.Z., P. Basnet, S.E.H. Murph, and Y.P. Zhao, *Ag Nanoparticle Embedded TiO<sub>2</sub> Composite Nanorod Arrays Fabricated by Oblique Angle Deposition: Toward Plasmonic Photocatalysis*. ACS Applied Materials & Interfaces, 2013. **5**(22): p. 11818-11827.
111. Xie, Z., B.M. Henry, K.R. Kirov, H.E. Smith, A. Barkhouse, C.R.M. Grovenor, H.E. Assender, G.A.D. Briggs, G.R. Webster, P.L. Burn, M. Kano, and Y. Tsukahara, *Study of the effect of changing the microstructure of titania layers on composite solar cell performance*. Thin Solid Films, 2006. **511**: p. 523-528.

112. Ishida, T., K. Tohma, H. Yoshida, and K. Shinohara, *More than 1 Gb/in(2) recording on obliquely oriented thin film tape*. IEEE Transactions on Magnetics, 2000. **36**(1): p. 183-188.
113. Taschuk, M.T., J.J. Steele, A.C. van Popta, and M.J. Brett, *Photocatalytic regeneration of interdigitated capacitor relative humidity sensors fabricated by glancing angle deposition*. Sensors and Actuators B-Chemical, 2008. **134**(2): p. 666-671.
114. Fu, J.X., A. Collins, and Y.P. Zhao, *Optical properties and biosensor application of ultrathin silver films prepared by oblique angle deposition*. Journal of Physical Chemistry C, 2008. **112**(43): p. 16784-16791.
115. Steele, J.J., M.T. Taschuk, and M.J. Brett, *Response time of nanostructured relative humidity sensors*. Sensors and Actuators B-Chemical, 2009. **140**(2): p. 610-615.
116. Zhao, Y., *Dynamic Shadowing Growth and Its Energy Applications*. Frontiers in Energy Research, 2014. **2**: p. 38.
117. Jensen, M.O. and M.J. Brett, *Periodically structured glancing angle deposition thin films*. IEEE Transactions on Nanotechnology, 2005. **4**(2): p. 269-277.
118. Han, C., H.M. Leung, and W.Y. Tam, *Chiral metamaterials by shadowing vapor deposition*. Journal of Optics 2013. **15**(7): p. 072101.
119. Yeom, B., H.N. Zhang, H. Zhang, J.I. Park, K. Kim, A.O. Govorov, and N.A. Kotov, *Chiral plasmonic nanostructures on achiral nanopillars*. Nano Letters, 2013. **13**(11): p. 5277-5283.
120. Hou, Y.D., S.H. Li, Y.R. Su, X. Huang, Y. Liu, L. Huang, Y. Yu, F.H. Gao, Z.Y. Zhang, and J.L. Du, *Design and fabrication of three-dimensional chiral nanostructures based on stepwise glancing angle deposition technology*. Langmuir, 2013. **29**(3): p. 867-872.

121. Zhang, J., Y. Li, X. Zhang, and B. Yang, *Colloidal self-assembly meets nanofabrication: from two-dimensional colloidal crystals to nanostructure arrays*. *Advanced Materials*, 2010. **22**(38): p. 4249-4269.
122. Vogel, N., C.K. Weiss, and K. Landfester, *From soft to hard: the generation of functional and complex colloidal monolayers for nanolithography*. *Soft Matter*, 2012. **8**(15): p. 4044-4061.
123. Liang, J.S., S.H. Chen, E.Y. Lin, D.F. Luo, and S.J. Jiang, *Morphology evolution of glancing angle deposition Ag films on nanosphere-array substrates: Kinetic Monte Carlo simulation*. *Computational Materials Science*, 2013. **79**: p. 31-35.
124. Hubartt, B.C., X.J. Liu, and J.G. Amar, *Large-scale molecular dynamics simulations of glancing angle deposition*. *Journal of Applied Physics*, 2013. **114**(8): p. 083517.
125. Buzea, C., K. Kaminska, G. Beydaghyan, T. Brown, C. Elliott, C. Dean, and K. Robbie, *Thickness and density evaluation for nanostructured thin films by glancing angle deposition*. *Journal of Vacuum Science & Technology B*, 2005. **23**(6): p. 2545-2552.
126. van Popta, A.C., M.J. Brett, and J.C. Sit, *Double-handed circular Bragg phenomena in polygonal helix thin films*. *Journal of Applied Physics*, 2005. **98**(8): p. 083517.
127. Kane, Y., *Numerical solution of initial boundary value problems involving maxwell's equations in isotropic media*. *Antennas and Propagation, IEEE Transactions on*, 1966. **14**(3): p. 302-307.
128. Hao, Y. and R. Mittra, *FDTD Modeling of Metamaterials : Theory and Applications*. 2009, Boston [i.e. Norwood], MA: Artech House, Inc.
129. Gai, H.F., J. Wang, and Q. Tian, *Modified Debye model parameters of metals applicable for broadband calculations*. *Applied Optics*, 2007. **46**(12): p. 2229-2233.

130. Sagor, R.H., M.G. Saber, M.T. Al-Amin, and A. Al Noor, *An optimization method for parameter extraction of metals using modified Debye model*. Springerplus, 2013. **2**: p. 426.
131. Larsen, G.K., Y. He, W. Ingram, and Y. Zhao, *Hidden chirality in superficially racemic patchy silver films*. Nano Letters, 2013. **13**(12): p. 6228-6232.
132. He, Y., K. Lawrence, W. Ingram, and Y. Zhao, *Strong local chiroptical response in racemic patchy silver films: enabling a large-area chiroptical device*. ACS Photonics, 2015. **2**(9): p. 1246-1252.
133. Landström, L., D. Brodoceanu, N. Arnold, K. Piglmayer, and D. Bäuerle, *Photonic properties of silicon-coated colloidal monolayers*. Applied Physics A, 2005. **81**(5): p. 911-913.
134. Yi, D.K., J.-H. Lee, J.A. Rogers, and U. Paik, *Two-dimensional nanohybridization of gold nanorods and polystyrene colloids*. Applied Physics Letters, 2009. **94**(8): p. 084104.
135. Jose-Yacaman, M., C. Gutierrez-Wing, M. Miki, D.Q. Yang, K.N. Piyakis, and E. Sacher, *Surface diffusion and coalescence of mobile metal nanoparticles*. Journal of Physical Chemistry B, 2005. **109**(19): p. 9703-9711.
136. Gibbs, J.G., A.G. Mark, S. Eslami, and P. Fischer, *Plasmonic nanohelix metamaterials with tailorable giant circular dichroism*. Applied Physics Letters, 2013. **103**(21): p. 213101.
137. Maier, S., *Plasmonics: Fundamentals and Applications*. 2007: Springer.
138. Miyazaki, H.T., H. Miyazaki, K. Ohtaka, and T. Sato, *Photonic band in two-dimensional lattices of micrometer-sized spheres mechanically arranged under a scanning electron microscope*. Journal of Applied Physics, 2000. **87**(10): p. 7152-7158.

139. Sun, J., Y.Y. Li, H. Dong, P. Zhan, C.J. Tang, M.W. Zhu, and Z.L. Wang, *Fabrication and light-transmission properties of monolayer square symmetric colloidal crystals via controlled convective self-assembly on 1D grooves*. *Advanced Materials*, 2008. **20**(1): p. 123-128.
140. Demetriadou, A. and J.B. Pendry, *Extreme chirality in Swiss roll metamaterials*. *Journal of Physics: Condensed Matter*, 2009. **21**(37): p. 376003.
141. Demetriadou, A. and J.B. Pendry, *Chirality in Swiss Roll metamaterials*. *Physica B: Condensed Matter*, 2010. **405**(14): p. 2943-2946.
142. Wiltshire, M.C., J.B. Pendry, I.R. Young, D.J. Larkman, D.J. Gilderdale, and J.V. Hajnal, *Microstructured magnetic materials for RF flux guides in magnetic resonance imaging*. *Science*, 2001. **291**(5505): p. 849-851.
143. Wiltshire, M.C.K., J.V. Hajnal, J.B. Pendry, D.J. Edwards, and C.J. Stevens, *Metamaterial endoscope for magnetic field transfer: near field imaging with magnetic wires*. *Optics Express*, 2003. **11**(7): p. 709-715.
144. Wiltshire, M.C.K., J.B. Pendry, W. Williams, and J.V. Hajnal, *An effective medium description of 'Swiss Rolls', a magnetic metamaterial*. *Journal of Physics: Condensed Matter*, 2007. **19**(45): p. 456216.
145. Wiltshire, M.C.K., J.B. Pendry, and J.V. Hajnal, *Sub-wavelength imaging at radio frequency*. *Journal of Physics: Condensed Matter*, 2006. **18**(22): p. L315-L321.
146. Wiltshire, M.C., J.B. Pendry, and J.V. Hajnal, *Chiral Swiss rolls show a negative refractive index*. *Journal of Physics: Condensed Matter*, 2009. **21**(29): p. 292201.

147. Cendula, P., S. Kiravittaya, Y. Mei, C. Deneke, and O. Schmidt, *Bending and wrinkling as competing relaxation pathways for strained free-hanging films*. Physical Review B, 2009. **79**(8): p. 085429.
148. Huang, G. and Y. Mei, *Thinning and shaping solid films into functional and integrative nanomembranes*. Advanced Materials 2012. **24**(19): p. 2517-2546.
149. Schwaiger, S., M. Bröll, A. Krohn, A. Stemmann, C. Heyn, Y. Stark, D. Stickler, D. Heitmann, and S. Mendach, *Rolled-up three-dimensional metamaterials with a tunable plasma frequency in the visible regime*. Physical Review Letters, 2009. **102**(16): p. 163903.
150. Schwaiger, S., A. Rottler, M. Bröll, J. Ehlermann, A. Stemmann, D. Stickler, C. Heyn, D. Heitmann, and S. Mendach, *Broadband operation of rolled-up hyperlenses*. Physical Review B, 2012. **85**(23): p. 235309.
151. Rottler, A., M. Harland, M. Bröll, S. Schwaiger, D. Stickler, A. Stemmann, C. Heyn, D. Heitmann, and S. Mendach, *Rolled-up nanotechnology for the fabrication of three-dimensional fishnet-type GaAs-metal metamaterials with negative refractive index at near-infrared frequencies*. Applied Physics Letters, 2012. **100**(15): p. 151104.
152. Ye, D.X., T. Karabacak, R.C. Picu, G.C. Wang, and T.M. Lu, *Uniform Si nanostructures grown by oblique angle deposition with substrate swing rotation*. Nanotechnology, 2005. **16**(9): p. 1717-1723.
153. Hsu, C.-M., S.T. Connor, M.X. Tang, and Y. Cui, *Wafer-scale silicon nanopillars and nanocones by Langmuir–Blodgett assembly and etching*. Applied Physics Letters, 2008. **93**(13): p. 133109.
154. He, Y., G.K. Larsen, W. Ingram, and Y. Zhao, *Tunable three-dimensional helically stacked plasmonic layers on nanosphere monolayers*. Nano Letters, 2014. **14**(4): p. 1976-1981.

155. Mark, J.E., *Polymer Data Handbook*. 1999: Oxford University Press.
156. Szunerits, S. and R. Boukherroub, *Sensing using localised surface plasmon resonance sensors*. Chemical Communications, 2012. **48**(72): p. 8999-9010.
157. Cao, J., T. Sun, and K.T.V. Grattan, *Gold nanorod-based localized surface plasmon resonance biosensors: A review*. Sensors and Actuators B-Chemical, 2014. **195**: p. 332-351.
158. Unser, S., I. Bruzas, J. He, and L. Sagle, *Localized surface plasmon resonance biosensing: current challenges and approaches*. Sensors, 2015. **15**(7): p. 15684-15716.
159. Weast, R.C., *CRC Handbook of Chemistry and Physics*. 64 ed. 1984, Boca Raton, FL: CRC Press.
160. Becker, J., A. Trügler, A. Jakab, U. Hohenester, and C. Sönnichsen, *The optimal aspect ratio of gold nanorods for plasmonic bio-sensing*. Plasmonics, 2010. **5**(2): p. 161-167.
161. Nemiroski, A., M. Gonidec, J.M. Fox, P. Jean-Remy, E. Turnage, and G.M. Whitesides, *Engineering shadows to fabricate optical metasurfaces*. ACS Nano, 2014. **8**(11): p. 11061-11070.